DNA Architectonics: Self-Assembly of Amphiphilic Oligonucleotides into Supramolecular Nanostructures

Inauguraldissertation
der Philosophisch-naturwissenschaftlichen Fakultät
der Universität Bern

vorgelegt von
Simon Rothenbühler
von Lauperswil

Leiter der Arbeit:
Prof. Dr. Robert Häner
Departement für Chemie, Biochemie und Pharmazie

This work is licensed under the CC BY-NC-ND 2.5 CH License. To view a copy of this license, visit http://creativecommons.org/licenses/by-nc-nd/2.5/ch/ or send a letter to Creative Commons, PO Box 1866, Mountain View, CA 94042, USA.

source: https://doi.org/10.48549/3969 | downloaded: 12.10.2024

DNA Architectonics: Self-Assembly of Amphiphilic Oligonucleotides into Supramolecular Nanostructures

Inauguraldissertation
der Philosophisch-naturwissenschaftlichen Fakultät
der Universität Bern

vorgelegt von
Simon Rothenbühler
von Lauperswil

Leiter der Arbeit:
Prof. Dr. Robert Häner
Departement für Chemie, Biochemie und Pharmazie

Von der Philosophisch-naturwissenschaftlichen Fakultät angenommen.

Bern, 13. Mai 2022

Der Dekan
Prof. Dr. Zoltan Balogh

Acknowledgments

I sincerely thank Prof. Dr. Robert Häner for the encouragement, expertise as well as giving me the opportunity to explore the exciting research field directed towards DNA-constructed self-assemblies. I express my thanks to Prof. Dr. Eugen Stulz and Prof. Dr. Paola Luciani for assessing my work.

Further, I express my gratitude for the cryo-EM specialists and collaborators Prof. Dr. Benoît Zuber and Dr. Ioan Iacovache. Cryo-EM experiments provided detailed and invaluable insights on how the DNA nanostructures are assembled.

I thank Prof. Dr. Antonia Neels and Dr. Neda Iranpour Anaraki for performing the SAXS measurements, Prof. Dr. Paola Luciani and Dr. Florian Weber for conducting the cytotoxicity experiments, and Prof. Dr. Ernst Meyer and his research group, especially Dr. Rémy Pawlak, Dr. Philipp D'Astolfo, and Dr. Antoine Hinaut, for the collaborative work about on-surface polymerization and cryo-force spectroscopy experiments.

Moreover, I thank for the inputs and help of all current and former members of the Häner research group. Particularly Dr. Simon Langenegger, for giving me useful advice and all the constructive discussions. In addition, I thank Adrian Gonzalez for his contribution in the course of his Master's thesis.

The DCBP staff members including all the in-house services as well as the financial support by the Swiss National Science Foundation (SNF) and the University of Bern are thankfully acknowledged.

Finally, my appreciation and thanks are devoted to my family and friends who supported me during all the years.

Table of Contents

Summary **1**

1 Introduction **2**

1.1 Supramolecular Polymers in Aqueous Medium 2

1.2 Structure of DNA 6

1.3 Preparation of Synthetic Oligonucleotides 8

1.4 Aggregation-Induced Emission-Active DNA Hybrids 9

1.5 DNA Nanostructures 11

2 Aim of the Thesis **16**

3 Self-Assembly of 3'-End Modified TPE-DNA Conjugates **17**

3.1 Results and Discussion 17

3.1.1 Spectroscopic Characterization of *E*-TPE Diol and *Z*-TPE Diol 17

3.1.2 Overview of 3'-End Modified TPE-DNA Conjugates 18

3.1.3 Spectroscopic Characterization of 3'-End Modified TPE-DNA Conjugates 20

3.1.4 Atomic Force Microscopy 22

3.1.5 Transmission Electron Microscopy 24

3.1.6 Cryo-Electron Microscopy 24

3.1.7 Ethidium Bromide Intercalation 30

3.1.8 Accessibility and Addressability Study with Light-Harvesting Experiments 33

3.1.9 Cytotoxicity Assays 37

3.2 Conclusions and Outlook 39
3.3 Appendix – Chapter 3 41
3.3.1 Organic Synthesis 41
3.3.2 NMR Spectra 47
3.3.3 Synthesis of Oligonucleotides 55
3.3.4 Spectroscopic and Microscopic Measurements 58
3.3.5 Cryo-EM Distance Measurements 69

4 Supramolecular Assembly of 3'-/5'-End Modified TPE-DNA Conjugates 71
4.1 Results and Discussion 71
4.2 Conclusions and Outlook 85
4.3 Appendix – Chapter 4 87
4.3.1 Synthesis of Oligonucleotides 87
4.3.2 Spectroscopic and Microscopic Measurements 97
4.3.3 Cryo-EM Distance Measurements 102

5 DNA Architectonics 105
5.1 Results and Discussion 105
5.1.1 Effect of Short PEG_6 Conjugated DNA 107
5.1.2 Influence of DNA-PEGylation 109
5.1.3 Impact of a Branched GalNAc Moiety 115
5.2 Conclusions and Outlook 122
5.3 Appendix – Chapter 5 124
5.3.1 Synthesis of Oligonucleotides 124
5.3.2 Spectroscopic and Microscopic Measurements 130
5.3.3 Cryo-EM Distance Measurements 138

6 Supramolecular Assembly of a 40-mer DNA 142

6.1 Results and Discussion 142

6.2 Conclusions and Outlook 148

6.3 Appendix – Chapter 6 149

6.3.1 Cryo-EM Distance Measurements 149

7 Self-Assembly of TPE Trimers 150

7.1 Synthetic Pathway for the Preparation of TPE Trimers 150

7.2 Results and Discussion 152

7.2.1 Spectroscopic Characterization of (*E*-TPE)$_3$ and (*Z*-TPE)$_3$ in Ethanol 152

7.2.2 Self-Assembly of (*E*-TPE)$_3$ and (*Z*-TPE)$_3$ in Aqueous Medium 153

7.3 Conclusions and Outlook 164

7.4 Appendix – Chapter 7 165

7.4.1 Organic Synthesis 165

7.4.2 NMR Spectra 169

7.4.3 MS Spectra 179

8 On-Surface Chemistry 181

8.1 Introduction 181

8.2 Results and Discussion 183

8.2.1 2,7-Dibromocyclopenta[*hi*]aceanthrylene 183

8.2.2 2,7-Dibromopyrene-4,5,9,10-tetraone 184

8.2.3 TerPy-Modified DNA 185

8.3 Conclusions and Outlook 186

8.4 Appendix – Chapter 8 187

8.4.1 Organic Synthesis of 2,7-Dibromopyrene-4,5,9,10-tetraone 187

8.4.2 Organic Synthesis of TerPy Phosphoramidite 188

8.4.3 NMR Spectra 189

8.4.4 Synthesis of Oligonucleotides 192

8.4.5 UV-Vis Measurement 197

9 Overall Conclusions and Future Perspectives 198

Abbreviations 200

General Methods 202

Bibliography 206

Declaration of Consent 218

Curriculum Vitae 219

Summary

The first chapter aims at introducing topics related to the thesis. These include supramolecular polymers in aqueous medium, some structural aspects of deoxyribonucleic acid (DNA), the preparation of synthetic oligomers, the concept of aggregation-induced emission (AIE), and different approaches for the construction of DNA nanostructures. This introduction, with a focus on what has been reported previously in our research group, is followed by elucidating the aim of the thesis in chapter 2. The results of the experimental lab work are discussed in the subsequent chapters.

In the third chapter, amphiphilic DNA conjugates exhibiting hydrophobic tetraphenylethylene (TPE) sticky ends at the 3'-ends are examined. Supramolecular assembly of such DNA duplexes results in two distinct vesicular morphologies – they either appear as prolate ellipsoids or spheres. The two different DNA architectures are characterized by their DNA duplex alignment within the supramolecular arrays. Only one type of DNA packing leads to the formation of DNA-addressable vesicular constructs.

The self-assembly of 3'-/5'-end TPE-modified DNA duplexes into vesicular nanostructures are explored in chapter 4. The objective of this chapter is to investigate the influence of the TPE sticky ends and DNA sequence length on the self-assembly behavior of the duplexes. The fifth chapter is devoted to further functionalize the supramolecular constructs, assembled from 3'-/5'-end TPE-modified DNA duplexes. Introduction of a terminal functionality into the duplexes governs the supramolecular assembly process and leads to clearly distinct DNA architectures, such as a star-shaped morphology. Chapter 6 provides an approach for the creation of DNA nanostructures, assembled from 3'-/5'-end TPE-modified DNA conjugates hybridized to a longer DNA complement.

In the seventh chapter, the self-assembly of phosphodiester-linked TPE trimers in aqueous medium under different conditions is presented.

Chapter 8 briefly describes a collaboration project, namely the synthesis of target compounds that are subsequently employed in on-surface polymerization and cryo-force spectroscopy experiments. Finally, overall conclusions are drawn, as well as outlining future perspectives.

1 Introduction

1.1 Supramolecular Polymers in Aqueous Medium

In nature, complex structures are often constructed from small and rather simple subunits that are held together by weak, non-covalent intermolecular forces.[1] This phenomenon might have inspired and stimulated the research field of supramolecular chemistry over the past years.[2] The self-assembly of monomeric units leads to supramolecular polymers, in which the repeating building blocks are connected through directional, non-covalent interactions.[3] Hydrophobic effects, hydrogen bonding, Coulomb interactions, van der Waals forces, and metal coordination are among the non-covalent interactions that drive self-assembly and account for the formation of supramolecular polymers.[4,5] Owing to the nature of these non-covalent interactions, supramolecular polymers may be dynamic, adaptive, reversible, self-healable, or stimuli-responsive.[6–15] Because the chemistry of life generally takes place in an aqueous environment, supramolecular polymers in aqueous media are of particular interest, *e.g.*, for bio-related applications.[16–18] An example of a supramolecular polymer in aqueous medium was reported by the group of Stupp *et al*. It was shown that a perylene monoimide based amphiphile (Figure 1a) self-assembles in water into supramolecular ribbons.

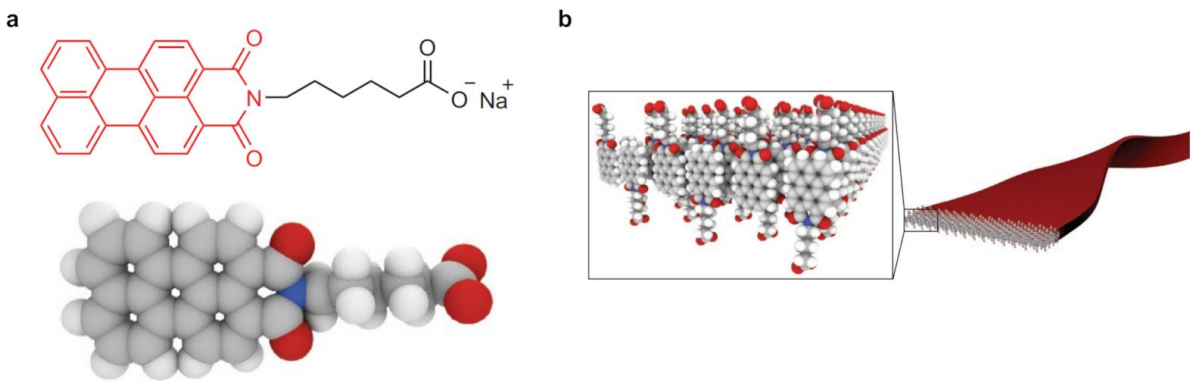

Figure 1. (**a**) Chemical structure and model representation of the perylene monoimide based amphiphile. (**b**) Illustration of stacked amphiphiles within the supramolecular ribbon structure. Figure adapted from ref. [19].

Small angle X-ray scattering (SAXS) data suggested the arrangement of the amphiphiles within the ribbons as illustrated in Figure 1b. The driving force for the formation of these supramolecular polymers can be explained by the π-stacking interactions between the hydrophobic, aromatic perylene moieties. This resulted in the reported supramolecular nanostructures, with the hydrophobic components of the amphiphile located inside the ribbon-like assemblies, while the negatively charged carboxylic acids pointed towards the polar, aqueous environment.

In our research group, supramolecular polymers assembled from different types of phosphodiester-linked amphiphilic oligomers have been demonstrated. They were based on various polycyclic aromatic hydrocarbons (PAHs), such as pyrene,[20–25] phenanthrene,[26,27] or anthracene,[28,29] and led to the formation of diverse morphologies. Such supramolecular polymers were prepared by a thermal assembly process and the formation of the self-assemblies is mainly driven by π-stacking forces between the hydrophobic PAHs in aqueous medium.

The thermal assembly process can be divided into two steps: disassembly followed by reassembly. Therefore, the sample solution is first heated to obtain molecularly dissolved oligomers. Then, the second step involves the controlled cooling of the sample solution with a defined cooling gradient (*e.g.*, 0.5 °C/min). During this cooling step, the oligomers gradually lose thermal energy, which in turn, induces the supramolecular assembly process of the oligomers.[25] Given that the cooling gradient is slow enough, the thermodynamically most stable supramolecular nanostructures can be expected.[24]

An example of a supramolecular polymer of our research group, assembled from a 3,6-disubstituted phosphodiester-linked phenanthrene trimer (oligomer **A**, Figure 2a) is described in more detail.[26] After performing a thermal assembly process in aqueous medium, oligomer **A** self-assembles into linear fibers. In these supramolecular polymers, the hydrophobic phenanthrenes are π-stacked, while the negatively charged phosphate groups point towards the aqueous environment, comparable to the previously described example by Stupp *et al*. Incorporation of small quantities of oligomer **B**, which consists of a phenanthrene trimer and an additional pyrene moiety (Figure 2a), leads to the formation of light-harvesting supramolecular polymers (Figure 2b). Phenanthrene excitation of those pyrene doped fibers at 322 nm results in intense pyrene fluorescence emission at 406 nm. Thus, after phenanthrene excitation, the excitation energy is efficiently transferred along the fiber from the phenanthrene units (donors) to the pyrene moieties (acceptors) over long distances (Figure 2c).

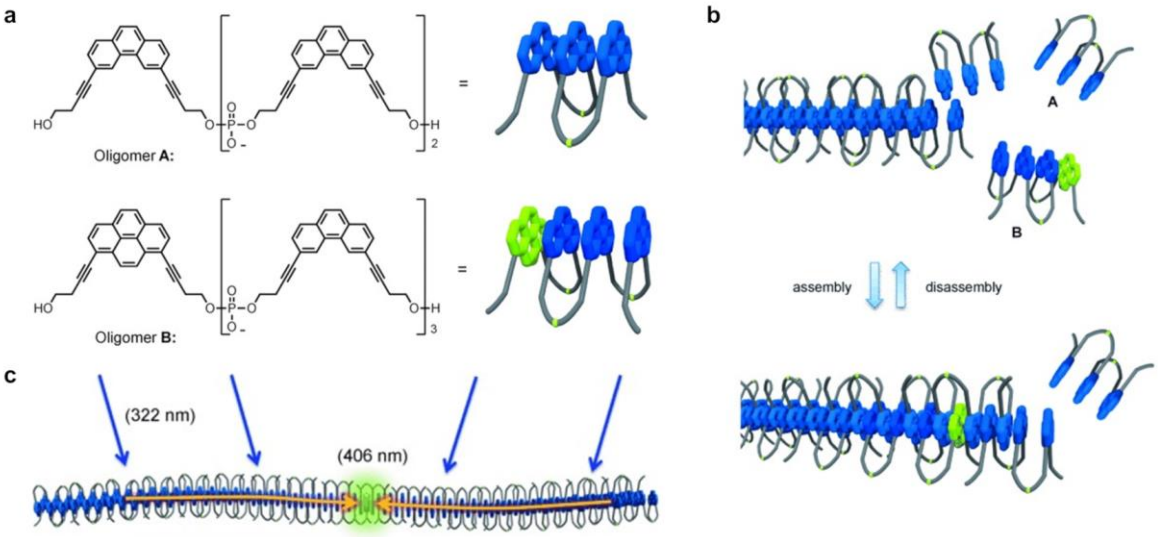

Figure 2. (**a**) Molecular structures and model representations of oligomers **A** and **B**. (**b**) Schematic representation of the supramolecular polymerization process. (**c**) Phenanthrene excitation leads to excitation energy transfer along the fiber to the next pyrene, which results in pyrene monomer fluorescence emission. Figure adapted from ref. [26].

The applicability of these phenanthrene fibers as light-harvesting antennae was further explored in a follow-up study.[30] Therefore, the supramolecular polymers were doped with various acceptor chromophores – in this case, not covalently linked to phenanthrene. Benzo[*a*]pyrene (Figure 3a) proved to be an excellent acceptor chromophore for this light-harvesting system assembled from oligomer **A**. Performing the supramolecular polymerization process in the presence of a dopant yielded light-harvesting supramolecular polymers (Figure 3b). Excitation of the phenanthrenes followed energy transfer to the acceptor molecules, evidenced by fluorescence emission of the acceptor chromophore.

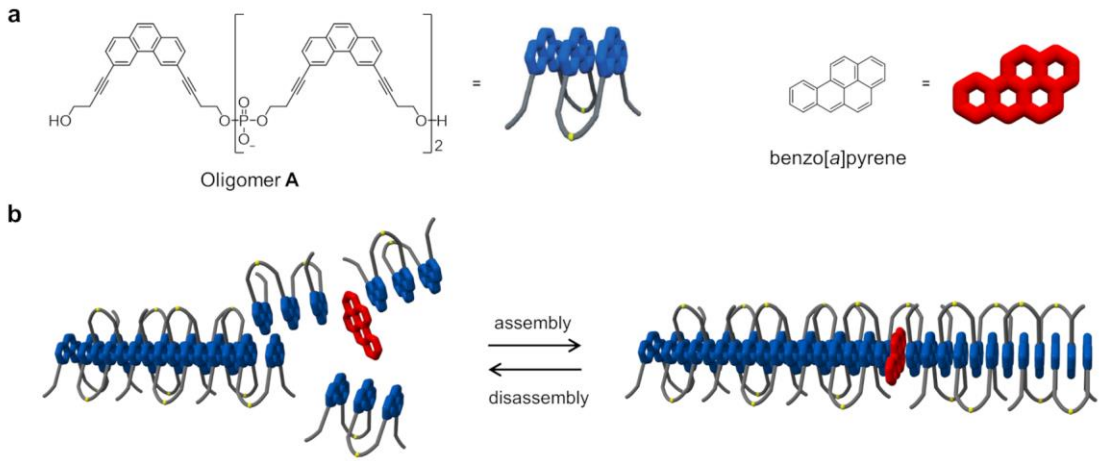

Figure 3. (**a**) Chemical structure of oligomer **A** and benzo[*a*]pyrene. (**b**) Schematic representation of the forming supramolecular fiber and random integration of a benzo[*a*]pyrene moiety. Figure adapted from ref. [30].

Utilizing the same phenanthrene-based light-harvesting antennae, but excitation energy transfer in a directional cascade fashion, has been demonstrated as well.[31] Combining supramolecular polymers with DNA-organized photonic wires allowed the construction of artificial light-harvesting systems with superior light-harvesting properties. The light-harvesting system was assembled from phenanthrene trimers (oligomer **A**), doped with a phenanthrene pentamer conjugated to a 20-mer single-stranded DNA (oligomer **B**) and equimolar concentrations of the fluorophore functionalized DNA single strands **C** and **D** (Figure 4a). Oligomer **B** served as a template for the construction of the DNA photonic wire, consisting of cyanine (Cy)-modified oligomers **C** and **D**, which are in part complementary to the DNA single strand and thus, hybridized to oligomer **B**. In this way, a Cy3 fluorophore was positioned in close proximity to the phenanthrenes, followed by Cy5 and Cy5.5 (Figure 4b).

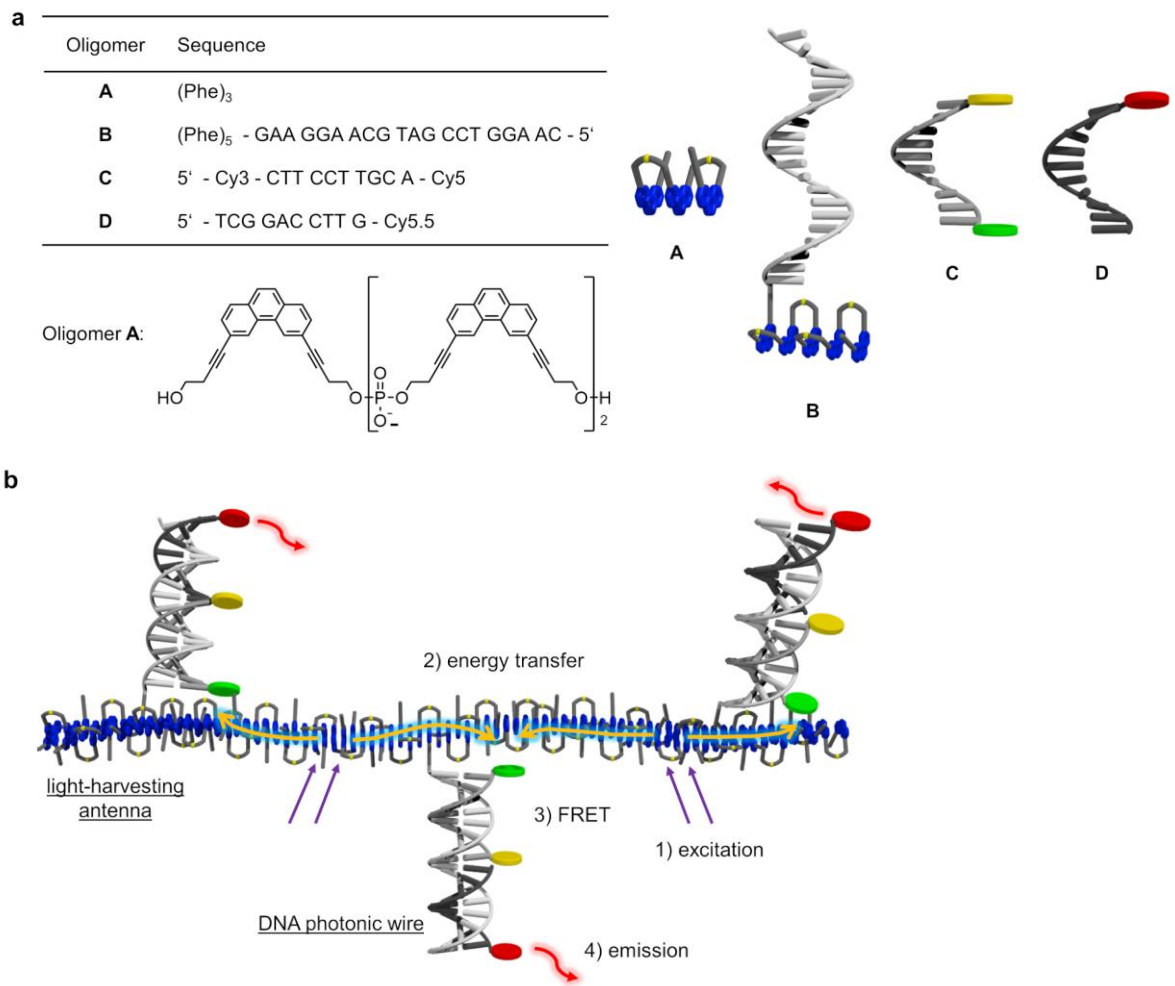

Figure 4. (**a**) Sequences and representations of oligomers **A**–**D**. (**b**) Illustration of integrated DNA photonic wires into the fibers. After phenanthrene excitation (1), the energy is transferred along the antenna to Cy3 (2). The DNA photonic wire further transfers the energy (3) to Cy5 and Cy5.5, which results in Cy5.5 fluorescence emission (4). Figure adapted from ref. [31].

Upon phenanthrene excitation, the excitation energy is transferred along the fiber to the next Cy3, which is arranged in the DNA scaffold. Afterwards, the excitation energy is transferred within the DNA-organized photonic wire in a directional, stepwise manner from Cy3 to Cy5, and eventually to Cy5.5. Successful energy transfer from the primary phenanthrene donor array to the final Cy5.5 acceptor was indicated by Cy5.5 fluorescence emission. A Förster resonance energy transfer (FRET)[32–36] mechanism is suggested for the propagation of the excitation energy within the DNA photonic wire. This study exemplifies that the well-defined scaffold of double-stranded DNA can serve as a tool of spatial control, to precisely position functional groups within space.

1.2 Structure of DNA

The beforementioned example of DNA as a scaffold highlights the importance of an understanding of some structural features of natural DNA. Nucleic acids are linear polymers, built up from monomers (nucleotides) that are covalently linked.[37] In DNA, the nucleotides are composed of any of the four DNA nucleobases (adenine, guanine, cytosine, or thymine; see Figure 5b), a 2'-deoxy-D-ribose sugar, and a phosphate residue.[38] The consecutive covalent linking between the 5'-hydroxyl group of one nucleoside with the 3'-hydroxyl group of another nucleoside *via* a phosphodiester bond leads to nucleic acid single strands. This defines the primary structure of the single strand – determined by the sequence of the DNA nucleobases.[39]

Two complementary DNA single strands can form in an antiparallel fashion a DNA double helix (duplex), wound around the same axis, which is attributed to the DNA's secondary structure (Figure 5a).[40] Different conformations have been reported for the DNA double helix, depending on the aqueous environment. At high humidity and low salt concentration, the right-handed B-conformation (B-DNA) is favored and thus, described below in more detail.[39,41] In this conformation, the hydrophobic nucleobases are located inside the double helix and nearly perpendicular to the helix axis, stacked above each other with a rise per base pair of about 3.4 Å (Figure 5a).[42,43] The nucleobase of one single strand is base-paired with a nucleobase of the complementary single strand in the same plane. G always base-pairs with C *via* hydrogen bonds, while A base-pairs with T, known as Watson-Crick base pairing (Figure 5b).[40] Instead of a straight alignment of the two glycosidic bonds in a Watson-Crick base pair, the angled orientation (illustrated best in the top view perspective, down the helical axis, Figure 5a) results in the formation of two distinct grooves between the phosphodiester backbones. Hence, the emergence of the major groove and minor groove is due to this angular aspect.[43]

The two hydrophilic sugar-phosphate backbones are facing the aqueous environment and are positioned on the outside of the double helix (Figure 5a).[40,42] Nucleobase stacking interactions, hydrogen bonding between complementary base-paired nucleobases, as well as the interactions of water molecules close to the double-stranded DNA, contribute to the stabilization of this helical arrangement.[39,43,44] Overall, the width of B-DNA is roughly 20 Å with a pitch of approximately 36 Å (Figure 5a).[38]

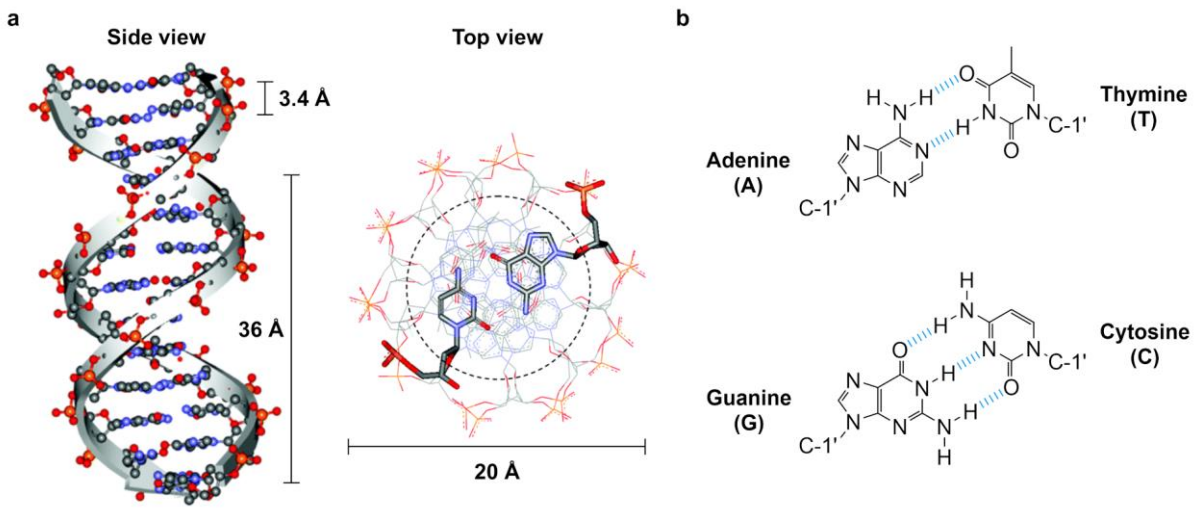

Figure 5. (**a**) Side view and top view illustrations of the double-stranded B-DNA, including some basic dimensions of the double helix. (**b**) Watson-Crick base pairing of the nucleobases; hydrogen bonds are illustrated in dashed blue lines. Figure adapted from ref. [41].

These distinct structural properties of DNA inspired many researchers to take advantage of the organizational power of the DNA scaffold. Therefore, the DNA scaffold was used to assemble multi-chromophore arrays,[45–54] to position functional groups with defined interchromophore distances,[55,56] or to investigate excitation energy transfer processes,[57–63] to name only a few. In all of these examples, chemically modified oligonucleotides were used. Indeed, incorporation of artificial nucleotide surrogates into oligonucleotides expand the scope of DNA beyond the classical role of DNA in biological systems as the carrier of genetic information.[64–66] These artificial building blocks present additional functionalities, relevant for applications in the fields of DNA nanotechnology or materials sciences.[67,68] However, this necessitated the development of a reliable method for the preparation of synthetic oligonucleotides.

1.3 Preparation of Synthetic Oligonucleotides

Solid-phase synthesis by the phosphoramidite approach is a straightforward, automated method for the efficient and sequence-defined preparation of short oligonucleotides.[69–71] As displayed in Figure 6 for the preparation of DNA, the solid-phase synthesis can be illustrated as a series of repeating steps and after each cycle, the oligomer is elongated by one nucleotide. To fulfil the requirements for the solid-phase synthesis cycle, the nucleosides are protected at the 5'-hydroxyl with a 4,4'-dimethoxytrityl (DMT) group, the nucleobases are protected with base labile protecting groups, and the 3'-hydroxyl group is derivatized to the corresponding phosphoramidite. During the solid-phase synthesis, the growing oligonucleotide chain is covalently attached to an insoluble solid-support. Long-chain alkyl-amino functionalized controlled pore glass (CPG) or polystyrene based solid-supports are frequently employed. Commonly, the 3'-terminal nucleoside is already bound *via* a succinyl linker to the solid-support. This implies that the synthesis proceeds in 3'→5' direction, opposite to the 5'→3' direction found in nature.[39]

The solid-phase synthesis cycle starts with the removal of the 5'-DMT protecting group (step 1 in Figure 6). This detritylation is accomplished under acidic conditions with 3% trichloroacetic acid in DCM. In the second step, the incoming DMT-protected nucleoside phosphoramidite is activated with a solution of 4,5-dicyanoimidazole in acetonitrile and reacted with the solid-support bound 5'-hydroxyl group to form a phosphite triester linkage (step 2 in Figure 6). Step 3 in the cycle aims at limiting the number of failure sequences. Therefore, unreacted 5'-hydroxyl groups are acetylated ("capped") with *in situ* mixed solutions of acetic anhydride/2,6-lutidine and *N*-methylimidazole (catalyst), both in THF. Consequently, failure sequences are blocked for all subsequent synthesis cycles. In the next step, the phosphite triester is oxidized into the corresponding phosphate triester with an oxidizing solution containing iodine, pyridine, water, and THF (step 4 in Figure 6). To close the cycle, the 5'-DMT group of the elongated oligomer is detritylated as previously described in the last step.

This cycle is repeated until the desired oligonucleotide is synthesized. Then, the oligomer is released under basic conditions (*e.g.*, ammonia) from the solid-support as well as all protecting groups are removed (*i.e.*, of the nucleobases and cyanoethyl groups on the phosphodiesters). Finally, the crude oligomers are purified, for example by high performance liquid chromatography (HPLC).[39]

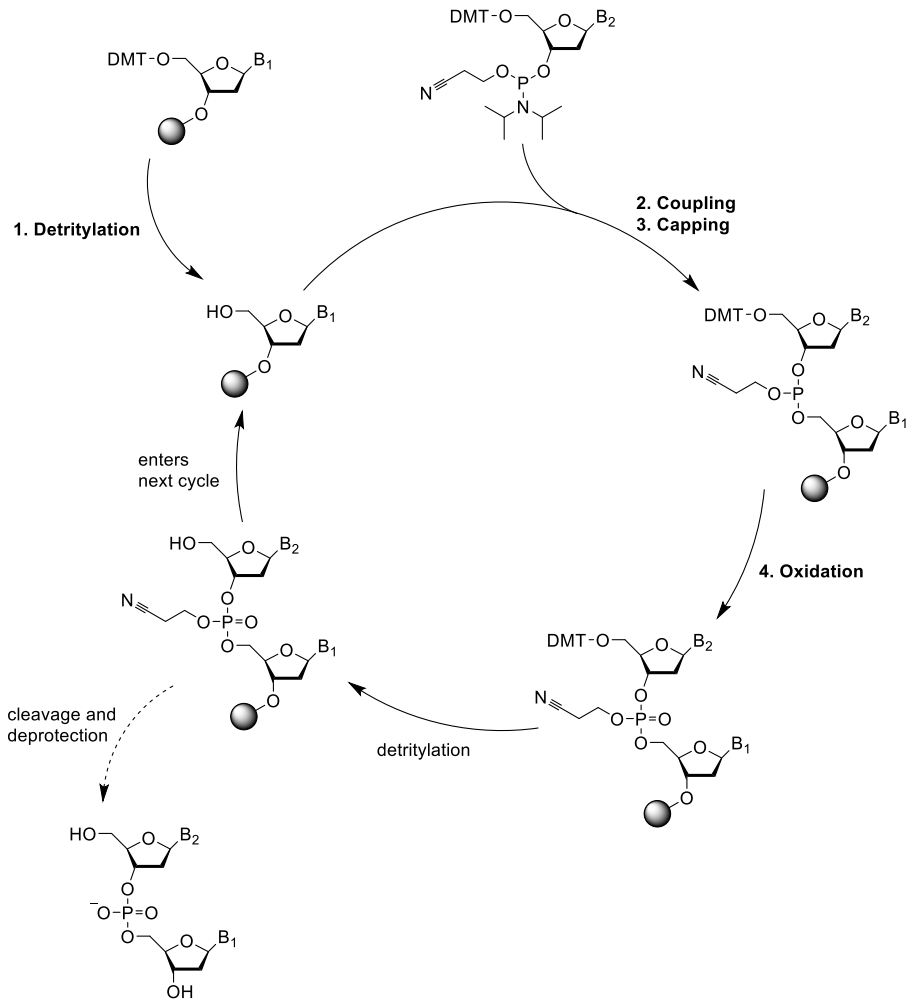

Figure 6. Individual steps involved in the solid-phase synthesis cycle, employing phosphoramidite chemistry.[39]

1.4 Aggregation-Induced Emission-Active DNA Hybrids

Due to the iterative and programmable solid-phase synthesis process, nucleotide surrogates can be incorporated at defined positions within the sequence and thus, allowing the preparation of sequence-defined, chemically modified oligonucleotides.[72,73]

Another representative example of our research group where functional units have been placed at defined positions in DNA sequences is described in more detail. DNA single strands have been modified in the middle of their sequences with a dialkynyl TPE unit.[74] TPE was selected due to the aggregation-induced emission (AIE) properties, which phenomenon was first described by Ben Zhong Tang and co-workers in 2001.[75] AIE-active molecules, so called AIEgens, are non-emissive in their molecularly

dissolved state but become highly emissive upon aggregation (Figure 7a). In the non-emissive, dissolved state, the phenyl rings of TPE can freely rotate and upon TPE excitation, the excitation energy is released *via* non-radiative pathways. However, the restriction of intramolecular rotation, caused by aggregation, leads to emissive aggregates.[76–80] Highly emissive molecular assemblies might find applications in biomolecular or chemical sensing,[81–83] bioimaging,[84–87] or artificial light-harvesting systems,[88–91] among others.[92–96] The work of our group revealed that AIE can be controlled by the hybridization of TPE-modified DNA conjugates.[74] While the individual DNA single strands only showed weak fluorescence emission, the duplex was highly emissive (Figure 7b). Therefore, after hybridization of the two complementary TPE-modified DNA single strands, molecular aggregation of the TPE units in the duplex accounted for the emergence of the observed luminescence.

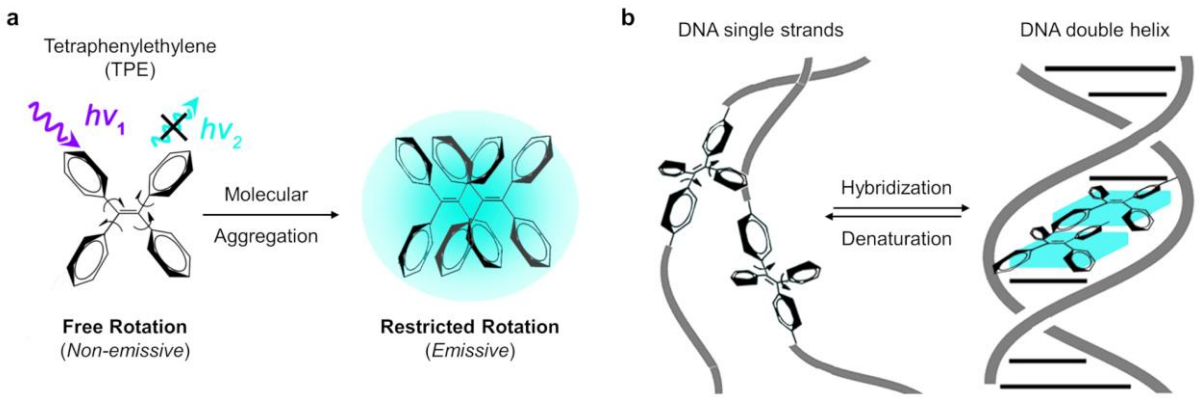

Figure 7. (**a**) Molecular structure of TPE and working principle of AIE. (**b**) TPE-modified DNA featuring AIE properties. Figure adapted from ref. [74].

This study also exemplifies two major advantages of DNA that renders DNA as an ideal material for nanotechnological applications: firstly, DNA hybridization is reversible. Denaturation of double-stranded DNA into the separate DNA single strands can be accomplished thermally by heating the DNA solution above the melting temperature (T_m). Secondly, specificity of DNA hybridization is ensured by specific Watson-Crick base pairing,[40] *i.e.*, pivotal for the development of sensitive DNA-based devices for diagnostic applications.[97–103] Hence, only complementary DNA single strands will form a double-stranded DNA duplex. These two central aspects are among the basic foundations for the construction of DNA-based nanostructures, which is the topic of the following section.

1.5 DNA Nanostructures

The assembly of branched, double-stranded DNA, exhibiting terminal single-stranded nucleotide overhangs, known as sticky ends, is one possible approach for the construction of well-defined DNA nanostructures. The seminal theoretical work of Nadrian C. Seeman in 1982 described the idea of immobile DNA junction motifs and their potential assembly into two-dimensional (2D) or three-dimensional (3D) networks, in which individual DNA fragments are connected *via* sticky ends (Figure 8).[104,105] Shortly thereafter, the existence of a tetrameric junction complex in solution was confirmed experimentally.[106] This pioneering work of Nadrian C. Seeman might have sparked the entire research field of DNA nanotechnology.[107–111]

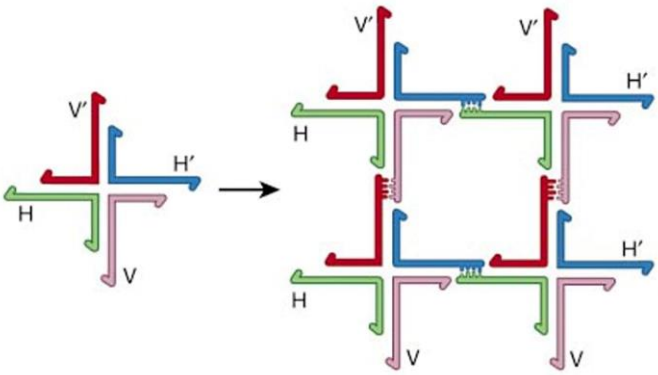

Figure 8. Assembly of a 2D lattice, from DNA sticky-ended immobile junction motifs *via* sticky end interactions. Figure adapted from ref. [107].

A more recent example for the hierarchical assembly of supramolecular 3D nanostructures *via* the sticky end strategy is depicted in Figure 9, which was reported by Chengde Mao and co-workers.[112] In this study, short DNA single strands hybridize to form a three-point-star motif (tile). This tile possesses 4 unpaired nucleotides at each end of the double-stranded part and act as sticky ends. Accordingly, the assembly of the individual tiles into the final DNA nanostructures is mediated through these complementary sticky ends. It was shown that depending on the loop length (colored red in Figure 9a) and the DNA concentration, different nanostructures could be obtained, such as DNA dodecahedra (Figure 9b). Different 2D and 3D supramolecular structures, assembled from DNA tiles with sticky ends, have been reported.[113–121]

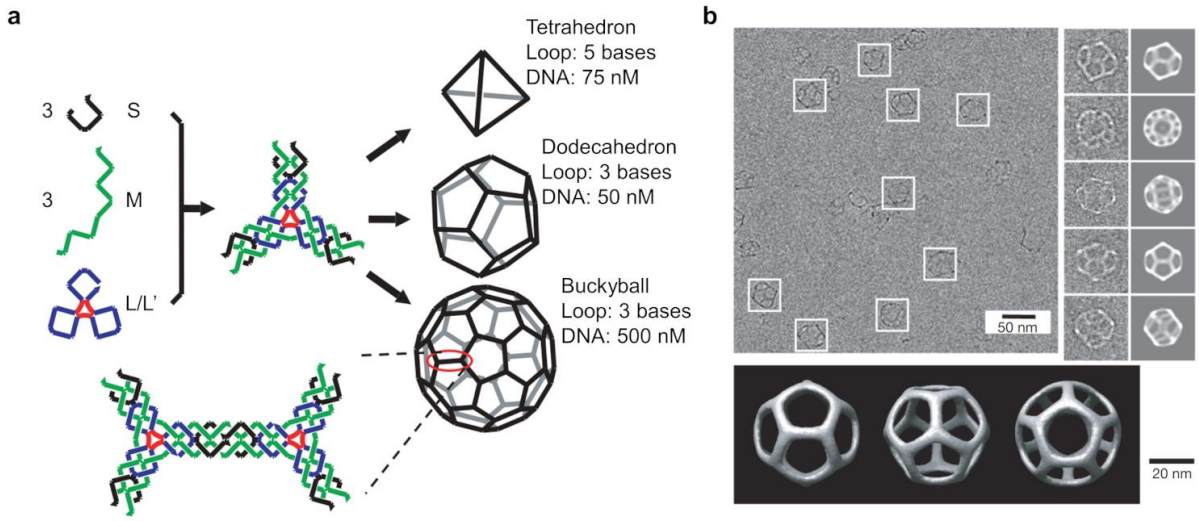

Figure 9. (**a**) Self-assembly of sticky-ended DNA tiles leads to the formation of different DNA nanostructures. (**b**) Cryo-EM images and schematic illustrations of DNA dodecahedra. Figure adapted from ref. [112].

In 2006, Paul W. K. Rothemund introduced an alternative approach for the bottom-up construction of complex DNA nanostructures, called DNA origami.[122] The reliability of nucleobase pairing as well as the programmability of nucleic acids folding are key aspects for this assembly strategy. The DNA origami approach relies on the use of a long single-stranded scaffold strand and a large set of different, short single-stranded staple strands (Figure 10a).

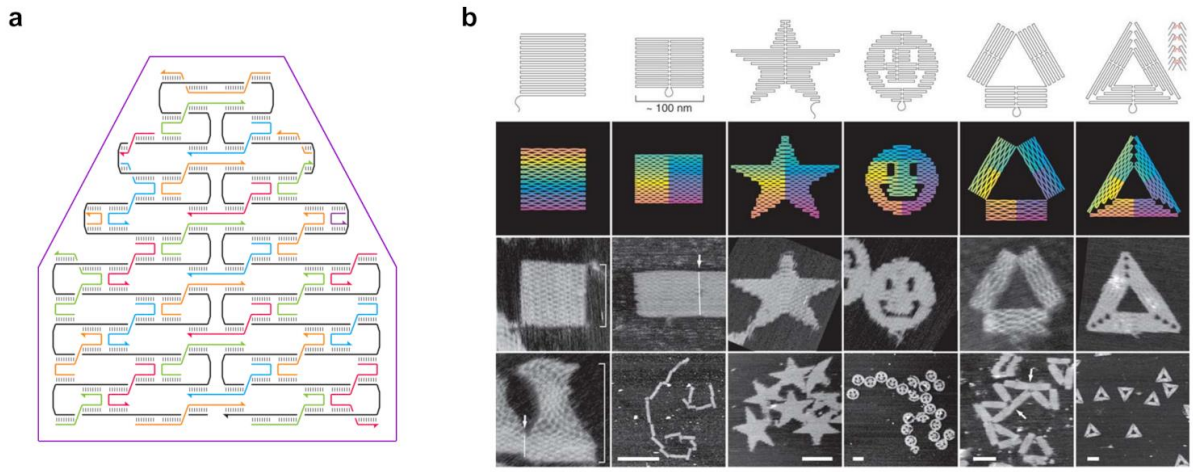

Figure 10. (**a**) DNA origami design for a desired shape (framed in purple), composed of a scaffold strand (black) and various staple strands (colored). (**b**) Different DNA origami shapes, with the corresponding folding paths (top two rows) and AFM images (bottom two rows). Figure adapted from ref. [122].

Folding of a 7 kilobase scaffold strand into a desired 2D shape was accomplished by annealing a set of over 200 staple strands to the scaffold strand. The staple strands hybridize to complementary fragments of the scaffold strand and thus, keep the scaffold in place. By rational design of the staple strands, DNA origami nanostructures with a predictable size and shape have been constructed (Figure 10b).

The creation of such DNA objects presumes comprehensive knowledge about the sequence design rules to construct a desired nanostructure.[123–125] To overcome this hurdle, different computer-aided design software tools have been elaborated over the years.[126–132] These tools tremendously facilitate the workflow towards straightforward fabrication of complex target DNA shapes.[133,134] For example, Mark Bathe and co-workers developed a sequence design algorithm that computes the required single-stranded DNA sequences in a top-down, and fully autonomous manner (Figure 11a).[135] The proof of principle of the computational algorithm was demonstrated by the construction of a variety of 3D DNA origami structures, such as a icosahedron (Figure 11b) or tetrahedron (Figure 11c).

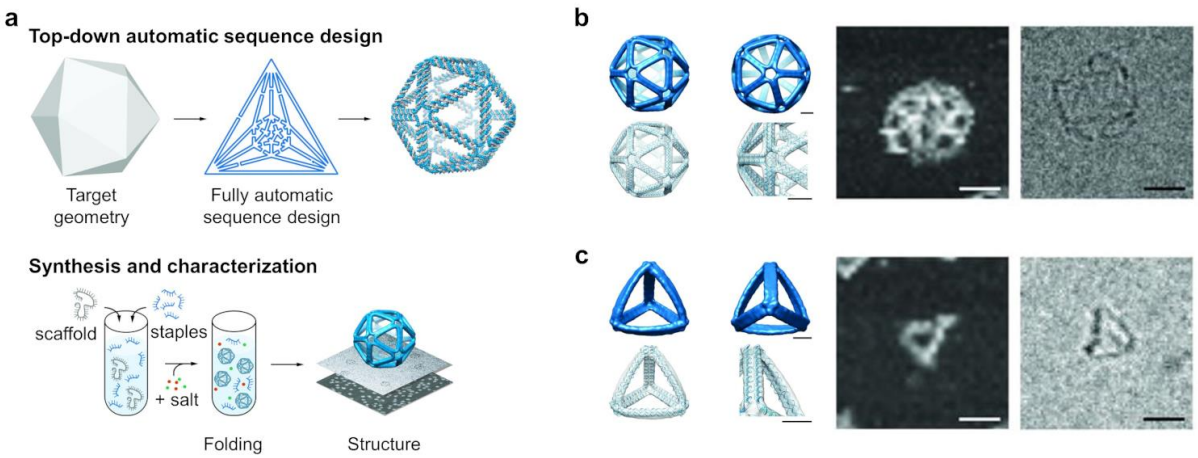

Figure 11. (**a**) DNA sequences of a target shape are automatically computed. The shape-specific single-stranded scaffold and staple strands are synthesized, annealed, and the desired structures are characterized by cryo-electron microscopy (cryo-EM). (**b**) Scaffolded DNA origami icosahedron (52 base pair edge-length). (**c**) DNA origami tetrahedron (63 base pair edge-length). Scale bars for cryo-EM images: 20 nm. Figure adapted from ref. [135].

In the previously described studies, the nanostructures were constructed entirely from canonical DNA nucleotides, stabilized largely *via* Watson-Crick base pairing. Combining these molecular recognition properties of DNA with orthogonal supramolecular interactions expand the scope of DNA architectures.[136–143] This can be achieved by the integration of artificial building blocks into DNA, which introduce additional functionality and account for the orthogonal supramolecular interactions of such DNA hybrid materials.[144–147] Several supramolecular arrays assembled from amphiphilic DNA conjugates have been reported.[148–157] Most of these supramolecular assemblies were largely governed by the intermolecular interactions between the artificial building blocks rather than the DNA part.

Previous work in our research group demonstrated the formation of DNA nanostructures, assembled from 3'-end modified phenanthrene-DNA duplexes (Figure 12a).[158] Depending on the duplex concentration, either sheet-like (Figure 12b) or vesicular structures (Figure 12c) were observed on mica. In this example, the assembly of the DNA conjugates into supramolecular arrays was enabled by the supramolecular interaction of the hydrophobic phenanthrene sticky ends. In addition, spermine (Figure 13) was required for the construction of these assemblies. This polyamine is positively charged at pH 7.2 and thus, assumed to reduce the coulombic repulsion between the negatively charged DNA duplexes. Such an electrostatic neutralization is essential, since the DNA duplexes are very close next to each other in these assemblies.

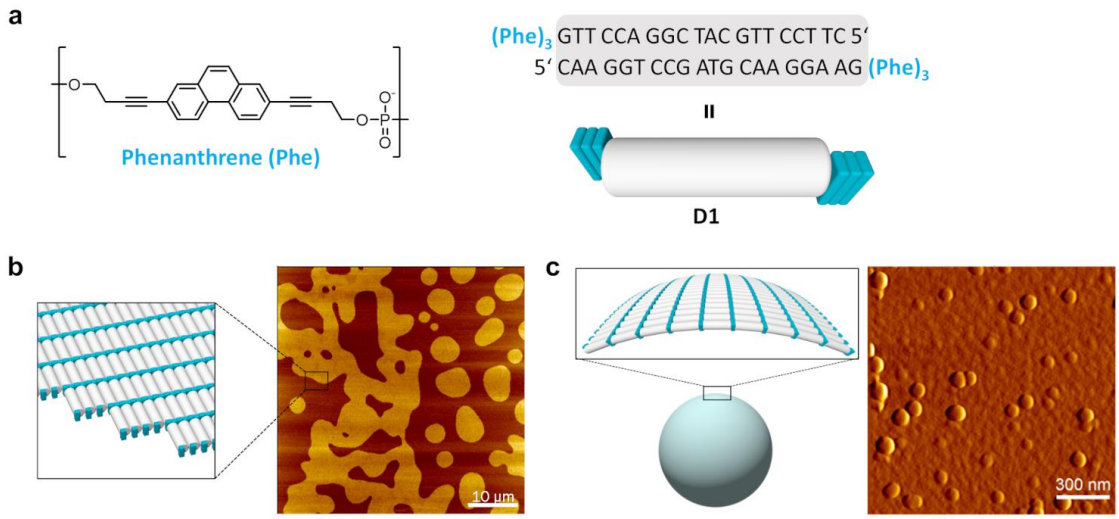

Figure 12. (**a**) Molecular structure of phenanthrene modification and graphical representation of the 3'-end modified phenanthrene DNA duplex **D1**. (**b**) At low DNA duplex concentrations (1 µM), monolayers of self-assembled **D1** were observed by AFM. (**c**) At increased DNA duplex concentrations (5 µM), **D1** self-assembles into vesicular structures as imaged by AFM. Figure adapted from ref. [158].

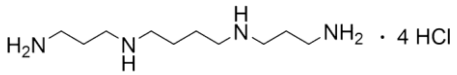

Figure 13. Molecular structure of spermine tetrahydrochloride.

Spermine is an abundant natural polycation and found at increased levels under conditions of high cell division, *e.g.*, in tumor cells.[159,160] The polyamine is associated with a variety of cellular functions, but the detailed mechanism of action is often still unclear.[39,161–163] Nonetheless, it is believed that spermine plays an important role in promoting DNA packaging and the stabilization of chromatin – also *via* electrostatic attraction to the negatively charged phosphate backbone of nucleic acids.[164–166] Due to the non-specific electrostatic Coulomb interaction between nucleic acids and polyamines, synthetic polymeric polycations were applied as transfection agents for the delivery of therapeutic nucleic acids to cells.[167–173]

2 Aim of the Thesis

Spatial control of individual building blocks in complex, hierarchically assembled supramolecular arrays is crucial for a wide range of chemical and biochemical processes.[174] For example, natural light-harvesting complexes reflect such well-ordered assemblies. In these arrays, light capturing chromophores are precisely embedded within large protein complexes, ensuring an efficient excitation energy transfer of the harvested light.[175,176]

In DNA nanotechnology, spatial control can be achieved by using the double-stranded DNA scaffold, which represents a well-defined structural building block for the bottom-up construction of DNA nanostructures. The previous study in our group on the self-assembly of phenanthrene sticky-ended DNA duplexes into supramolecular nanostructures initiated this current work.[158] It also exemplifies the approach of combining two orthogonal supramolecular interactions, *i.e.*, DNA hybridization with hydrophobic interactions derived from chemically modified sticky ends.

The aim of this thesis is to further explore the influence of the chemical modification of the sticky ends and the DNA conjugates design on the supramolecular assembly behavior, as well as the functionalization of such DNA architectures – overall termed as *DNA architectonics*. Therefore, the phenanthrene overhangs will be replaced by TPE, primarily due to the appealing AIE properties of TPE. The 3'-/5'-end modified TPE-DNA conjugate design will come into the focus of this study as it offers the possibility for the straightforward introduction of an additional functionality on the complementary DNA single strand. It will be shown that such an additional terminal moiety plays a key role in the emergence of a variety of distinct morphologies.

3 Self-Assembly of 3’-End Modified TPE-DNA Conjugates

The supramolecular assembly behavior of 3'-end modified TPE-DNA conjugates will be studied. Two different vesicular architectures are observed by cryo-EM, which were formed *via* hydrophobic TPE sticky end and spermine mediated interactions. The two AIE active vesicular constructs are defined by their DNA duplex arrangement. Either an extended DNA duplex alignment (type I vesicles) or a compact arrangement of the amphiphilic duplexes (type II vesicles) was revealed by cryo-EM imaging. The accessibility of the DNA duplexes within the two morphologies was investigated by DNA intercalation experiments and is determined by the type of the DNA packing. Upon incorporation of small amounts of a Cy3-labelled DNA single strand, artificial light-harvesting complexes were constructed.

Part of this work has been published:

Supramolecular Assembly of DNA-Constructed Vesicles

S. Rothenbühler, I. Iacovache, S. M. Langenegger, B. Zuber, R. Häner, *Nanoscale* **2020**, *12*, 21118–21123.

3.1 Results and Discussion

3.1.1 Spectroscopic Characterization of *E*-TPE Diol and *Z*-TPE Diol

E- and *Z*-TPE diol **2** and **3** (Figure 14a) were measured first in ethanol. Under these conditions, it is assumed that TPE is molecularly dissolved and not aggregated. Therefore, these measurements serve as a comparison for following studies in aqueous medium, to verify if the TPE units are aggregated or not under certain conditions and temperatures. Depicted in Figure 14b are the ultraviolet-visible (UV-Vis)

absorption profiles of *E*- and *Z*-TPE diol **2** and **3** in ethanol at 20 °C. Both isomers exhibit two distinct, featureless absorption bands: *E*-TPE diol **2** shows one maximum at 259 nm and a second one at 329 nm. *Z*-TPE diol **3** features a maximum at 266 nm and one maximum at 329 nm as well. In agreement with the AIE concept, TPE diols **2** and **3** are almost non-emissive in the well-solubilizing solvent ethanol and only a weak emission band centered around 500 nm is observed after TPE excitation at 335 nm (Figure 14c).

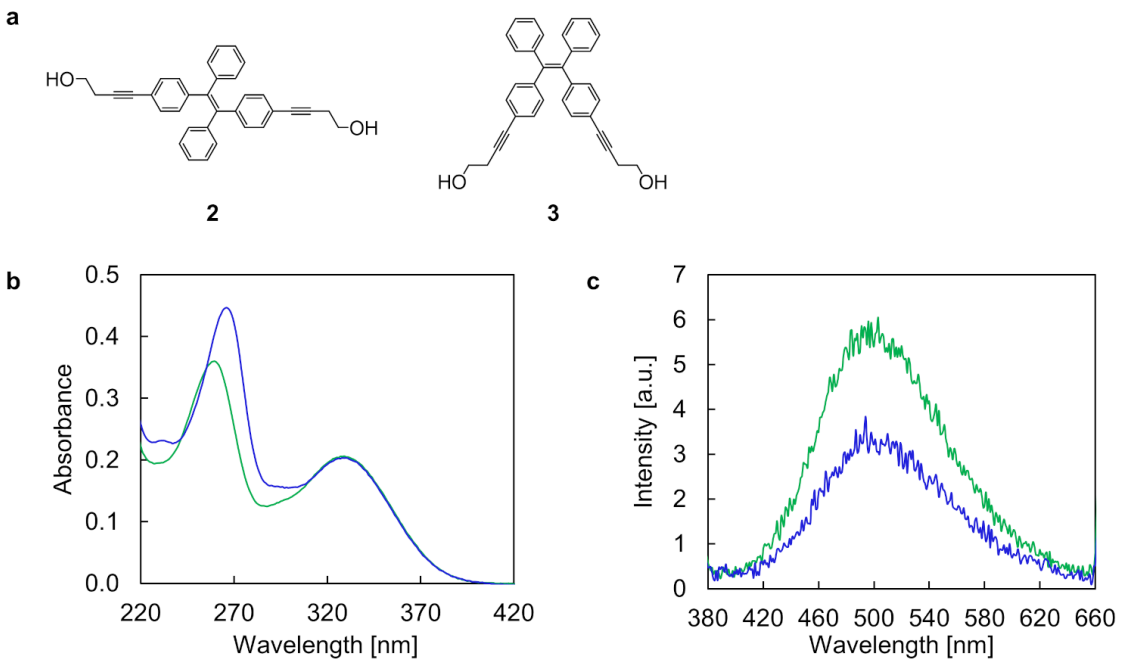

Figure 14. (**a**) Molecular structures of *E*-TPE diol **2** and *Z*-TPE diol **3**. (**b**) UV-Vis absorption and (**c**) fluorescence emission spectra of *E*-TPE diol **2** (green) and *Z*-TPE diol **3** (blue). Conditions: 10 µM TPE diol in ethanol, 20 °C, $\lambda_{ex.}$: 335 nm, excitation slit: 5 nm, emission slit: 5 nm.

3.1.2 Overview of 3'-End Modified TPE-DNA Conjugates

Listed in Figure 15a are the DNA single strands that were used in this study. **ON1** to **ON4** were prepared *via* solid-phase synthesis and purified by HPLC. Detailed experimental procedures are provided in sections 3.3.1–3.3.3. These four oligonucleotides consist of 20 DNA nucleotides and three phosphodiester-linked TPE units at their 3'-ends. Due to the complementarity of **ON1** and **ON2**, as well as **ON3** and **ON4**, DNA duplexes can be formed that exhibit TPE overhangs (sticky ends) on both sides of the duplexes (Figure 15b). DNA duplexes modified either with *E*-TPEs (**ON1*ON2**) or Z-TPEs (**ON3*ON4**) were investigated to compare the self-assembly behavior of the two different

stereoisomers. This is of interest because it was reported previously that for example the substitution pattern on phenanthrene affects the morphology of the supramolecular polymers. While the 3,6-phosphodieseter-linked phenanthrene trimer self-assembled into fibers,[26] nanotubes were formed from 2,7-phosphodiester-linked phenanthrene trimers.[27] Therefore, the *E*- and *Z*-stereoisomer of TPE might also have an effect on the morphology of the supramolecular assemblies. **ON5** to **ON8** were purchased from Microsynth (Switzerland). **ON5** and **ON6** served as control and reference DNA, whereas the Cy3-labelled oligonucleotides **ON7** and **ON8** were utilized in light-harvesting experiments.

a

Strand	Sequence
ON1	5′-CAA GGT CCG ATG CAA GGA AG-(*E*-TPE)$_3$
ON2	(*E*-TPE)$_3$-GTT CCA GGC TAC GTT CCT TC-5′
ON3	5′-CAA GGT CCG ATG CAA GGA AG-(*Z*-TPE)$_3$
ON4	(*Z*-TPE)$_3$-GTT CCA GGC TAC GTT CCT TC-5′
ON5	5′-CAA GGT CCG ATG CAA GGA AG-3′
ON6	3′-GTT CCA GGC TAC GTT CCT TC-5′
ON7	3′-GTT CCA GGC TAC GTT CCT TC-Cy3
ON8	3′-TCG TTC TAG CCT AGC TTC CG-Cy3

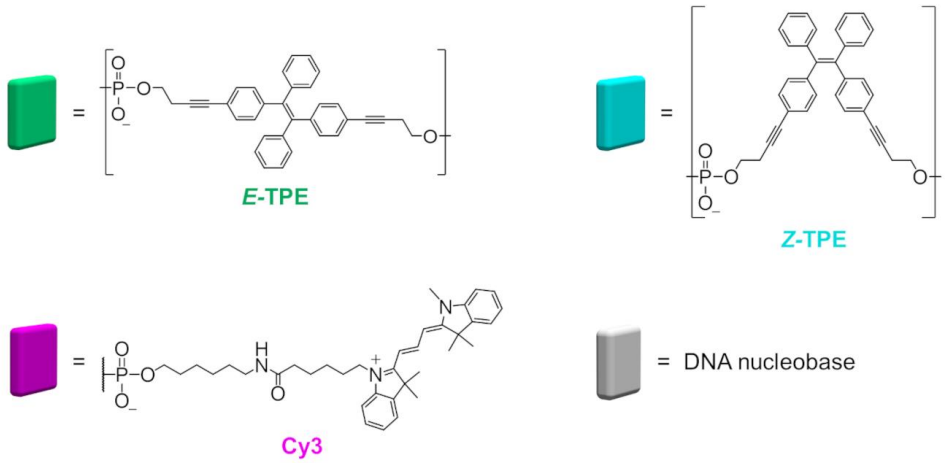

b

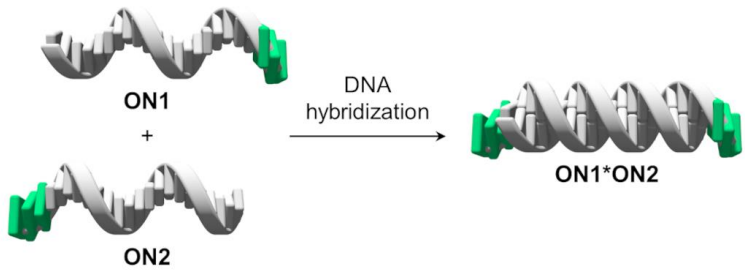

Figure 15. (**a**) Summary of DNA sequences and molecular structures of the modifications. (**b**) Because the two single strands **ON1** and **ON2** are complementary, they can hybridize to form duplex **ON1*ON2**.

3.1.3 Spectroscopic Characterization of 3'-End Modified TPE-DNA Conjugates

Displayed in Figure 16 are the temperature-dependent UV-Vis absorption spectra of **ON1*ON2** and **ON3*ON4**. The similar absorption profiles can be divided into two parts: the peak around 260 nm stems from combined absorption of the DNA nucleobases and the TPE units. However, the absorption band around 330 nm originates from TPE absorption only. Controlled cooling of the sample solutions from 75 °C to 20 °C (gradient: 0.5 °C/min) results in hypochromicity around 260 nm and is due to DNA hybridization. A T_m of the reference DNA **ON5*ON6** was measured to be 53 °C (Figure 60). The bathochromic shifts from 326 nm to 333 nm for **ON1*ON2** and from 328 nm to 334 nm for **ON3*ON4** is ascribed to TPE interactions. These differences in the absorption profiles at two different temperatures, together with the T_m of the reference DNA, imply for aggregation at 20 °C.

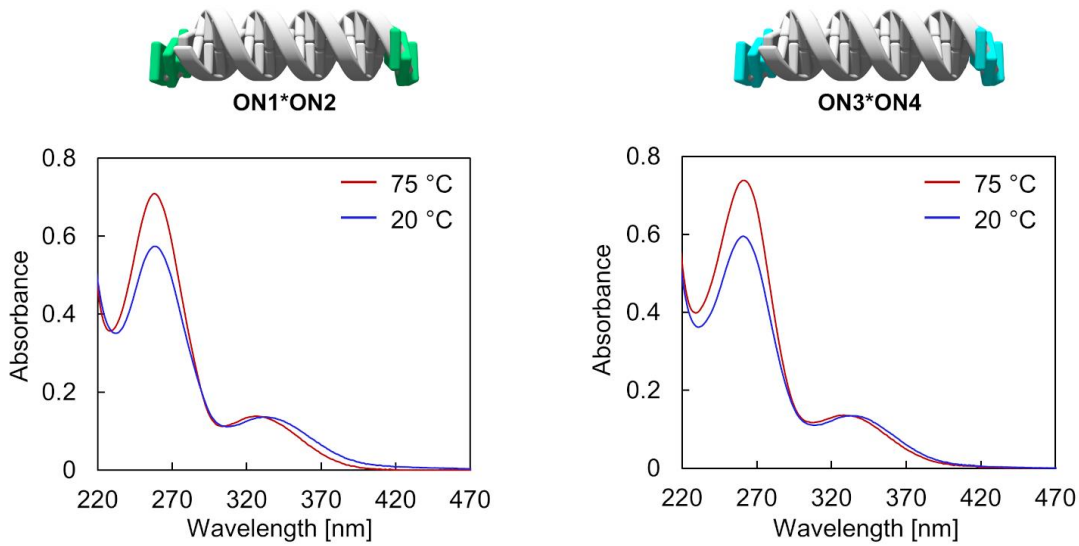

Figure 16. Temperature-dependent UV-Vis absorption spectra of **ON1*ON2** (left) and **ON3*ON4** (right). Conditions: 1 µM each single strand, 10 mM sodium phosphate buffer pH 7.2, 0.1 mM spermine · 4 HCl, 20 vol% ethanol.

The temperature-dependent fluorescence emission spectra of **ON1*ON2** and **ON3*ON4** shown in Figure 17a and fluorescence quantum yields (Φ_{FL}, Table 1) evidence the AIE behavior of the TPE-DNA conjugates. While the fluorescence emission is negligible at 75 °C (Φ_{FL} <1%), an intense emission signal centered around 490 nm is detected at 20 °C for both duplexes. This is also reflected by the significantly increased fluorescence quantum yields after TPE excitation at 335 nm (Table 1). Fluorescence quantum

yields were determined according to published procedures[177] relative to quinine sulfate (in 0.5 M sulfuric acid) as a standard.[178] The excitation spectra at 20 °C verify that the observed fluorescence is due to the TPE moieties because the profiles resemble the absorption profiles of the respective TPE diol (Figure 14b).

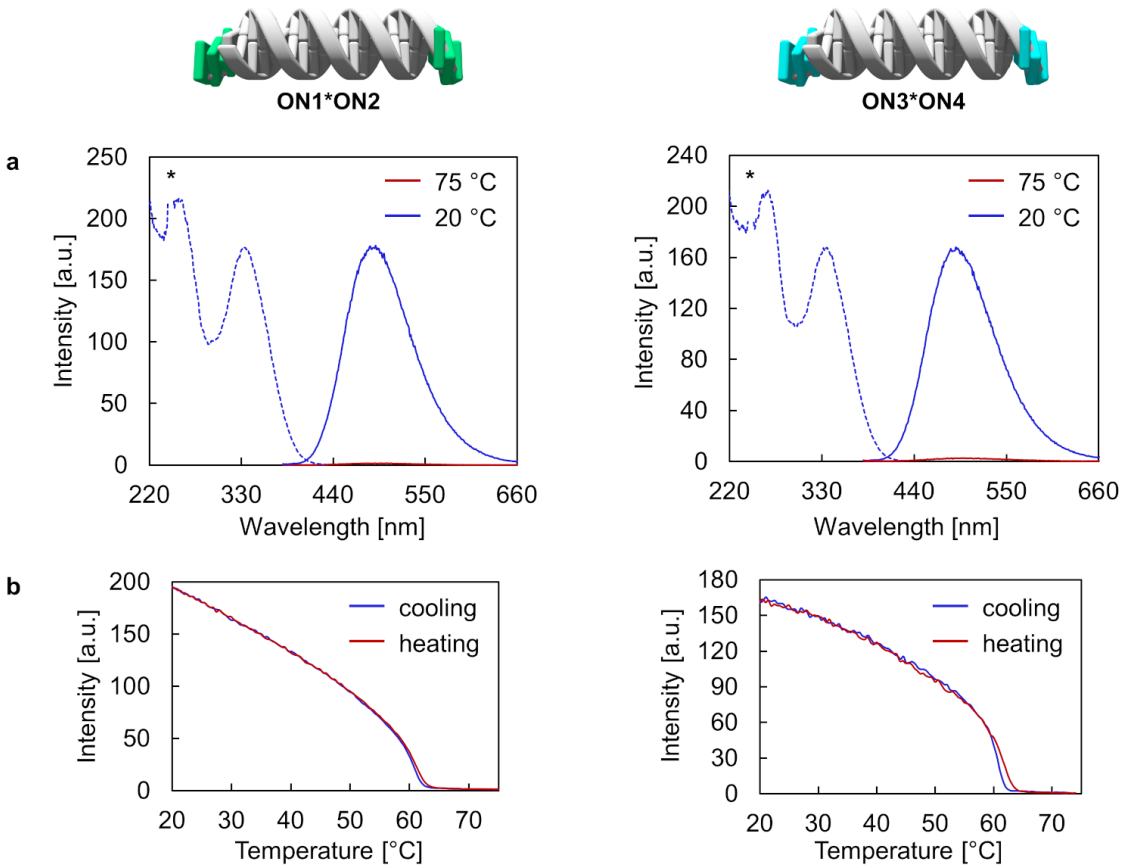

Figure 17. (**a**) Temperature-dependent fluorescence emission (solid line) and excitation (dotted line) spectra, and (**b**) fluorescence-monitored annealing and melting curves of **ON1*ON2** (left) and **ON3*ON4** (right). Conditions: 1 µM each single strand, 10 mM sodium phosphate buffer pH 7.2, 0.1 mM spermine · 4 HCl, 20 vol% ethanol, $\lambda_{ex.}$: 335 nm, $\lambda_{em.}$: 490 nm, gradient: 0.5 °C/min, * denotes second-order diffraction.

Table 1. Fluorescence quantum yields (Φ_{FL}) of **ON1*ON2** and **ON3*ON4** either at 75 °C (disassembled state) or at 20 °C (assembled state).

	Φ_{FL} [%] at 75 °C	Φ_{FL} [%] at 20 °C, after thermal assembly process
ON1*ON2	<1	31 ± 1
ON3*ON4	<1	22 ± 1

The AIE properties of the TPE overhangs enables the study of the supramolecular assembly process by fluorescence-monitored annealing curves (Figure 17b). As discussed before, the fluorescence is close to zero at elevated temperatures, but emerges distinctively during the thermal annealing process (controlled cooling of 0.5 °C/min). This hints at a certain self-assembly mechanism of **ON1*ON2** and **ON3*ON4**, because the non-sigmoidal shape of the annealing curves strongly implies for a cooperative nucleation-elongation growth mechanism.[179–185] Therefore, the temperature, at which a pronounced increase in the emission is observed, corresponds to the nucleation temperature, short T_{FL}(nucleation). The nucleation temperature basically signifies the start of the supramolecular assembly process and was determined to be 62 °C (based on the annealing curves) for **ON1*ON2** as well as for **ON3*ON4**. The reversibility of the assembly and disassembly process is demonstrated by the nearly overlapping curves of the annealing and melting curves.

In summary, based on the T_m value of 53 °C for the reference DNA **ON5*ON6**, it can be assumed that the DNA duplexes **ON1*ON2** and **ON3*ON4** are denatured at 75 °C. This is further supported by the low fluorescence emission intensities at this temperature, which suggest insignificant TPE aggregation. After the thermal assembly process at 20 °C, however, there are clear signs for DNA hybridization and at the same time TPE interactions (*i.e.*, aggregation).

3.1.4 Atomic Force Microscopy

Atomic force microscopy (AFM) was utilized to visualize the nanostructures of **ON1*ON2** and **ON3*ON4** formed after thermal assembly. Figure 18 shows spherical assemblies of **ON1*ON2**, deposited on (3-aminopropyl)triethoxysilane (APTES)-modified mica. Thus, **ON1*ON2** self-assembles into vesicular objects, with a height ranging roughly between 20–70 nm and 50–150 nm in diameter. Regular and well-defined nanostructures were obtained only when the duplex exhibits TPE sticky ends on both sides of the duplex. Small, undefined aggregates were obtained when the TPE overhangs are present just on one side (duplex **ON2*ON5**, Figure 61). Compared to **ON1*ON2**, the absence of any sharp fluorescence onset in the fluorescence-monitored annealing curve of **ON2*ON5** further indicates that the assembly process was less defined (Figure 62c). As one might have expected, the stereoisomers have a slightly different self-assembly behavior. The corresponding *Z*-TPE isomer, **ON3*ON4**, forms smaller aggregates with diameters in most cases below 100 nm and heights of up to 50 nm (Figure 19). However, it seems that these nanostructures tend to agglomerate further into more ill-defined aggregates. Because **ON3*ON4** forms less defined supramolecular arrays compared to **ON1*ON2**, only nanostructures assembled from the *E*-stereoisomer, **ON1*ON2**, were investigated in more detail.

With the help of Beatrice Frey from the Department of Chemistry, Biochemistry and Pharmaceutical Sciences of the University of Bern, scanning electron microscopy (SEM) experiments were conducted to elucidate the surface topography of self-assembled **ON1*ON2**. While the experiments confirmed the spherical structure, no additional information of the surface topography could be gained (Figure 63).

To elucidate structural properties of the vesicular membrane, small angle X-ray scattering (SAXS) experiments were performed in collaboration with Prof. Dr. Antonia Neels and Dr. Neda Iranpour Anaraki from the Swiss Federal Laboratories for Materials Science and Technology (Empa), St. Gallen. However, no additional insights on the structural properties of aggregated **ON1*ON2** could be obtained because the signal intensity was too low. It is assumed that either the concentration of the vesicles was too low, or that the nanostructures have been damaged during the exposure time.

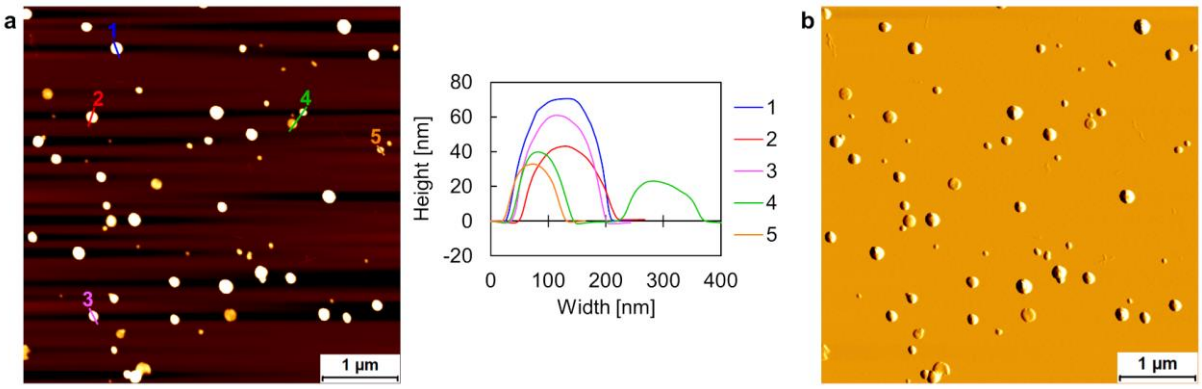

Figure 18. (**a**) AFM scan with corresponding cross sections and (**b**) deflection scan of assembled **ON1*ON2**. Conditions: 1 µM **ON1*ON2**, 10 mM sodium phosphate buffer pH 7.2, 0.1 mM spermine · 4 HCl, 20 vol% ethanol.

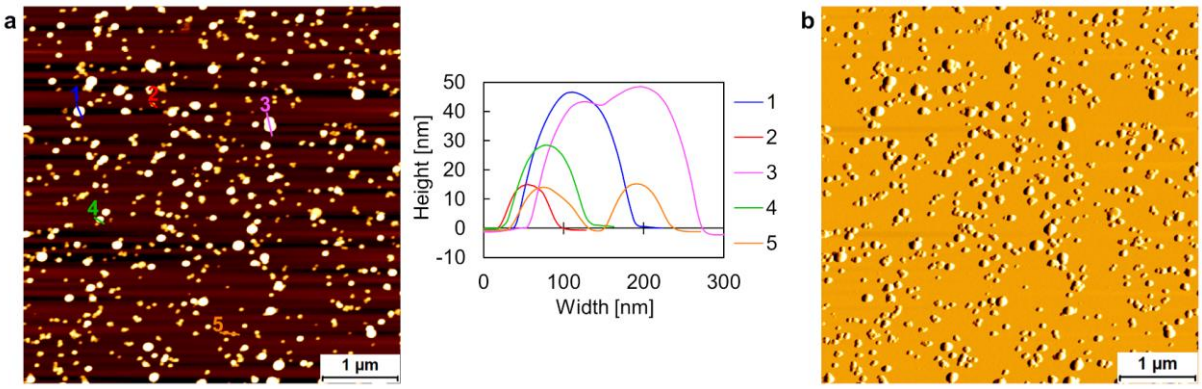

Figure 19. (**a**) AFM scan with corresponding cross sections and (**b**) deflection scan of assembled **ON3*ON4**. Conditions: 1 µM **ON3*ON4**, 10 mM sodium phosphate buffer pH 7.2, 0.1 mM spermine · 4 HCl, 20 vol% ethanol.

3.1.5 Transmission Electron Microscopy

Transmission electron microscopy (TEM) confirmed the vesicular structure of self-assembled **ON1*ON2** (Figure 20). Their size range of about 50–200 nm is comparable to the dimensions observed by AFM (Figure 18). Noteworthy, TEM imaging reveals an incredibly exciting feature of the nanostructures, namely the regular pattern. The distance between the regular, darker bands is around 7–8 nm, which would be in well agreement with the length of a single DNA duplex **ON1*ON2**. Intrigued by the regular patterns observed on the vesicular structures, the nanostructures were further explored by cryo-electron microscopy (cryo-EM) in collaboration with Prof. Dr. Benoît Zuber and Dr. Ioan Iacovache from the Institute of Anatomy of the University of Bern.

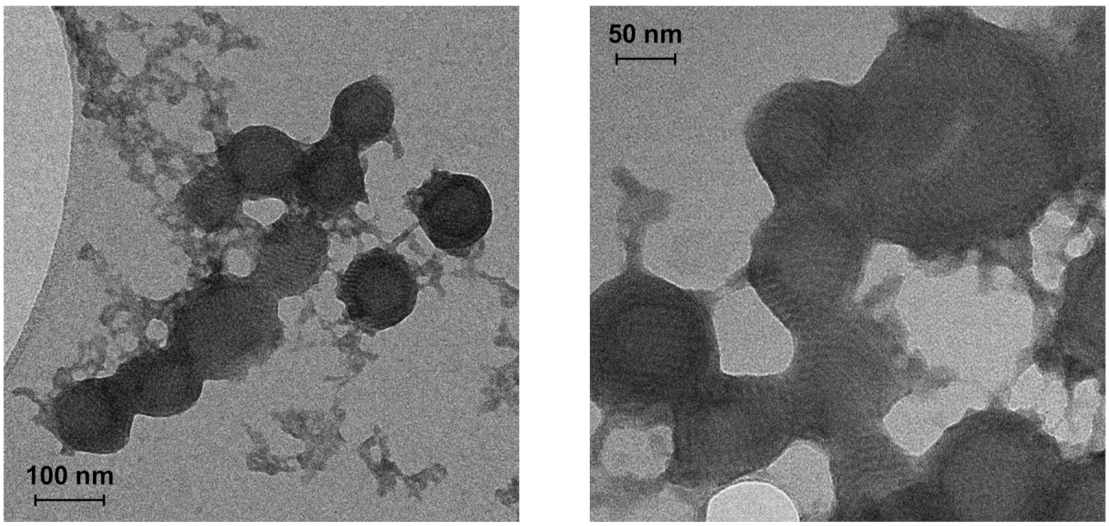

Figure 20. TEM images of self-assembled **ON1*ON2** on holey carbon films on copper grids; UA-Zero staining. Conditions: 1 µM **ON1*ON2**, 10 mM sodium phosphate buffer pH 7.2, 0.1 mM spermine · 4 HCl, 20 vol% ethanol.

3.1.6 Cryo-Electron Microscopy

In contrast to AFM, SEM, and TEM, which depend largely on surface adsorption processes and drying effects, cryo-EM imaging of vitrified specimens allows the visualization of nanostructures as they are in their actual morphology in solution.[186,187] Additionally, cryo-EM does not require any staining agents and thus, potential artifacts due to staining can be excluded.[188] However, due to the vulnerability of the DNA structures, the total electron dose had to be adjusted to less than 20 $e^-/Å^2$. Cryo-EM imaging unveiled that supramolecular assembly of **ON1*ON2** leads to the coexistence of two different vesicular

morphologies. The first morphology, type I vesicles, are presented in Figure 21 and their prolate, ellipsoidal shape resembles them of a rugby-ball. The overall size of these type I vesicular constructs varies between 50 and 100 nm. Cryo-EM imaging also shows a regular pattern of discrete bands, as it was previously described for the structures observed by TEM (Figure 20). Due to the increased resolution of cryo-EM imaging, the distances between the darker bands could be determined more precisely and was measured to be 7.8 ± 0.5 nm in average (see section 3.3.5). This distance agrees very well with the length of the 23-mer duplex of **ON1*ON2**. In some areas of the vesicles, a regular pattern with a distance of about 2.4 ± 0.5 nm between the darker rods can be observed (see inset in Figure 21), which corresponds to the width of a single DNA duplex. Thus, cryo-EM imaging allowed to elucidate the DNA duplex arrangement within the vesicular structures and is schematically represented by the illustrations in Figure 21.

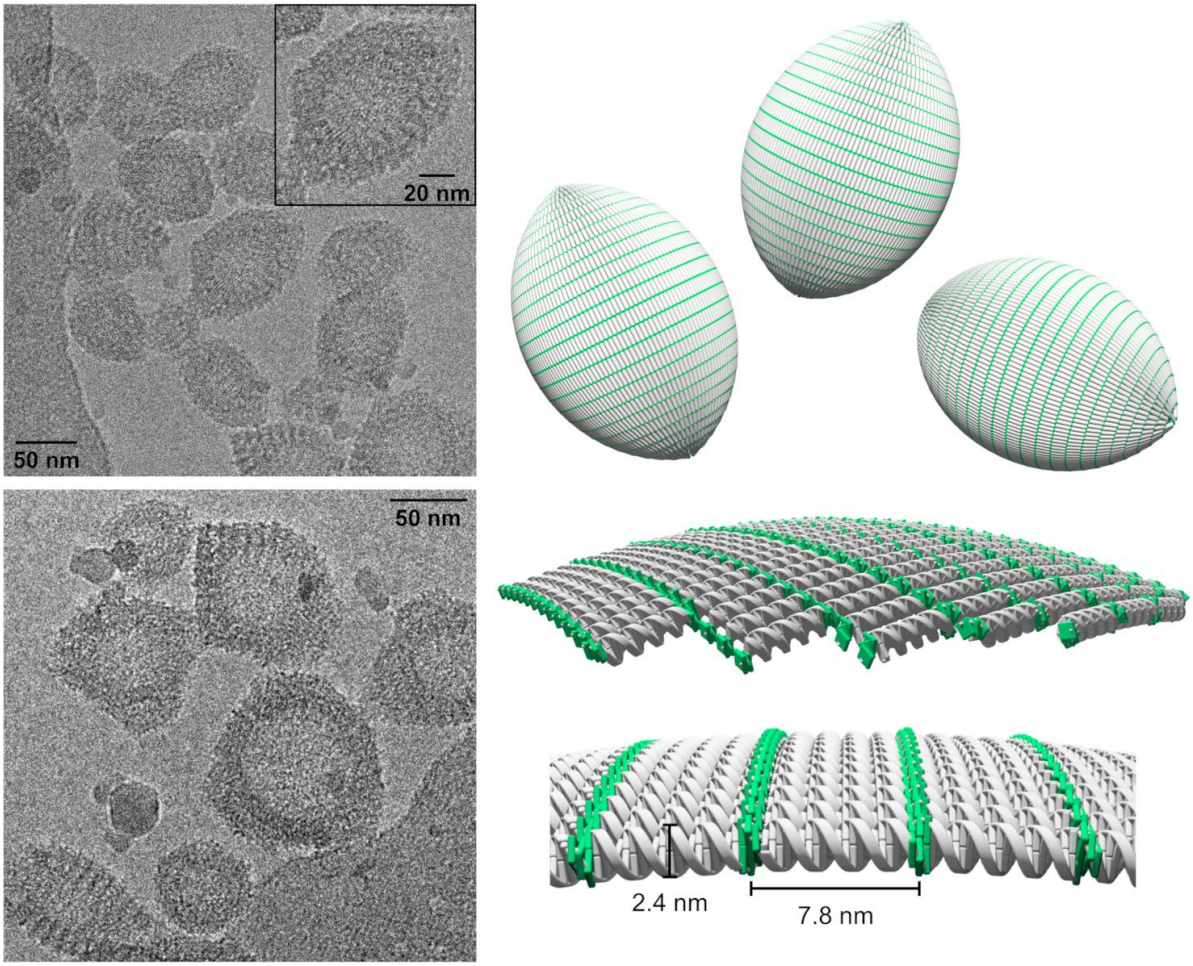

Figure 21. Type I supramolecular assemblies of **ON1*ON2** visualized by cryo-EM and schematic representations. Conditions: 1 μM **ON1*ON2**, 10 mM sodium phosphate buffer pH 7.2, 0.1 mM spermine · 4 HCl, 20 vol% ethanol.

In contrast to the extended arrangement of the DNA duplexes in type I vesicles, the second morphology (type II vesicles) is characterized by a more compact, columnar alignment of the DNA duplexes (Figure 22). In this type II architecture, the vesicular membrane was measured to be 10.9 ± 0.5 nm and the DNA width about 2.5 ± 0.5 nm (see illustration in Figure 22). Compared to type I vesicular constructs, type II vesicles also have a different diameter and range between 200–350 nm. Because the TPE sticky ends are located on both sides of the membrane, double-layered type II vesicles can be formed *via* π-stacking of the TPEs. Such a behavior of an additional assembly of a second layer is frequently visible in type II constructs. Additional cryo-EM images of both morphologies are provided in Figure 64.

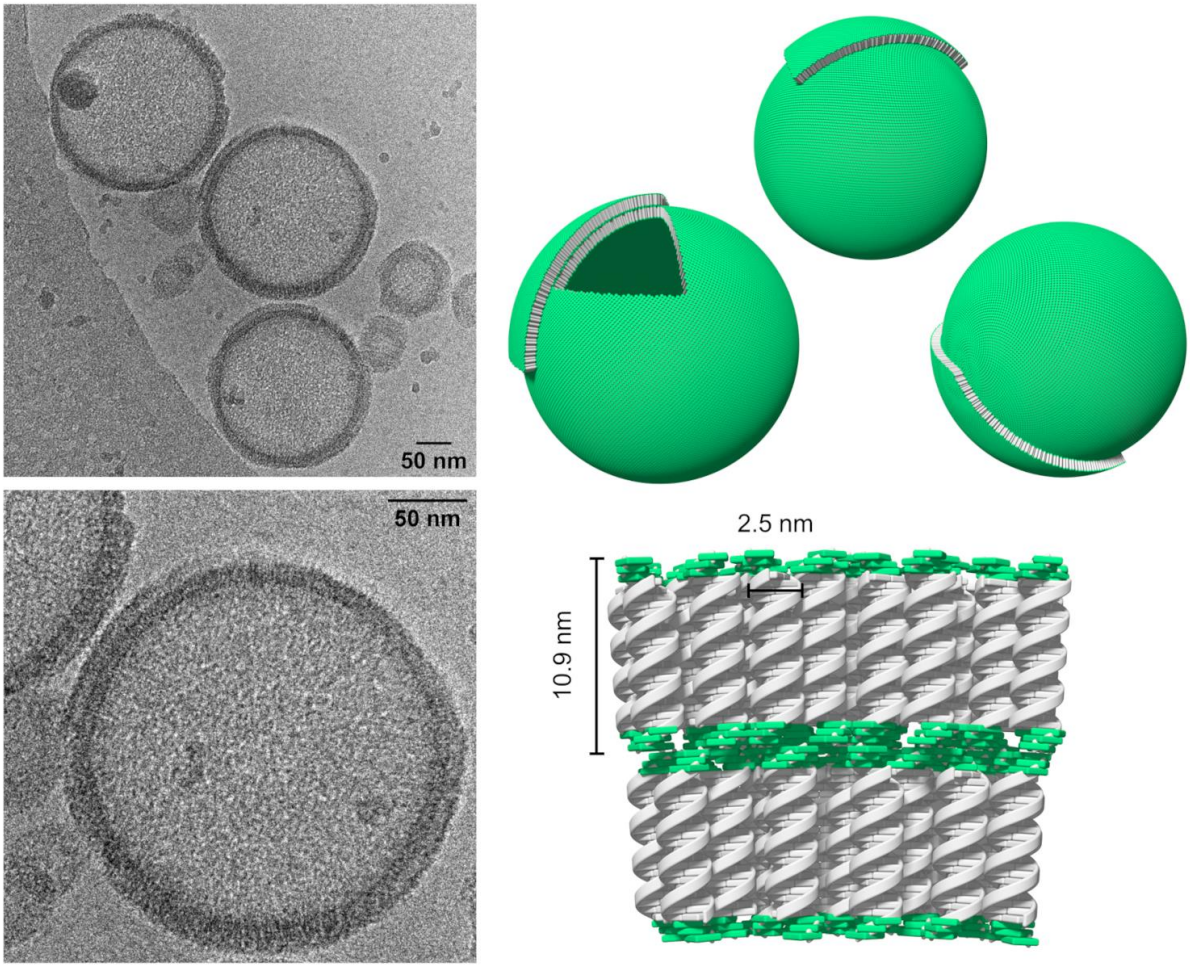

Figure 22. Type II supramolecular assemblies of **ON1*ON2** visualized by cryo-EM and schematic representations. Conditions: 1 µM **ON1*ON2**, 10 mM sodium phosphate buffer pH 7.2, 0.1 mM spermine · 4 HCl, 20 vol% ethanol.

In both types of vesicular architectures, the negatively charged DNA backbones of neighboring DNA duplexes within the assemblies are close to each other. This rather tight DNA packing induces a coulombic repulsion, which needs to be neutralized by spermine and thus, spermine is crucial for the formation of the vesicles. If the thermal assembly process has been performed in the absence of the polycation, no nanostructures were found by cryo-EM imaging (Figure 23). While the spectroscopic data still suggest DNA hybridization, it does not indicate for supramolecular polymerization, particularly due to the absence of any discernible nucleation temperature in the fluorescence-monitored annealing curve (Figure 65). This assumption is further supported by the small dark spots (some are representatively encircled in Figure 23), which might be ascribed to individual DNA duplexes.

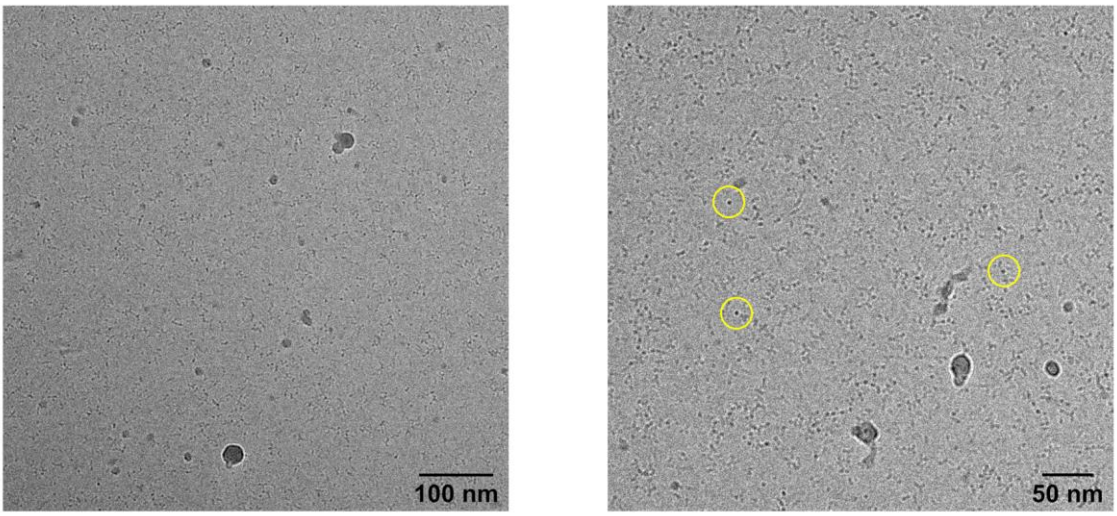

Figure 23. Cryo-EM imaging of **ON1*ON2** after the thermal assembly process has been performed in the absence of spermine · 4 HCl. The encircled dark spots might be ascribed to individual DNA duplexes. Conditions: 1 µM **ON1*ON2**, 10 mM sodium phosphate buffer pH 7.2, 20 vol% ethanol.

If these DNA-constructed vesicles are envisioned for example as potential drug carriers, the ethanol fraction of the aqueous medium poses substantial problems regarding biocompatibility. Therefore, the thermal assembly process has been performed in the absence of ethanol. However, the spectroscopic data (Figure 24) suggests incomplete disassembly at 75 °C, mainly evidenced by the significant fluorescence emission at this temperature and no distinct nucleation temperature in the fluorescence-monitored annealing curve. The corresponding cryo-EM images are presented in Figure 25, which show undefined, small aggregates. Thus, the ethanol fraction is required during the thermal assembly process to afford such well-defined type I and type II vesicular constructs.

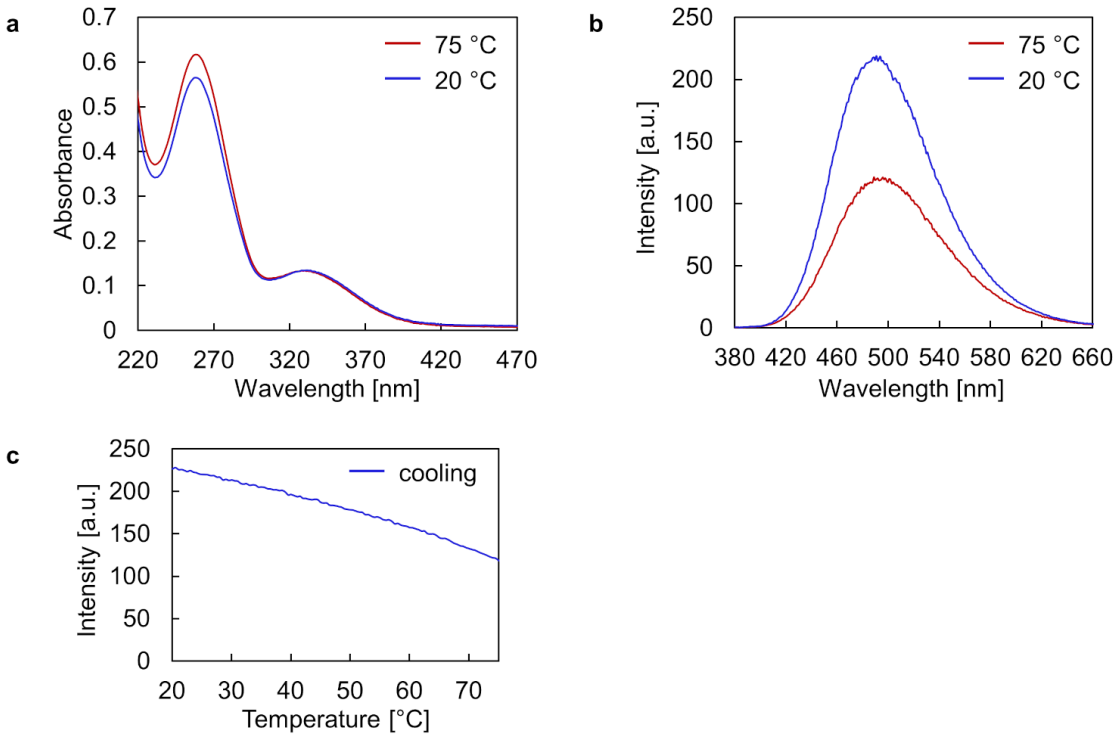

Figure 24. (**a**) UV-Vis absorption spectra, (**b**) fluorescence emission spectra, and (**c**) fluorescence-monitored annealing curve of **ON1*ON2** in the absence of ethanol. Conditions: 1 µM **ON1*ON2**, 10 mM sodium phosphate buffer pH 7.2, 0.1 mM spermine · 4 HCl, $\lambda_{ex.}$: 335 nm, $\lambda_{em.}$: 490 nm, gradient: 0.5 °C/min.

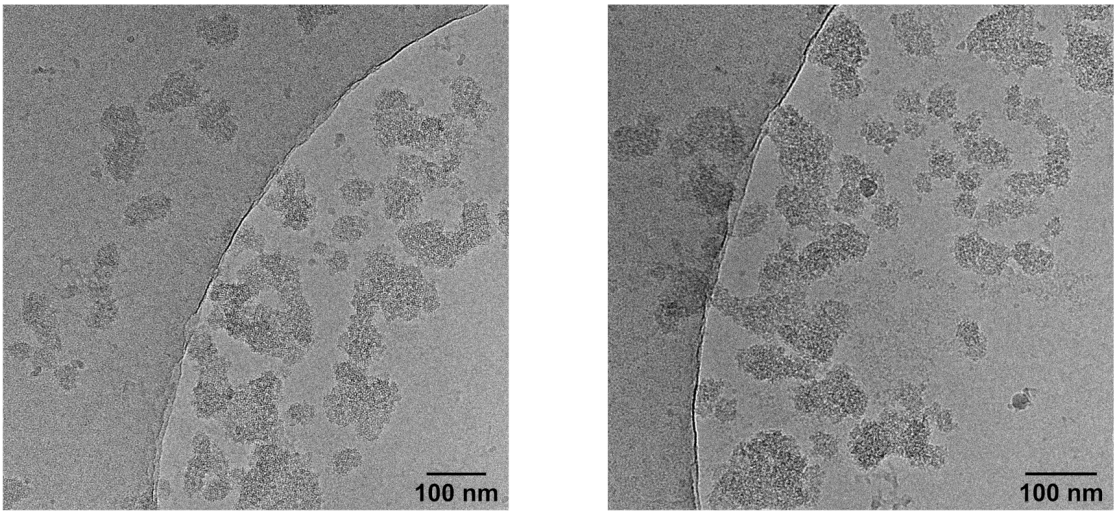

Figure 25. Cryo-EM images of aggregated **ON1*ON2** after the thermal assembly process has been performed in the absence of the ethanol fraction. Conditions: 1 µM **ON1*ON2**, 10 mM sodium phosphate buffer pH 7.2, 0.1 mM spermine · 4 HCl.

Well-defined vesicles without any ethanol present in the aqueous medium were only obtained by a two-step procedure. First, a thermal assembly process has been performed in the presence of ethanol. In the second step, the ethanol fraction was removed by dialysis against 10 mM sodium phosphate buffer pH 7.2, containing 0.1 mM spermine · 4 HCl. The successful removal of the ethanol fraction was verified by measuring the refractive index of a control, that was treated identically to the respective sample and compared against a calibration curve (Figure 66). After dialysis, the absorbance, and the fluorescence signal decreased (Figure 67), as well as Φ_{FL} (23 ± 2%). Depicted in Figure 26 is a cryo-EM image of the nanostructures after dialysis (for additional images, see Figure 68). The ratio between the two types of vesicular architectures basically inverted. While 94% of the vesicles belonged to the type I architecture before dialysis, more than 90% of all observed vesicles are associated to the type II DNA duplex arrangement after ethanol removal. The vesicular membrane thickness was not affected significantly (10.6 ± 0.6 nm), but the diameter of the vesicles decreased to about 50–150 nm.

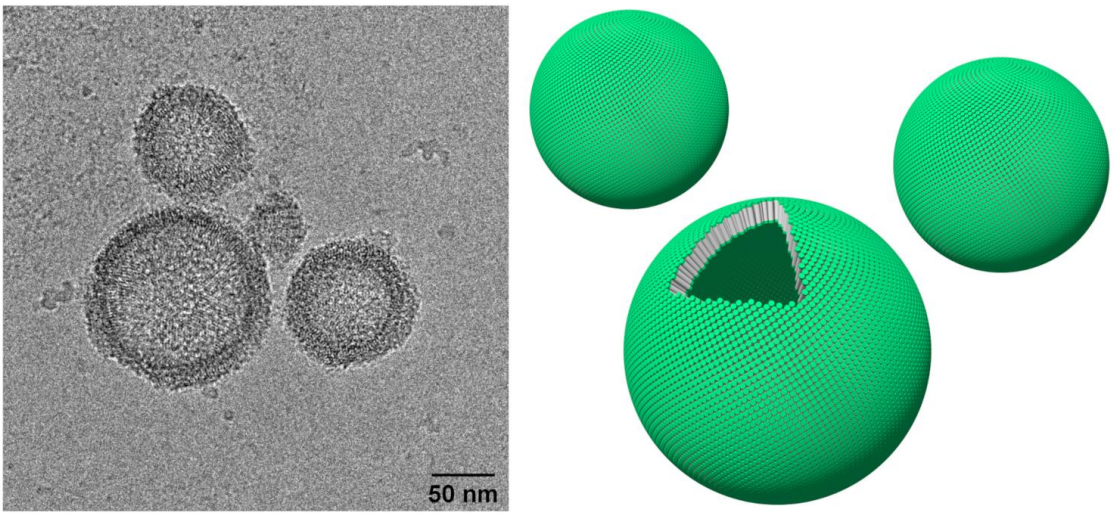

Figure 26. Cryo-EM image and schematic representations of type II vesicles of **ON1*ON2** after removal of ethanol by dialysis. Conditions: 1 µM **ON1*ON2**, 10 mM sodium phosphate buffer pH 7.2, 0.1 mM spermine · 4 HCl, <0.5 vol% ethanol.

In summary, in the presence of ethanol, type I vesicles are predominant, while the vast majority belongs to type II vesicles after removal of the ethanol fraction by dialysis. This allows to investigate the accessibility and addressability of the DNA of the two different vesicular morphologies separately and is the topic of the next two subchapters 3.1.7 and 3.1.8.

3.1.7 Ethidium Bromide Intercalation

The accessibility of the DNA within the two different vesicular morphologies was examined by DNA intercalation experiments. Ethidium bromide (EthBr, Figure 27) represents one of the classical DNA intercalators and was therefore selected for this study.[189–194] Following the neighbor exclusion principle,[195] a maximum of 10 EthBr units can intercalate into a 20-mer DNA duplex, as illustrated in Figure 27a. For the following experiments, it was approximated that EthBr only intercalates into the double-stranded DNA part of **ON1*ON2** (Figure 27b).

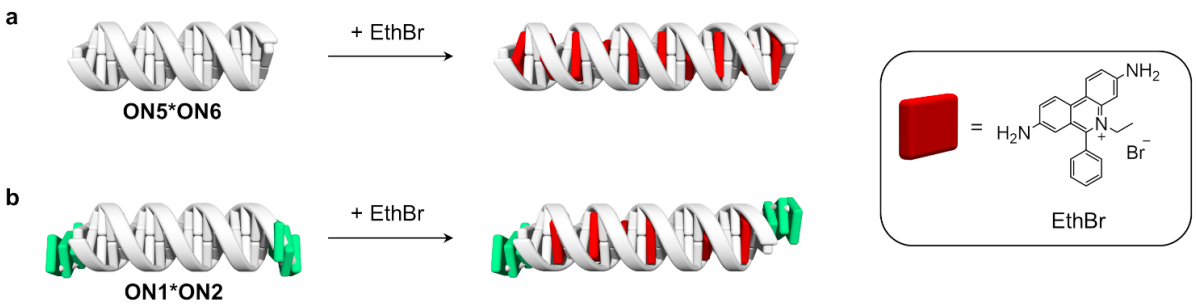

Figure 27. Illustration of ethidium bromide (EthBr) intercalation into reference duplex **ON5*ON6** (**a**) and TPE-modified duplex **ON1*ON2** (**b**), and chemical structure of EthBr.

EthBr intercalation was first studied by fluorescence spectroscopy. Compared to the intrinsic fluorescence emission of free EthBr in solution, intercalated EthBr shows increased emission.[196,197] Therefore, 10 µM of EthBr was added to preformed type I vesicular constructs of **ON1*ON2**. After TPE excitation ($\lambda_{ex.}$: 335 nm), the emission of TPE is almost quenched entirely (Figure 28b). On the other hand, emission from EthBr emerged around 610 nm, which indicates that the excitation energy from the TPEs is transferred to EthBr. However, to calculate the EthBr intercalation efficiency into self-assembled **ON1*ON2**, the excitation wavelength was adjusted to 520 nm. At this wavelength, the observed absorbance solely originates from EthBr (Figure 28a). The integrated fluorescence intensity of the reference DNA duplex **ON5*ON6** in the presence of 10 µM of EthBr (Figure 70) was set to 100% intercalation efficiency (after subtraction of the intrinsic fluorescence of free EthBr in solution, Figure 69). This corresponds to the maximum of 10 EthBr units intercalated into **ON5*ON6** (Table 2). According to the relative integrated fluorescence intensities between the reference DNA duplex **ON5*ON6** and type I vesicles of **ON1*ON2**, about 6 EthBr units intercalate per **ON1*ON2** duplex (Table 2 and Figure 27b).

The same experiments were also performed with type II vesicles. The vesicles were prepared by the thermal assembly procedure, followed by ethanol removal by dialysis to obtain type II vesicular constructs. In this case, it was calculated that only about 2 EthBr molecules intercalate per DNA duplex **ON1*ON2** (Figure 71–Figure 73, and Table 2).

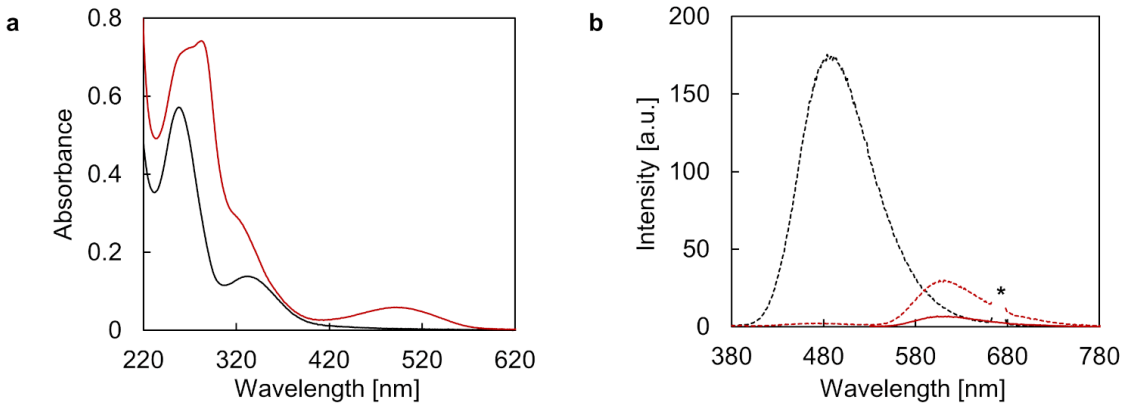

Figure 28. (**a**) UV-Vis absorption spectra and (**b**) fluorescence emission spectra (dotted line: $\lambda_{ex.}$: 335 nm; solid line: $\lambda_{ex.}$: 520 nm) of **ON1*ON2** before (black) and after 10 µM EthBr addition (red) to type I vesicles. Conditions: 1 µM **ON1*ON2**, 10 mM sodium phosphate buffer pH 7.2, 0.1 mM spermine · 4 HCl, 20 vol% ethanol, 20 °C, * denotes second-order diffraction.

Table 2. Mean values for the calculation of the intercalation efficiency. Conditions: 10 µM EthBr, 10 mM sodium phosphate buffer pH 7.2, 0.1 mM spermine · 4 HCl, 20 resp. <0.5 vol% ethanol, 20 °C. [a] Integrated fluorescence intensity between 540–740 nm, $\lambda_{ex.}$: 520 nm. [b] Assuming that the reference DNA duplex **ON5*ON6** is maximally intercalated with 10 EthBr units.

Sample	FL_{area}[a]	Sample-Blank	[%]	Number of intercalated EthBr
Aqueous medium, containing 20 vol% ethanol	362.8	0	0	0
ON5*ON6 (1 µM), containing 20 vol% ethanol	877.2	514.4	100[b]	10[b]
EthBr added to type I vesicles of **ON1*ON2** (1 µM)	655.2	292.4	57	6
Aqueous medium, without ethanol	149.9	0	0	0
ON5*ON6 (1 µM), without ethanol	1340.4	1190.5	100[b]	10[b]
EthBr added to type II vesicles of **ON1*ON2** (1 µM)	434.1	284.2	24	2

EthBr intercalation was also studied by cryo-EM imaging, which should lead to a widening of the discrete bands that were observed in the cryo-EM images (distance x in Figure 29). Upon intercalation, the DNA helix is lengthened by roughly 3.4 Å per intercalated EthBr.[39,198] Indeed, successful intercalation of EthBr into type I vesicles was confirmed by a statistically significant extension of the distance x from originally 7.8 ± 0.5 nm to 9.9 ± 0.6 nm after EthBr addition. This lengthening corresponds to about 6 intercalated EthBr units. It is noteworthy that the overall morphology of the vesicular constructs is not affected after EthBr addition (see also Figure 74). Conversely, no statistically significant widening of the vesicular membrane was found after EthBr addition to the type II vesicular architecture (Figure 29 and Figure 75). These results agree very well with the fluorescence spectroscopy data and suggest that only the extended DNA alignment of type I vesicular constructs is accessible for efficient EthBr DNA intercalation.

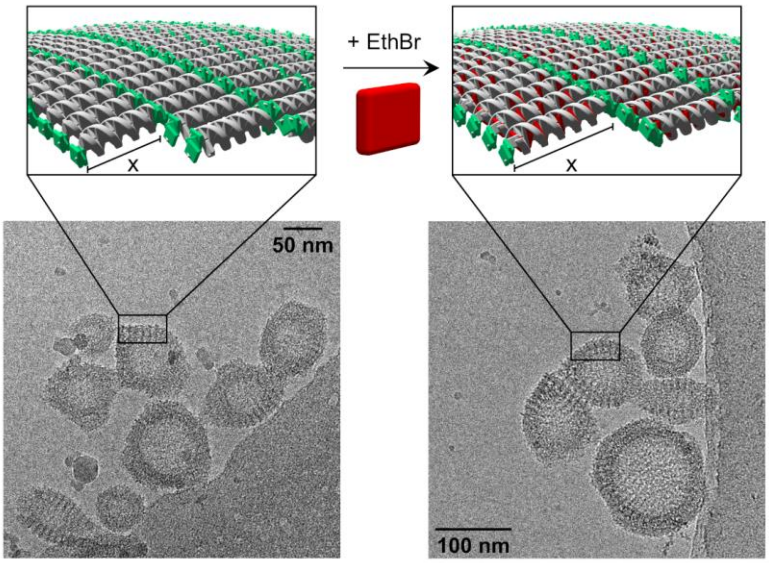

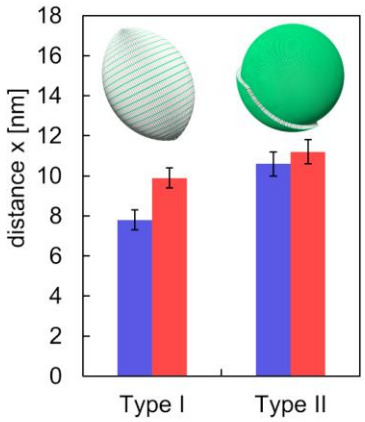

EthBr [μM]	Type I	Type II
0	7.8 ± 0.5	10.6 ± 0.6
10	9.9 ± 0.6	11.2 ± 0.6

Figure 29. Cryo-EM images before and after EthBr addition to type I vesicles as well as a summary of the corresponding distance measurements for both types of morphologies.

3.1.8 Accessibility and Addressability Study with Light-Harvesting Experiments

Doping experiments with a Cy3-labelled DNA single strand **ON7** have been performed to investigate the addressability and accessibility of the two different vesicular architectures. First, type I vesicles have been prepared by the thermal assembly procedure, before minute amounts of the complementary strand **ON7** (1 mol% Cy3 per TPE unit) were added at 20 °C. Incorporation of **ON7** into the vesicular membrane is assumed to take place *via* strand exchange (Figure 30). Upon TPE excitation, successful incorporation would result in excitation energy transfer from the TPE donors to the Cy3 acceptor, leading to Cy3 emission.

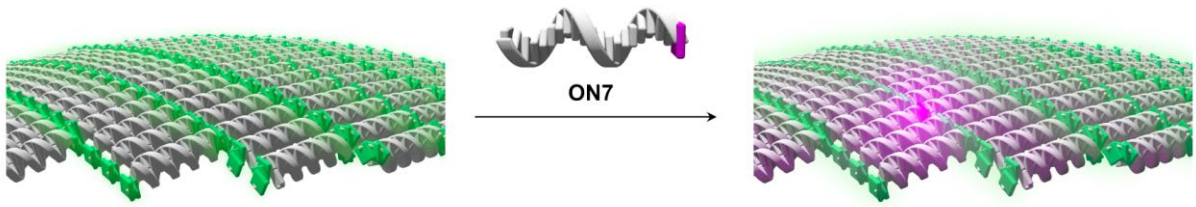

Figure 30. Schematic representation for the doping of type I vesicles with Cy3-labelled **ON7**, leading to a light-harvesting system.

The corresponding fluorescence emission results for type I vesicles are presented in Figure 31a (for UV-Vis absorption spectra, see Figure 76a). After the addition of **ON7** and TPE excitation at 335 nm, TPE fluorescence (around 490 nm) is reduced and emission from Cy3 (around 570 nm) emerges, indicative for excitation energy transfer from TPE to Cy3. A Förster resonance energy transfer (FRET)[32–36] mechanism is proposed due to the spectral overlap between TPE emission and Cy3 absorbance. The spectroscopic characterization of **ON7** is presented in Figure 77. Deconvolution of the blue curve in Figure 31a leads to the individual emission components for TPE and Cy3 (illustrated in Figure 32) and allows the calculation of the FRET efficiency. Based on the integrated TPE fluorescence intensities, it was calculated that the excitation energy from about 22 ± 4 TPEs is transferred to a Cy3 acceptor. Hence, the TPE units act as light-harvesting antennae and transfer the excitation energy to Cy3 acceptor moieties. According to the calculated FRET radius of R_0 = 49 Å,[199–201] it is assumed that energy is transferred predominantly only along one band of TPEs in type I vesicles. Doping of type I vesicles with **ON7** has no effect on the morphology of the assemblies, as evidenced by the AFM images displayed in Figure 33. Vesicular structures with a comparable size range as observed in the absence of

ON7 were found. After removal of the ethanol fraction by dialysis, the light-harvesting properties are sustained (green curve, Figure 31a).

On the other hand, direct addition of **ON7** (1 mol% Cy3 per TPE unit) to type II vesicles leads to neglectable excitation energy transfer only (green curve, Figure 31b). This marginal energy transfer might be ascribed to edge effects in partially double-layered type II constructs. At the edges of an additional layer, the duplex alignment resembles the type I vesicular membrane.

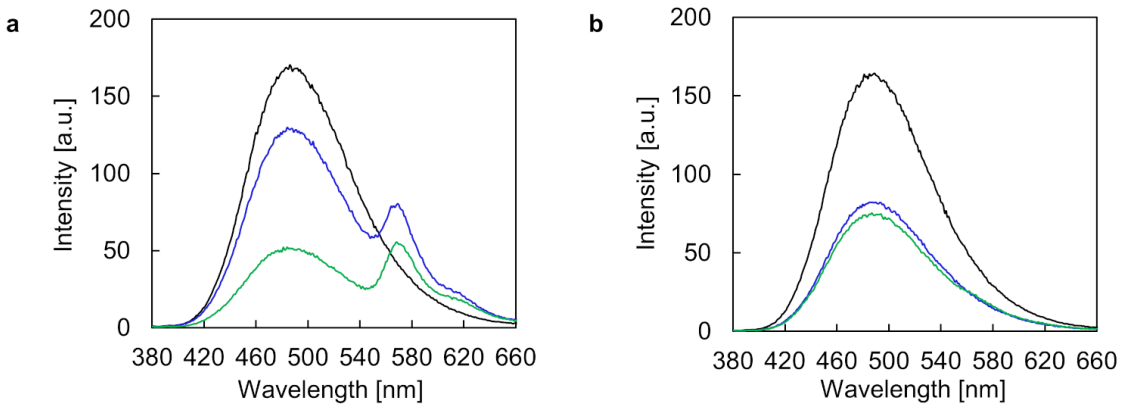

Figure 31. (**a**) Fluorescence emission spectra of self-assembled vesicles of **ON1*ON2** in the absence (black) and presence of 1 mol% **ON7**, before (blue) and after (green) removal of ethanol by dialysis. (**b**) Fluorescence emission spectra of self-assembled vesicles of **ON1*ON2** in the absence of **ON7** before (black) and after (blue) dialysis, and after dialysis in the presence of 1 mol% **ON7** (green). Conditions: 1 µM **ON1*ON2**, 10 mM sodium phosphate buffer pH 7.2, 0.1 mM spermine · 4 HCl, 20 resp. <0.5 vol% ethanol, 20 °C, $\lambda_{ex.}$: 335 nm.

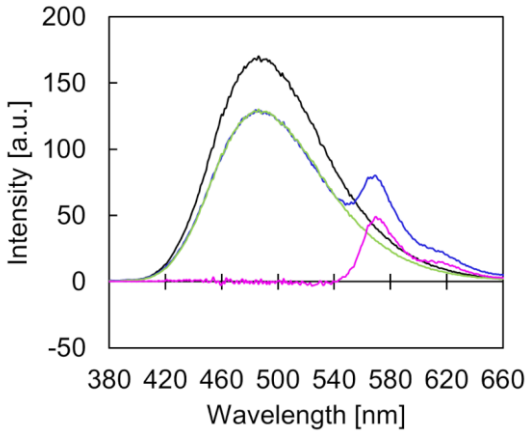

	FL_{area} [a]
Undoped **ON1*ON2**	18891.4
1 mol% Cy3 doped **ON1*ON2**	16777.4
TPE part of doped **ON1*ON2**	14732.6
Cy3 part of doped **ON1*ON2**	2044.8

Figure 32. Deconvoluted fluorescence emission spectra as well as corresponding integrated fluorescence intensities for the calculation of the light-harvesting efficiency before removal of the ethanol fraction by dialysis. Undoped type I vesicles of **ON1*ON2** (black), 1 mol% **ON7** doped **ON1*ON2** (blue), deconvoluted TPE part of doped **ON1*ON2** (light green), and deconvoluted Cy3 part of doped **ON1*ON2** (pink). [a] Integration between 380–660 nm, $\lambda_{ex.}$: 335 nm.

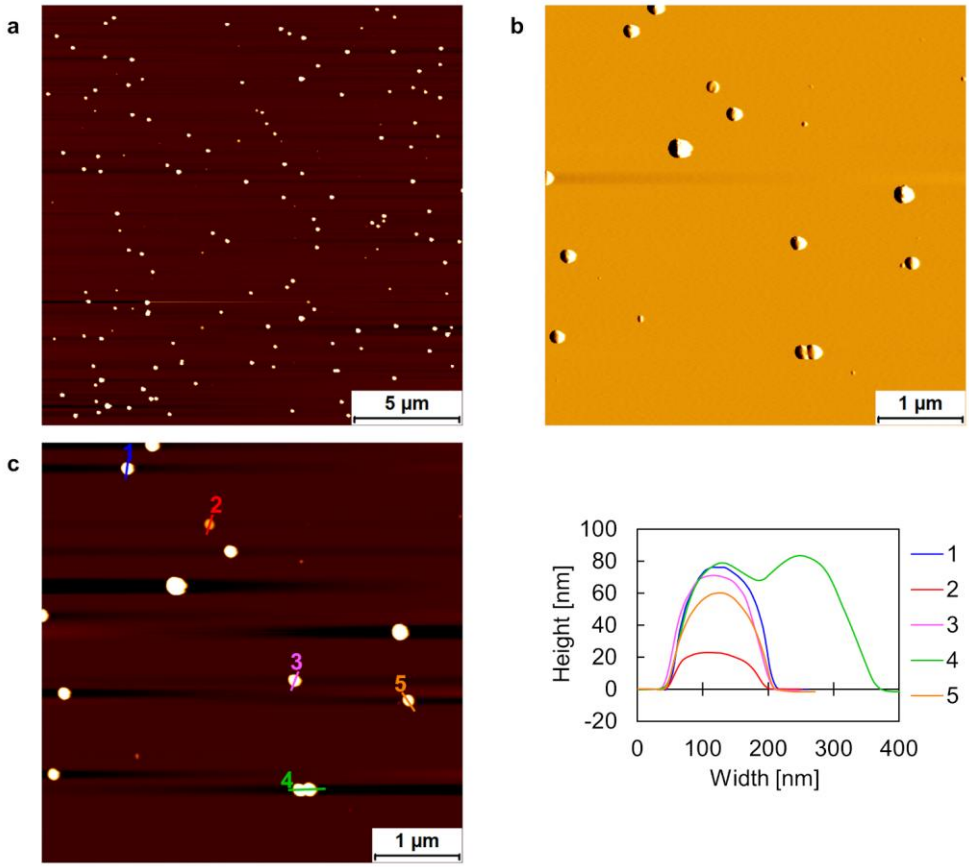

Figure 33. (**a**) AFM overview scan, (**b**) deflection scan, and (**c**) zoom with corresponding cross sections of Cy3-doped assemblies of **ON1*ON2**. Conditions: 1 µM **ON1*ON2**, 1 mol% **ON7**, 10 mM sodium phosphate buffer pH 7.2, 0.1 mM spermine · 4 HCl, 20 vol% ethanol.

The specificity of the doping process was confirmed by the addition of a non-complementary, Cy3-labelled DNA single strand. **ON8** exhibits the same base composition as **ON7** but is not complementary to any of the TPE-DNA conjugates **ON1** or **ON2**. Addition of **ON8** to either type I or type II vesicles does not lead to light-harvesting complexes (Figure 34). Therefore, **ON8** is not incorporated into the vesicular constructs and thus, excludes excitation energy transfer.

These results are in line with the data obtained from ethidium bromide intercalation experiments. Type I vesicles are more accessible than type II constructs for EthBr intercalation and the incorporation of a Cy3-labelled DNA single strand. The compact, columnar arrangement of the DNA duplexes in type II vesicular architecture seems to be rather inaccessible.

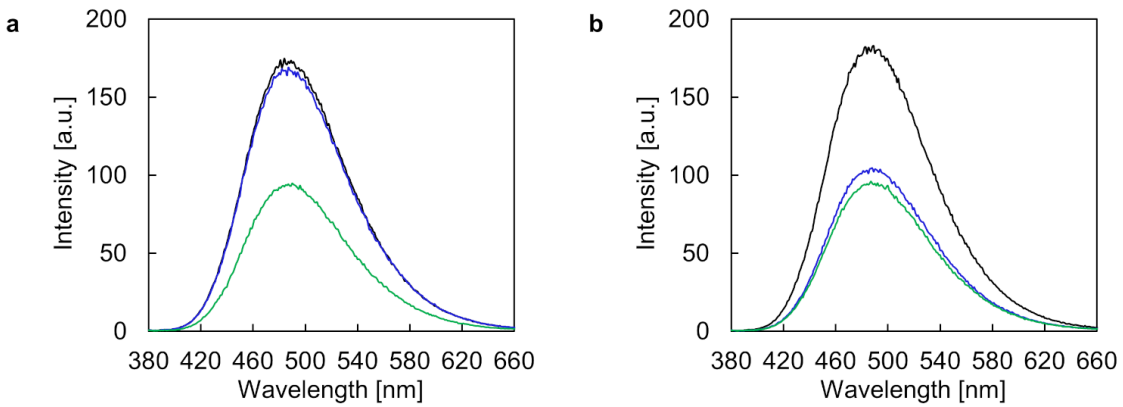

Figure 34. (**a**) Fluorescence emission spectra of self-assembled vesicles of **ON1*ON2** in the absence (black) and presence of 1 mol% **ON8**, before (blue) and after (green) removal of ethanol by dialysis. (**b**) Fluorescence emission spectra of self-assembled vesicles of **ON1*ON2** in the absence of **ON8** before (black) and after (blue) dialysis, and after dialysis in the presence of 1 mol% **ON8** (green). Conditions: 1 µM **ON1*ON2**, 10 mM sodium phosphate buffer pH 7.2, 0.1 mM spermine · 4 HCl, 20 resp. <0.5 vol% ethanol, 20 °C, $\lambda_{ex.}$: 335 nm.

The successful doping was further verified by nanoparticle tracking analysis (NTA) experiments. Figure 35 displays the size distribution plots of type I vesicles before and after doping with 1 mol% of the Cy3-modified DNA single strand **ON7** and the results are summarized in Table 3. Very similar diameters were found for the measurements in scatter mode before and after doping. The sizes also match the dimensions of the vesicular nanostructures found by AFM, TEM, and cryo-EM.

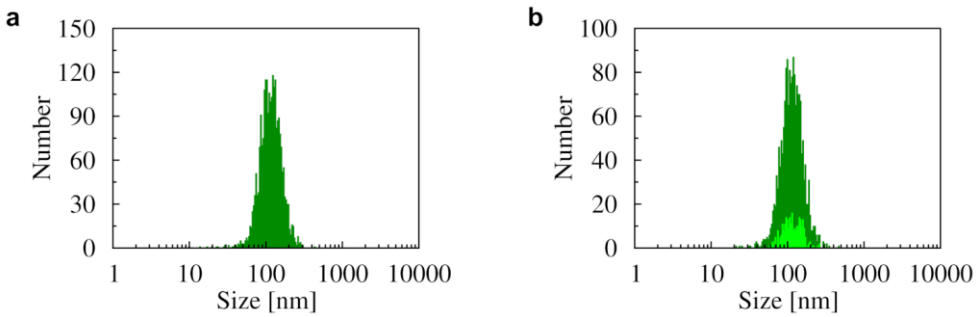

Figure 35. (**a**) NTA size distribution result (scatter mode) of self-assembled **ON1*ON2**. Conditions: 1 µM **ON1*ON2**, 10 mM sodium phosphate buffer pH 7.2, 0.1 mM spermine · 4 HCl, 20 vol% ethanol, 25 °C. (**b**) NTA size distribution result of Cy3-doped type I vesicles of **ON1*ON2**. Conditions: 1 µM **ON1*ON2**, 1 mol% **ON7**, 10 mM sodium phosphate buffer pH 7.2, 0.1 mM spermine · 4 HCl, 20 vol% ethanol, 25 °C, scatter mode (dark green), fluorescence mode (light green, $\lambda_{ex.}$: 488 nm).

Table 3. Summary of size distribution and ζ-potential results of type I vesicles obtained by NTA before and after Cy3 doping. Conditions as in Figure 35. [a] $\lambda_{ex.}$: 488 nm.

	NTA size [d.nm]	F-NTA size[a] [d.nm]	ζ-potential [mV]
Type I vesicles of **ON1*ON2**	121 ± 40	-	–17 ± 1
Cy3-doped type I vesicles of **ON1*ON2**	120 ± 41	121 ± 36	–16 ± 1

Furthermore, Cy3 doping allowed NTA measurements in fluorescence mode (F-NTA). The mean value of the F-NTA size distribution (121 ± 36 nm) is nearly identical to the mean value obtained in scatter mode (120 ± 41 nm). Therefore, it is suggested that there is no preference for the incorporation of **ON7** either into small or large type I vesicles within the observed size distribution.

The measured ζ-potentials (Table 3) suggest that spermine strongly interacts with the negatively charged phosphate backbone of the DNA, thus neutralizing the negative charges present in the DNA backbone to some extent.

3.1.9 Cytotoxicity Assays

Ethidium bromide intercalation and light-harvesting experiments demonstrated the addressability of the DNA in type I vesicles. This dynamic nature of the vesicular constructs of **ON1*ON2** suggests potential applications as DNA-addressable nanocarriers for drug delivery. However, before any drug delivery experiments can be conducted, it must be excluded that neither the nanocarrier nor the aqueous medium itself shows considerable cytotoxicity. Therefore, cytotoxicity assays were performed in collaboration with Prof. Dr. Paola Luciani and Dr. Florian Weber from the Department of Chemistry, Biochemistry and Pharmaceutical Sciences of the University of Bern. The cytotoxicity of the vesicles was tested on the HepG2 cancer cell line, which is a human hepatoblastoma-derived liver cell line.[202–204] Obviously, the aqueous medium required for the thermal assembly process (*i.e.*, 20 vol% ethanol) would be toxic. Consequently, only type II vesicles after removal of the ethanol fraction could be analyzed in these cytotoxicity assays. This implies that the drug loading would rather need to be accomplished before dialyzing off the ethanol fraction, because type II vesicles were shown to be significantly less accessible and addressable.

In a first set of experiments, the toxicity of the aqueous medium, denoted as buffer (10 mM sodium phosphate buffer pH 7.2, 0.1 mM spermine · 4 HCl), was investigated. Therefore, HepG2 cells were treated with different fractions of buffer solution. Figure 36 summarizes the results and show that the HepG2 cells tolerate well buffer fractions of up to 40% (83 ± 2% cell viability).

In a second set of experiments, the toxicity of type II vesicles assembled from **ON1*ON2** was tested (Figure 37). No considerable cytotoxicity was observed in the tested concentration range. However, there are several steps that one would need to investigate in more detail if the vesicles are envisioned for drug delivery applications. Firstly, the stability of the vesicles in the cell medium at 37 °C would need to be studied. At this point, there is no experimental evidence that the vesicles were stable during the incubation period. Thus, the results presented in Figure 37 reflect the toxicity of the vesicles as well as potential degradation products formed during incubation. Secondly, the maximum concentration of the nanocarrier was relatively low (200 nM **ON1*ON2** duplex concentration). This concentration is probably simply too low to achieve any desired therapeutic effect. One approach to concentrate the vesicles is by means of ultrafiltration. However, this resulted in massive agglomerates of individual vesicles, as evidenced by cryo-EM images (Figure 38).

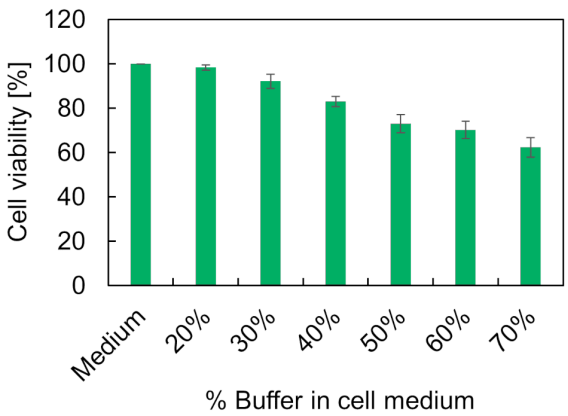

Figure 36. Cell viability of HepG2 after 24 h of treatment with buffer solution. Buffer solution, containing 10 mM sodium phosphate buffer pH 7.2, 0.1 mM spermine · 4 HCl. Medium: Carl Roth, RPMI-1640, without phenol red.

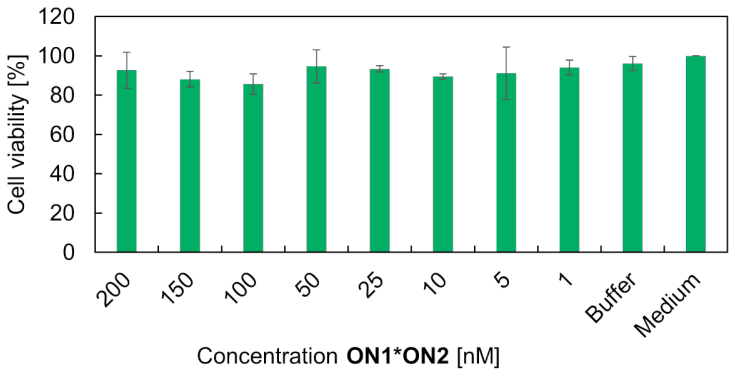

Figure 37. Cell viability of HepG2 after 24 h of treatment with vesicular constructs of **ON1*ON2**. Buffer: 10 mM sodium phosphate buffer pH 7.2, 0.1 mM spermine · 4 HCl. Medium: Carl Roth, RPMI-1640, without phenol red.

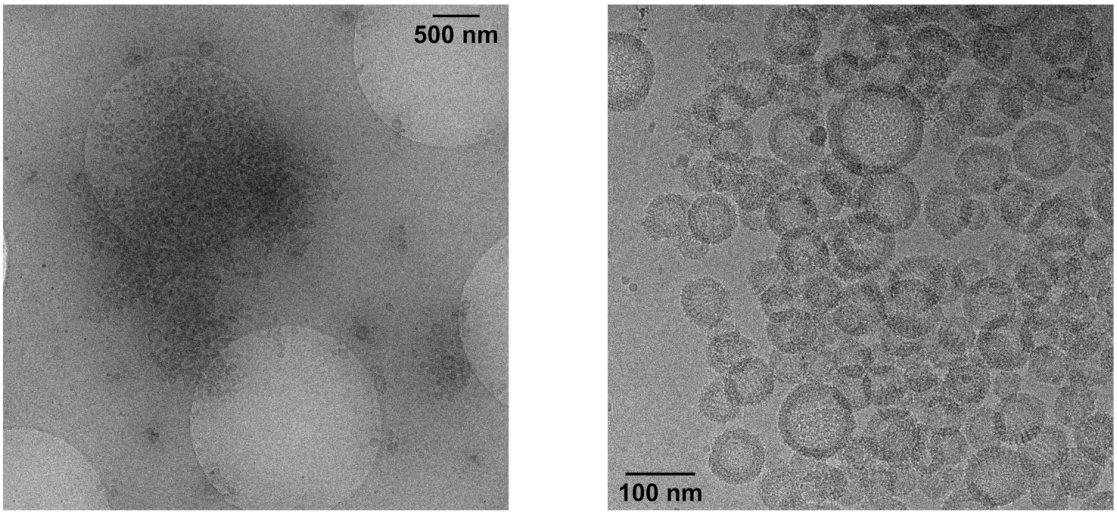

Figure 38. Cryo-EM images of concentrated vesicles by ultrafiltration. Conditions: 1 μM **ON1*ON2**, 10 mM sodium phosphate buffer pH 7.2, 0.1 mM spermine · 4 HCl, 20 vol% ethanol.

3.2 Conclusions and Outlook

In summary, the self-assembly of amphiphilic 3'-end modified TPE-DNA conjugates has been described. Owing to the TPE overhangs in the chemically modified oligonucleotides, the resulting supramolecular assemblies possess AIE properties, which were demonstrated by temperature-dependent fluorescence spectroscopy. DNA duplexes with TPE overhangs on both sides self-assembled into vesicular constructs *via* TPE sticky end interactions and spermine mediated interactions between duplexes.

In the case of *E*-TPE overhangs (**ON1*ON2**), cryo-EM imaging revealed two distinct types of vesicular architectures at the resolution level of the width of a single DNA duplex. The two DNA architectures are characterized by a different DNA duplex alignment. In type I vesicles, the DNA duplexes are arranged in an extended fashion, while type II vesicles are specified by a more compact, columnar DNA duplex alignment. In addition to a buffered aqueous medium, spermine and ethanol were found to be essential for the assembly of such well-defined nanostructures. The ethanol fraction ensures complete disassembly at 75 °C and is required during the thermal assembly process. The abundance of type I and type II vesicles is greatly influenced by the ethanol content. In the presence of ethanol, most of the vesicles belong to the type I architecture. However, after removal of the ethanol content by dialysis, type II vesicular constructs were predominantly found.

The type of DNA alignment determines the accessibility of the DNA duplexes. Only the extended DNA duplex arrangement in type I vesicular constructs were accessible for ethidium bromide intercalation or doping with a Cy3-labelled DNA single strand. In the case of EthBr intercalation, the successful intercalation was demonstrated by fluorescence spectroscopy as well as directly visualized by cryo-EM imaging. For the incorporation of the Cy3-modified oligonucleotide *via* strand exchange, light-harvesting vesicular complexes were constructed, in which the excitation energy from the TPEs is transferred to Cy3.

So far, it was assumed that energy was only harvested along a single band of TPEs, due to the calculated FRET radius. To increase the antennae effect by harvesting energy from at least two bands of TPEs, one might position the acceptor (*i.e.*, Cy3) in the middle of the complementary strand.

Because these well-defined types of vesicular architectures were only formed when the duplex featured TPE overhangs on both sides, the study of 3’-/5’-end modified TPE-DNA conjugates was intended. In the case of such 3’-/5’-end modifications, the TPE residues are on the same DNA single strand. Thus, the TPEs are always on both sides in the corresponding duplex, providing more variability of the complements in terms of additional modifications. In the next chapter, the influence of different oligonucleotide designs, composed of 3’-/5’-end modified TPE-DNA conjugates hybridized to an unmodified complement, on the supramolecular assembly behavior will be investigated.

3.3 Appendix – Chapter 3

3.3.1 Organic Synthesis

The synthesis of *E*- and *Z*-TPE phosphoramidites **6** and **7** respectively, was adapted from published procedures (Scheme 1).[74]

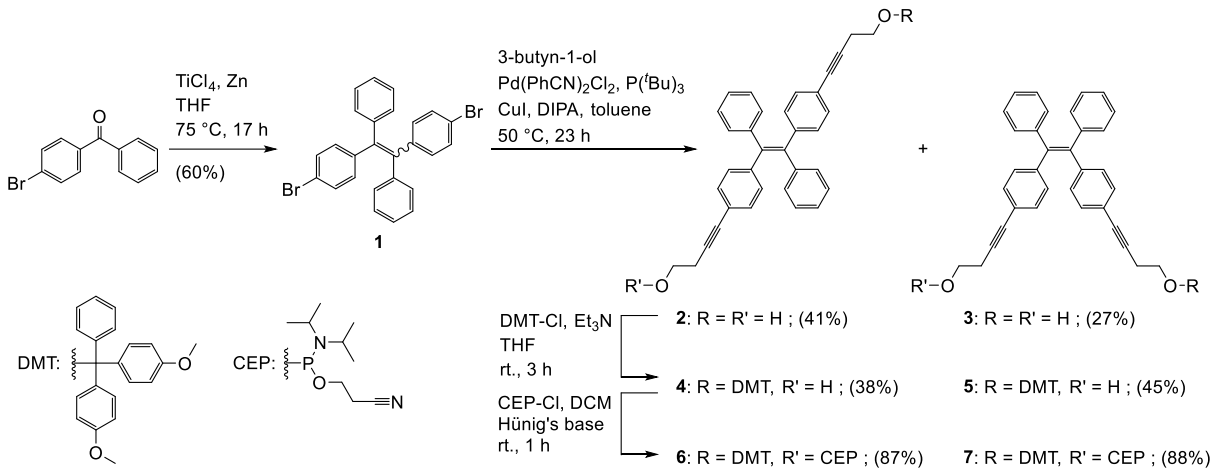

Scheme 1. Synthesis of *E*-TPE phosphoramidite **6** and *Z*-TPE phosphoramidite **7**.

1,2-Bis(4-bromophenyl)-1,2-diphenylethene (1)

4-Bromobenzophenone (6.53 g, 25.01 mmol) and Zn dust powder (4.92 g, 75.25 mmol) were suspended in THF (150 mL). The grey suspension was cooled to 0 °C, before $TiCl_4$ (4.1 mL, 37.40 mmol) was added slowly. After the reaction mixture was warmed to rt., it was refluxed at 77 °C for 15 h. TLC (DCM) showed disappearance of starting material. The reaction mixture was cooled to rt., before aq. 10% K_2CO_3 (125 mL) was added. The reaction mixture was filtered through *celite* and the filter cake was washed thoroughly with THF, followed by DCM. The yellow filtrate was extracted three times with DCM (3x80 mL). The combined organic layers were washed once with brine (100 mL), dried over $MgSO_4$, filtered, and concentrated *in vacuo*. The resulting yellow, oily residue was dissolved in DCM (4 mL), then precipitated into cold MeOH (625 mL) while stirring. The forming white solid was filtered off and washed with cold MeOH. An *E*-/*Z*- mixture of compound **1** was isolated as a white powder (3.65 g, 7.45 mmol, 60%). R_f = 0.88 (DCM); ^{1}H NMR (400 MHz, DCM-d_2) δ 7.30–7.21 (m, 4H), 7.17–7.10 (m, 6H), 7.04–6.99 (m, 4H), 6.93–6.87 (m, 4H); ^{13}C NMR (101 MHz, DCM-d_2) δ 143.57, 143.44, 143.12, 143.00, 140.97, 133.44, 131.69, 131.58, 131.39, 128.53, 128.35, 127.47, 127.35, 121.20, 121.06; HRMS-NSI (*m/z*): $[M–e]^+$ calcd for $C_{26}H_{18}Br_2$, 487.9770; found, 487.9762.

(*E*)-4,4'-((1,2-diphenylethene-1,2-diyl)bis(4,1-phenylene))bis(but-3-yn-1-ol) (2) and (*Z*)-4,4'-((1,2-diphenylethene-1,2-diyl)bis(4,1-phenylene))bis(but-3-yn-1-ol) (3)

The *E*-/*Z*- mixture of starting material **1** (1.084 g, 2.21 mmol), $Pd(PhCN)_2Cl_2$ (54 mg, 6 mol%), and CuI (30 mg, 6 mol%) were dissolved in toluene (22.5 mL) and DIPA (5.6 mL). A 1 M solution of $P(^tBu)_3$ in toluene (0.27 mL, 12 mol%) was added carefully, followed by 3-butyn-1-ol (0.25 mL, 3.3 mmol). The reaction mixture was heated to 50 °C and stirred at this temperature for 5 h. 3-Butyn-1-ol (0.17 mL, 2.3 mmol) was added and the reaction mixture was stirred at 50 °C for further 18 h. TLC (DCM/MeOH 99:1) showed disappearance of starting material **1**, the appearance of mono-reacted byproduct and the desired products **2** and **3**. The dark brown reaction mixture was cooled to rt., before it was diluted with toluene (10 mL) and filtered through *celite*. The grey filter cake was washed with toluene (20 mL), followed by DCM (50 mL). The filtrate was further diluted with DCM (100 mL). The organic layer was washed once with aq. 10% citric acid (150 mL), once with aq. sat. $NaHCO_3$ (200 mL), once with brine (200 mL), dried over $MgSO_4$, filtered, and concentrated *in vacuo*. The residue was purified by flash column chromatography on silica gel (DCM/toluene/^{i}PrOH 95.5:4:0.5 → 70:20:10) to yield a preliminary separation of product **2** and **3**, respectively. Crude product **2** (600 mg) was repurified by flash column chromatography on silica gel (DCM/MeOH 99.9:0.1 → 98:2). Product **2** was afforded as a yellowish foam (424 mg, 0.90 mmol, 41%). R_f = 0.24 (DCM/MeOH 99:1); ^{1}H NMR (400 MHz, CD_3CN, 333 K) δ 7.18–7.11 (m, 10H), 7.08–7.03 (m, 4H), 7.01–6.95 (m, 4H), 3.66 (q, J = 6.4 Hz, 4H), 2.74 (t, J = 6.0 Hz, 2H), 2.56 (t, J = 6.5 Hz, 4H); ^{13}C NMR (101 MHz, CD_3CN, 333K) δ 144.50, 144.41, 142.41, 132.20, 132.16, 131.98, 129.10, 128.02, 123.24, 89.43, 82.32, 61.76, 24.59; HRMS-NSI (*m/z*): $[M–e]^+$ calcd for $C_{34}H_{28}O_2$, 468.2084; found, 468.2083. Crude product **3** (310 mg) was repurified by flash column chromatography on silica gel (DCM/MeOH 99.5:0.5 → 97:3). Product **3** was isolated as a yellowish foam (281 mg, 0.60 mmol, 27%). R_f = 0.10 (DCM/MeOH 99:1); ^{1}H NMR (400 MHz, CD_3CN, 333 K) δ 7.18–7.11 (m, 10H), 7.08–7.03 (m, 4H), 7.00–6.96 (m, 4H), 3.67 (q, J = 6.4 Hz, 4H), 2.76 (t, J = 6.0 Hz, 2H), 2.57 (t, J = 6.5 Hz, 4H); ^{13}C NMR (101 MHz, CD_3CN, 333 K) δ 144.47, 144.40, 142.40, 132.21, 132.13, 132.06, 129.01, 127.94, 123.32, 89.49, 82.34, 61.76, 24.61; HRMS-ESI (*m/z*): $[M–e]^+$ calcd for $C_{34}H_{28}O_2$, 468.2084; found, 468.2082.

(*E*)-4-(4-(2-(4-(4-(bis(4-methoxyphenyl)(phenyl)methoxy)but-1-yn-1-yl)phenyl)-1,2-diphenyl vinyl)phenyl)but-3-yn-1-ol (4)

Starting material **2** (798 mg, 1.70 mmol) was dissolved in THF (20 mL) and Et_3N (5 mL). DMT-Cl (289 mg, 0.85 mmol) was added to the clear, yellow solution at rt. After 20 min, DMT-Cl (288 mg, 0.85 mmol) was added. The reaction mixture was stirred at rt. for further 2 h 40 min, before it was diluted with EtOAc (150 mL). The organic layer was washed three times with aq. 10% citric acid (3x150 mL), twice with aq. sat. $NaHCO_3$ (2x150 mL), once with brine (150 mL), dried over $MgSO_4$, filtered, and concentrated *in vacuo*. The residue (1.35 g) was purified by flash column chromatography on silica gel (hexane/EtOAc 7:3 + 1% Et_3N → 4:6 + 1% Et_3N). Product **4** was isolated as a yellow foam (490 mg, 0.64 mmol, 38%). R_f = 0.30 (hexane/EtOAc 4:6 + 1% Et_3N); ^{1}H NMR (400 MHz, CD_3CN) δ 7.49–7.45 (m, 2H), 7.36–7.32 (m, 4H), 7.30–7.19 (m, 3H), 7.16–7.11 (m, 10H), 7.04–7.00 (m, 4H), 6.98–6.94 (m, 4H), 6.86–6.82 (m, 4H), 3.75 (s, 6H), 3.63 (q, *J* = 6.3 Hz, 2H), 3.17 (t, *J* = 6.4 Hz, 2H), 2.92 (t, *J* = 5.3 Hz, 1H), 2.60 (t, *J* = 6.4 Hz, 2H), 2.53 (t, *J* = 6.6 Hz, 2H); ^{13}C NMR (101 MHz, CD_3CN) δ 159.66, 146.26, 144.30, 144.08, 142.01, 141.99, 137.19, 132.07, 132.02, 131.96, 131.72, 131.68, 130.93, 128.99, 128.87, 128.81, 127.82, 127.80, 122.82, 114.02, 89.58, 62.84, 61.35, 55.90, 24.27, 21.43; HRMS-NSI (*m/z*): $[M–e]^+$ calcd for $C_{55}H_{46}O_4$, 770.3391; found, 770.3401.

(*Z*)-4-(4-(2-(4-(4-(bis(4-methoxyphenyl)(phenyl)methoxy)but-1-yn-1-yl)phenyl)-1,2-diphenyl vinyl)phenyl)but-3-yn-1-ol (5)

Starting material **3** (562 mg, 1.20 mmol) was dissolved in THF (14 mL) and Et_3N (3.5 mL). DMT-Cl (204 mg, 0.60 mmol) was added to the clear, yellow solution at rt. After 20 min, DMT-Cl (203 mg, 0.60 mmol) was added. The reaction mixture was stirred at rt. For further 2 h 40 min, before it was diluted with EtOAc (100 mL). The organic layer was washed three times with aq. 10% citric acid (3x100 mL), twice with aq. sat. $NaHCO_3$ (2x100 mL), once with brine (100 mL), dried over $MgSO_4$, filtered, and concentrated *in vacuo*. The residue (980 mg) was purified by flash column chromatography on silica gel (hexane/EtOAc 7:3 + 1% Et_3N → 4:6 + 1% Et_3N). Product **5** was isolated as a yellow foam (420 mg, 0.54 mmol, 45%). R_f = 0.43 (hexane/EtOAc 4:6 + 1% Et_3N); ^{1}H NMR (400 MHz, CD_3CN) δ 7.50–7.46 (m, 2H), 7.36–7.32 (m, 4H), 7.29–7.20 (m, 3H), 7.15–7.10 (m, 10H), 7.05–7.00 (m, 4H), 6.97–6.93 (m, 4H), 6.86–6.82 (m, 4H), 3.75 (s, 6H), 3.63 (t, *J* = 6.6 Hz, 2H), 3.18 (t, *J* = 6.4 Hz, 2H), 2.94 (s, 1H), 2.61 (t, *J* = 6.4 Hz, 2H), 2.53 (t, *J* = 6.6 Hz, 2H); ^{13}C NMR (101 MHz, CD_3CN) δ 159.65, 144.26, 144.17, 144.12, 144.11, 141.99, 141.97, 137.18, 132.09, 132.03, 131.94, 131.80, 131.76, 130.94, 128.99, 128.80, 127.82, 127.74, 122.90, 122.81, 114.03, 89.62, 86.88, 81.97, 81.97, 62.86, 61.36, 55.90, 24.31, 21.45; HRMS-NSI (*m/z*): $[M–e]^+$ calcd for $C_{55}H_{46}O_4$, 770.3391; found, 770.3398.

(*E*)-4-(4-(2-(4-(4-(bis(4-methoxyphenyl)(phenyl)methoxy)but-1-yn-1-yl)phenyl)-1,2-diphenyl vinyl)phenyl)but-3-yn-1-yl (2-cyanoethyl) diisopropylphosphoramidite (6)

Starting material **4** (460 mg, 0.60 mmol) was dissolved in DCM (6 mL) and Hünig's base (0.3 mL). CEP-Cl (143 mg, 0.60 mmol) was added dropwise to the clear, yellow solution at rt. The reaction mixture was stirred at rt. for 2 h. The yellowish reaction mixture was concentrated *in vacuo*. The crude product (760 mg) was purified by a short flash column chromatography on silica gel (hexane/EtOAc 7:3 + 1% Et_3N). Product **6** was isolated as a yellowish foam (509 mg, 0.52 mmol, 87%). R_f = 0.55 (hexane/EtOAc 6:4 + 1% Et_3N); ^{1}H NMR (400 MHz, DMSO-d_6) δ 7.45–7.41 (m, 2H), 7.30–7.11 (m, 17H), 6.99–6.84 (m, 12H), 3.80–3.65 (m, 10H), 3.62–3.52 (m, 2H), 3.10 (t, *J* = 6.4 Hz, 2H), 2.75 (td, *J* = 6.4, 1.4 Hz, 2H), 2.66 (q, *J* = 6.2 Hz, 4H), 1.12 (dd, *J* = 6.5, 5.7 Hz, 12H); ^{13}C NMR (101 MHz, DMSO-d_6) δ 158.05, 144.83, 142.73, 142.70, 142.52, 142.50, 140.45, 140.44, 135.63, 130.83, 130.76, 130.66, 130.62, 129.59, 127.96, 127.79, 127.61, 126.84, 126.82, 126.64, 121.14, 121.11, 118.90, 113.15, 88.73, 88.17, 85.44, 81.18, 81.13, 61.59, 61.47, 61.29, 58.34, 58.16, 54.99, 42.58, 42.45, 24.36, 24.35, 24.29, 24.28, 21.77, 21.70, 20.18, 19.81, 19.74; ^{31}P NMR (162 MHz, DMSO-d_6) δ 147.13; HRMS-NSI (*m/z*): $[M+H]^+$ calcd for $C_{64}H_{64}O_5N_2P$, 971.4558; found, 971.4565.

(*Z*)-4-(4-(2-(4-(4-(bis(4-methoxyphenyl)(phenyl)methoxy)but-1-yn-1-yl)phenyl)-1,2-diphenyl vinyl)phenyl)but-3-yn-1-yl (2-cyanoethyl) diisopropylphosphoramidite (7)

Starting material **5** (376 mg, 0.49 mmol) was dissolved in DCM (4.9 mL) and Hünig's base (0.25 mL). CEP-Cl (120 mg, 0.51 mmol) was added dropwise to the clear, yellow solution at rt. The reaction mixture was stirred at rt. for 2 h. The yellowish reaction mixture was concentrated *in vacuo*. The crude product (612 mg) was purified by a short flash column chromatography on silica gel (hexane/EtOAc 7:3 + 1% Et_3N). Product **7** was isolated as a yellowish foam (417 mg, 0.43 mmol, 88%). R_f = 0.57 (hexane/EtOAc 6:4 + 1% Et_3N); ^{1}H NMR (400 MHz, DMSO-d_6) δ 7.45–7.41 (m, 2H), 7.30–7.10 (m, 17H), 6.98–6.85 (m, 12H), 3.80–3.66 (m, 10H), 3.60–3.51 (m, 2H), 3.11 (t, *J* = 6.5 Hz, 2H), 2.74 (td, *J* = 6.2, 1.4 Hz, 2H), 2.67 (q, *J* = 6.3 Hz, 4H), 1.11 (dd, *J* = 6.7, 5.9 Hz, 12H); ^{13}C NMR (101 MHz, DMSO-d_6) δ 158.06, 144.84, 142.72, 142.66, 142.56, 140.46, 140.44, 135.64, 130.86, 130.80, 130.76, 130.60, 129.60, 127.87, 127.79, 127.62, 126.77, 126.66, 121.26, 121.20, 118.90, 113.16, 88.69, 88.23, 85.46, 81.21, 81.14, 61.60, 61.53, 61.35, 58.32, 58.14, 54.99, 42.59, 42.47, 24.34, 24.33, 24.27, 24.26, 21.79, 21.72, 20.22, 19.81, 19.75; ^{31}P NMR (162 MHz, DMSO-d_6) δ 147.17; HRMS-NSI (*m/z*): $[M+H]^+$ calcd for $C_{64}H_{64}O_5N_2P$, 971.4558; found, 971.4564.

E-TPE-modified solid-support (9)

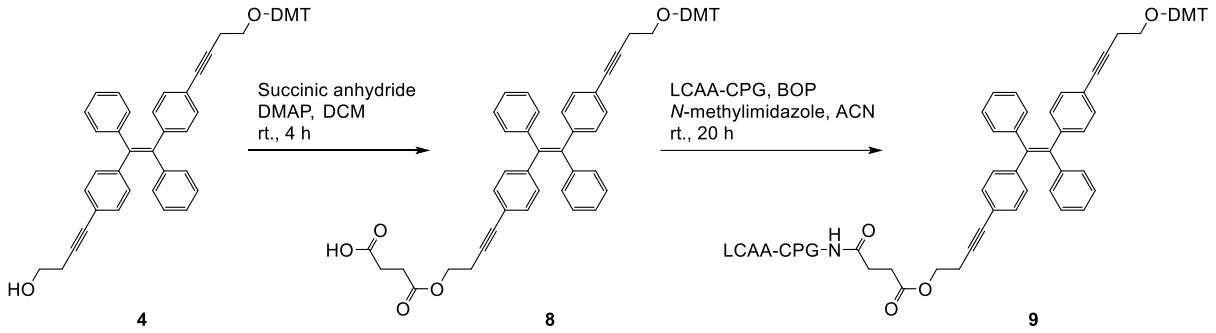

Scheme 2. Synthetic approach for *E*-TPE-modified solid-support **9**.

The synthesis of *E*-TPE-modified solid-support **9** (Scheme 2) was adapted from published procedures.[27] Compound **4** (31.2 mg, 0.04 mmol) was dissolved in DCM (0.2 mL). Succinic anhydride (4.1 mg, 0.04 mmol), followed by DMAP (7.9 mg, 0.06 mmol) were added and the reaction mixture was stirred at rt. for 4 h. The reaction mixture was diluted with DCM (3 mL) and the organic layer was washed once with aq. 10% citric acid (5 mL), once with brine (5 mL), dried over $MgSO_4$, filtered, and concentrated *in vacuo* to yield compound **8**. Compound **8** was dissolved in acetonitrile (3 mL) and 2.8 mL of this solution (about 37 μmol of compound **8**) was added to LCAA-CPG (301.3 mg, 500 Å, amine loading: 82 μmol/g). BOP (33.8 mg, 0.08 mmol) and *N*-methylimidazole (12 μL, 0.15 mmol) were added. The suspension was shaken at rt. for 20 h. The solid-support **9** was filtered off and washed with acetonitrile and DCM. A solution of pyridine and acetic anhydride (3:1, 3.6 mL) was added to the solid-support **9**. DMAP (32.3 mg, 0.26 mmol) was added and the suspension was shaken at rt. for 2 h. The solid-support **9** was filtered off and washed with DCM. The loading was determined according to the Beer-Lambert law: solid-support **9** (2.5 mg) was added to 3% trichloroacetic acid in DCM (10 mL). After a 1:1 dilution, the absorbance was measured at 498 nm. For the calculation of the loading, a molar absorptivity of the DMT cation of ε: 70'000 L/mol·cm was used. The loading of solid-support **9** was calculated to be 70 μmol/g.

Z-TPE-modified solid-support (11)

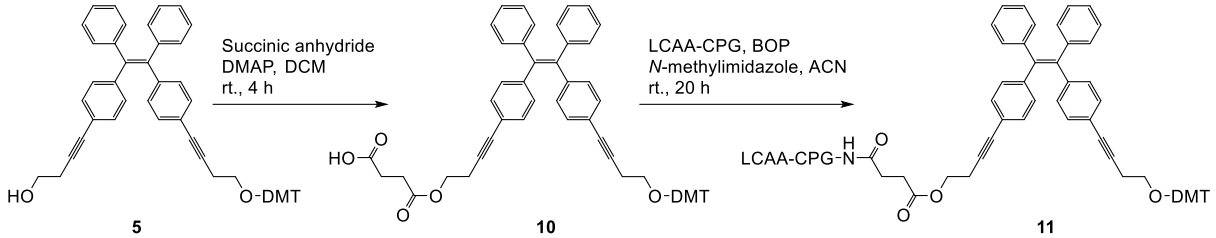

Scheme 3. Synthetic approach for *Z*-TPE-modified solid-support **11**.

The synthesis of *Z*-TPE-modified solid-support **11** (Scheme 3) was adapted from published procedures.[27] Compound **5** (30.9 mg, 0.04 mmol) was dissolved in DCM (0.2 mL). Succinic anhydride (4.2 mg, 0.04 mmol), followed by DMAP (8.0 mg, 0.07 mmol) were added and the reaction mixture was stirred at rt. for 4 h. The reaction mixture was diluted with DCM (3 mL) and the organic layer was washed once with aq. 10% citric acid (5 mL), once with brine (5 mL), dried over $MgSO_4$, filtered, and concentrated *in vacuo* to yield compound **10**. Compound **10** was dissolved in acetonitrile (3 mL) and 2.8 mL of this solution (about 37 μmol of compound **10**) was added to LCAA-CPG (301.0 mg, 500 Å, amine loading: 82 μmol/g). BOP (33.6 mg, 0.08 mmol) and *N*-methylimidazole (12 μL, 0.15 mmol) were added. The suspension was shaken at rt. for 20 h. The solid-support **11** was filtered off and washed with acetonitrile and DCM. A solution of pyridine and acetic anhydride (3:1, 3.6 mL) was added to the solid-support **11**. DMAP (32.1 mg, 0.26 mmol) was added and the suspension was shaken at rt. for 2 h. The solid-support **11** was filtered off and washed with DCM. The loading was determined according to the Beer-Lambert law: solid-support **11** (2.4 mg) was added to 3% trichloroacetic acid in DCM (10 mL). After a 1:1 dilution, the absorbance was measured at 498 nm. For the calculation of the loading, a molar absorptivity of the DMT cation of ε: 70'000 L/mol·cm was used. The loading of solid-support **11** was calculated to be 76 μmol/g.

3.3.2 NMR Spectra

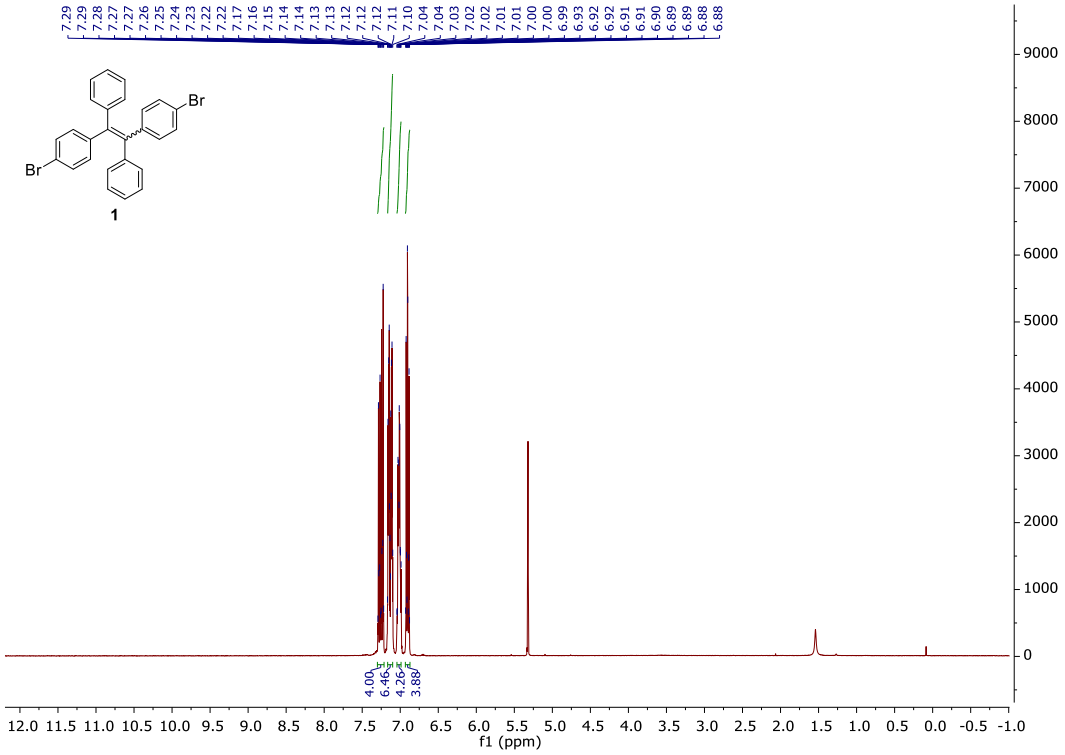

Figure 39. ^{1}H NMR of compound **1** in DCM-d_2.

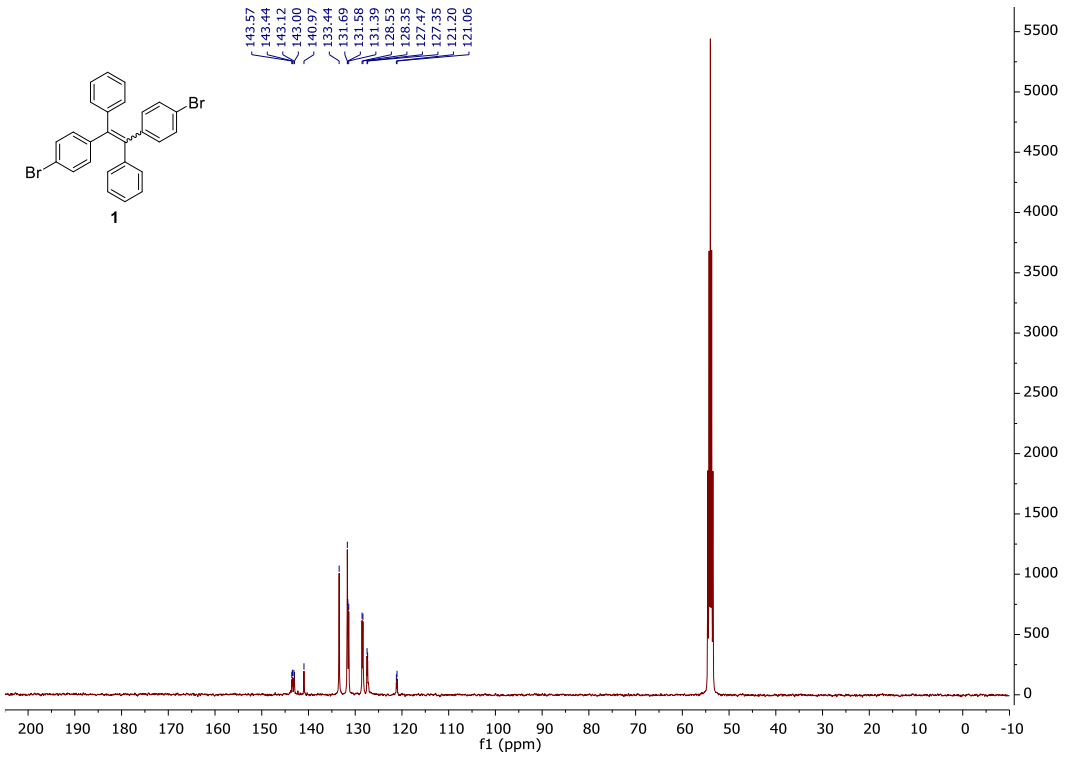

Figure 40. ^{13}C NMR of compound **1** in DCM-d_2.

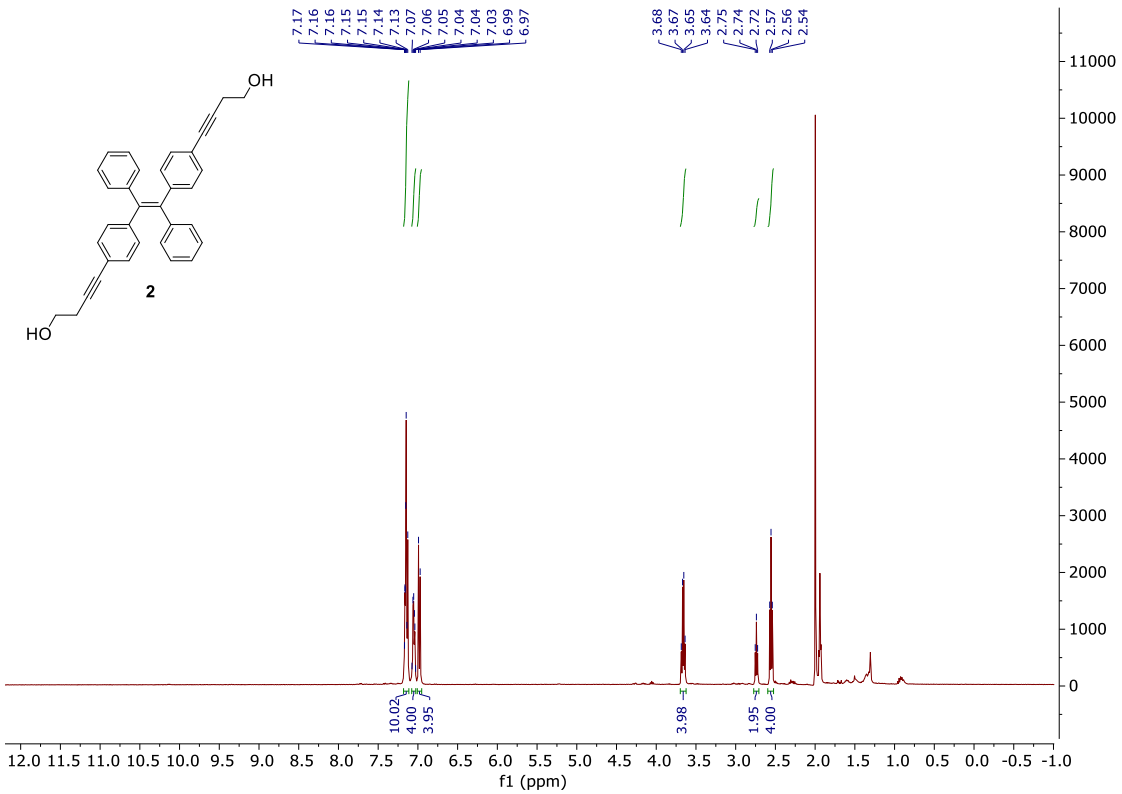

Figure 41. ^{1}H NMR of compound **2** in CD_3CN at 333 K.

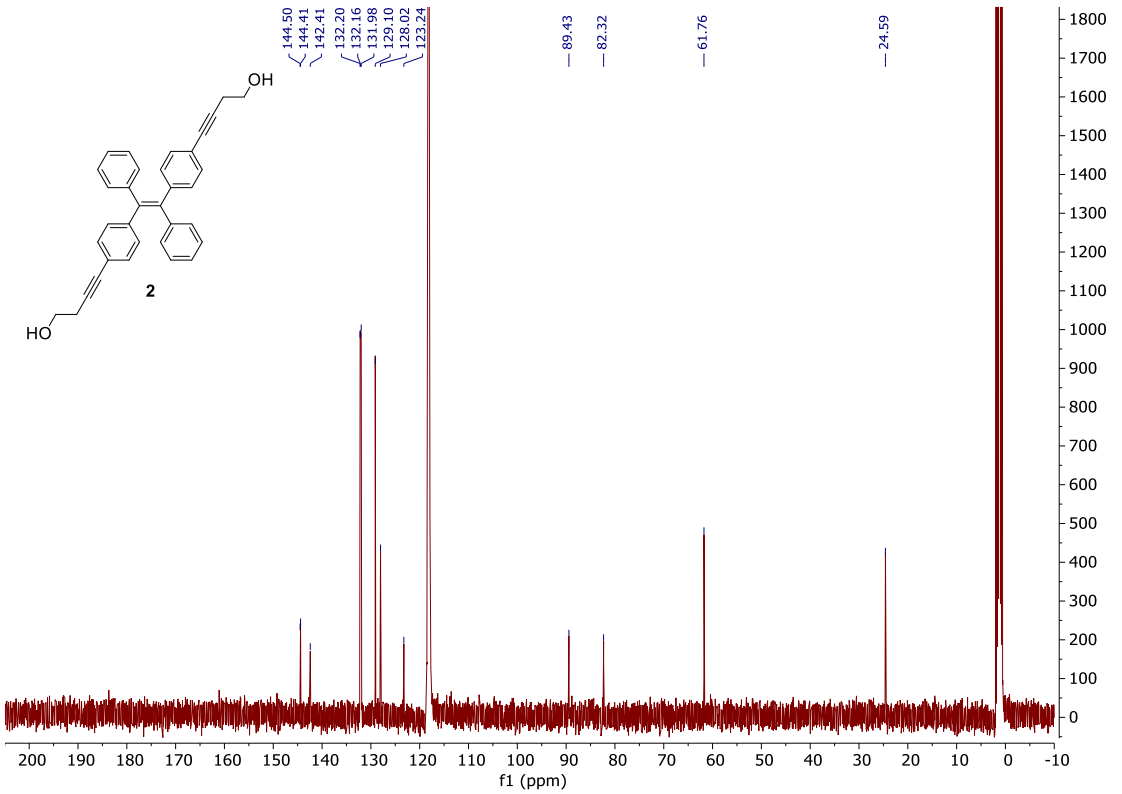

Figure 42. ^{13}C NMR of compound **2** in CD_3CN at 333 K.

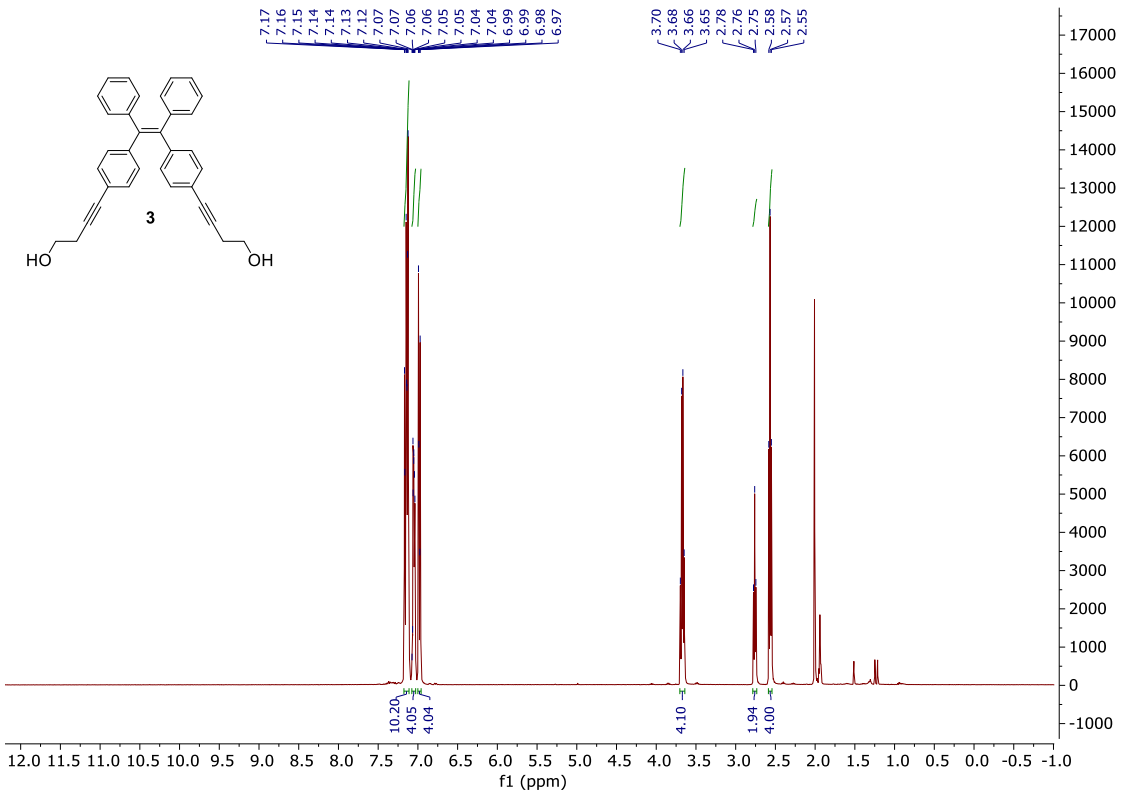

Figure 43. ^{1}H NMR of compound **3** in CD_3CN at 333 K.

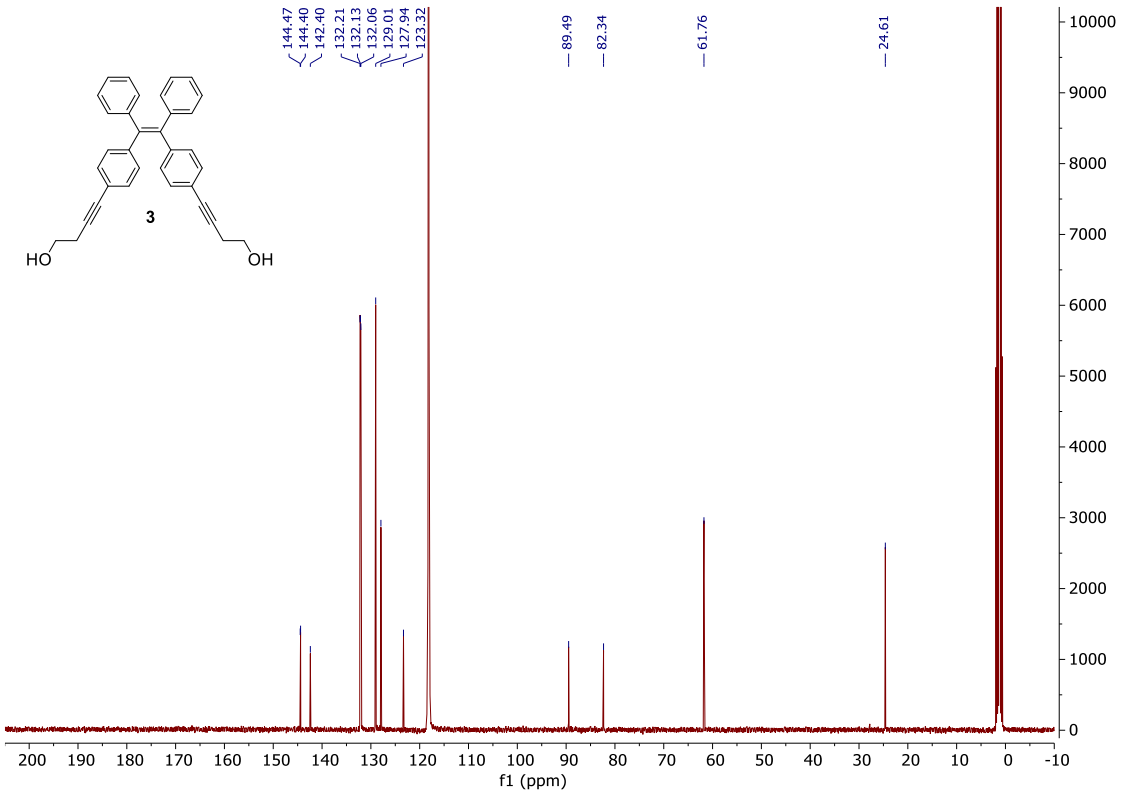

Figure 44. ^{13}C NMR of compound **3** in CD_3CN at 333 K.

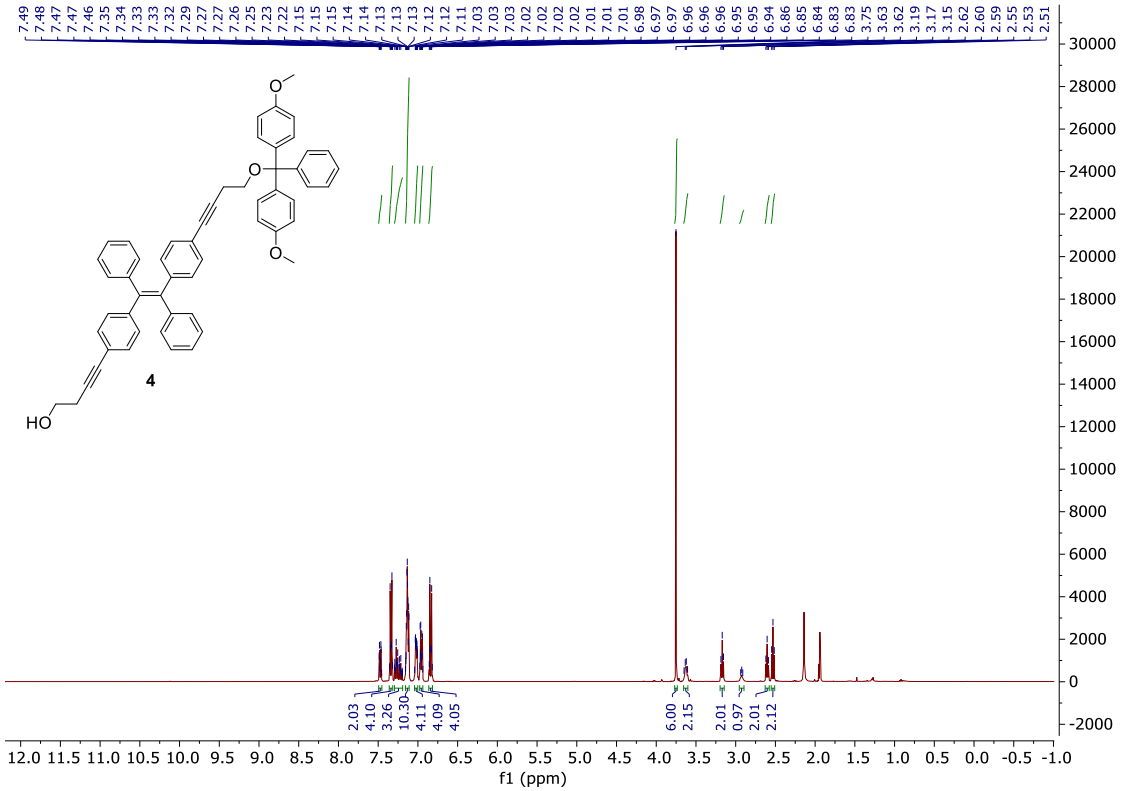

Figure 45. ^{1}H NMR of compound **4** in CD_3CN.

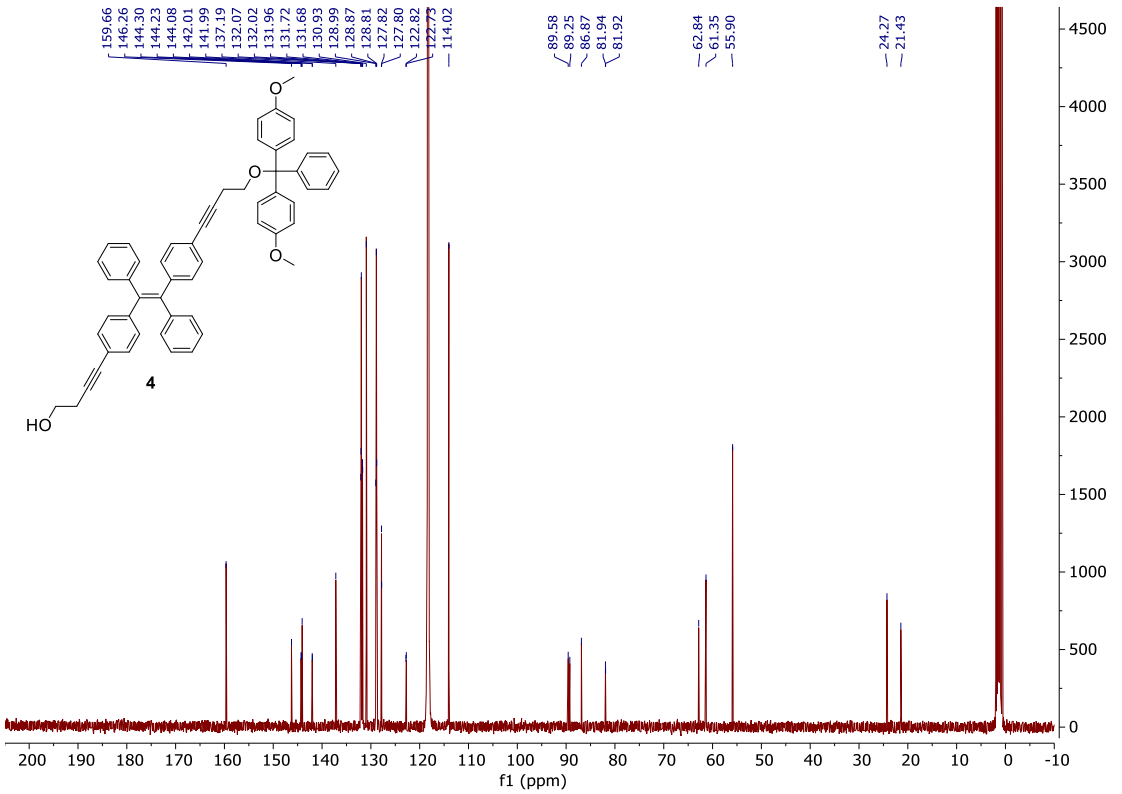

Figure 46. ^{13}C NMR of compound **4** in CD_3CN.

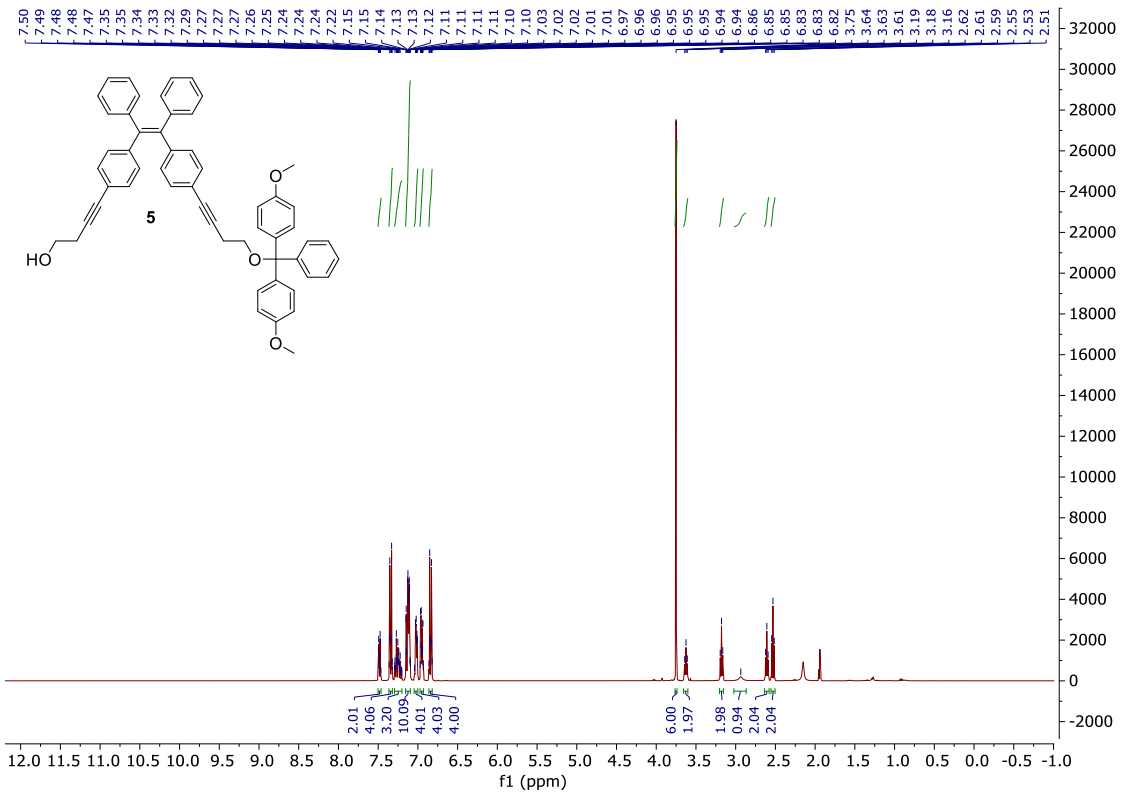

Figure 47. ^{1}H NMR of compound **5** in CD_3CN.

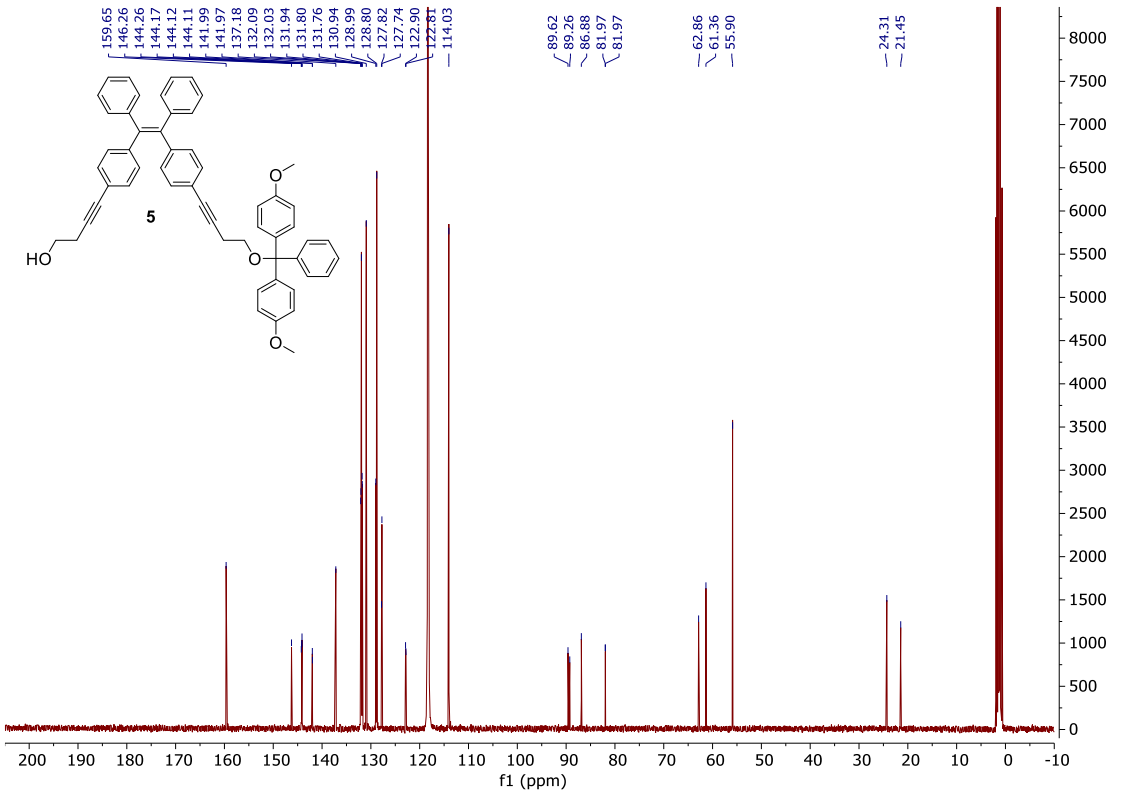

Figure 48. ^{13}C NMR of compound **5** in CD_3CN.

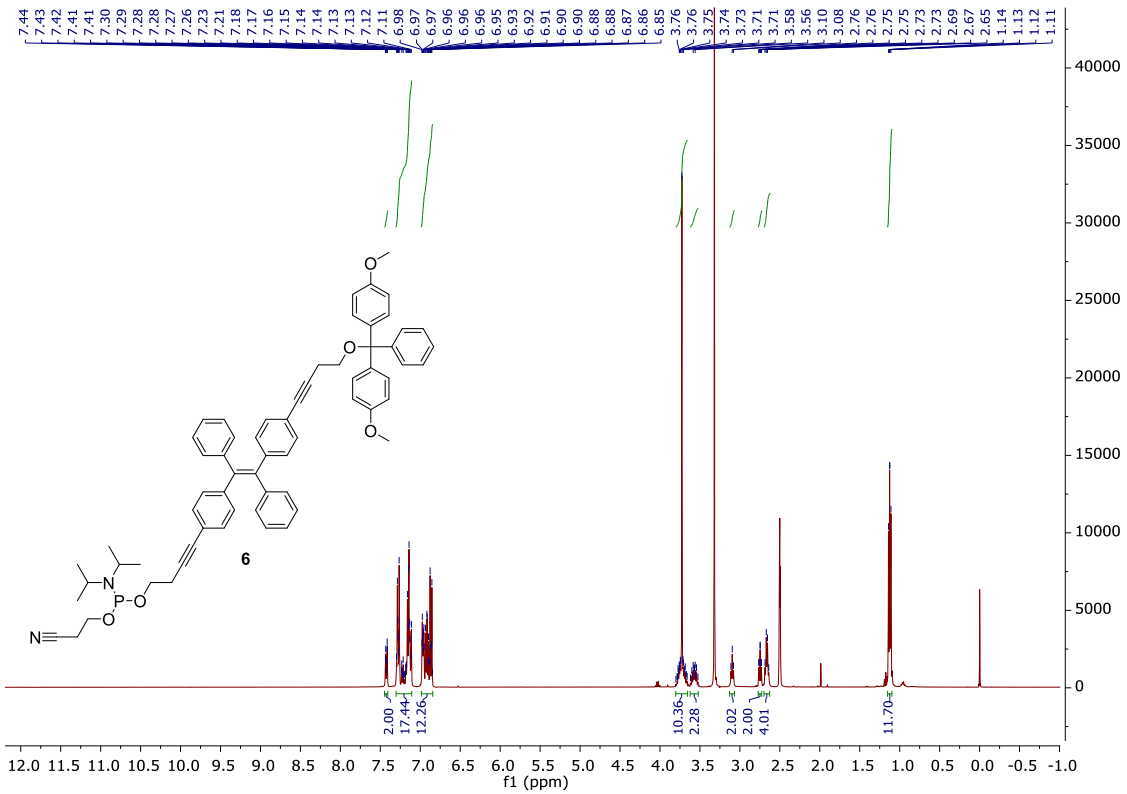

Figure 49. ^{1}H NMR of compound **6** in DMSO-d_6.

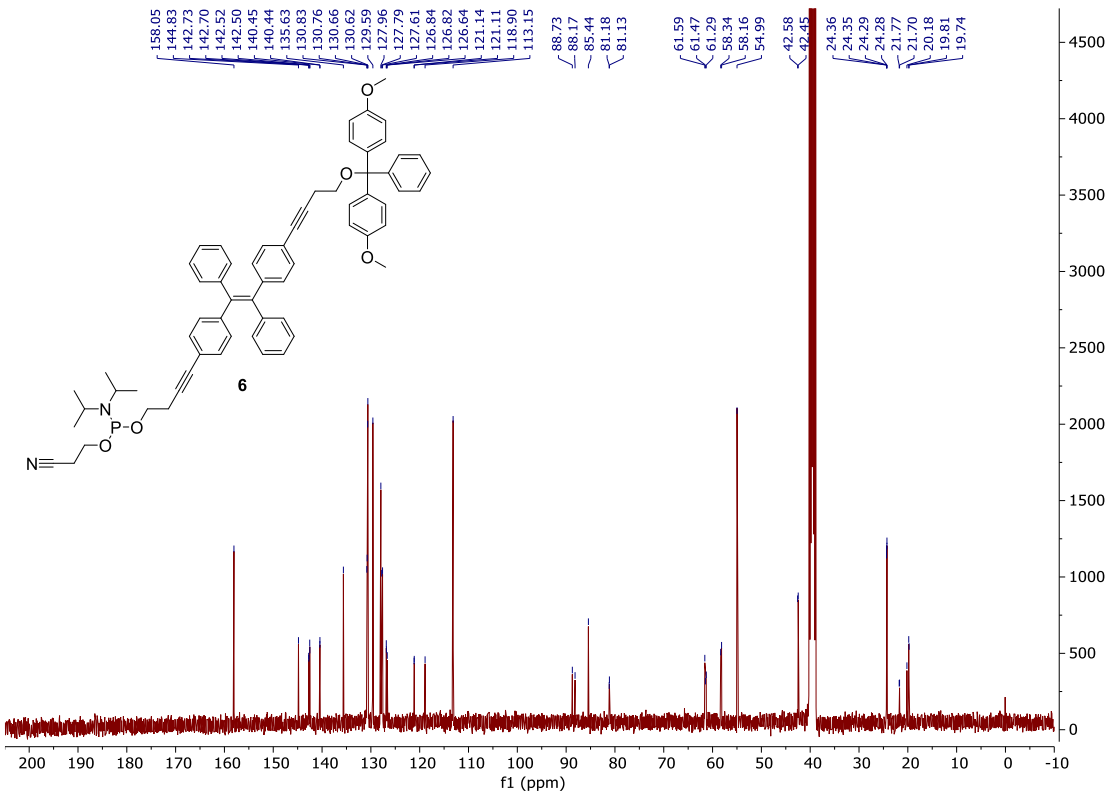

Figure 50. ^{13}C NMR of compound **6** in DMSO-d_6.

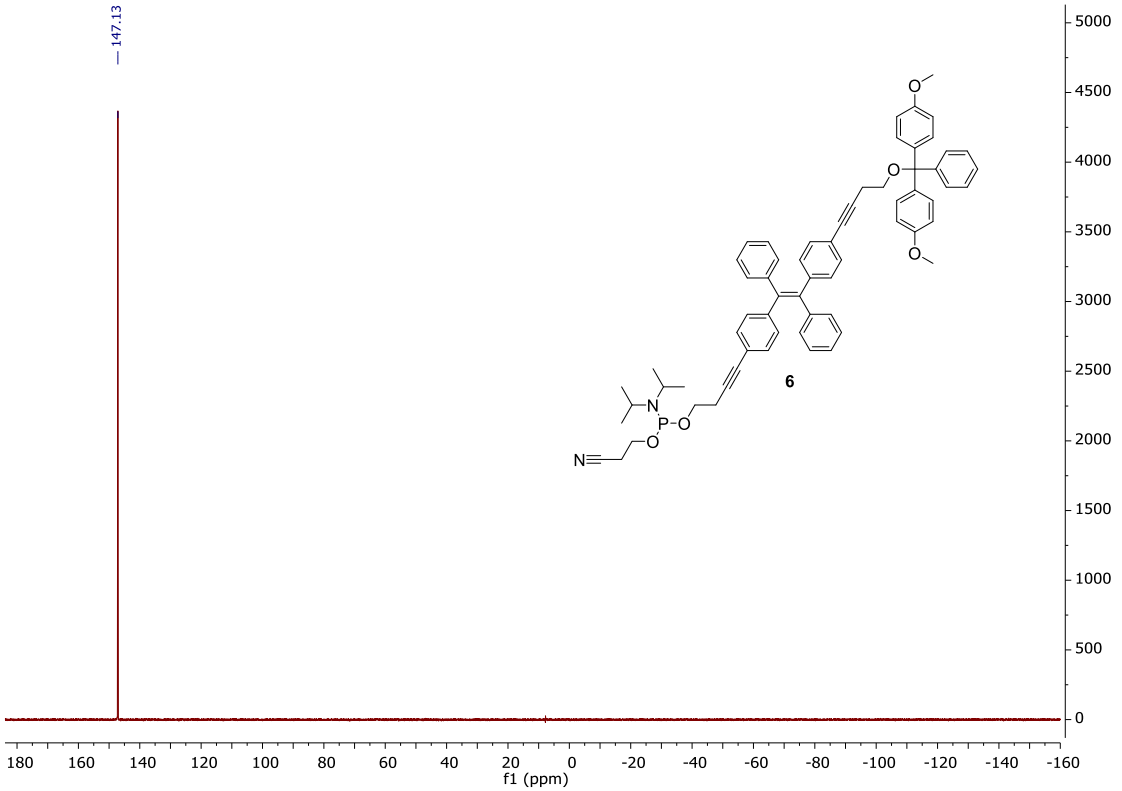

Figure 51. ^{31}P NMR of compound **6** in DMSO-d_6.

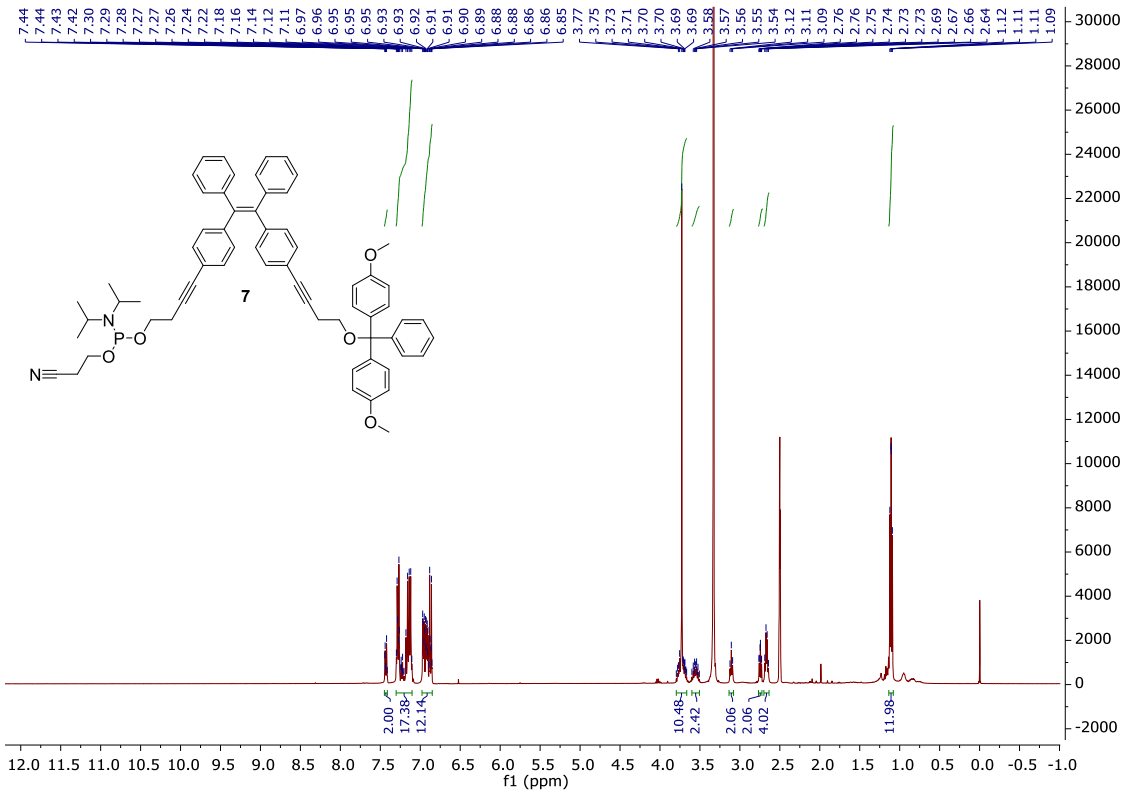

Figure 52. ^{1}H NMR of compound **7** in DMSO-d_6.

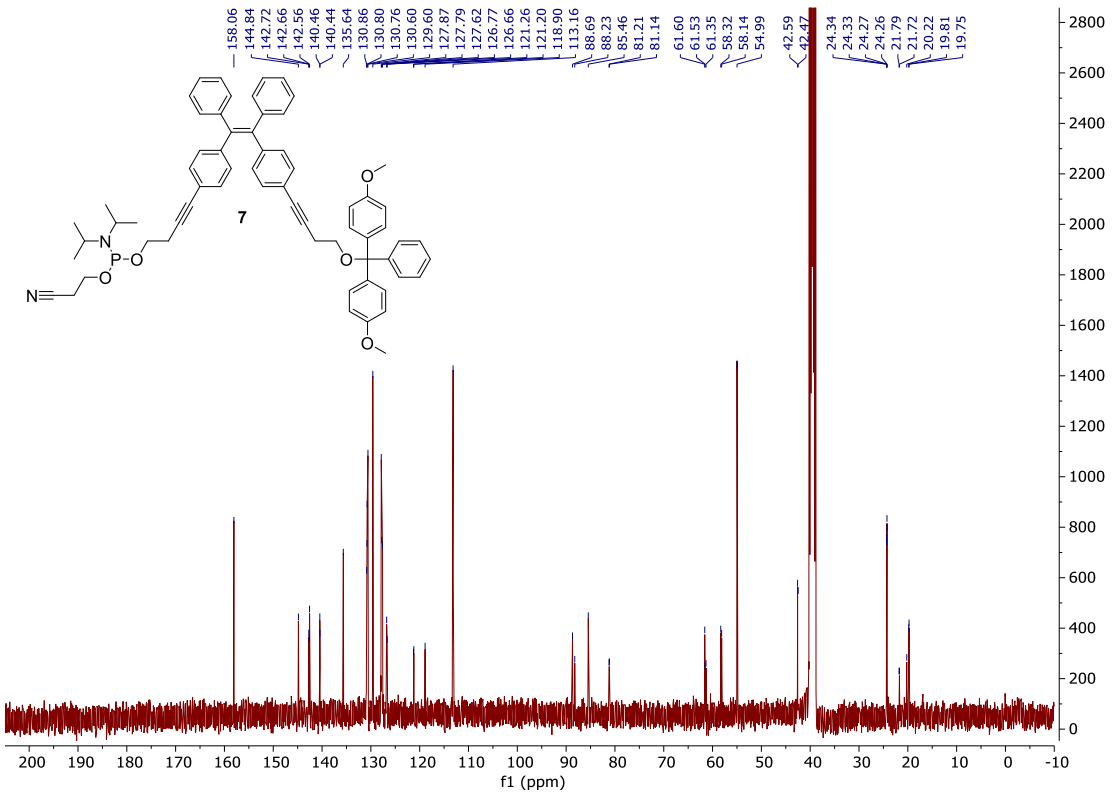

Figure 53. ^{13}C NMR of compound **7** in DMSO-d_6.

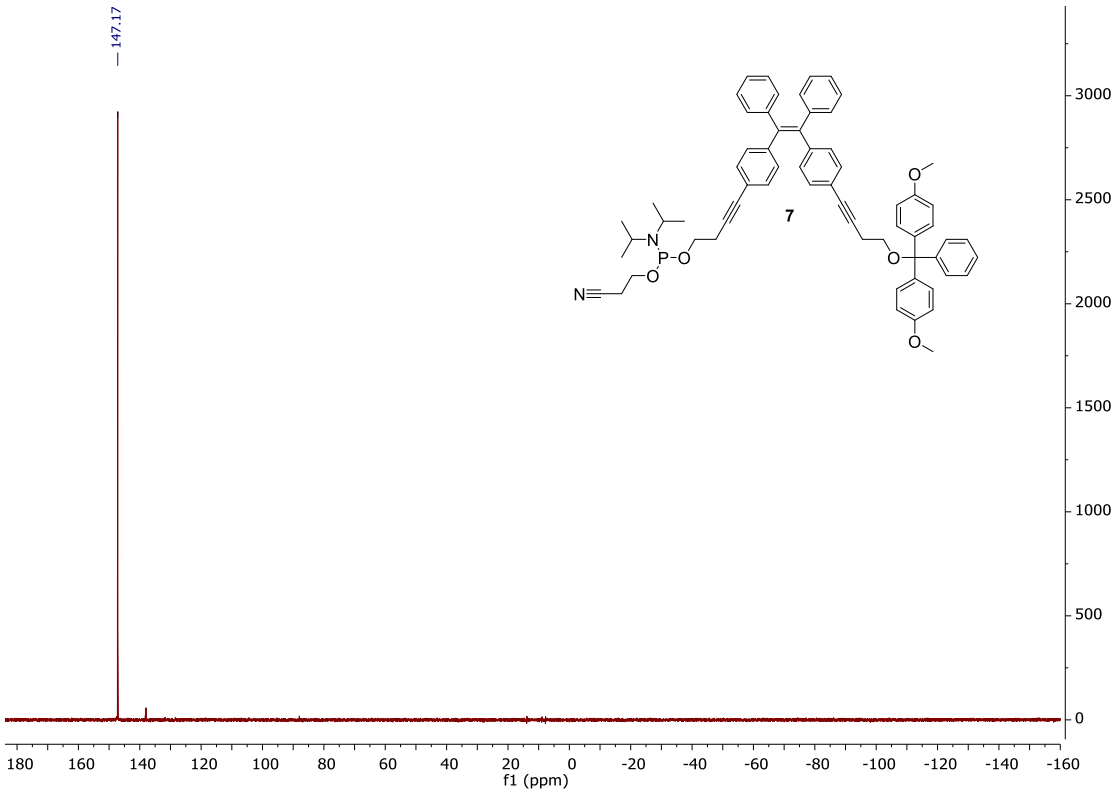

Figure 54. ^{31}P NMR of compound **7** in DMSO-d_6.

3.3.3 Synthesis of Oligonucleotides

E-TPE-DNA conjugates **ON1** and **ON2**, and *Z*-TPE-DNA conjugates **ON3** and **ON4** were synthesized on an *Applied Biosystems 394 DNA/RNA synthesizer* applying a standard cyanoethyl phosphoramidite coupling protocol on a 1 µmol scale. A coupling time of 30 s was employed for the DNA nucleobases and 2 min for the TPE modifications. *E*- and *Z*-TPE phosphoramidites **6** and **7**, respectively, were dissolved in 1,2-DCE to create 0.1 M solutions. The synthesis was started with *E*- or *Z*-TPE-modified solid-support **9** and **11**, respectively. After the solid-phase synthesis, the TPE-DNA conjugates **ON1**–**ON4** were cleaved and deprotected by treatment with aqueous NH_4OH (28-30%) at 55 °C overnight. The supernatants were collected, and the solid-supports were washed three times with a solution of ethanol and Milli-Q H_2O (1:1, 3x1 mL), before the crude TPE-DNA conjugates were lyophilized.
The crude oligomers were purified by reversed-phase HPLC (Shimadzu LC-20AT, LiChrospher 100 RP-18, 5 µm, 250 x 4 mm) at 40 °C (**ON1** and **ON2**) or 50 °C (**ON3** and **ON4**) with a flow rate of 1 mL/min, λ: 330 nm. Solvent A: 50 mM aqueous NH_4OAc; solvent B: acetonitrile; B [%] (t_R [min]) = 20 (0), 60 (24). The purified TPE-DNA conjugates were dissolved in Milli-Q H_2O (1 mL). The absorbance was measured at 260 nm to determine the concentration of the stock solutions and the yields of the oligomers. The calculation was according to the Beer-Lambert law. The following molar absorptivities (at 260 nm) in [L/mol·cm] were used for the DNA nucleobases: ε_A: 15'300; ε_T: 9'000; ε_G: 11'700; ε_C: 7'400. A molar absorptivity of $\varepsilon_{E\text{-TPE}}$: 35'975 was used for *E*-TPE and $\varepsilon_{Z\text{-TPE}}$: 40'788 was used for *Z*-TPE. The MS results are listed in Table 4, the corresponding HPLC traces of **ON1**–**ON4** are displayed in Figure 55, and the MS spectra are presented in Figure 56–Figure 59.

Table 4. Oligomer sequences of **ON1**–**ON4**, calculated and found masses by NSI-MS, and yields.

Oligomer	Sequence (5'→3')	Calc. mass	Found mass	Yield [%]
ON1	CAA GGT CCG ATG CAA GGA AG-(***E*-TPE**)$_3$	7790.6101	7790.6080	34
ON2	CTT CCT TGC ATC GGA CCT TG-(***E*-TPE**)$_3$	7625.4699	7625.5320	36
ON3	CAA GGT CCG ATG CAA GGA AG-(***Z*-TPE**)$_3$	7790.6101	7790.6059	23
ON4	CTT CCT TGC ATC GGA CCT TG-(***Z*-TPE**)$_3$	7625.4699	7625.5263	27

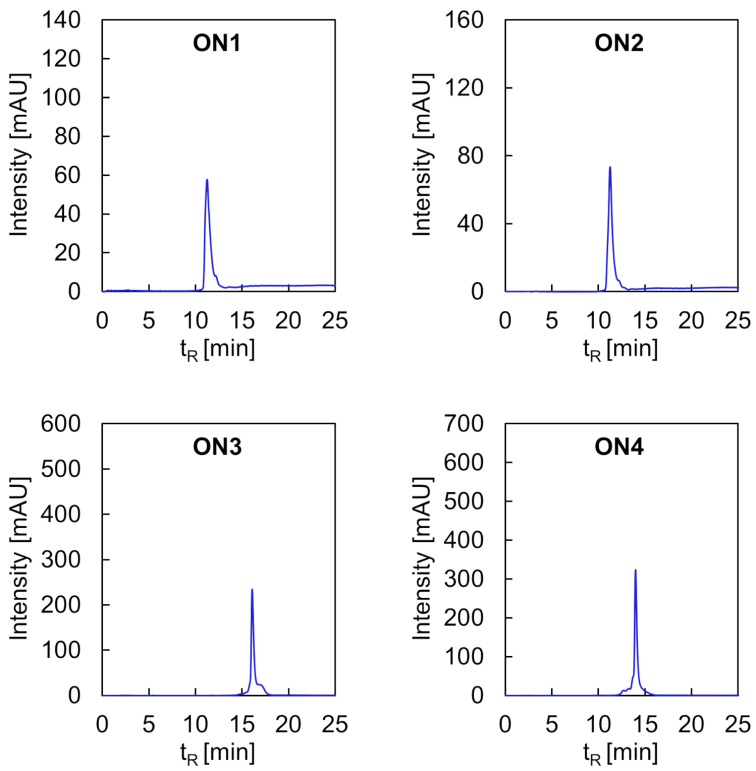

Figure 55. HPLC traces of TPE-DNA conjugates **ON1**–**ON4**.

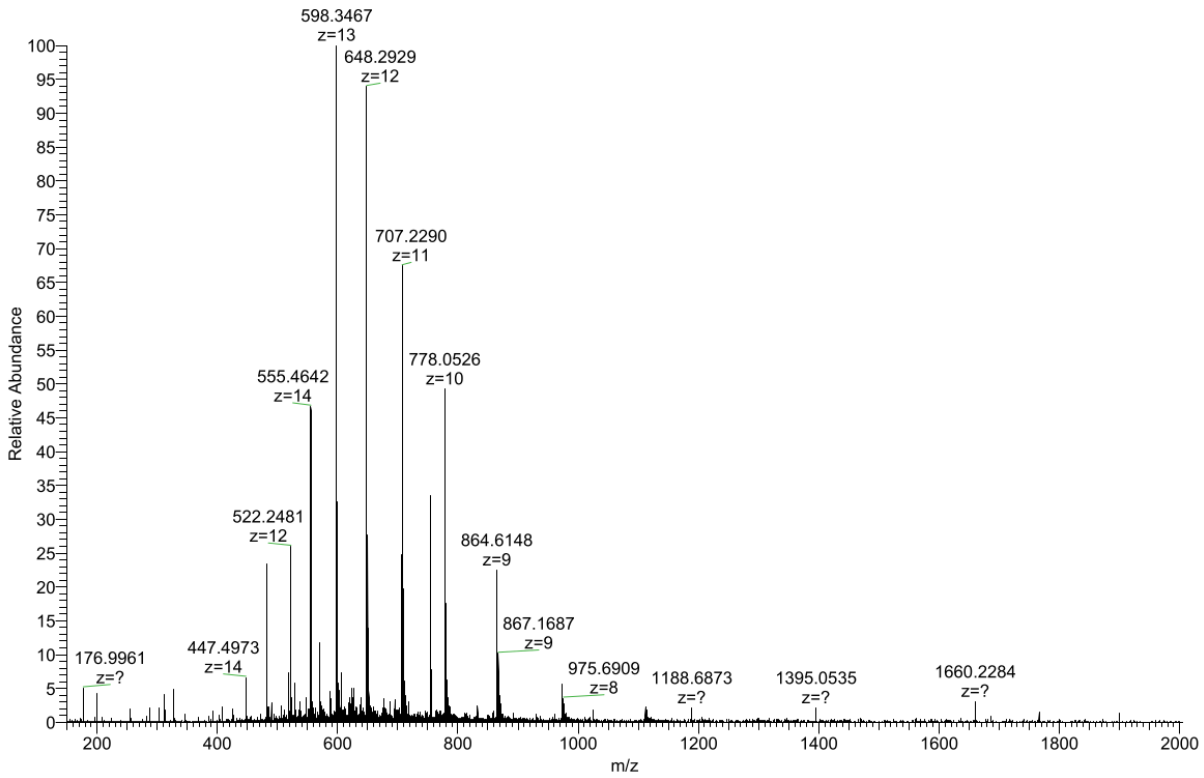

Figure 56. MS spectrum of **ON1**.

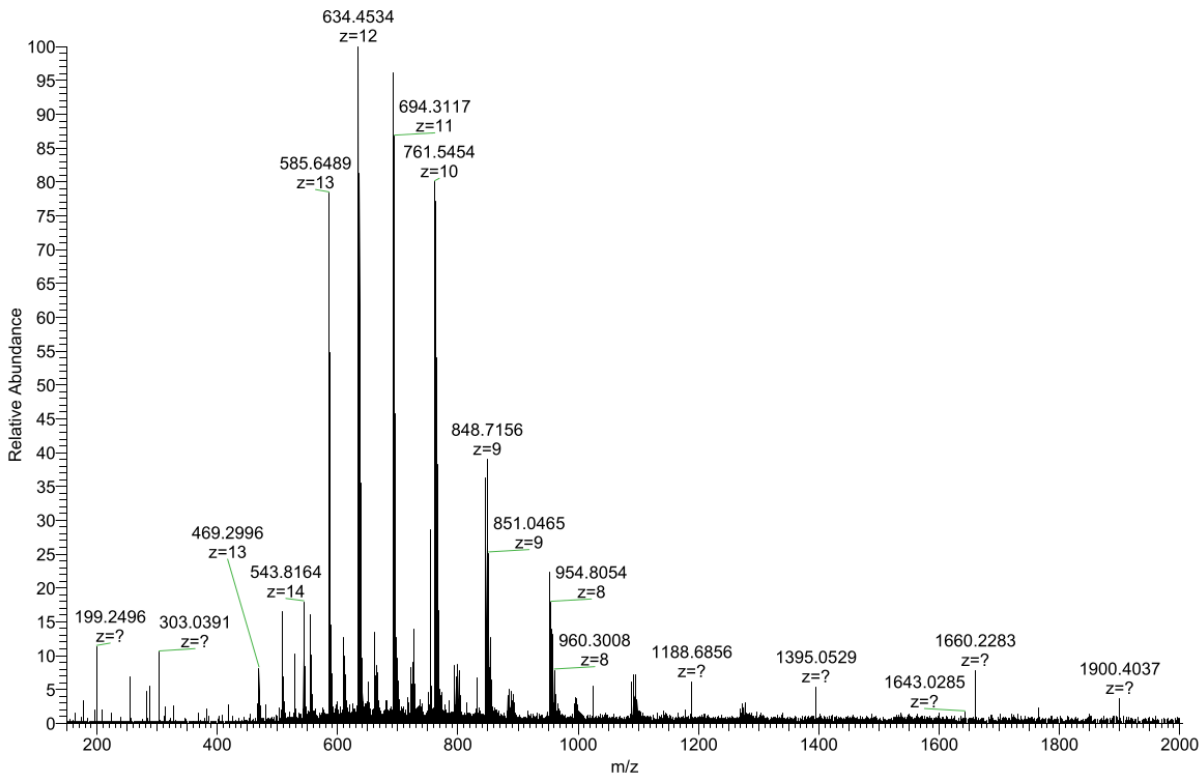

Figure 57. MS spectrum of **ON2**.

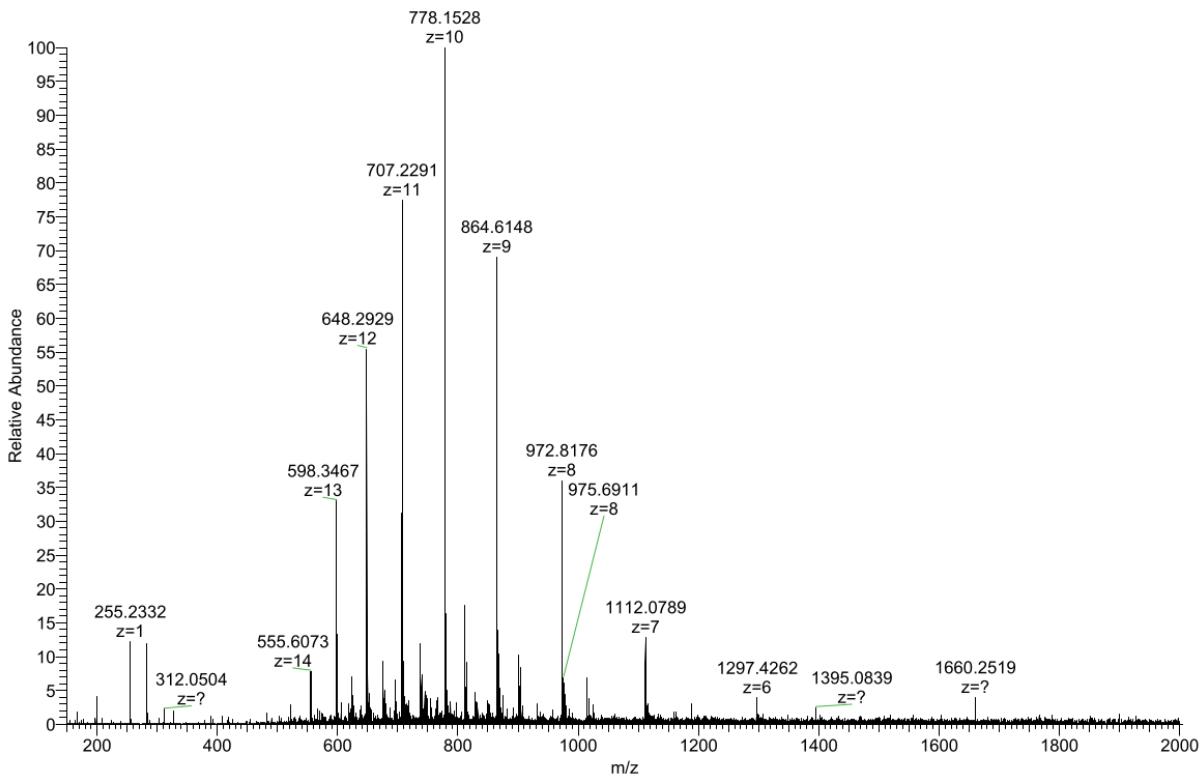

Figure 58. MS spectrum of **ON3**.

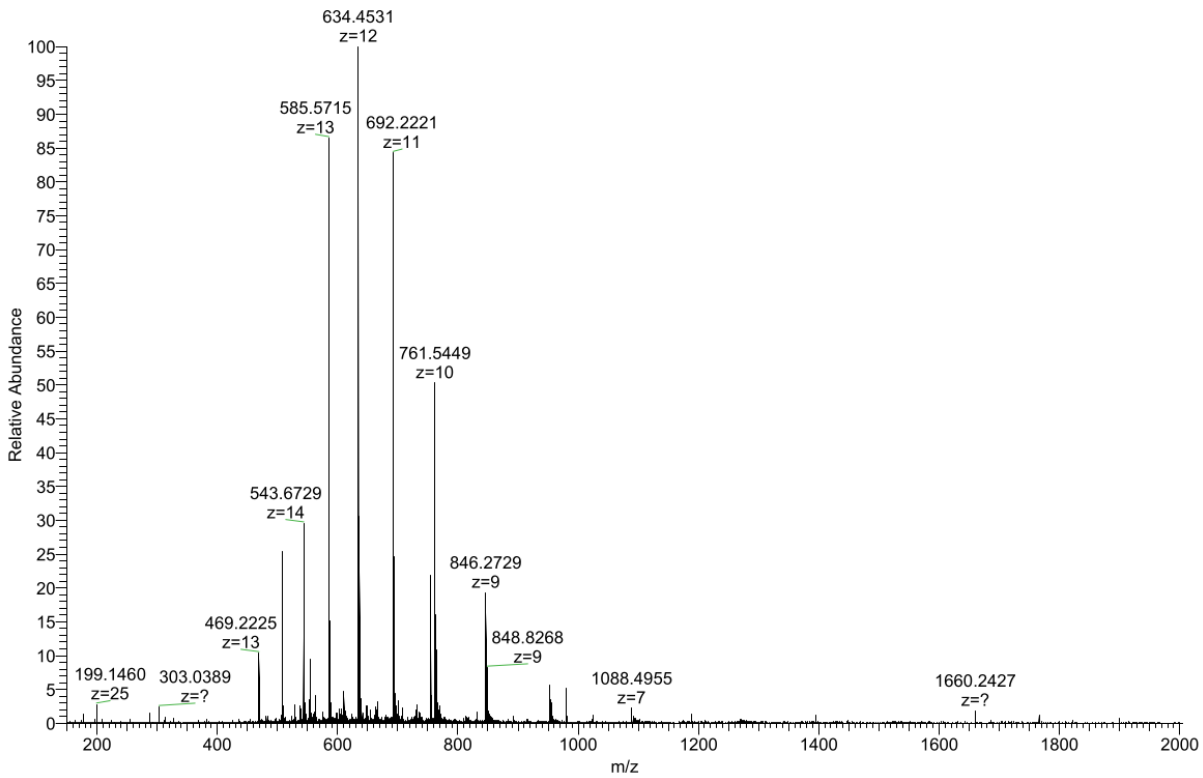

Figure 59. MS spectrum of **ON4**.

3.3.4 Spectroscopic and Microscopic Measurements

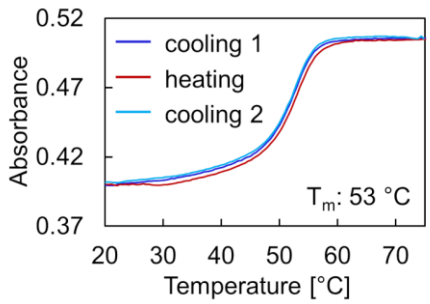

Figure 60. UV-Vis-monitored annealing (blue and light blue) and melting (red) curves of **ON5*ON6**. Conditions: 1 µM **ON5*ON6**, 10 mM sodium phosphate buffer pH 7.2, 0.1 mM spermine · 4 HCl, 20 vol% ethanol, λ: 260 nm, gradient: 0.5 °C/min.

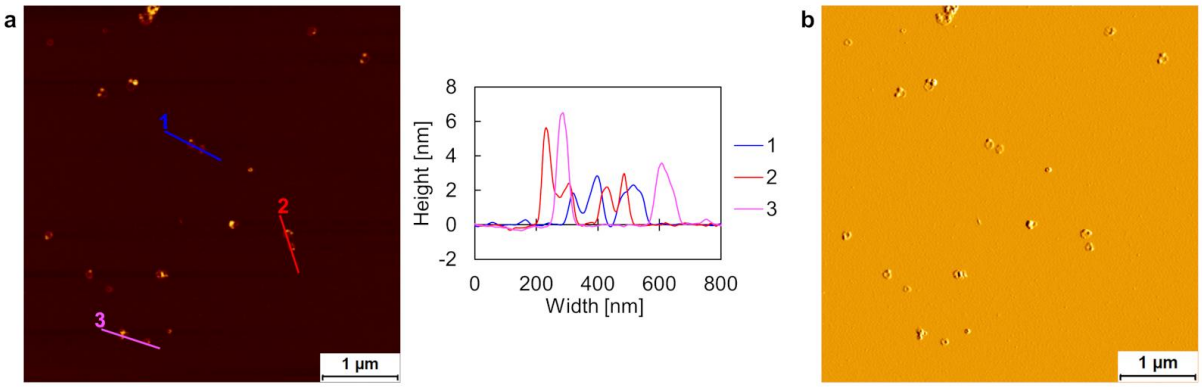

Figure 61. (**a**) AFM scan with corresponding cross sections and (**b**) deflection scan of assembled **ON2*ON5**. Conditions: 1 µM **ON2*ON5**, 10 mM sodium phosphate buffer pH 7.2, 0.1 mM spermine · 4 HCl, 20 vol% ethanol.

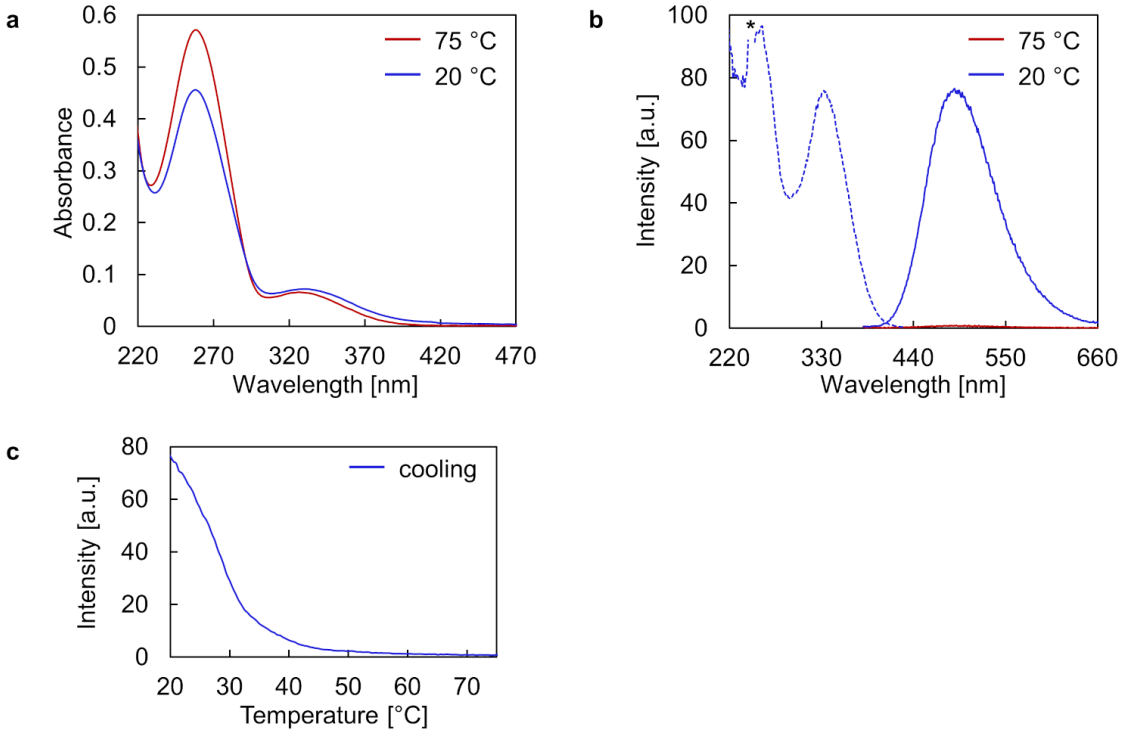

Figure 62. (**a**) UV-Vis absorption spectra, (**b**) fluorescence emission (solid line) and excitation (dotted line) spectra, and (**c**) fluorescence-monitored annealing curve of **ON2*ON5**. Conditions: 1 µM **ON2*ON5**, 10 mM sodium phosphate buffer pH 7.2, 0.1 mM spermine · 4 HCl, 20 vol% ethanol, $\lambda_{ex.}$: 335 nm, $\lambda_{em.}$: 490 nm, gradient: 0.5 °C/min, * denotes second-order diffraction.

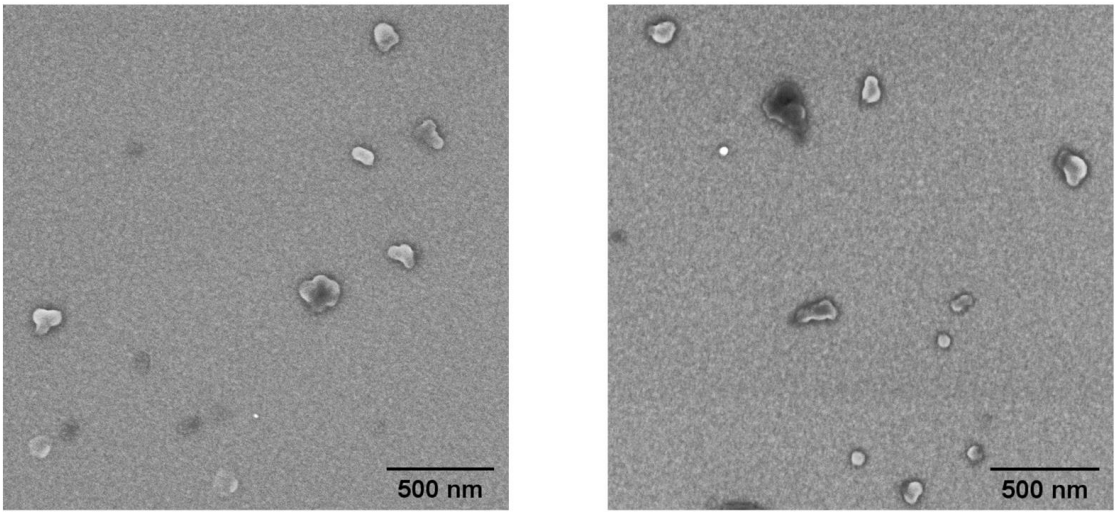

Figure 63. SEM images of self-assembled **ON1*ON2**. Conditions: 1 μM **ON1*ON2**, 10 mM sodium phosphate buffer pH 7.2, 0.1 mM spermine · 4 HCl, 20 vol% ethanol.

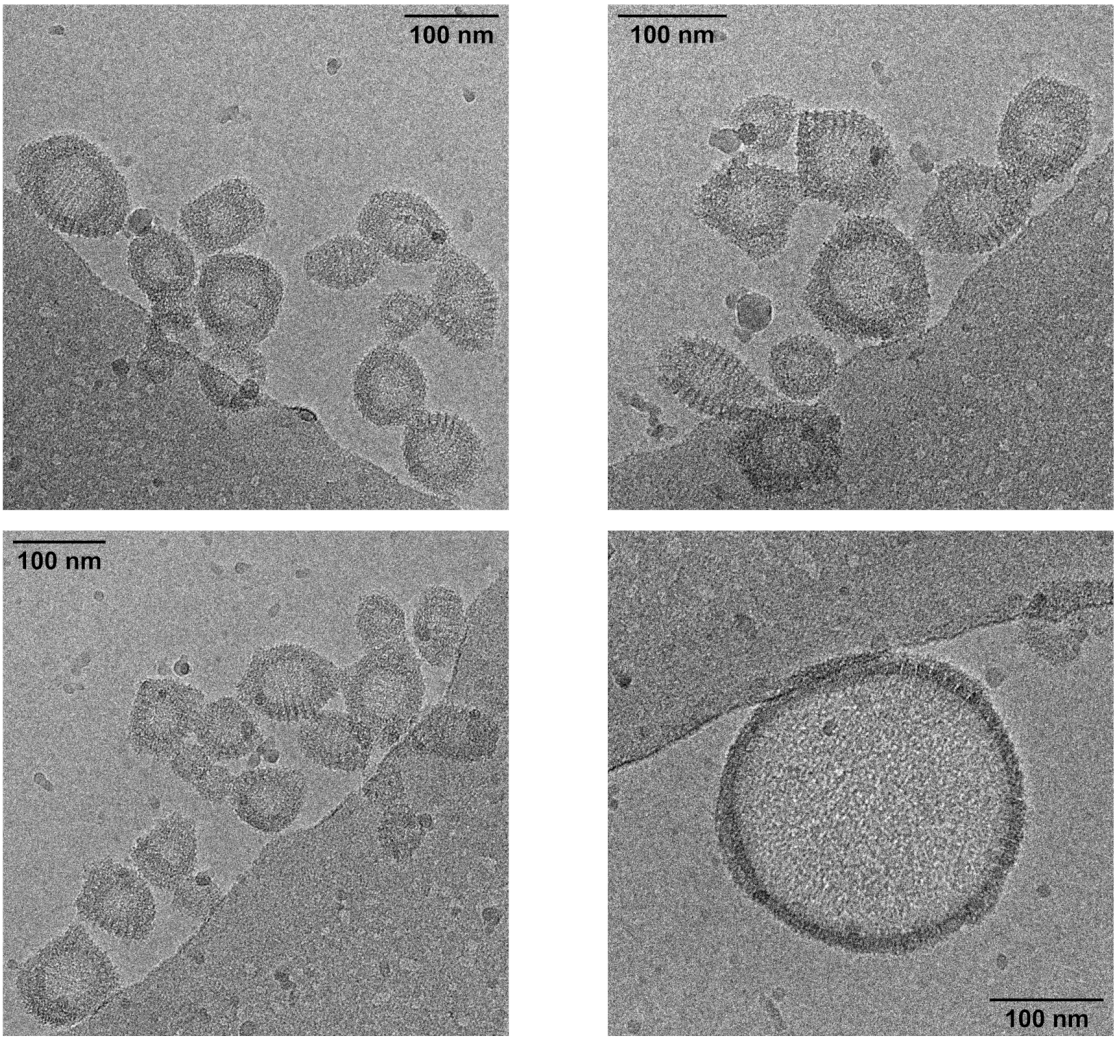

Figure 64. Additional cryo-EM images of type I and type II vesicles of **ON1*ON2**. Conditions: 1 μM **ON1*ON2**, 10 mM sodium phosphate buffer pH 7.2, 0.1 mM spermine · 4 HCl, 20 vol% ethanol.

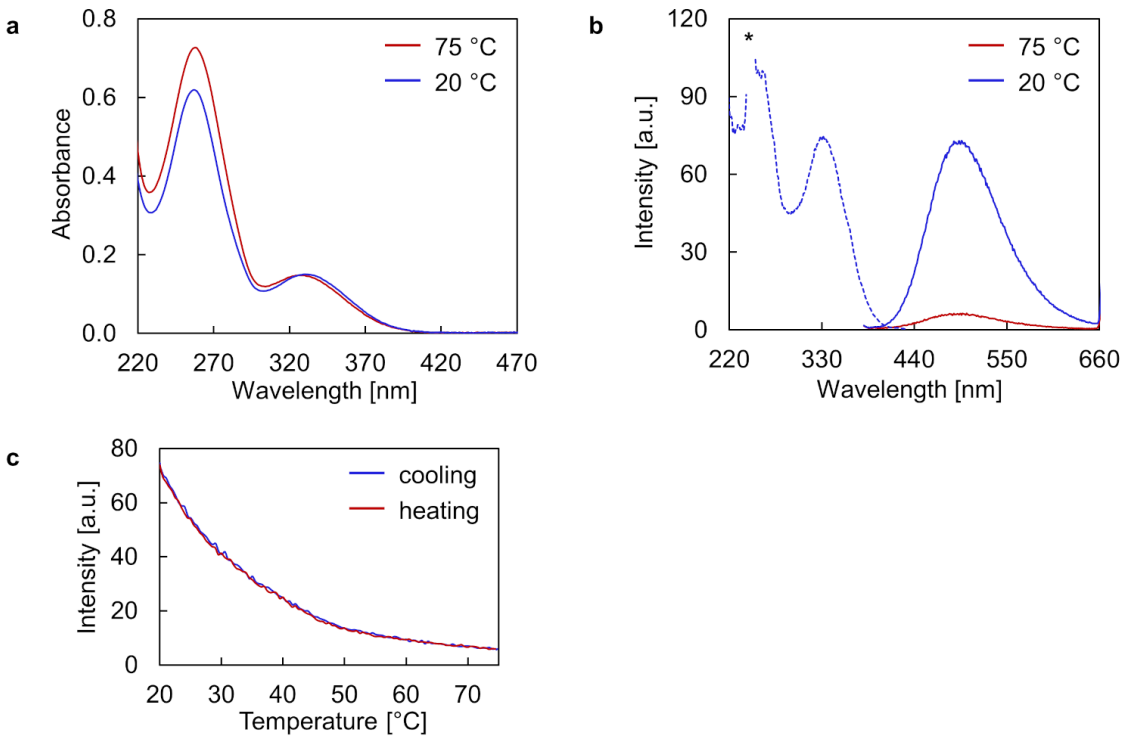

Figure 65. (**a**) UV-Vis absorption spectra, (**b**) fluorescence emission (solid line) and excitation (dotted line) spectra, and (**c**) fluorescence-monitored annealing and melting curves of **ON1*ON2** in the absence of spermine · 4 HCl. Conditions: 1 µM **ON1*ON2**, 10 mM sodium phosphate buffer pH 7.2, 20 vol% ethanol, $\lambda_{ex.}$: 335 nm, $\lambda_{em.}$: 490 nm, excitation slit: 5 nm, emission slit: 5 nm, gradient: 0.5 °C/min, * denotes second-order diffraction.

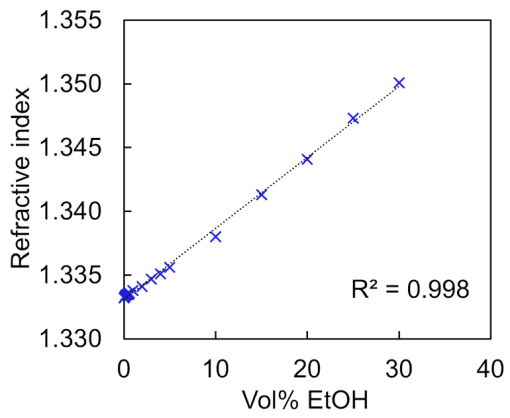

Vol% ethanol	n_D^{20}	Vol% ethanol	n_D^{20}
0	1.3332	3	1.3347
0.1	1.3333	4	1.3351
0.2	1.3334	5	1.3356
0.3	1.3335	10	1.3380
0.4	1.3335	15	1.3413
0.5	1.3335	20	1.3441
0.6	1.3336	25	1.3473
1	1.3338	30	1.3501
2	1.3341		

Figure 66. Refractive index (n_D^{20}) calibration curve of aqueous medium. Conditions: 10 mM sodium phosphate buffer pH 7.2, 0.1 mM spermine · 4 HCl, varying ethanol fraction.

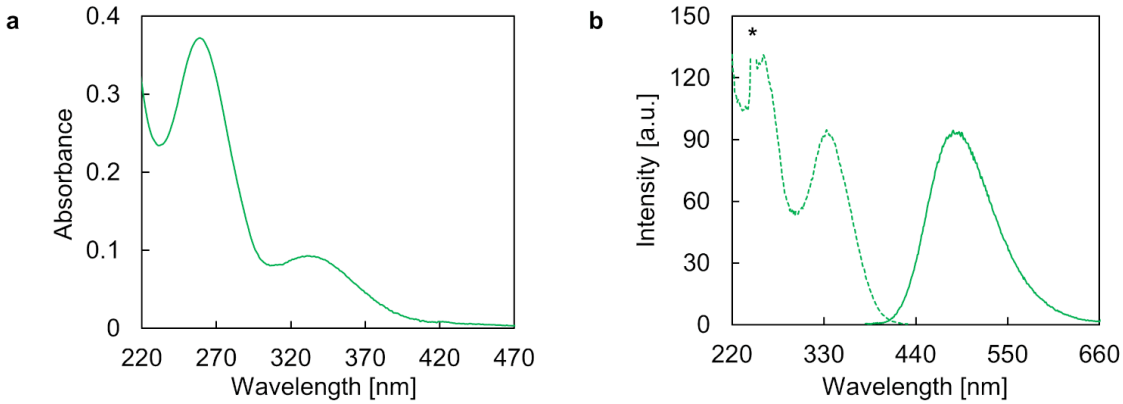

Figure 67. (**a**) UV-Vis absorption spectrum and (**b**) fluorescence emission (solid line) and excitation (dotted line) spectra of **ON1*ON2** after removal of the ethanol by dialysis. Conditions: 1 µM **ON1*ON2**, 10 mM sodium phosphate buffer pH 7.2, 0.1 mM spermine · 4 HCl, <0.5 vol% ethanol, $\lambda_{ex.}$: 335 nm, $\lambda_{em.}$: 490 nm, * denotes second-order diffraction.

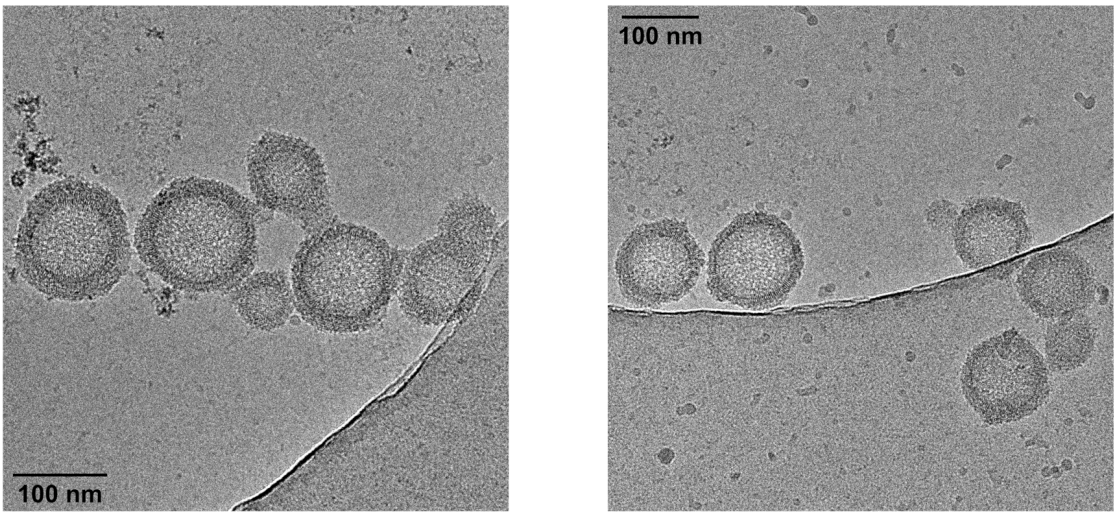

Figure 68. Additional cryo-EM images of type II vesicles of **ON1*ON2** after removal of ethanol by dialysis. Conditions: 1 µM **ON1*ON2**, 10 mM sodium phosphate buffer pH 7.2, 0.1 mM spermine · 4 HCl, <0.5 vol% ethanol.

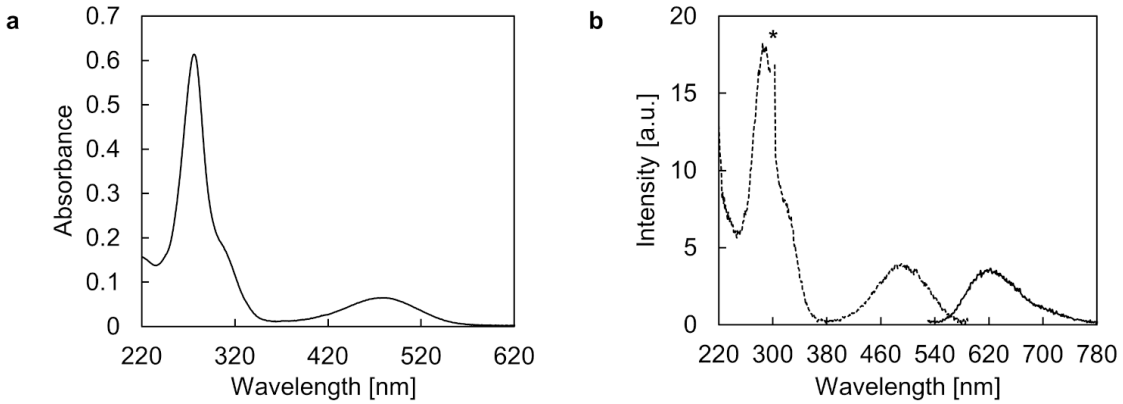

Figure 69. (**a**) Absorption spectrum, (**b**) fluorescence emission (solid line) and excitation spectrum (dotted line) of EthBr in aqueous medium containing 20 vol% ethanol. Conditions: 10 µM EthBr, 10 mM sodium phosphate buffer pH 7.2, 0.1 mM spermine · 4 HCl, 20 vol% ethanol, $\lambda_{ex.}$: 520 nm, $\lambda_{em.}$: 600 nm, 20 °C, * denotes second-order diffraction.

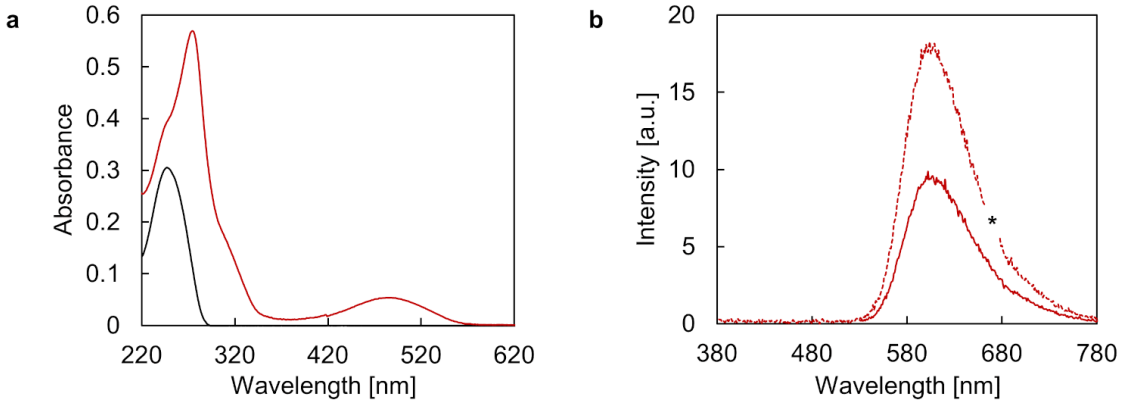

Figure 70. (**a**) UV-Vis absorption spectra and (**b**) fluorescence emission spectra (dotted line: $\lambda_{ex.}$: 335 nm; solid line: $\lambda_{ex.}$: 520 nm) of **ON5*ON6** before (black) and after 10 µM EthBr addition (red) in aqueous medium containing 20 vol% ethanol. Conditions: 1 µM **ON5*ON6**, 10 mM sodium phosphate buffer pH 7.2, 0.1 mM spermine · 4 HCl, 20 vol% ethanol, 20 °C, * denotes second-order diffraction.

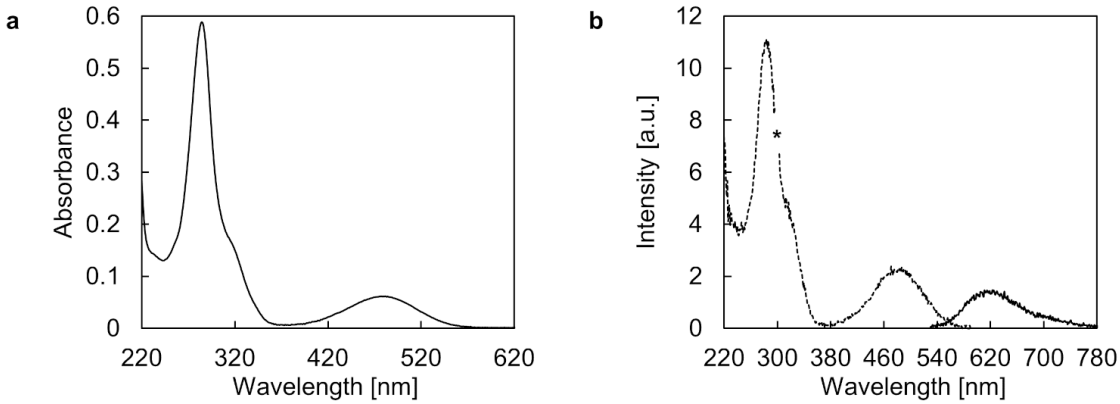

Figure 71. (**a**) Absorption spectrum, (**b**) fluorescence emission (solid line) and excitation spectrum (dotted line) of EthBr in aqueous medium. Conditions: 10 µM EthBr, 10 mM sodium phosphate buffer pH 7.2, 0.1 mM spermine · 4 HCl, $\lambda_{ex.}$: 520 nm, $\lambda_{em.}$: 600 nm, 20 °C, * denotes second-order diffraction.

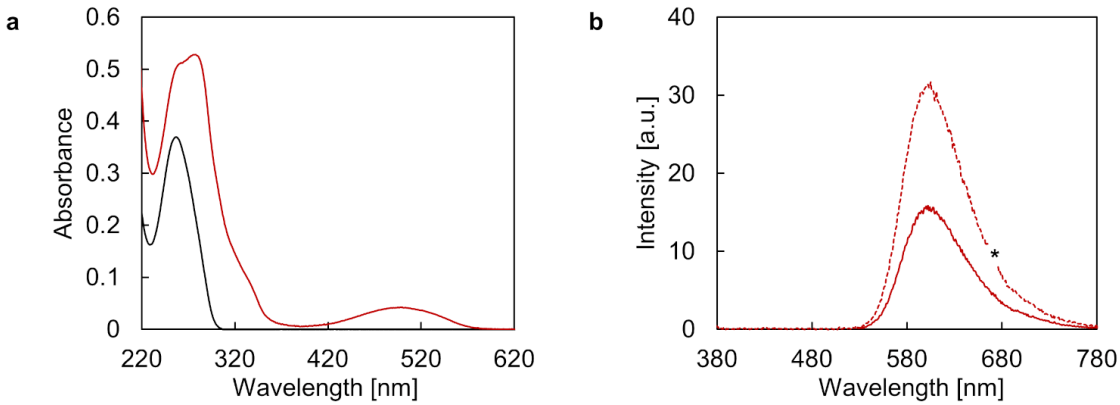

Figure 72. (**a**) UV-Vis absorption spectra and (**b**) fluorescence emission spectra (dotted line: $\lambda_{ex.}$: 335 nm; solid line: $\lambda_{ex.}$: 520 nm) of **ON5*ON6** before (black) and after 10 µM EthBr addition (red) in aqueous medium. Conditions: 1 µM **ON5*ON6**, 10 mM sodium phosphate buffer pH 7.2, 0.1 mM spermine · 4 HCl, 20 °C, * denotes second-order diffraction.

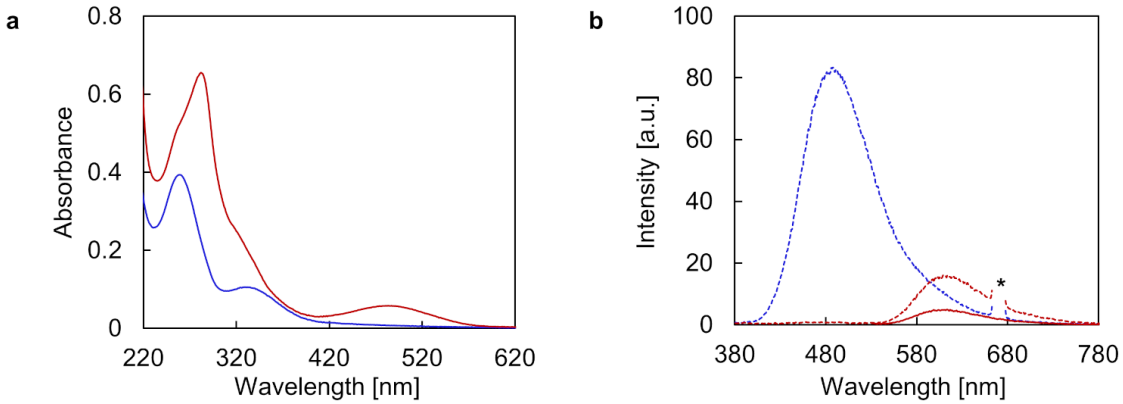

Figure 73. (**a**) UV-Vis absorption spectra and (**b**) fluorescence emission spectra (dotted line: $\lambda_{ex.}$: 335 nm; solid line: $\lambda_{ex.}$: 520 nm) of **ON1*ON2** before (blue) and after 10 µM EthBr addition (red) to type II vesicles. Conditions: 1 µM **ON1*ON2**, 10 mM sodium phosphate buffer pH 7.2, 0.1 mM spermine · 4 HCl, <0.5 vol% ethanol, 20 °C, * denotes second-order diffraction.

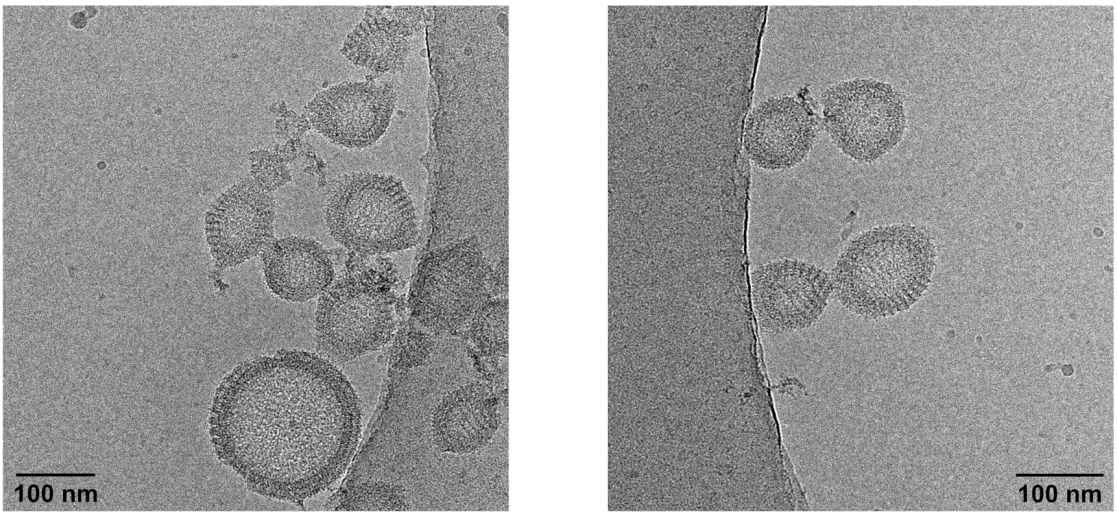

Figure 74. Additional cryo-EM images after EthBr addition to type I vesicles. Conditions: 1 µM **ON1*ON2**, 10 µM EthBr, 10 mM sodium phosphate buffer pH 7.2, 0.1 mM spermine · 4 HCl, 20 vol% ethanol.

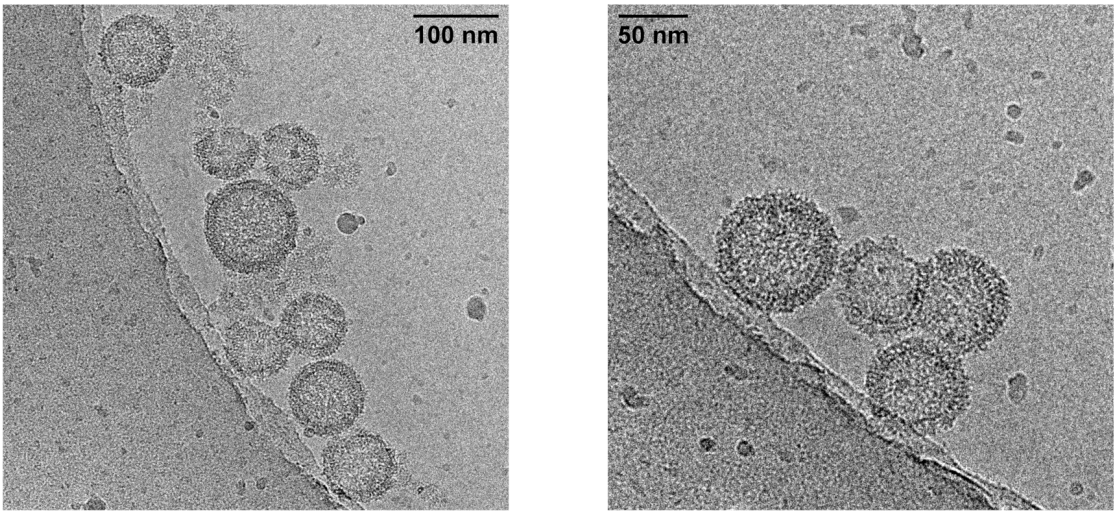

Figure 75. Cryo-EM imaging after EthBr addition to type II vesicles. Conditions: 1 µM **ON1*ON2**, 10 µM EthBr, 10 mM sodium phosphate buffer pH 7.2, 0.1 mM spermine · 4 HCl, <0.5 vol% ethanol.

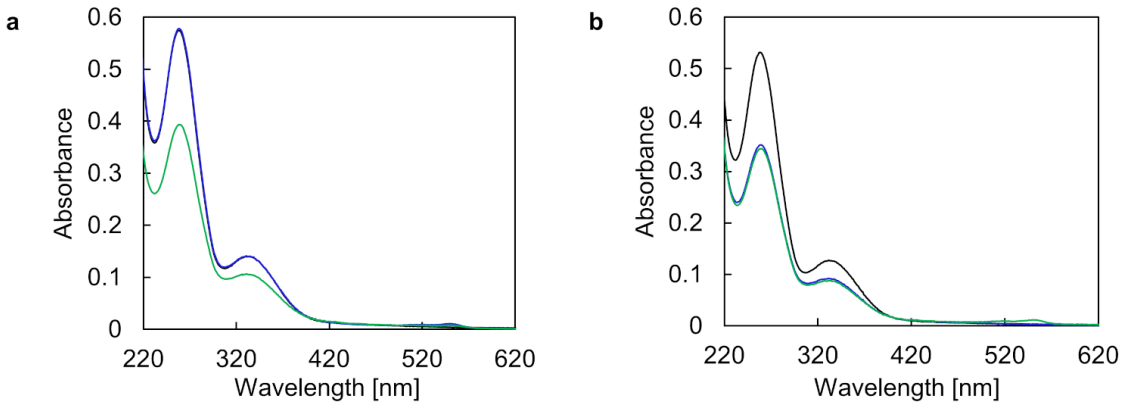

Figure 76. (**a**) UV-Vis absorption spectra of self-assembled vesicles of **ON1*ON2** in the absence (black) and presence of 1 mol% **ON7**, before (blue) and after (green) removal of ethanol by dialysis. (**b**) UV-Vis absorption spectra of self-assembled vesicles of **ON1*ON2** in the absence of **ON7** before (black) and after (blue) dialysis, and after dialysis in the presence of 1 mol% **ON7** (green). Conditions: 1 µM **ON1*ON2**, 10 mM sodium phosphate buffer pH 7.2, 0.1 mM spermine · 4 HCl, 20 resp. <0.5 vol% ethanol, 20 °C.

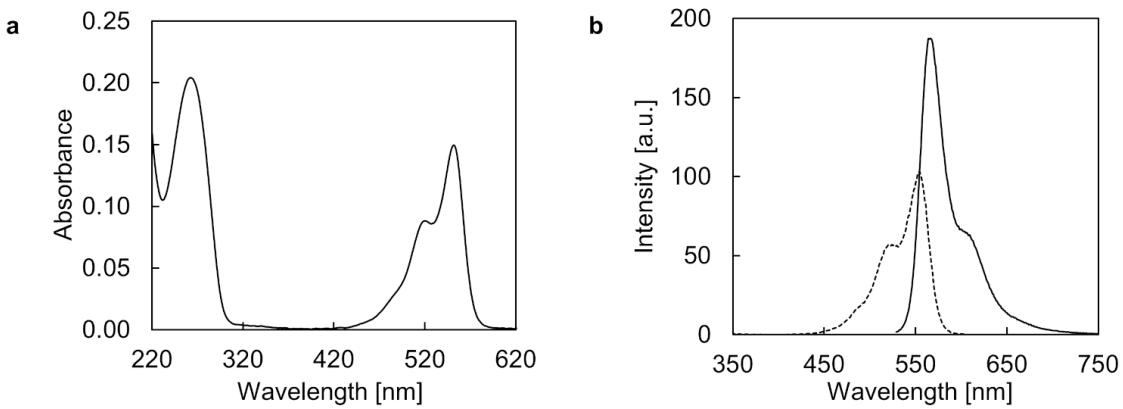

Figure 77. (**a**) UV-Vis absorption spectrum and (**b**) fluorescence emission (solid line) and excitation (dotted line) spectra of **ON7**. Conditions: 1 µM **ON7**, 10 mM sodium phosphate buffer pH 7.2, 0.1 mM spermine · 4 HCl, $\lambda_{ex.}$: 519 nm, $\lambda_{em.}$: 615 nm, 20 °C.

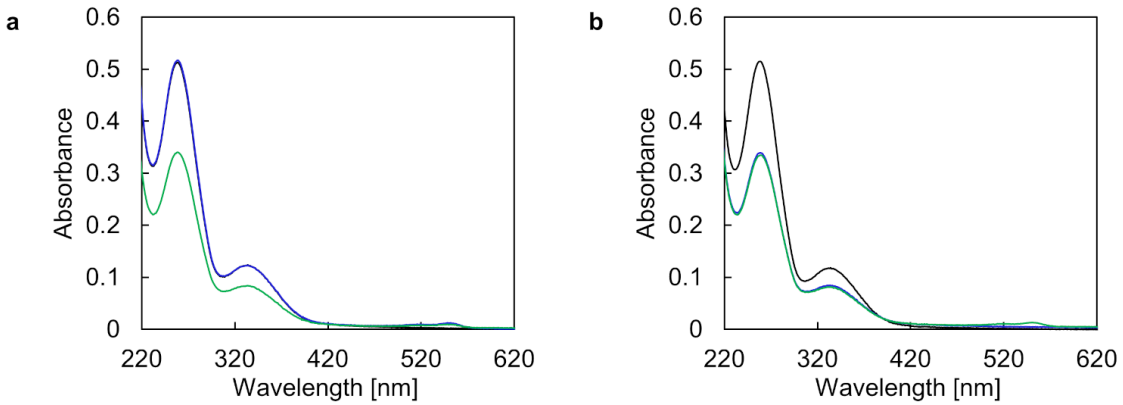

Figure 78. (**a**) UV-Vis absorption spectra of self-assembled vesicles of **ON1*ON2** in the absence (black) and presence of 1 mol% **ON8**, before (blue) and after (green) removal of ethanol by dialysis. (**b**) UV-Vis absorption spectra of self-assembled vesicles of **ON1*ON2** in the absence of **ON8** before (black) and after (blue) dialysis, and after dialysis in the presence of 1 mol% **ON8** (green). Conditions: 1 µM **ON1*ON2**, 10 mM sodium phosphate buffer pH 7.2, 0.1 mM spermine · 4 HCl, 20 resp. <0.5 vol% ethanol, 20 °C.

3.3.5 Cryo-EM Distance Measurements

Table 5. Summary of distance measurements. The reported distances are mean values with the corresponding standard deviation, along with the number of measurements in brackets.

Vesicular type	DNA length	DNA width
Type I	7.8 ± 0.5 nm (*n* = 32)	2.4 ± 0.5 nm (*n* = 10)
Type II	10.9 ± 0.5 nm (*n* = 34)	2.5 ± 0.5 nm (*n* = 19)

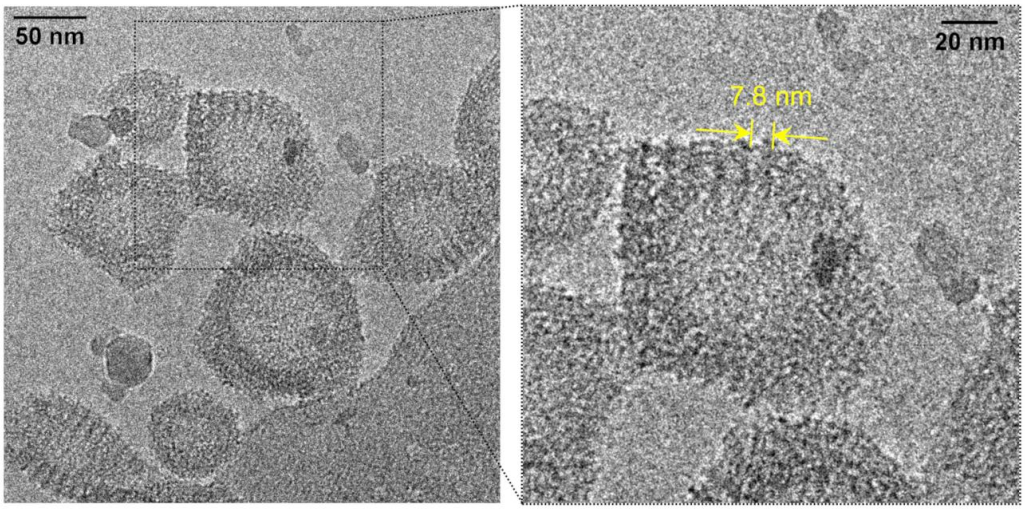

Figure 79. Representative DNA length measurement in a type I vesicle of self-assembled **ON1*ON2**. Conditions: 1 μM **ON1*ON2**, 10 mM sodium phosphate buffer pH 7.2, 0.1 mM spermine · 4 HCl, 20 vol% ethanol.

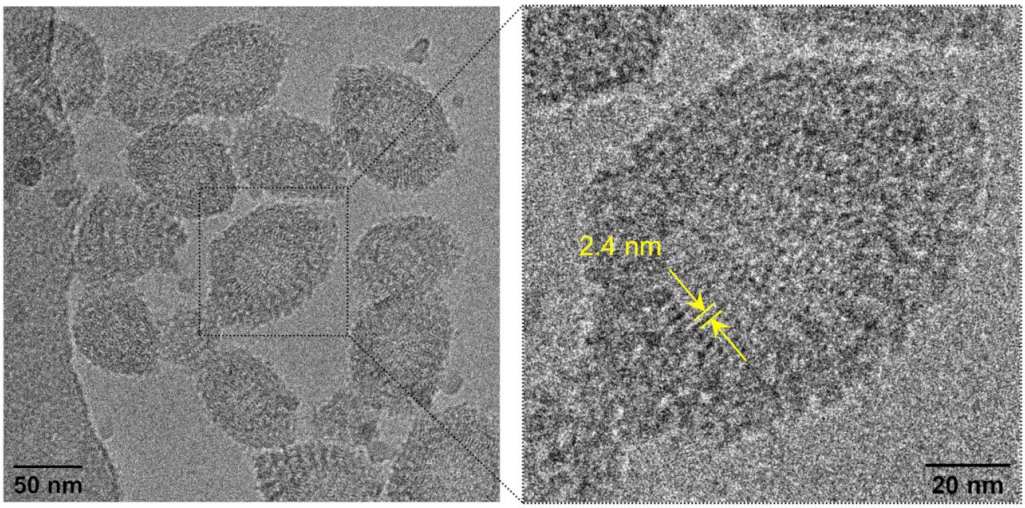

Figure 80. Representative DNA width measurement in a type I vesicle of self-assembled **ON1*ON2**. Conditions: 1 μM **ON1*ON2**, 10 mM sodium phosphate buffer pH 7.2, 0.1 mM spermine · 4 HCl, 20 vol% ethanol.

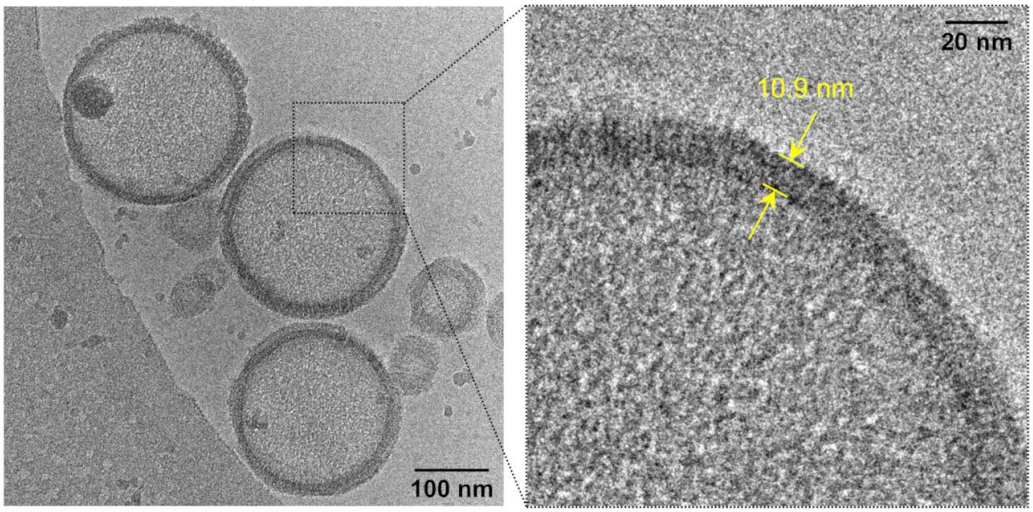

Figure 81. Representative DNA length measurement in a type II vesicle of self-assembled **ON1*ON2**. Conditions: 1 μM **ON1*ON2**, 10 mM sodium phosphate buffer pH 7.2, 0.1 mM spermine · 4 HCl, 20 vol% ethanol.

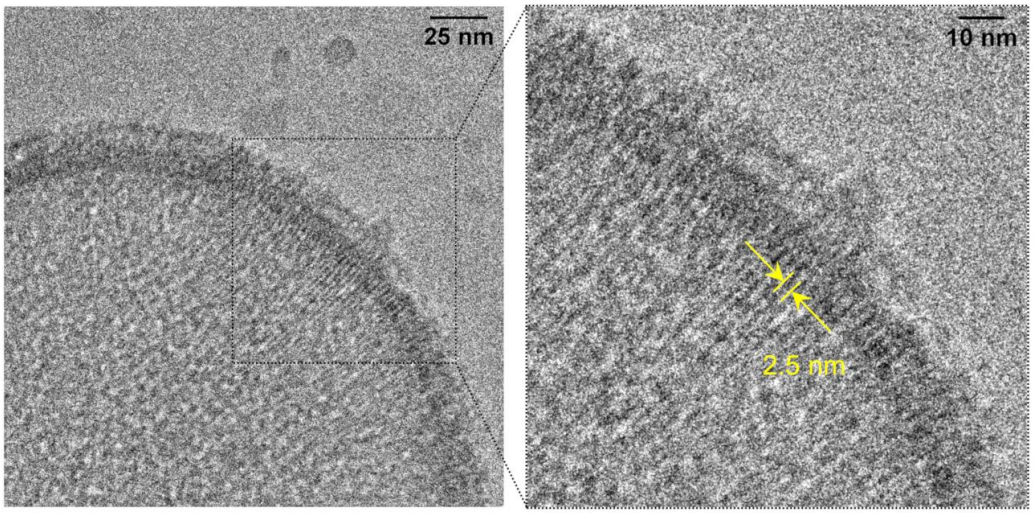

Figure 82. Representative DNA width measurement in a type II vesicle of self-assembled **ON1*ON2**. Conditions: 1 μM **ON1*ON2**, 10 mM sodium phosphate buffer pH 7.2, 0.1 mM spermine · 4 HCl, 20 vol% ethanol.

4 Supramolecular Assembly of 3’-/5’-End Modified TPE-DNA Conjugates

The influence of the oligonucleotide design of 3'-/5'-end modified TPE-DNA conjugates on the self-assembly behavior will be investigated. The assembly units are composed of a 3’-/5’-end modified TPE-DNA conjugate hybridized to an unmodified complement. Either the length of the TPE sticky ends or the DNA sequence length has been varied. The formation of vesicular structures needs a minimum of two TPE units per overhang. In contrast to a required minimum length of the TPE sticky ends, DNA duplexes of varied lengths affect the overall supramolecular assembly process to a lesser extent.

Adrian Gonzalez synthesized some of the oligonucleotides presented in this chapter in the context of a Master’s thesis (Adrian Gonzalez, *AIE-Active Supramolecular Assemblies of TPE-Modified DNA Conjugates*, Master’s thesis, University of Bern, 2021).

Part of this work has been published:

Tetraphenylethylene-DNA Conjugates: Influence of Sticky Ends and DNA Sequence Length on the Supramolecular Assembly of AIE-Active Vesicles

S. Rothenbühler, A. Gonzalez, I. Iacovache, S. M. Langenegger, B. Zuber, R. Häner, *Organic & Biomolecular Chemistry* **2022**, DOI: 10.1039/d2ob00357k.

4.1 Results and Discussion

Figure 83a provides an overview of the DNA single strands utilized in this chapter. **ON5** served as the complementary strand for the 3’-/5’-end modified oligonucleotides **ON9**–**ON11**. In the series from **ON9**

to **ON11**, the length of the *E*-TPE sticky ends was shortened from three TPE units (**ON9**) to one TPE residue (**ON11**) per sticky end. The DNA part remained unchanged at 20 DNA nucleotides. A representative illustration for a resulting duplex, **ON5*ON10**, is shown in Figure 83b. On the other hand, **ON12**–**ON15** were employed to investigate the influence of the DNA sequence length on the self-assembly behavior, while the number of *E*-TPEs was kept constant at three moieties per sticky end. Therefore, a duplex with a 15-mer DNA (**ON12*ON13**) and a 25-mer DNA (**ON14*ON15**) were examined. Changes in the DNA sequences were implemented in the middle of the strands, thus, retaining the same DNA sequences towards the ends of the DNA duplexes. Duplex **ON5*ON16**, functionalized with *Z*-TPE overhangs, was compared with the corresponding *E*-TPE-modified duplex **ON5*ON9** to analyze the influence of the *E*-/*Z*-stereoisomers of TPE on the morphology of the supramolecular nanostructures. Oligonucleotide **ON17** was hybridized to **ON9** in order to form a duplex with a total number of 12 TPE units present in the sticky ends. All TPE-modified DNA single strands were synthesized *via* solid-phase synthesis and purified by HPLC (see section 4.3.1).

a

Strand	Sequence (5'→3')
ON5	CAA GGT CCG ATG CAA GGA AG
ON9	(*E*-TPE)$_3$-CTT CCT TGC ATC GGA CCT TG-(*E*-TPE)$_3$
ON10	(*E*-TPE)$_2$-CTT CCT TGC ATC GGA CCT TG-(*E*-TPE)$_2$
ON11	*E*-TPE-CTT CCT TGC ATC GGA CCT TG-*E*-TPE
ON12	(*E*-TPE)$_3$-CTT CCT TGG ACC TTG-(*E*-TPE)$_3$
ON13	CAA GGT CCA AGG AAG
ON14	(*E*-TPE)$_3$-CTT CCT TGC ACT GAA TCG GAC CTT G-(*E*-TPE)$_3$
ON15	CAA GGT CCG ATT CAG TGC AAG GAA G
ON16	(*Z*-TPE)$_3$-CTT CCT TGC ATC GGA CCT TG-(*Z*-TPE)$_3$
ON17	(*E*-TPE)$_3$-CAA GGT CCG ATG CAA GGA AG-(*E*-TPE)$_3$

b

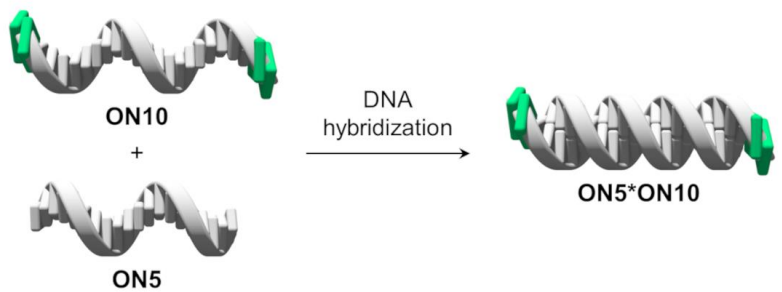

Figure 83. (**a**) Summary of the DNA sequences used in this study. For molecular structures of the modifications, see Figure 15a. (**b**) Single strands **ON10** and **ON5** are complementary and hybridize to form duplex **ON5*ON10**.

Figure 84 displays representative temperature-dependent UV-Vis and fluorescence spectra of **ON5*ON9**, which show similar absorption profiles and fluorescence bands, as described for the 3'-end modified duplex **ON1*ON2** (see section 3.1.3). Comparable spectroscopic results were obtained for duplexes **ON5*ON10** (Figure 118), **ON5*ON11** (Figure 119), **ON12*ON13** (Figure 120), and **ON14*ON15** (Figure 121), which all feature characteristic AIE properties (**ON5*ON11** excluded).

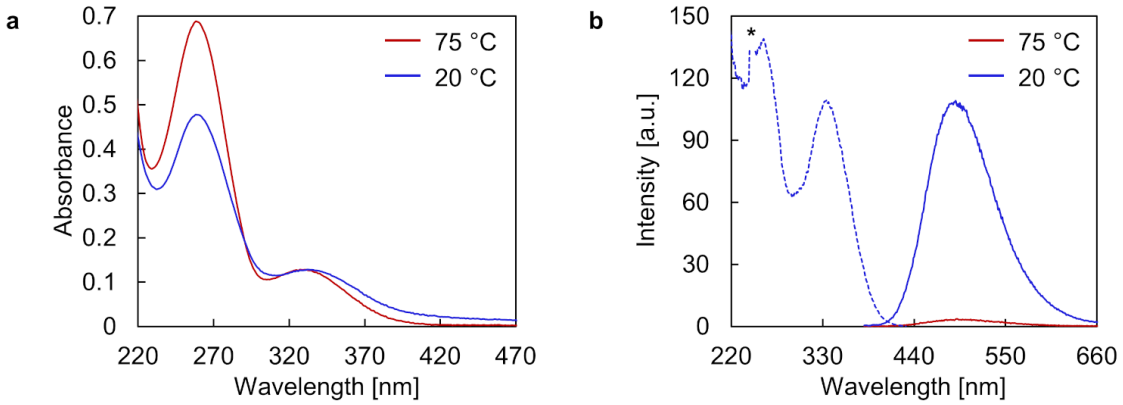

Figure 84. (**a**) UV-Vis absorption spectra and (**b**) fluorescence emission (solid line) and excitation (dotted line) spectra of **ON5*ON9**. Conditions: 1 µM **ON5*ON9**, 10 mM sodium phosphate buffer pH 7.2, 0.1 mM spermine · 4 HCl, 20 vol% ethanol, $\lambda_{ex.}$: 335 nm, $\lambda_{em.}$: 490 nm, * denotes second-order diffraction.

In the first series of experiments, duplexes **ON5*ON9**, **ON5*ON10**, and **ON5*ON11** were analyzed and compared. The goal was to study the morphological effects of nanostructures assembled from duplexes with varied lengths of TPE overhangs. It is assumed that the strength of the sticky ends increases with an increasing number of hydrophobic TPE residues. AFM experiments were performed to visualize the supramolecular nanostructures, after a thermal assembly process has been conducted (controlled cooling of the sample solution from 75 °C to 20 °C, 0.5 °C/min). In the case of **ON5*ON9**, a vesicular morphology with a maximum height of about 40 nm was detected (Figure 85). But most of the structures are in the range between 15–25 nm in height (Figure 122). Besides the individual spherical aggregates, agglomerated assemblies are discernible as well. Reducing the hydrophobic sticky end interaction by shortening the overhangs by one TPE unit on each side (**ON5*ON10**), resulted in the formation of single vesicular aggregates, as displayed in Figure 86. Additionally, the size range increased to about 20–80 nm in height with an average diameter of roughly 100 nm (see also Figure 123). Dynamic light scattering (DLS) experiments displayed an average hydrodynamic diameter of 235 ± 59 nm for these vesicles (Figure 124). For **ON5*ON11** with only one TPE residue on both ends of the duplex, the thermal assembly process yielded no detectable nanostructures (Figure 87 and Figure 125).

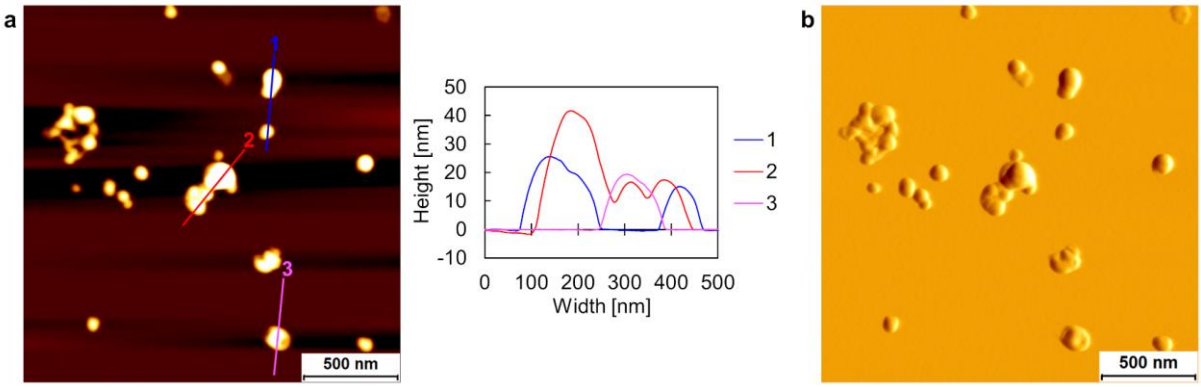

Figure 85. (**a**) AFM scan with corresponding cross sections and (**b**) deflection scan of assembled **ON5*ON9**. Conditions: 1 µM **ON5*ON9**, 10 mM sodium phosphate buffer pH 7.2, 0.1 mM spermine · 4 HCl, 20 vol% ethanol.

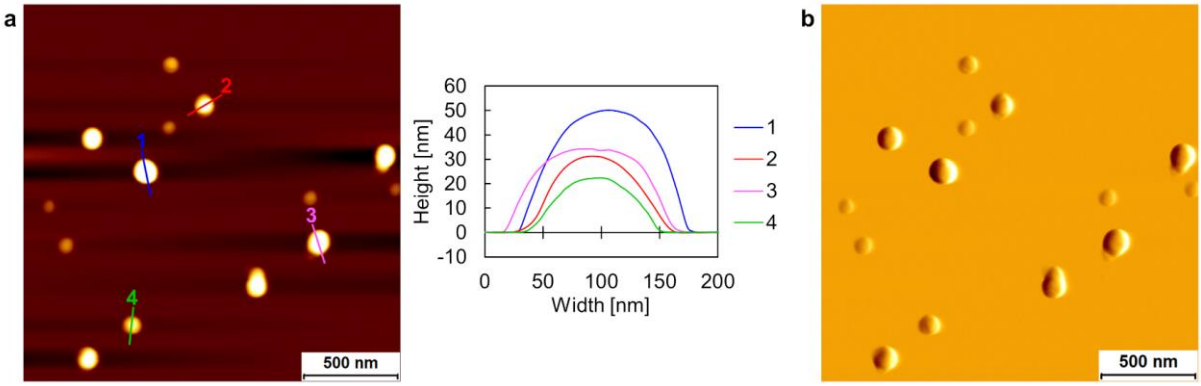

Figure 86. (**a**) AFM scan with corresponding cross sections and (**b**) deflection scan of assembled **ON5*ON10**. Conditions: 1 µM **ON5*ON10**, 10 mM sodium phosphate buffer pH 7.2, 0.1 mM spermine · 4 HCl, 20 vol% ethanol.

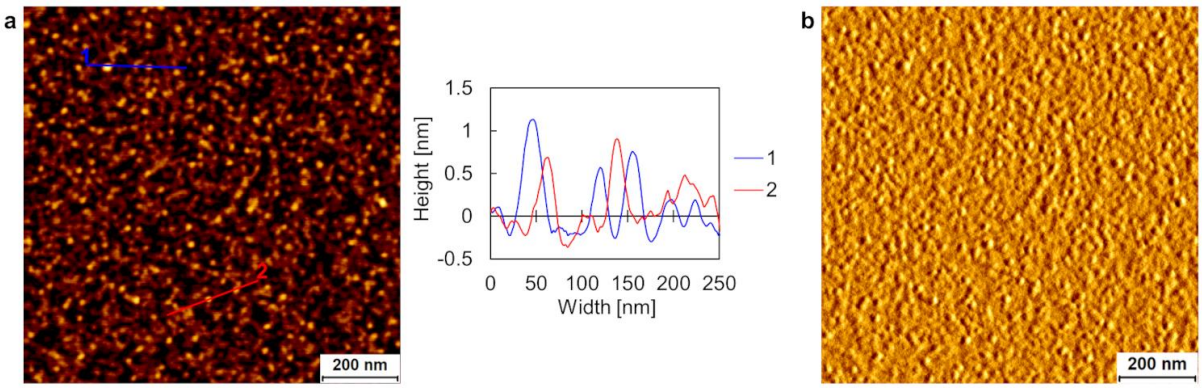

Figure 87. (**a**) AFM scan with corresponding cross sections and (**b**) deflection scan of assembled **ON5*ON11**. Conditions: 1 µM **ON5*ON11**, 10 mM sodium phosphate buffer pH 7.2, 0.1 mM spermine · 4 HCl, 20 vol% ethanol.

However, the height profiles in the AFM image (up to 1 nm) suggest that some material adsorbed on the surface, because the surface is rougher than a plain APTES-modified mica surface. Figure 126 illustrates this, where the cross sections have been measured apart from any adsorbed nanostructures and evidence that in this case, the height profiles do not exceed +/- 150 pm in height. Therefore, it is assumed that the hydrophobic TPE interactions were in this case too weak to enable the assembly of large supramolecular assemblies.

The results from AFM imaging were confirmed by nucleation temperatures obtained from fluorescence-monitored annealing curves (Figure 88). The absence of any T_{FL}(nucleation) for **ON5*ON11** reflects that no larger aggregates were formed. On the other hand, a characteristic AIE behavior was found for **ON5*ON9** and **ON5*ON10**. A nucleation temperature of 53 °C was determined for **ON5*ON10** and the overall shape of the annealing curve suggests a nucleation-elongation assembly process.[179–185] For **ON5*ON9**, a T_{FL}(nucleation) of 60–62 °C was assigned. A temperature range was specified, because the increase in fluorescence is not as sharp as compared to **ON5*ON10**. The nucleation temperatures for the three duplexes show a clear trend: the longer the TPE sticky ends, the higher T_{FL}(nucleation) is. This is mainly attributed to the increase in the hydrophobic interactions between the TPE sticky ends.

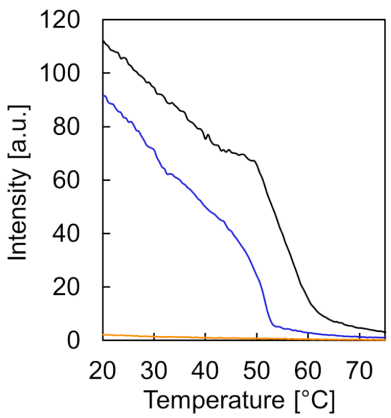

Duplex	T_{FL}(nucleation)[a] [°C]	Morphology
ON5*ON9	60–62	agglomerated vesicles
ON5*ON10	53	single vesicles
ON5*ON11	-	no aggregates

Figure 88. Fluorescence-monitored annealing curves of **ON5*ON9** (black), **ON5*ON10** (blue), and **ON5*ON11** (orange), as well as a summary of nucleation temperatures T_{FL}(nucleation) and observed morphologies by AFM. Conditions: 1 µM each single strand, 10 mM sodium phosphate buffer pH 7.2, 0.1 mM spermine · 4 HCl, 20 vol% ethanol, $\lambda_{ex.}$: 335 nm, $\lambda_{em.}$: 490 nm, gradient: 0.5 °C/min. [a] Nucleation temperature, determined by fluorescence onset temperature in annealing curve.

The influence of the DNA sequence length on the supramolecular assembly behavior was examined in another series of experiments, while the number of TPEs per sticky end remained unchanged at three units. It is assumed that the DNA sequence length (*i.e.*, number of phosphate groups) influences the spermine mediated interaction between the DNA duplexes. Therefore, DNA duplexes **ON12*ON13** and **ON14*ON15** were analyzed by AFM and compared with **ON5*ON9**. Duplex **ON12*ON13**, which is composed of a 15-mer DNA, self-assembles predominantly into agglomerated spherical nanostructures (Figure 89). A similar size range of about 20–30 nm in height was observed for **ON12*ON13** as previously described for **ON5*ON9**. In the case of the 25-mer DNA containing duplex **ON14*ON15**, almost exclusively agglomerated vesicles were observed (Figure 90). AFM overview scans of **ON12*ON13** and **ON14*ON15** are presented in Figure 127 and Figure 128, respectively. However, compared to the substantial influence of the TPE sticky end length on the morphology, varying the DNA sequence length does not change the morphology to such a significant extent.

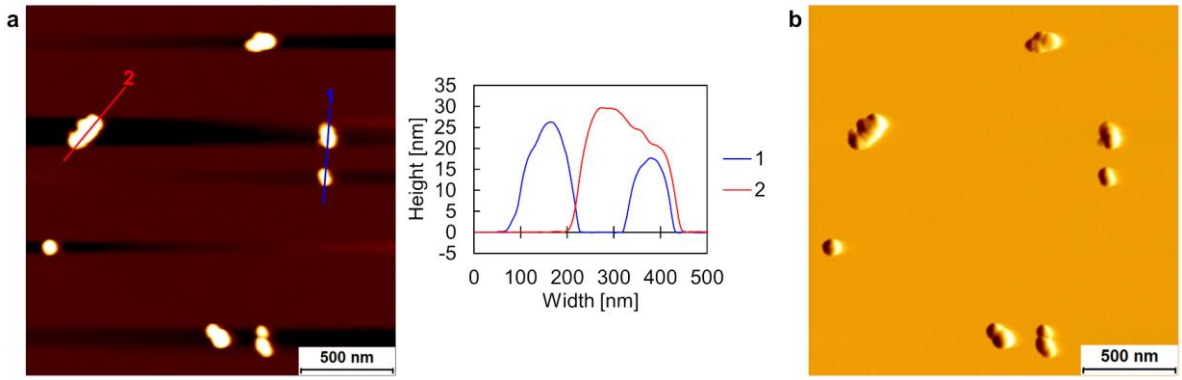

Figure 89. (**a**) AFM scan with corresponding cross sections and (**b**) deflection scan of assembled **ON12*ON13**. Conditions: 1 µM **ON12*ON13**, 10 mM sodium phosphate buffer pH 7.2, 0.1 mM spermine · 4 HCl, 20 vol% ethanol.

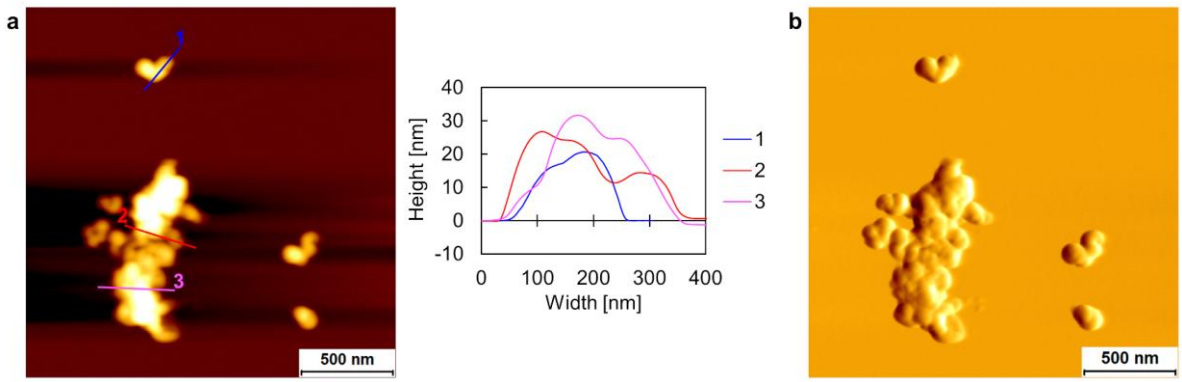

Figure 90. (**a**) AFM scan with corresponding cross sections and (**b**) deflection scan of assembled **ON14*ON15**. Conditions: 1 µM **ON14*ON15**, 10 mM sodium phosphate buffer pH 7.2, 0.1 mM spermine · 4 HCl, 20 vol% ethanol.

This observation is also supported by the nucleation temperatures deduced from fluorescence-monitored annealing curves. As shown in Figure 91, the nucleation temperatures are all within a similar range (56–64 °C). Thus, it is believed that the length of the DNA (within the scope of this analysis) only plays a minor role in the formation of such supramolecular assemblies.

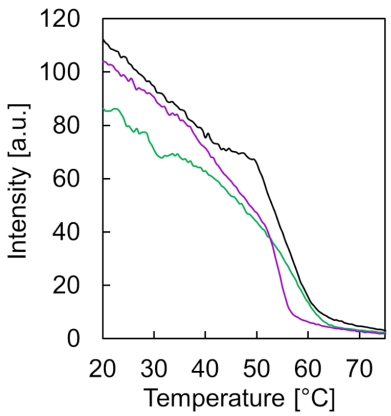

Duplex	T_{FL}(nucleation)[a] [°C]	Morphology
ON12*ON13	62–64	agglomerated vesicles
ON5*ON9	60–62	agglomerated vesicles
ON14*ON15	56	agglomerated vesicles

Figure 91. Fluorescence-monitored annealing curves of **ON12*ON13** (green), **ON5*ON9** (black), and **ON14*ON15** (purple), as well as a summary of nucleation temperatures T_{FL}(nucleation) and observed morphologies by AFM. Conditions: 1 µM each single strand, 10 mM sodium phosphate buffer pH 7.2, 0.1 mM spermine · 4 HCl, 20 vol% ethanol, $\lambda_{ex.}$: 335 nm, $\lambda_{em.}$: 490 nm, gradient: 0.5 °C/min. [a] Nucleation temperature, determined by fluorescence onset temperature in annealing curve.

As depicted in Figure 85, **ON5*ON9** self-assembles into agglomerated vesicles. Agglomeration is likely due to intermolecular hydrophobic TPE interactions between vesicles. Optimization of the aqueous conditions might reduce these interactions. Therefore, the ethanol fraction of the aqueous medium was increased from 20 vol% to 30 vol%, resulting in less polar aqueous conditions. The corresponding fluorescence-monitored annealing curve is displayed in Figure 92. Changing the conditions leads to two important differences in the annealing curves of **ON5*ON9**. Firstly, the nucleation temperature T_{FL}(nucleation) was lowered from 60–62 °C to 49 °C in the presence of 30 vol% ethanol. Secondly, the overall shape of the annealing curve suggests a more cooperative assembly process with a well-defined fluorescence onset temperature.[179–185] Interestingly, this change in conditions has about the same effect on the nucleation temperature as shortening the TPE overhangs by one residue on each end (duplex **ON5*ON10**, Figure 88). The UV-Vis and fluorescence spectra of **ON5*ON9** are shown in Figure 93, which are comparable to the results obtained for **ON5*ON9** in the presence of 20 vol% ethanol (Figure 84). Potential morphological effects of the conditions on the nanostructures were investigated by AFM and cryo-EM imaging.

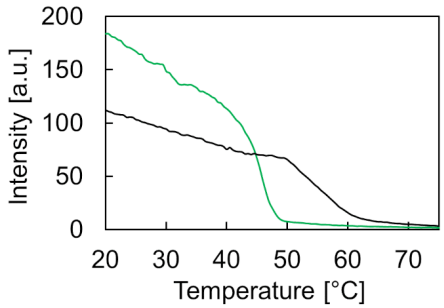

Ethanol fraction	T_{FL}(nucleation)[a] [°C]
20 vol%	60–62
30 vol%	49

Figure 92. Fluorescence-monitored annealing curves of **ON5*ON9** in the presence of either 20 vol% ethanol (black) or 30 vol% ethanol (green), as well as a summary of nucleation temperatures T_{FL}(nucleation). Conditions: 1 µM **ON5*ON9**, 10 mM sodium phosphate buffer pH 7.2, 0.1 mM spermine · 4 HCl, $\lambda_{ex.}$: 335 nm, $\lambda_{em.}$: 490 nm, gradient: 0.5 °C/min. [a] Nucleation temperature, determined by fluorescence onset temperature in annealing curve.

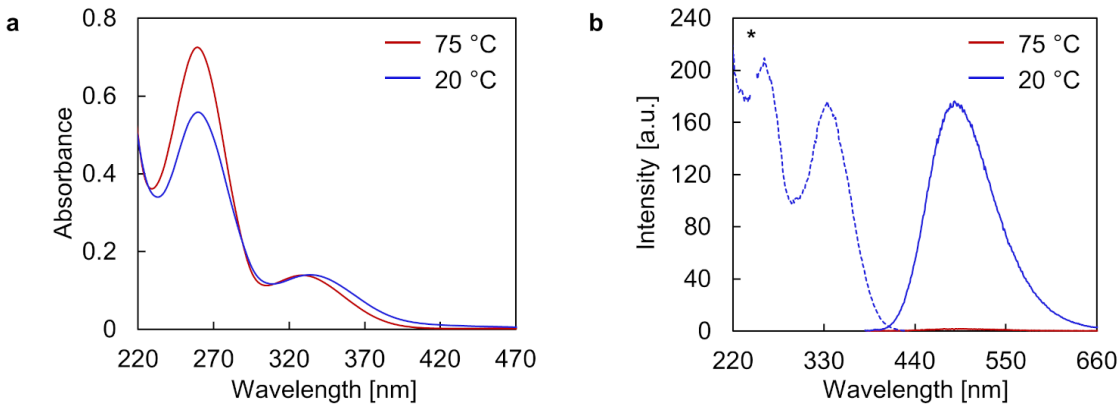

Figure 93. (**a**) UV-Vis absorption spectra and (**b**) fluorescence emission (solid line) and excitation (dotted line) spectra of **ON5*ON9**. Conditions: 1 µM **ON5*ON9**, 10 mM sodium phosphate buffer pH 7.2, 0.1 mM spermine · 4 HCl, 30 vol% ethanol, $\lambda_{ex.}$: 335 nm, $\lambda_{em.}$: 490 nm, * denotes second-order diffraction.

Increasing the ethanol fraction to 30 vol% results in the formation of single vesicular nanostructures of **ON5*ON9**, as presented in Figure 94 and the overview AFM scan in Figure 129. In addition, the size range increased to 60–100 nm in height and 50–150 nm in diameter. This observation verifies that the composition of the aqueous medium affects the resulting supramolecular morphology (*i.e.*, size range and degree of agglomeration).

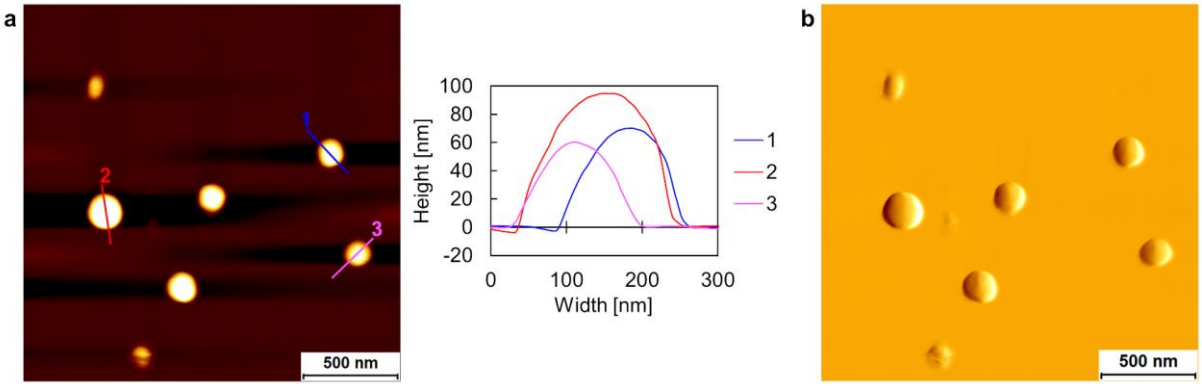

Figure 94. (**a**) AFM scan with corresponding cross sections and (**b**) deflection scan of assembled **ON5*ON9**. Conditions: 1 µM **ON5*ON9**, 10 mM sodium phosphate buffer pH 7.2, 0.1 mM spermine · 4 HCl, 30 vol% ethanol.

Cryo-EM experiments were conducted in collaboration with Prof. Dr. Benoît Zuber and Dr. Ioan Iacovache from the Institute of Anatomy of the University of Bern to further elucidate the nanostructures assembled from **ON5*ON9** under optimized conditions. Figure 95a shows a vesicular morphology, with individual vesicles exhibiting diameters of roughly 140–200 nm (for additional images, see Figure 130). A closer look at the structures suggests that they are assembled from different types of membranes. In the core, a columnar DNA duplex alignment is revealed, with the characteristic rod-like pattern visible in some areas (comparable to type II vesicles assembled from **ON1*ON2**, Figure 22). A membrane thickness of 10.5 ± 0.6 nm and a DNA width of 2.4 ± 0.5 nm was measured (see section 4.3.3). However, the vesicular constructs are surrounded by a membrane, distinctive for a DNA arrangement as described for type I vesicles (Figure 21). A distance of 8.0 ± 0.5 nm was measured between the dark bands, which is in agreement with the distance reported in type I vesicles (7.8 ± 0.5 nm). Thus, a hybrid structure, type III, composed of the two types of DNA alignments is assumed, as illustrated schematically in Figure 95b.

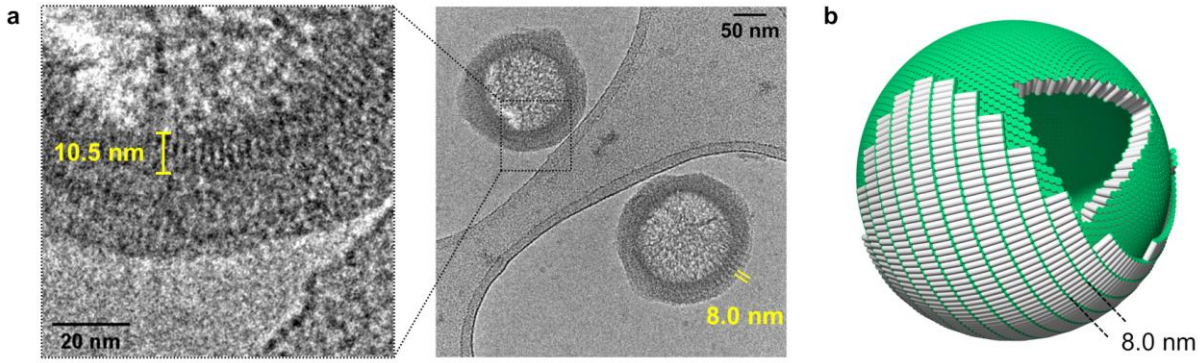

Figure 95. (**a**) Cryo-EM image of assembled **ON5*ON9**. (**b**) Schematic representation of a type III vesicle constructed from **ON5*ON9**. Conditions: 1 μM **ON5*ON9**, 10 mM sodium phosphate buffer pH 7.2, 0.1 mM spermine · 4 HCl, 30 vol% ethanol.

This hybrid structure is further supported by gray value plots deduced from cryo-EM images (Figure 96). The gray values across the supramolecular structures were measured, then normalized (dotted gray line) and smoothened by displaying the moving average (solid black line). In these plots, white is assigned to the value 1, while 0 is set for black. Figure 96a shows the gray value plot of a type I vesicle assembled from **ON1*ON2**. Along the line from the blue starting point towards the red end point, the gray value decreases at the start of the vesicular structure. Then, across the structure, a curved progression is visible towards the end of the vesicle, before the gray value returns to the background level. Conversely, the densely packed columnar membrane of type II vesicles from **ON1*ON2** leads to a significant decrease in the gray value but remains constant within the core of the vesicle (Figure 96b). Finally, the hybrid structure of type III vesicles assembled from **ON5*ON9**, is kind of an overlay of the gray value plots of type I and type II vesicles (Figure 96c). A pronounced decrease in the gray value, due to the dense type II membrane, as well as a curved progression over the vesicular core, which is characteristic for type I vesicles. Therefore, the proposal of such type III vesicles constructed from **ON5*ON9** is based on the interpretation of the gray value plots of the three different types of architectures, together with the distance measurements deduced from cryo-EM images.

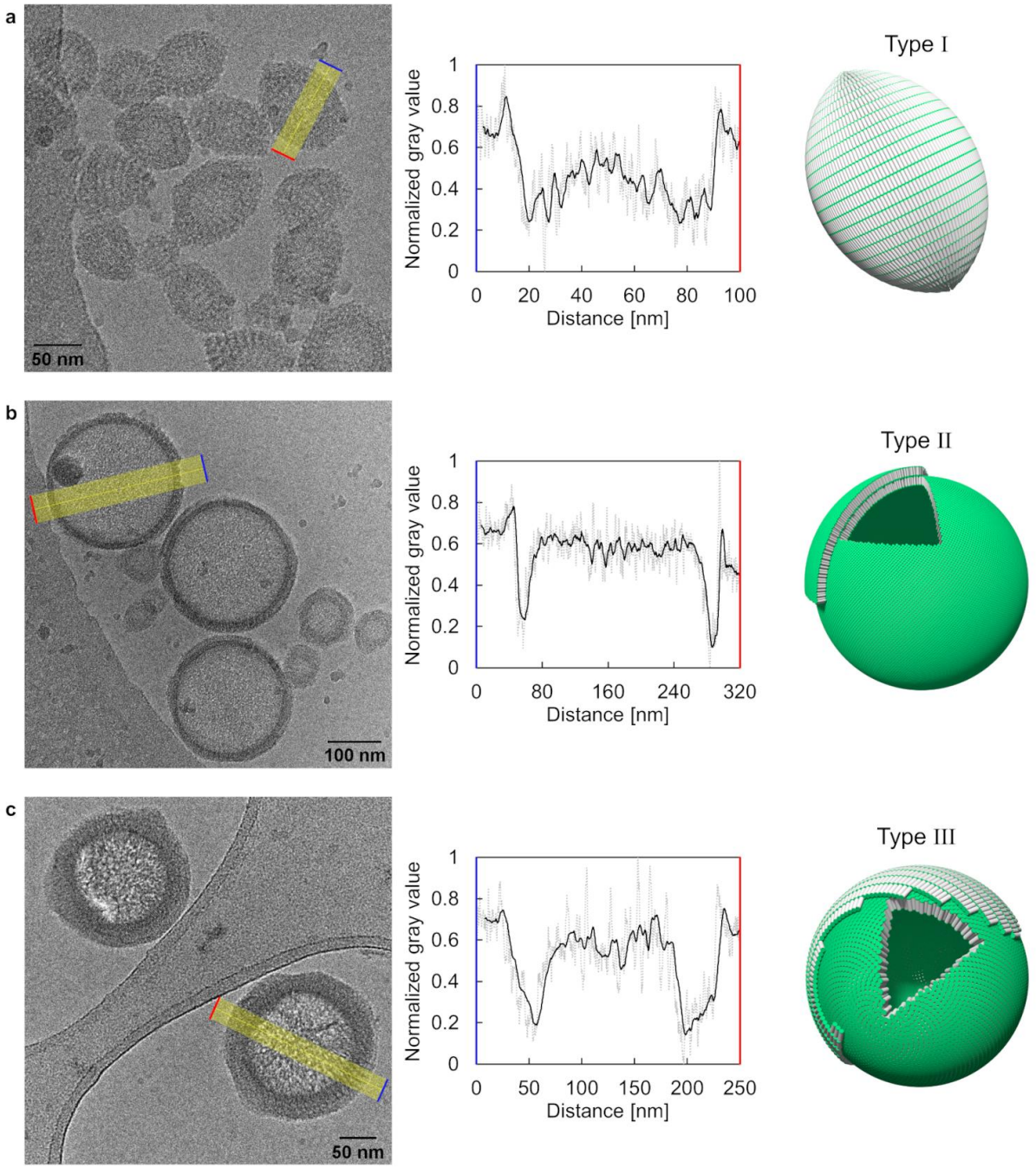

Figure 96. Different types of vesicles, classified by gray value plots. (**a**) Type I vesicles assembled from **ON1*ON2**. (**b**) Type II vesicles assembled from **ON1*ON2**. (**c**) Type III vesicles assembled from **ON5*ON9**.

To test the effect of the *E*-/*Z*-stereoisomers of TPE on the self-assembly behavior and morphology of the supramolecular nanostructures, duplex **ON5*ON16** was investigated, which is modified with *Z*-TPE sticky ends (Figure 83). The temperature-dependent UV-Vis and fluorescence spectra in Figure 97 show a comparable behavior as it was shown previously for the respective *E*-TPE-modified duplex **ON5*ON9** (Figure 93).

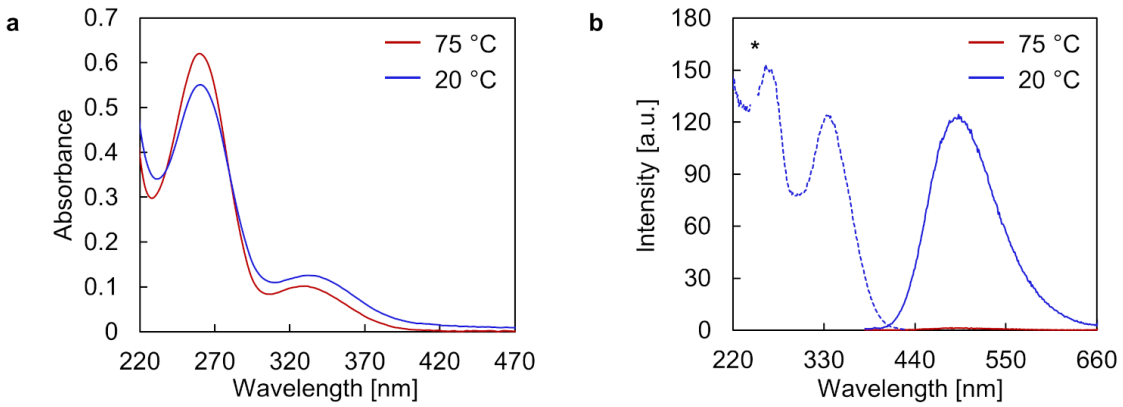

Figure 97. (**a**) UV-Vis absorption spectra and (**b**) fluorescence emission (solid line) and excitation (dotted line) spectra of **ON5*ON16**. Conditions: 1 µM **ON5*ON16**, 10 mM sodium phosphate buffer pH 7.2, 0.1 mM spermine · 4 HCl, 30 vol% ethanol, $\lambda_{ex.}$: 335 nm, $\lambda_{em.}$: 490 nm, * denotes second-order diffraction.

The nucleation temperature of **ON5*ON16** is only lowered by 2 °C to 47 °C, compared to the T_{FL}(nucleation) of **ON5*ON9** (Figure 98). However, the shape of the annealing curve of **ON5*ON16** implies for a slightly less cooperative assembly process due to the rather linear increase in fluorescence in the temperature range from 40 °C to 20 °C.[179–185]

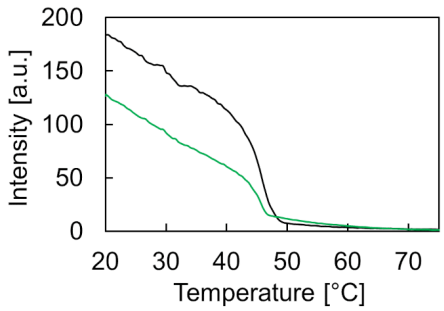

Duplex	T_{FL}(nucleation)[a] [°C]
ON5*ON9	49
ON5*ON16	47

Figure 98. Fluorescence-monitored annealing curves of **ON5*ON9** (black) and **ON5*ON16** (green), as well as a summary of nucleation temperatures T_{FL}(nucleation). Conditions: 1 µM each single strand, 10 mM sodium phosphate buffer pH 7.2, 0.1 mM spermine · 4 HCl, 30 vol% ethanol, $\lambda_{ex.}$: 335 nm, $\lambda_{em.}$: 490 nm, gradient: 0.5 °C/min. [a] Nucleation temperature, determined by fluorescence onset temperature in annealing curve.

Depicted in Figure 99 is an AFM image of self-assembled **ON5*ON16**. Mainly small vesicular nanostructures with heights of up to 30 nm were observed. Additionally, some vesicles appear to be collapsed, probably due to surface adsorption or drying effects during sample preparation. Compared to the respective AFM scans of *E*-TPE-modified duplex **ON5*ON9** (Figure 94), **ON5*ON16** self-assembles into considerably smaller and less defined aggregates. Therefore, the supramolecular arrays of **ON5*ON16** were not analyzed in more detail by other techniques.

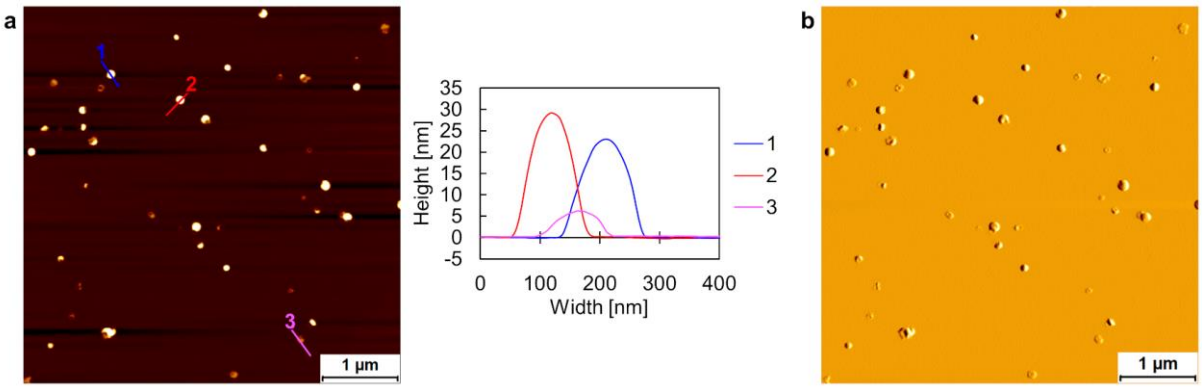

Figure 99. (**a**) AFM scan with corresponding cross sections and (**b**) deflection scan of assembled **ON5*ON16**. Conditions: 1 µM **ON5*ON16**, 10 mM sodium phosphate buffer pH 7.2, 0.1 mM spermine · 4 HCl, 30 vol% ethanol.

The effect of increasing the number of TPE sticky ends on the supramolecular assembly behavior was examined next. Accordingly, duplex **ON9*ON17** (Figure 83), exhibiting a total number of 12 TPE units per duplex, was investigated. This duplex would also be beneficial for potential light-harvesting applications, comparable to the experiments described previously in section 3.1.8. Duplex **ON9*ON17** would be promising because FRET efficiencies generally depend on the number of donor chromophores, spatially located within the FRET radius. Thus, as many as possible donor chromophores should be positioned within this FRET radius for an efficient light-harvesting performance. In the case of **ON9*ON17**, double the amount of TPEs are theoretically within the FRET radius, compared to duplex **ON1*ON2** (Figure 15).

Apart from increased absorbance and fluorescence intensities, analogous spectroscopic characteristics were determined for duplex **ON9*ON17** (Figure 100), as outlined in section 3.1.3 for the 3'-end modified duplex **ON1*ON2**.

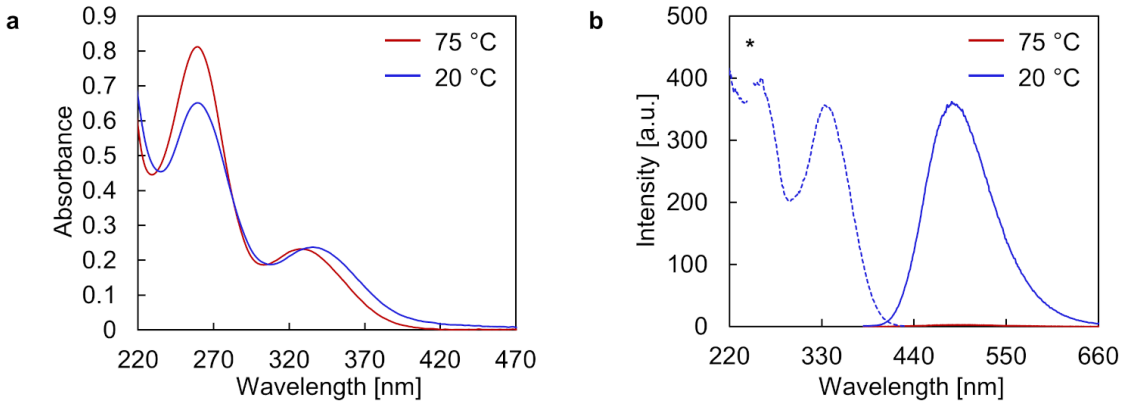

Figure 100. (**a**) UV-Vis absorption spectra and (**b**) fluorescence emission (solid line) and excitation (dotted line) spectra of **ON9*ON17**. Conditions: 1 µM **ON9*ON17**, 10 mM sodium phosphate buffer pH 7.2, 0.1 mM spermine · 4 HCl, 30 vol% ethanol, $\lambda_{ex.}$: 335 nm, $\lambda_{em.}$: 490 nm, * denotes second-order diffraction.

Compared to **ON5*ON9**, a noticeable difference was discovered for **ON9*ON17** in the nucleation temperature of the fluorescence-monitored annealing curve (Figure 101). While a T_{FL}(nucleation) of 49 °C was determined for **ON5*ON9**, the nucleation temperature was increased to 64 °C for **ON9*ON17**. This difference of 15 °C is ascribed to the increased strength of the hydrophobic TPE sticky end interactions. Importantly, complete disassembly at 75 °C into the individual single strands can still be assumed due to the very low fluorescence emission intensity at this temperature. Complete disassembly is presumed essential for the formation of well-defined nanostructures during the thermal assembly process.

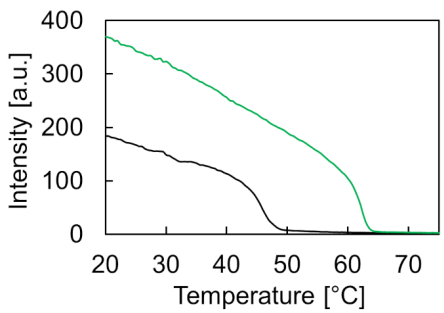

Duplex	T_{FL}(nucleation)[a] [°C]
ON5*ON9	49
ON9*ON17	64

Figure 101. Fluorescence-monitored annealing curves of **ON5*ON9** (black) and **ON9*ON17** (green), as well as a summary of nucleation temperatures T_{FL}(nucleation). Conditions: 1 µM each single strand, 10 mM sodium phosphate buffer pH 7.2, 0.1 mM spermine · 4 HCl, 30 vol% ethanol, $\lambda_{ex.}$: 335 nm, $\lambda_{em.}$: 490 nm, gradient: 0.5 °C/min. [a] Nucleation temperature, determined by fluorescence onset temperature in annealing curve.

However, undefined aggregates of self-assembled **ON9*ON17** were found by AFM, as depicted in Figure 102. It seems that the large aggregates with heights of up to 120 nm are composed of smaller assemblies (apparent heights of about 40 nm). It might be that due to the increased strength of the TPE sticky ends, π-stacking interactions of the TPEs lead to these ill-defined, agglomerated large nanostructures.

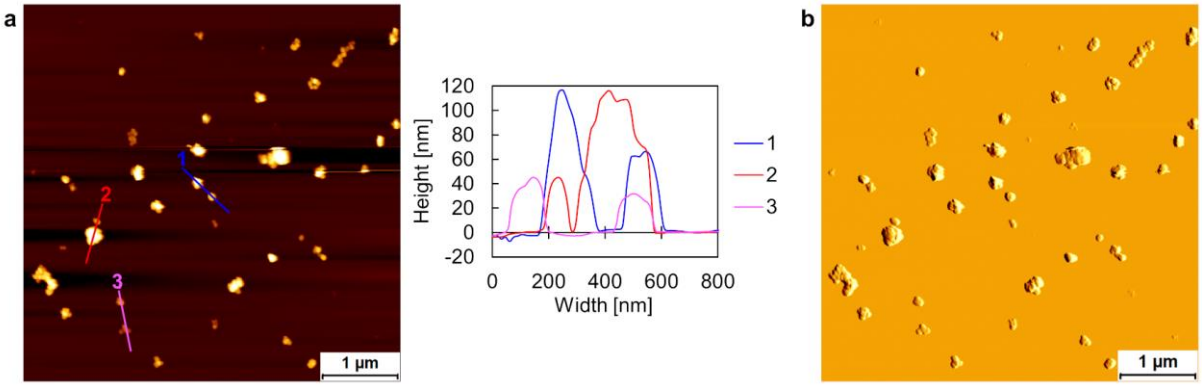

Figure 102. (**a**) AFM scan with corresponding cross sections and (**b**) deflection scan of assembled **ON9*ON17**. Conditions: 1 µM **ON9*ON17**, 10 mM sodium phosphate buffer pH 7.2, 0.1 mM spermine · 4 HCl, 30 vol% ethanol.

4.2 Conclusions and Outlook

In conclusion, the self-assembly of DNA duplexes, composed of 3'-/5'-end modified TPE-DNA conjugates hybridized to an unmodified complement, has been described. The oligonucleotide design has an impact on the overall supramolecular assembly behavior. This was demonstrated by two different series of oligonucleotides, where either the length of the TPE sticky ends or the DNA sequence length has been varied. The number of the TPE moieties in the overhangs was correlated to the strength of the sticky end interaction. The more TPE units were present in the overhangs, the stronger the hydrophobic sticky end interactions, which was reflected by an increase in the nucleation temperatures deduced from fluorescence-monitored annealing curves. At least two TPE residues per overhang were needed for the formation of vesicular assemblies, as evidenced by AFM experiments. In the second series, the DNA sequence length has been varied to investigate the effect of the spermine mediated interaction between the DNA duplexes. Opposite to the first series, DNA duplexes of varied lengths only showed a rather

insignificant influence on the nucleation temperatures and the morphology of the vesicular nanostructures. Thus, in contrast to a critical length of the TPE sticky ends, the DNA part offers more variability in the overall sequence design of 3’-/5’-end modified TPE-DNA conjugates.

As demonstrated for duplex **ON5*ON9**, the ethanol fraction in the aqueous medium affects the nucleation temperature, size range, and degree of agglomeration of the vesicles. Increasing the ethanol content from 20 vol% to 30 vol% influenced the above-mentioned aspects in a positive manner. Another vesicular architecture (type III) was discovered by cryo-EM imaging of self-assembled **ON5*ON9** under these conditions. This type III vesicular construct is assumed to be kind of a hybrid structure of the two types of architectures previously reported for the vesicles assembled from **ON1*ON2**. It features a core membrane (DNA alignment analogous to type II vesicles) and an outer membrane with a DNA arrangement that was found in type I vesicles.

Compared to the *E*-TPE-modified duplex **ON5*ON9**, the corresponding *Z*-TPE functionalized duplex **ON5*ON16** self-assembles into smaller and less defined vesicular nanostructures. But in general, no tremendous differences were found between the self-assembly behaviors of the two stereoisomers of TPE.

Supramolecular assembly of the DNA duplex exhibiting totally 12 TPE moieties (**ON9*ON17**, with three TPEs per overhang), showed a significant increase in the strength of the hydrophobic TPE interactions and resulted in undefined, agglomerated, large aggregates.

Overall, among all tested duplexes, the structures assembled under optimized conditions from duplex **ON5*ON9** showed the most promising results. This duplex is composed of a 20-mer DNA and three *E*-TPEs per sticky end on the single-stranded TPE-DNA conjugate. This 3’-/5’-end modified TPE-DNA conjugate, **ON9**, will therefore be employed in the subsequent chapter. Different terminal functionalities will be conjugated to the single-stranded DNA complement, and the self-assembly behavior of the resulting duplexes will be investigated.

4.3 Appendix – Chapter 4

4.3.1 Synthesis of Oligonucleotides

Adrian Gonzalez synthesized **ON10**–**ON12** and **ON14** (Adrian Gonzalez, *AIE-Active Supramolecular Assemblies of TPE-Modified DNA Conjugates*, Master's thesis, University of Bern, 2021).

E-TPE-DNA conjugates **ON9**–**ON12**, **ON14**, and **ON17**, as well as *Z*-TPE-DNA conjugate **ON16** were synthesized on an Applied Biosystems 394 DNA/RNA synthesizer applying a standard cyanoethyl phosphoramidite coupling protocol on a 1 μmol scale. A coupling time of 30 s was employed for the DNA nucleobases and 2 min for the TPE modifications. *E*- and *Z*-TPE phosphoramidites **6** and **7**, respectively, were dissolved in 1,2-DCE to create 0.1 M solutions (see section 3.3.1 for detailed synthetic procedures). The synthesis was started with *E*- or *Z*-TPE-modified solid-support **9** and **11**, respectively. After the solid-phase synthesis, the TPE-DNA conjugates were cleaved and deprotected by treatment with aqueous NH_4OH (28-30%) at 55 °C overnight. The supernatants were collected, and the solid-supports were washed three times with a solution of ethanol and Milli-Q H_2O (1:1, 3x1 mL), before the crude oligonucleotides were lyophilized.
The crude oligomers were purified by reversed-phase HPLC (Shimadzu LC-20AT, LiChrospher 100 RP-18, 5 μm, 250 x 4 mm) at 50 °C with a flow rate of 1 mL/min, λ: 330 nm. Solvent A: aqueous 2.1 mM triethylamine (TEA) / 25 mM 1,1,1,3,3,3-hexafluoropropan-2-ol (HFIP) pH 8; solvent B: acetonitrile; applying the gradients listed in Table 6. The purified TPE-DNA conjugates **ON9**, **ON12**, **ON14**, and **ON16**–**ON17** were dissolved in a 1:1 ethanol/Milli-Q H_2O mixture (1 mL). Oligonucleotides **ON10** and **ON11** were dissolved in Milli-Q H_2O (1 mL). The absorbance was measured at 260 nm to determine the concentration of the stock solutions and the yields of the oligomers. The calculation was according to the Beer-Lambert law. The following molar absorptivities (at 260 nm) in [L/mol·cm] were used for the DNA nucleobases: ε_A: 15'300; ε_T: 9'000; ε_G: 11'700; ε_C: 7'400. A molar absorptivity of $\varepsilon_{E\text{-TPE}}$: 35'975 was used for *E*-TPE and $\varepsilon_{Z\text{-TPE}}$: 40'788 was used for *Z*-TPE. The MS results of **ON9**–**ON12**, **ON14**, and **ON16**–**ON17** are listed in Table 6, the corresponding HPLC traces are displayed in Figure 103, and the MS spectra are presented in Figure 104–Figure 117.

Table 6. TPE-DNA oligonucleotide sequences of **ON9**–**ON12**, **ON14**, and **ON16**–**ON17**, HPLC gradients, calculated and found masses by NSI-MS, and yields.

Oligomer	Sequence (5'→3')	HPLC gradient B [%] (t_R [min])	Calc. mass	Found mass	Yield [%]
ON9	(***E*-TPE**)$_3$-CTT CCT TGC ATC GGA CCT TG-(***E*-TPE**)$_3$	5 (0), 50 (24)	9215.9945	9216.0492	25
ON10	(***E*-TPE**)$_2$-CTT CCT TGC ATC GGA CCT TG-(***E*-TPE**)$_2$	5 (0), 40 (24)	8155.6448	8155.6722	9
ON11	***E*-TPE**-CTT CCT TGC ATC GGA CCT TG-***E*-TPE**	5 (0), 40 (24)	7095.2951	7095.3432	10
ON12	(***E*-TPE**)$_3$-CTT CCT TGG ACC TTG-(***E*-TPE**)$_3$	5 (0), 50 (24)	7691.0132	7690.7916	21
ON14	(***E*-TPE**)$_3$-CTT CCT TGC ACT GAA TCG GAC CTT G-(***E*-TPE**)$_3$	5 (0), 50 (24)	10765.0008	10765.2660	7
ON16	(***Z*-TPE**)$_3$-CTT CCT TGC ATC GGA CCT TG-(***Z*-TPE**)$_3$	10 (0), 60 (24)	9215.9945	9216.0194	28
ON17	(***E*-TPE**)$_3$-CAA GGT CCG ATG CAA GGA AG-(***E*-TPE**)$_3$	5 (0), 50 (24)	9381.1347	9381.0924	13

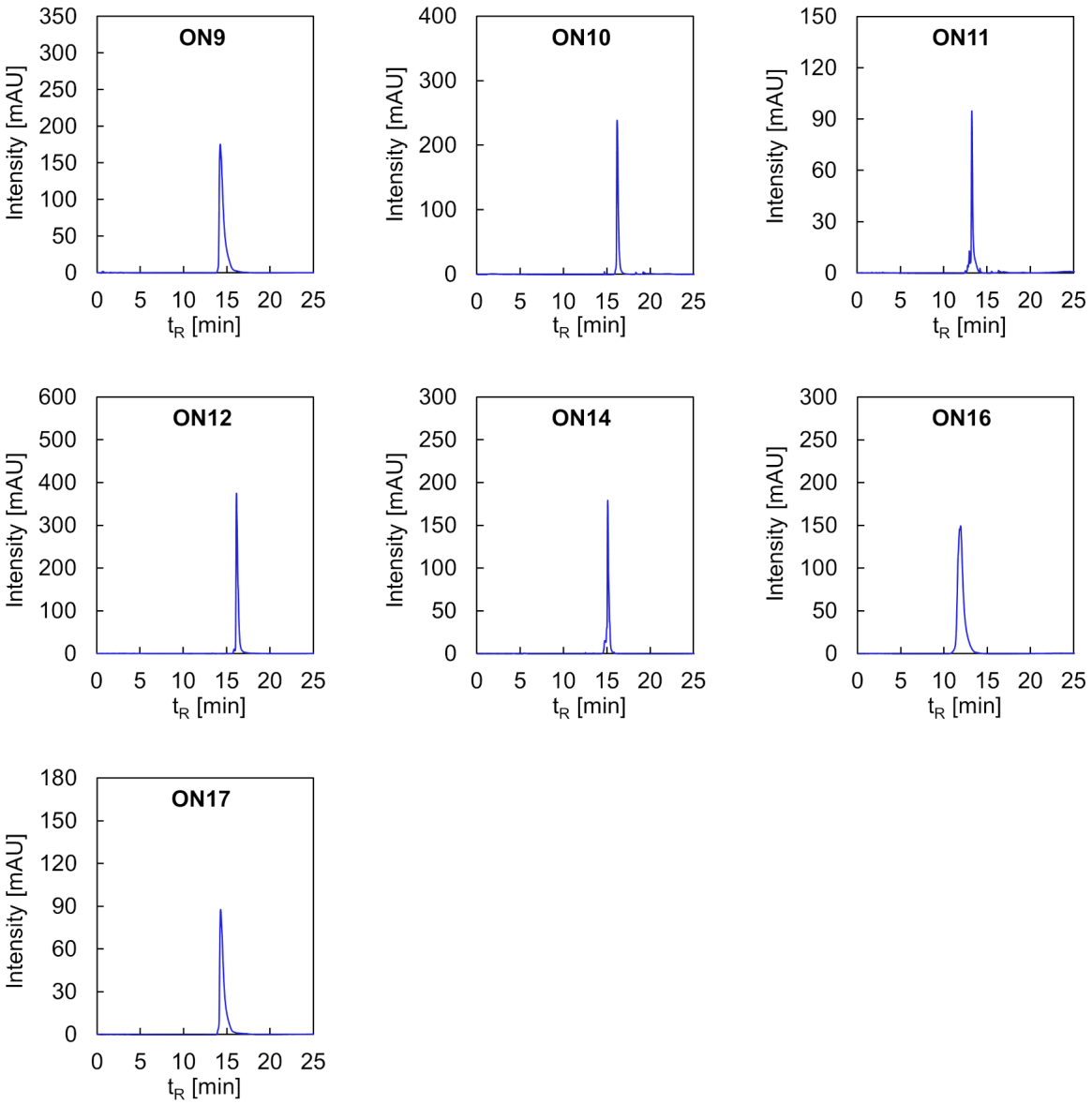

Figure 103. HPLC traces of TPE-DNA conjugates **ON9**–**ON12**, **ON14**, and **ON16**–**ON17**.

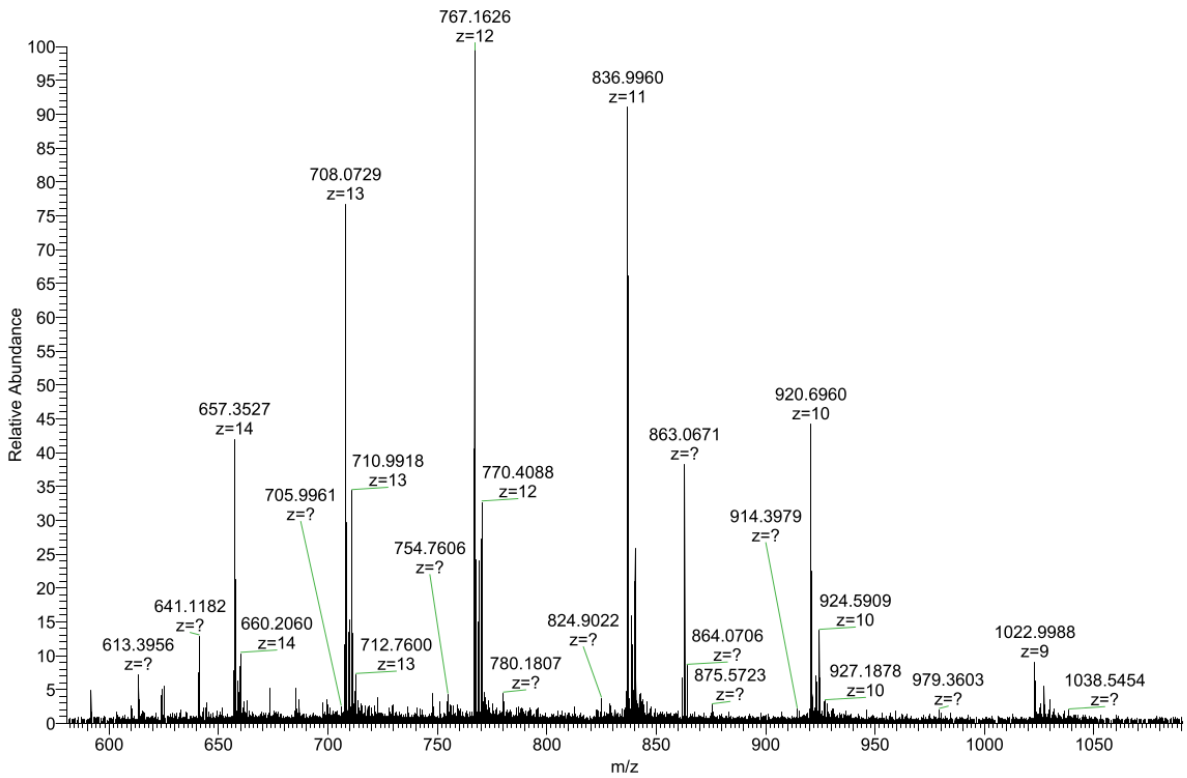

Figure 104. MS spectrum of **ON9**.

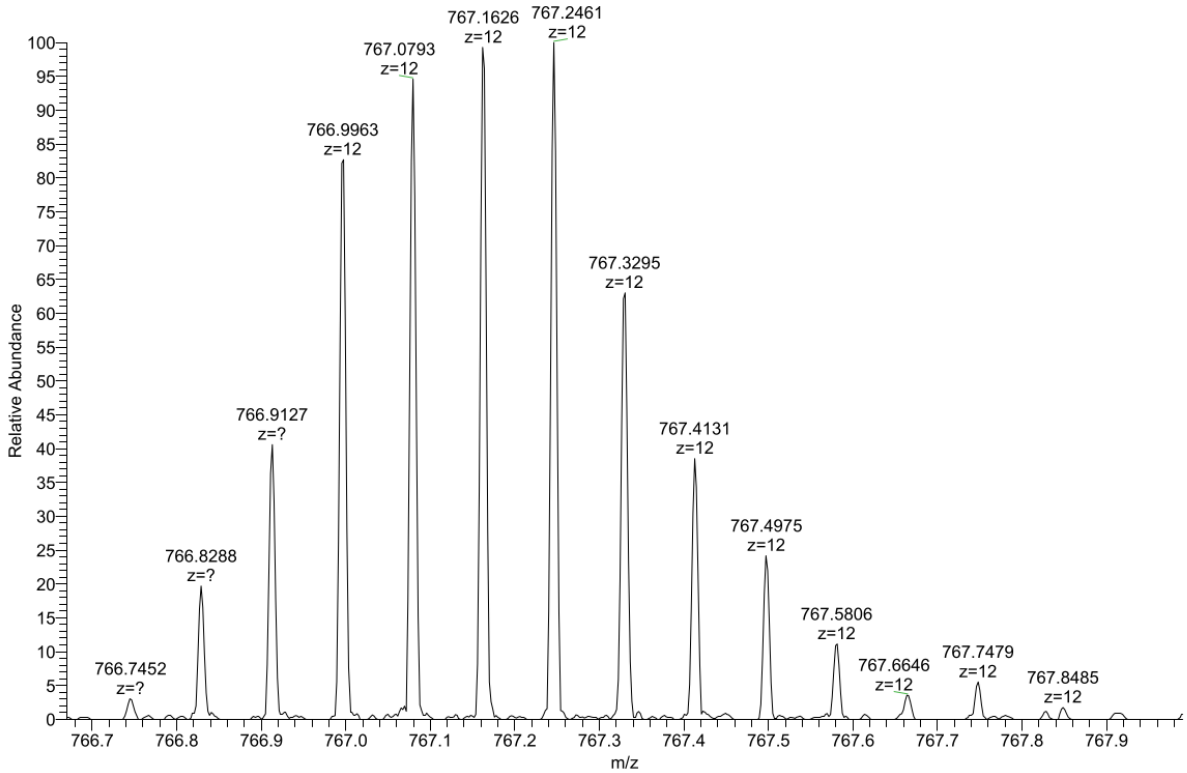

Figure 105. MS spectrum (zoom) of **ON9**.

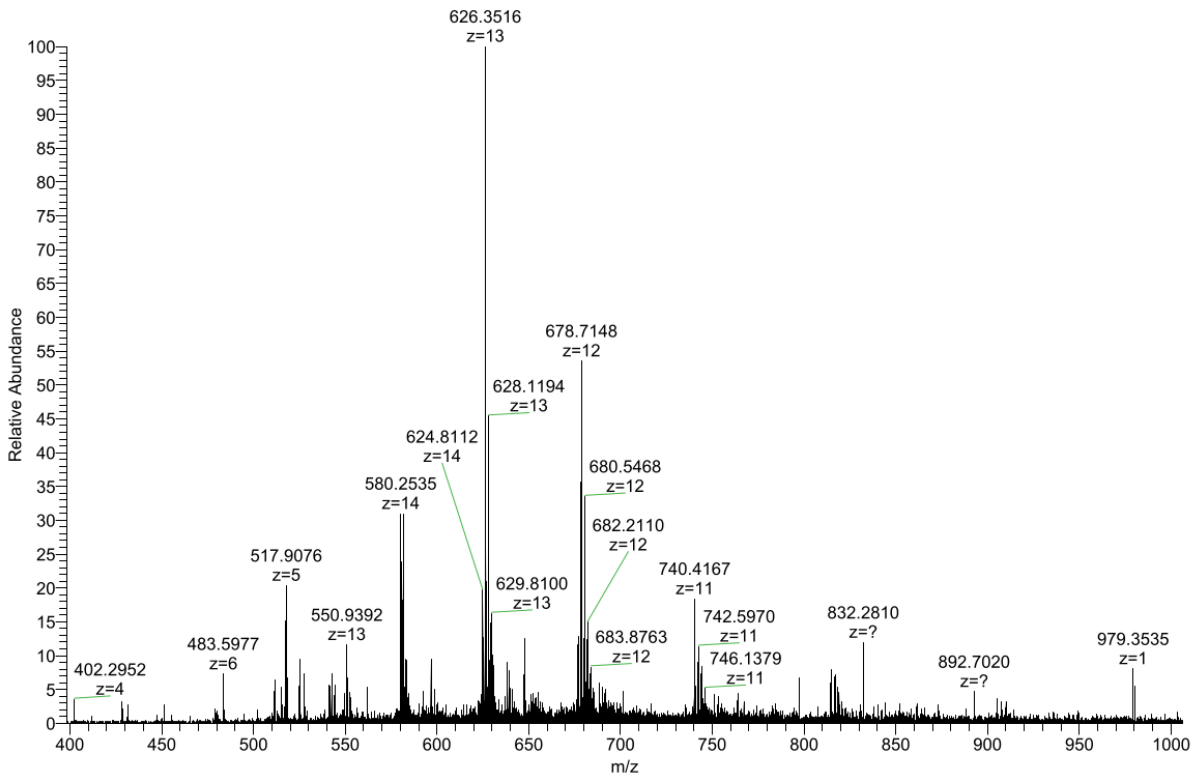

Figure 106. MS spectrum of **ON10**.

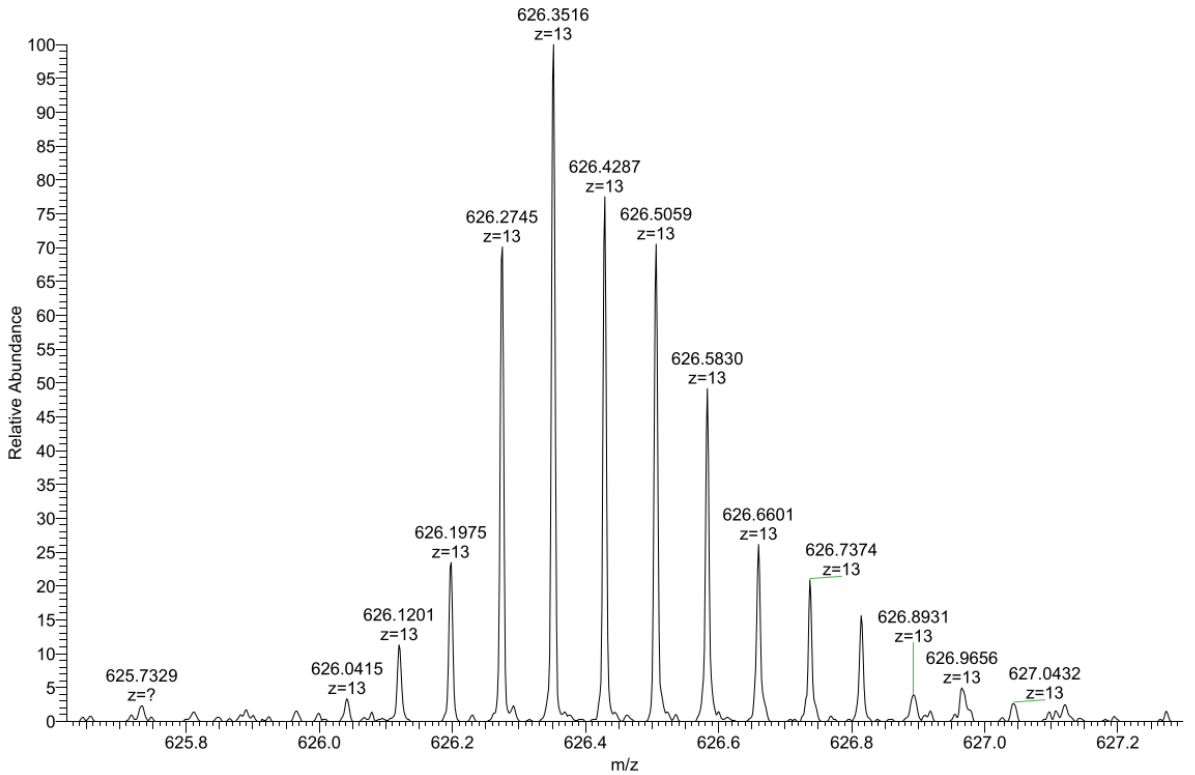

Figure 107. MS spectrum (zoom) of **ON10**.

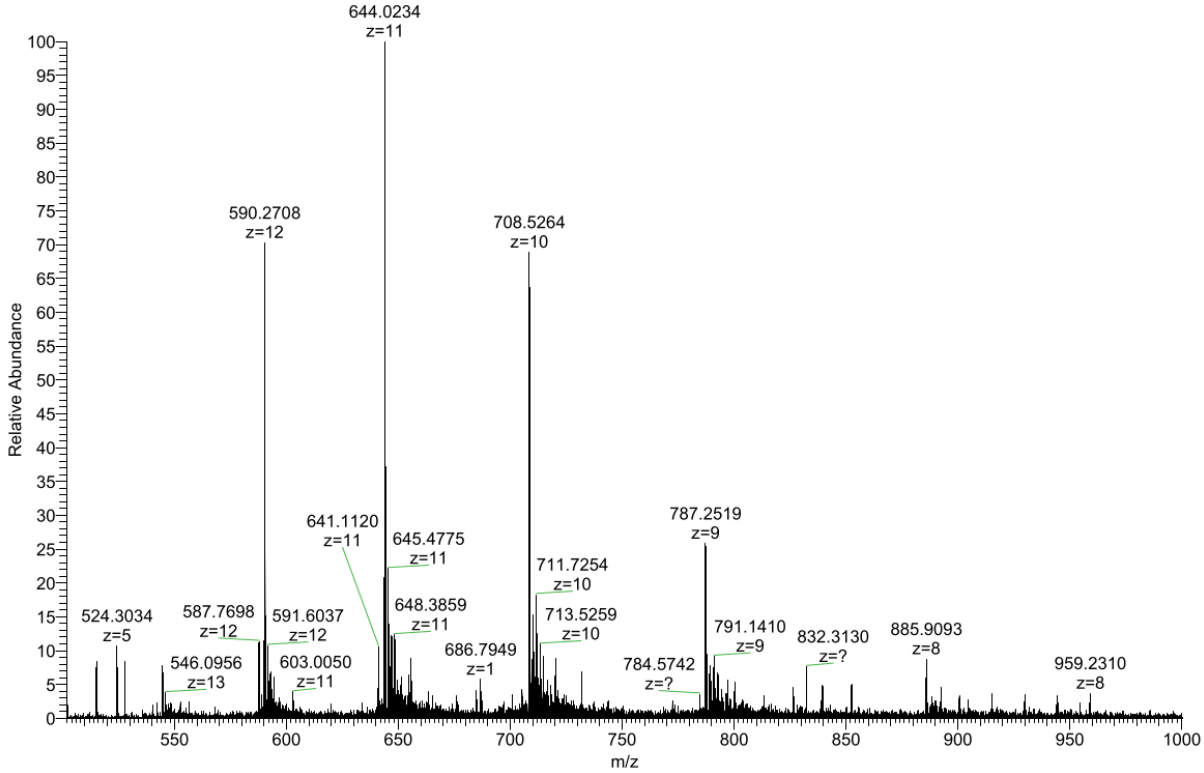

Figure 108. MS spectrum of **ON11**.

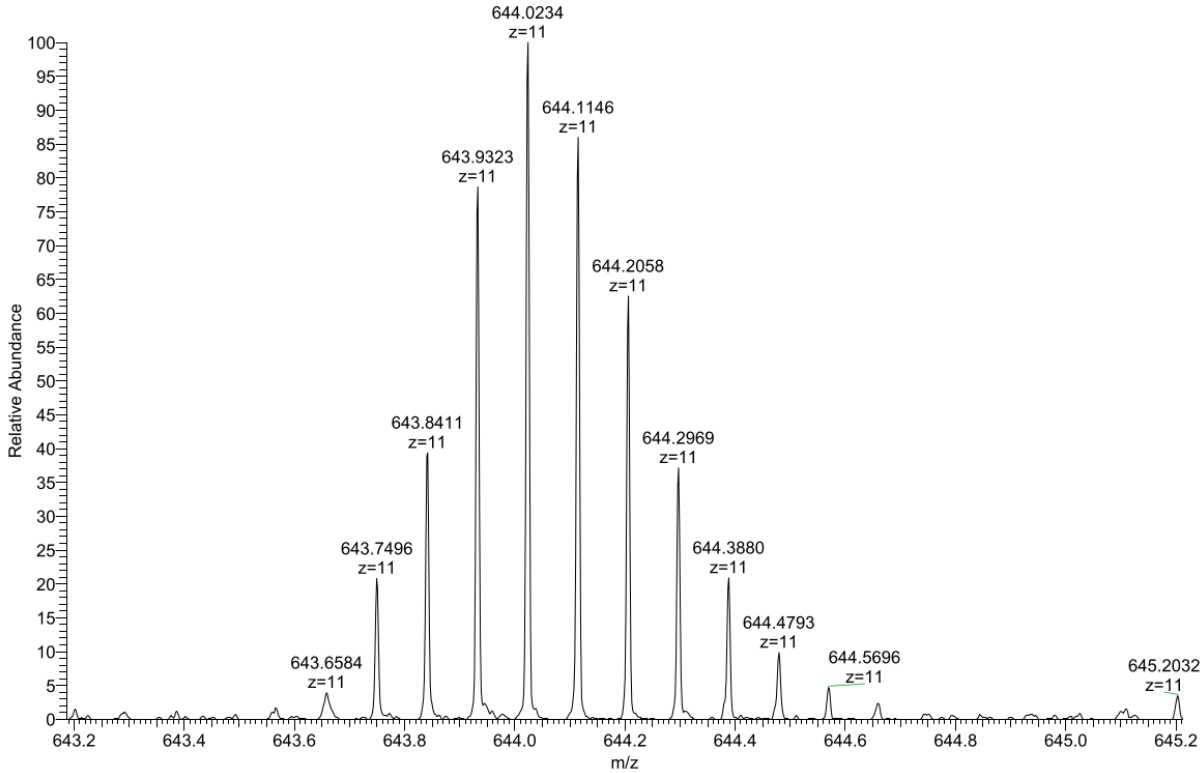

Figure 109. MS spectrum (zoom) of **ON11**.

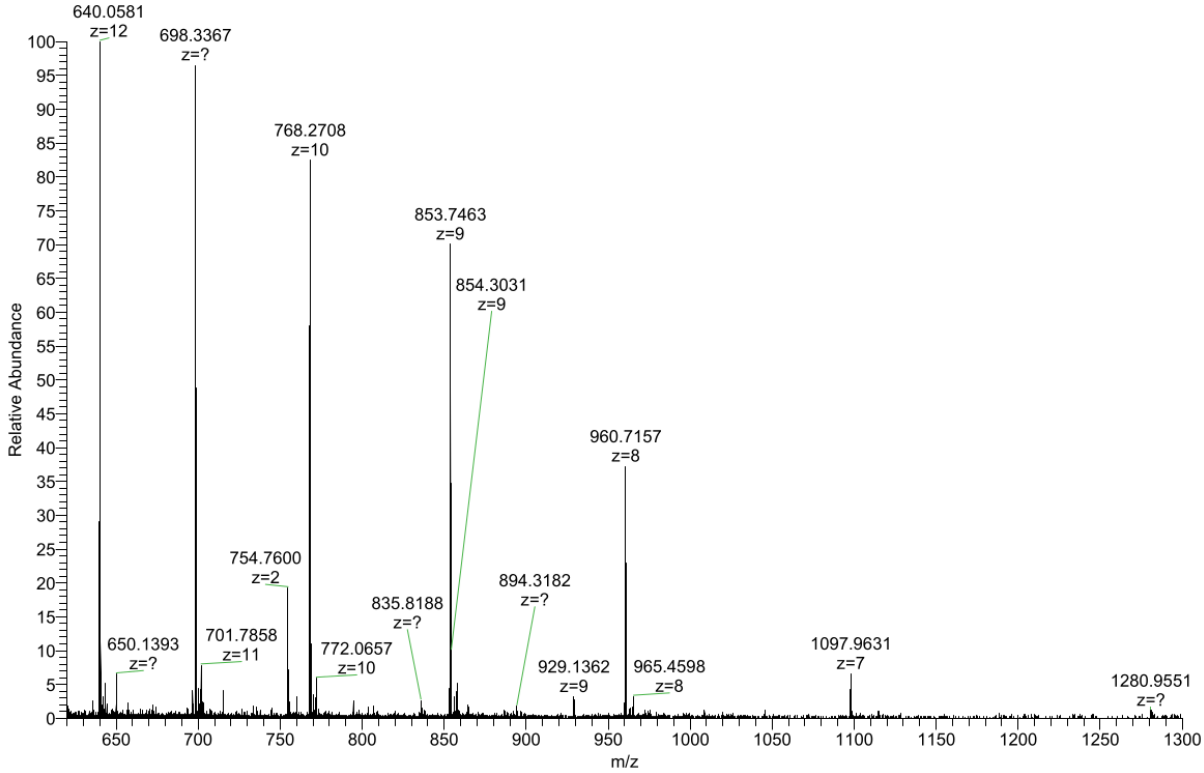

Figure 110. MS spectrum of **ON12**.

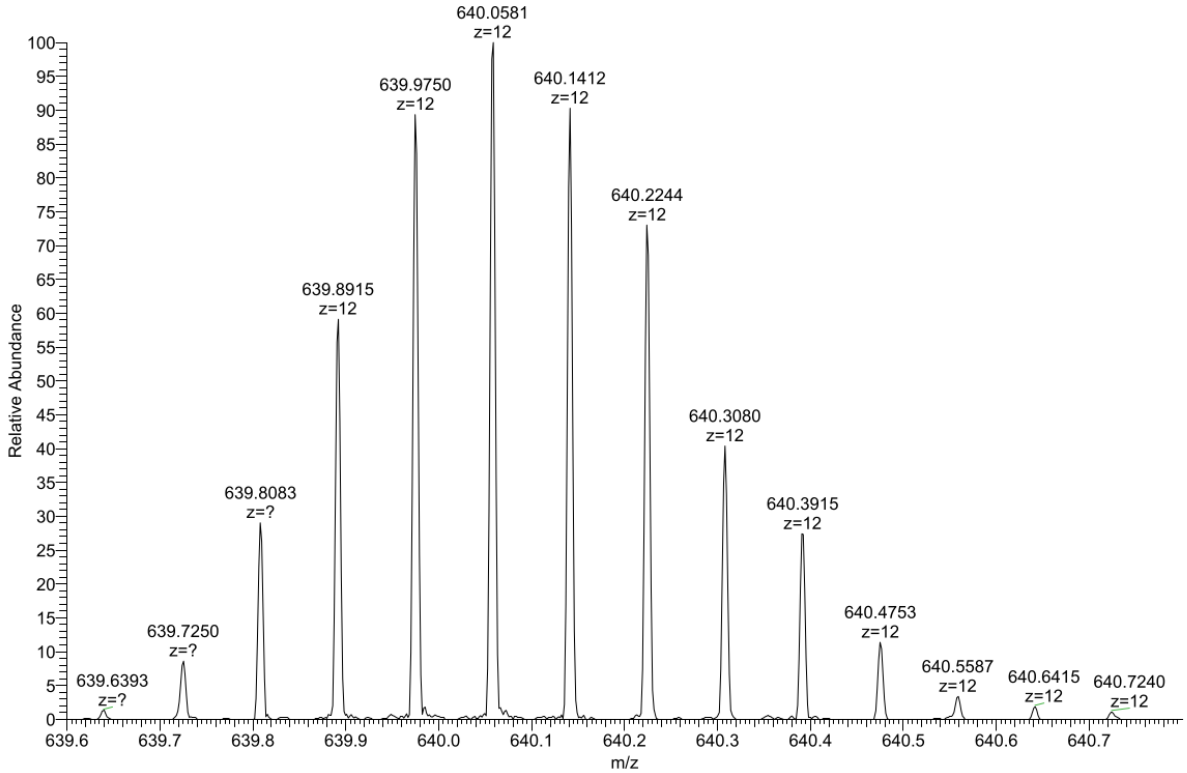

Figure 111. MS spectrum (zoom) of **ON12**.

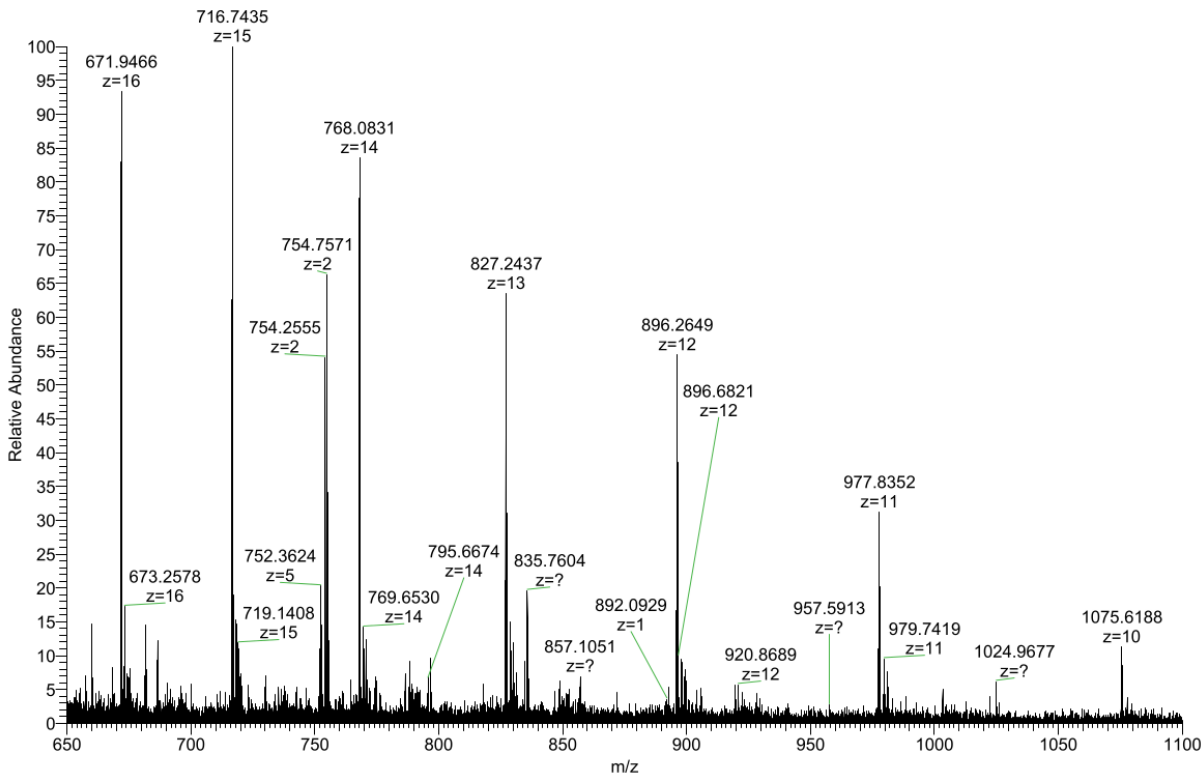

Figure 112. MS spectrum of **ON14**.

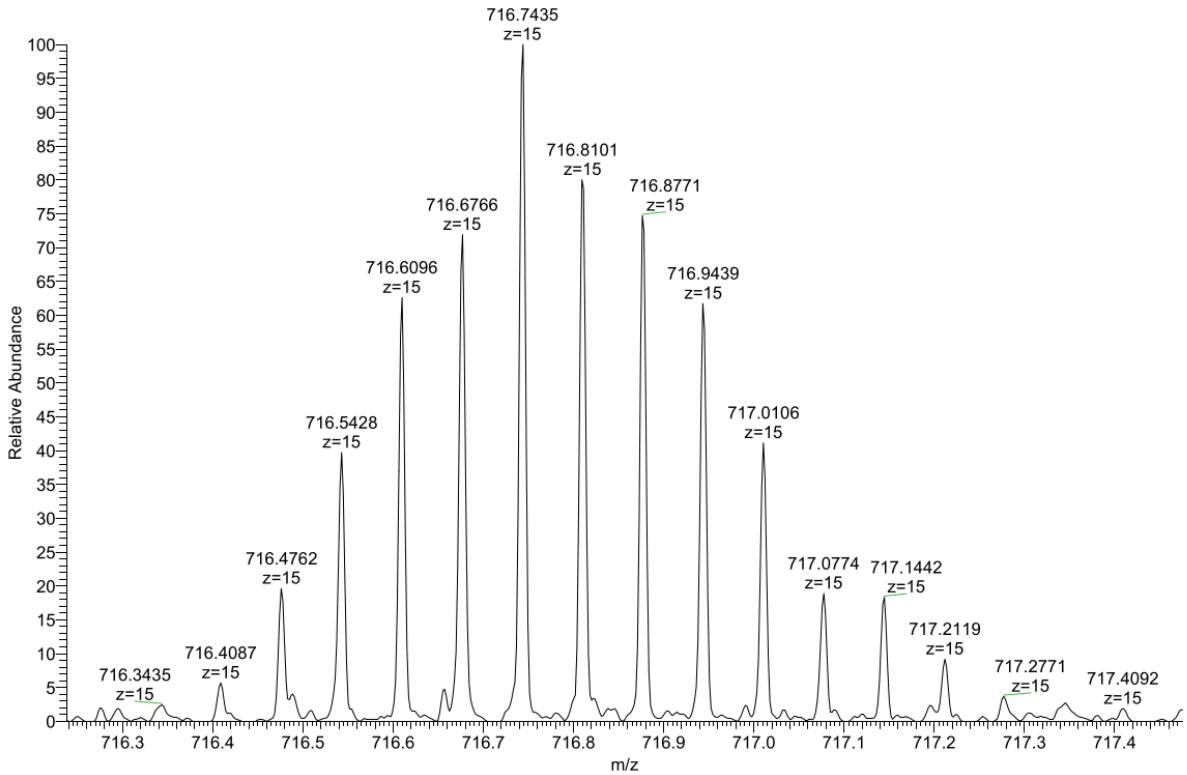

Figure 113. MS spectrum (zoom) of **ON14**.

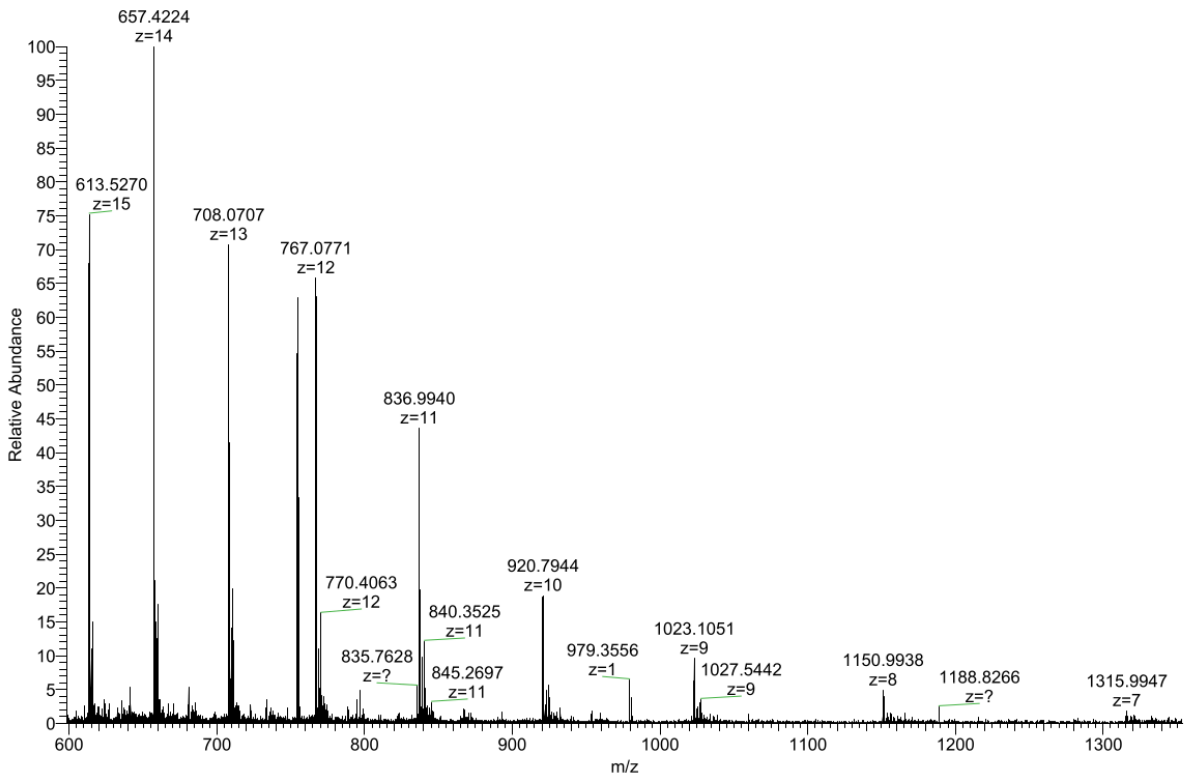

Figure 114. MS spectrum of **ON16**.

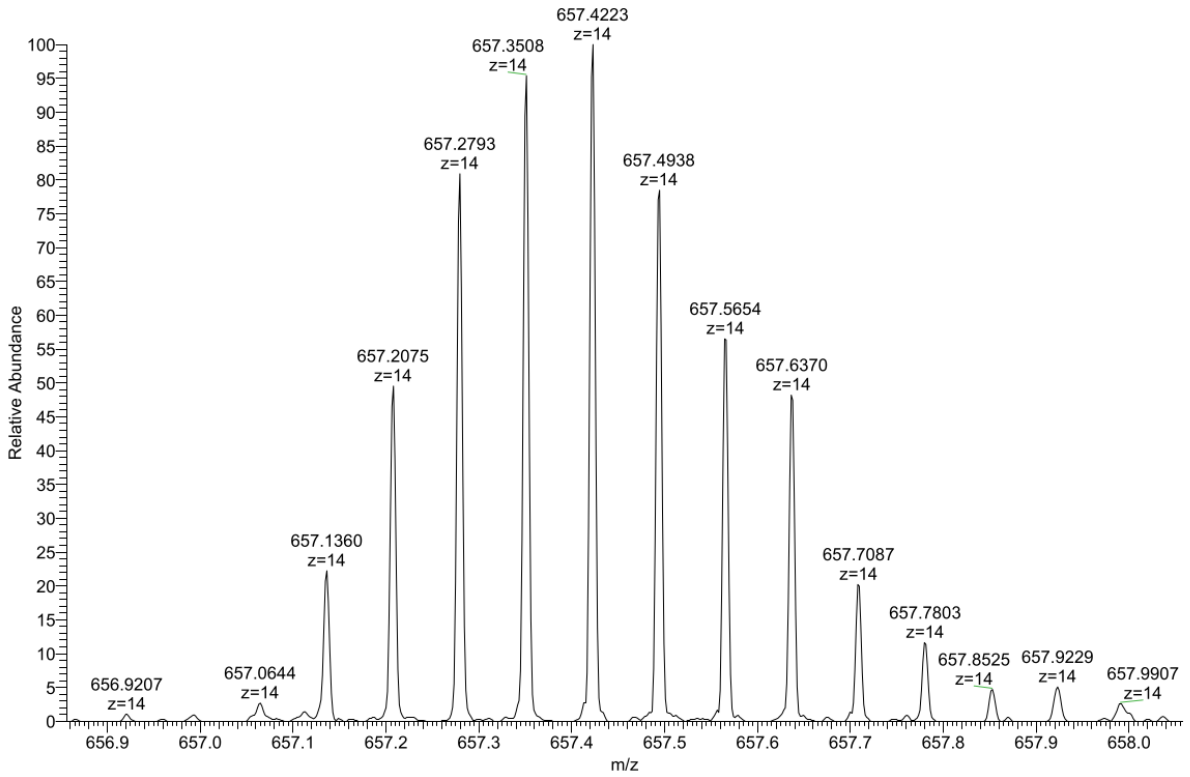

Figure 115. MS spectrum (zoom) of **ON16**.

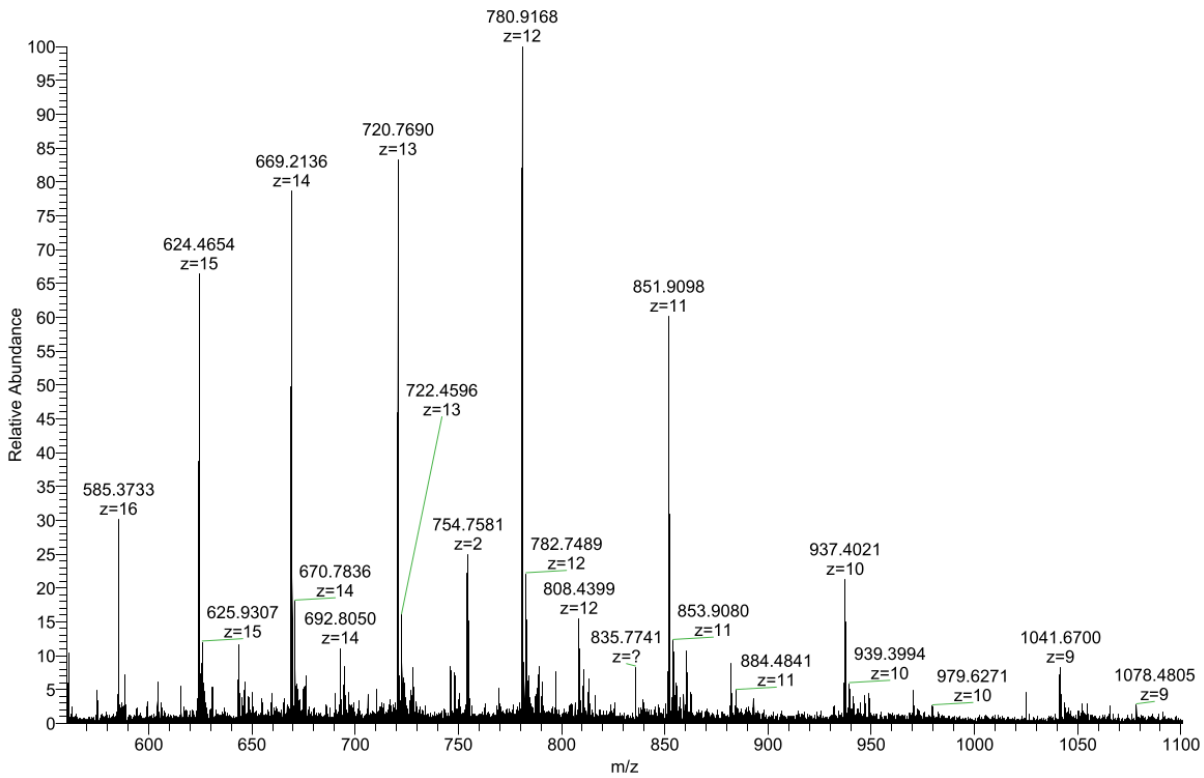

Figure 116. MS spectrum of **ON17**.

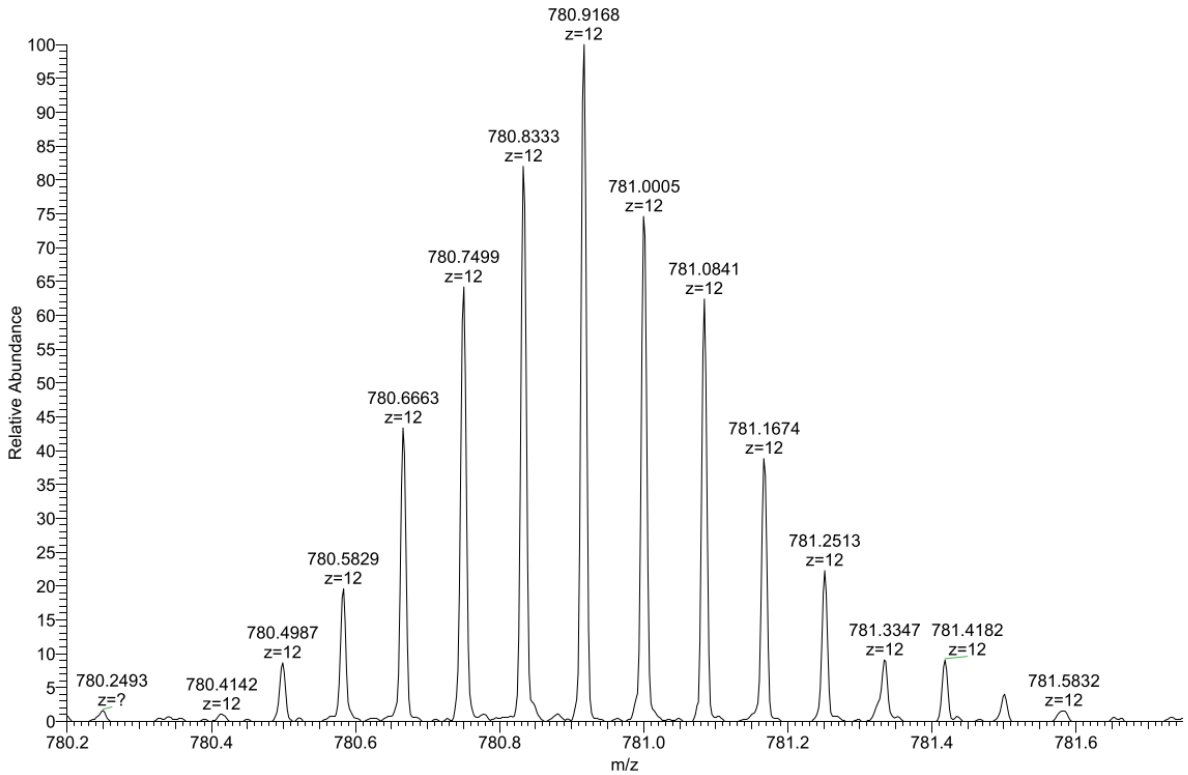

Figure 117. MS spectrum (zoom) of **ON17**.

4.3.2 Spectroscopic and Microscopic Measurements

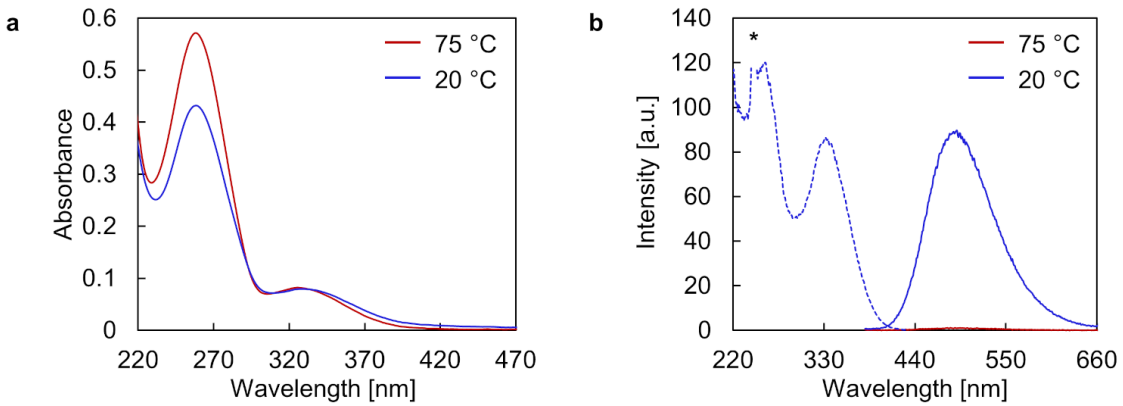

Figure 118. (**a**) UV-Vis absorption spectra and (**b**) fluorescence emission (solid line) and excitation (dotted line) spectra of **ON5*ON10**. Conditions: 1 µM **ON5*ON10**, 10 mM sodium phosphate buffer pH 7.2, 0.1 mM spermine · 4 HCl, 20 vol% ethanol, $\lambda_{ex.}$: 335 nm, $\lambda_{em.}$: 490 nm, * denotes second-order diffraction.

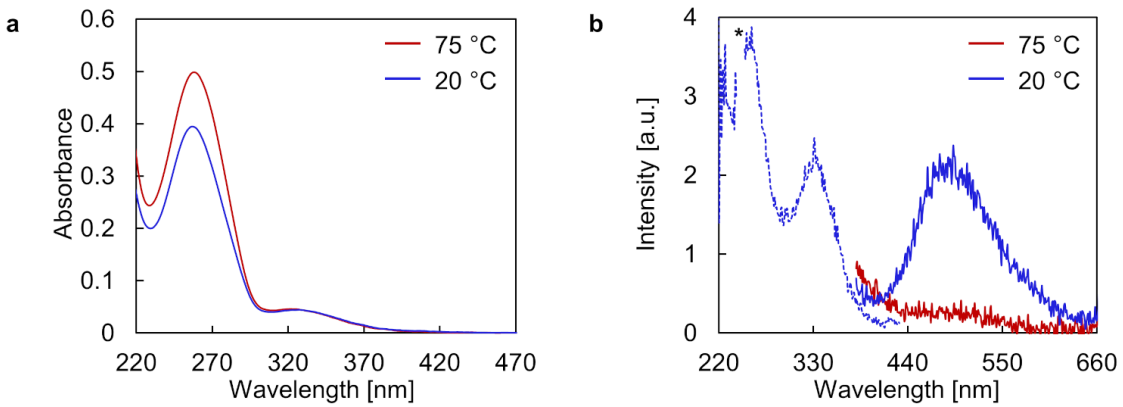

Figure 119. (**a**) UV-Vis absorption spectra and (**b**) fluorescence emission (solid line) and excitation (dotted line) spectra of **ON5*ON11**. Conditions: 1 µM **ON5*ON11**, 10 mM sodium phosphate buffer pH 7.2, 0.1 mM spermine · 4 HCl, 20 vol% ethanol, $\lambda_{ex.}$: 335 nm, $\lambda_{em.}$: 490 nm, * denotes second-order diffraction.

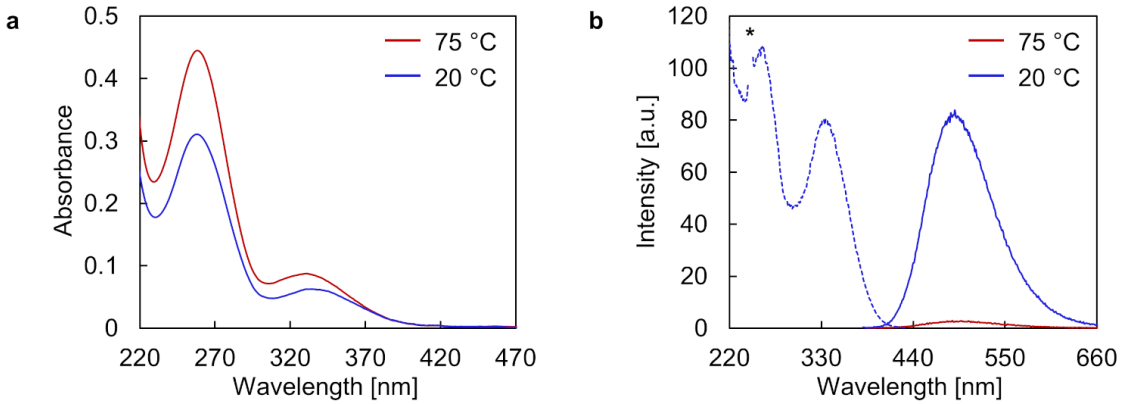

Figure 120. (**a**) UV-Vis absorption spectra and (**b**) fluorescence emission (solid line) and excitation (dotted line) spectra of **ON12*ON13**. Conditions: 1 µM **ON12*ON13**, 10 mM sodium phosphate buffer pH 7.2, 0.1 mM spermine · 4 HCl, 20 vol% ethanol, $\lambda_{ex.}$: 335 nm, $\lambda_{em.}$: 490 nm, * denotes second-order diffraction.

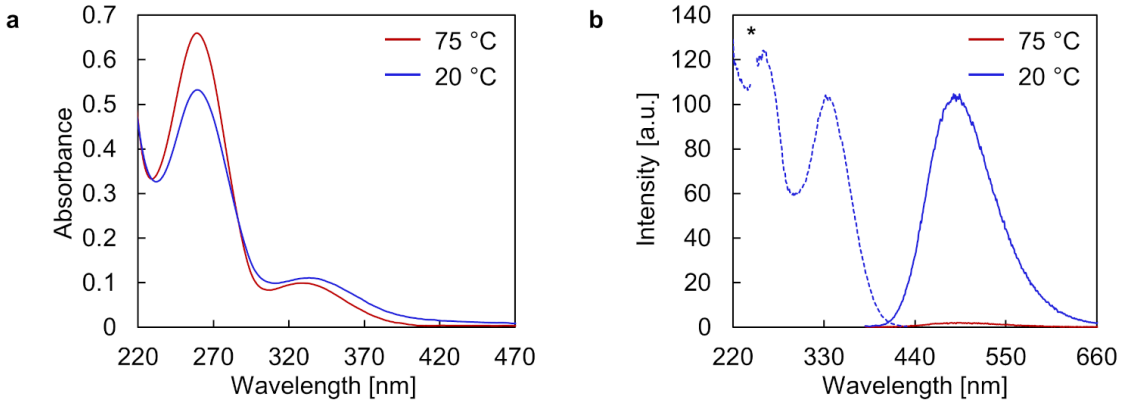

Figure 121. (**a**) UV-Vis absorption spectra and (**b**) fluorescence emission (solid line) and excitation (dotted line) spectra of **ON14*ON15**. Conditions: 1 µM **ON14*ON15**, 10 mM sodium phosphate buffer pH 7.2, 0.1 mM spermine · 4 HCl, 20 vol% ethanol, $\lambda_{ex.}$: 335 nm, $\lambda_{em.}$: 490 nm, * denotes second-order diffraction.

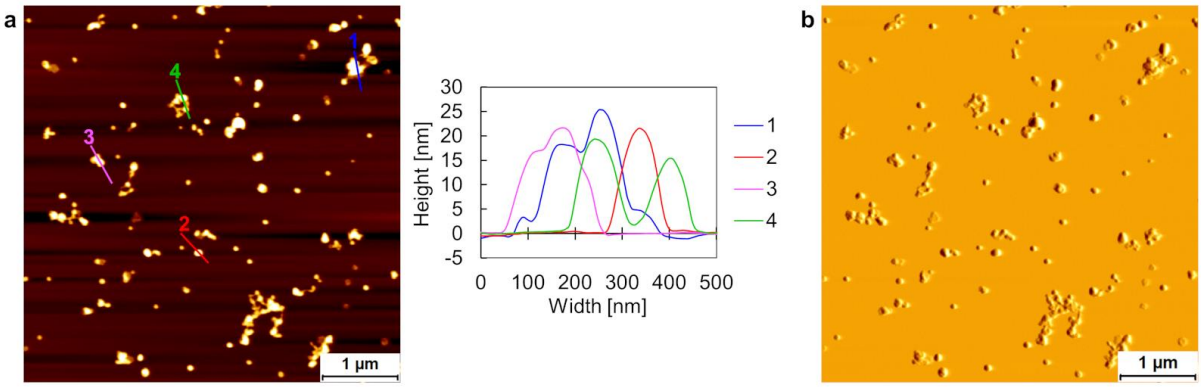

Figure 122. (**a**) AFM overview scan with corresponding cross sections and (**b**) deflection scan of assembled **ON5*ON9**. Conditions: 1 µM **ON5*ON9**, 10 mM sodium phosphate buffer pH 7.2, 0.1 mM spermine · 4 HCl, 20 vol% ethanol.

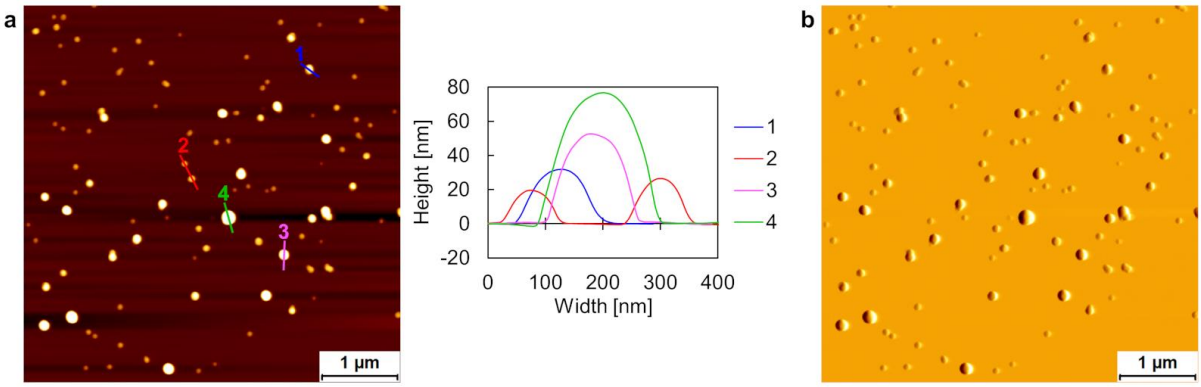

Figure 123. (**a**) AFM overview scan with corresponding cross sections and (**b**) deflection scan of assembled **ON5*ON10**. Conditions: 1 µM **ON5*ON10**, 10 mM sodium phosphate buffer pH 7.2, 0.1 mM spermine · 4 HCl, 20 vol% ethanol.

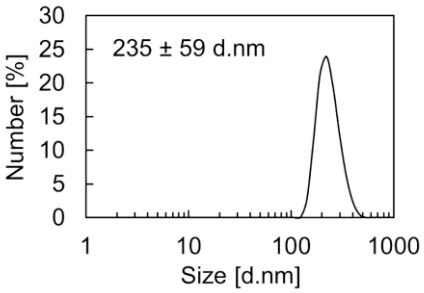

Figure 124. DLS data of vesicles assembled from **ON5*ON10**. Conditions: 1 µM **ON5*ON10**, 10 mM sodium phosphate buffer pH 7.2, 0.1 mM spermine · 4 HCl, 20 vol% ethanol.

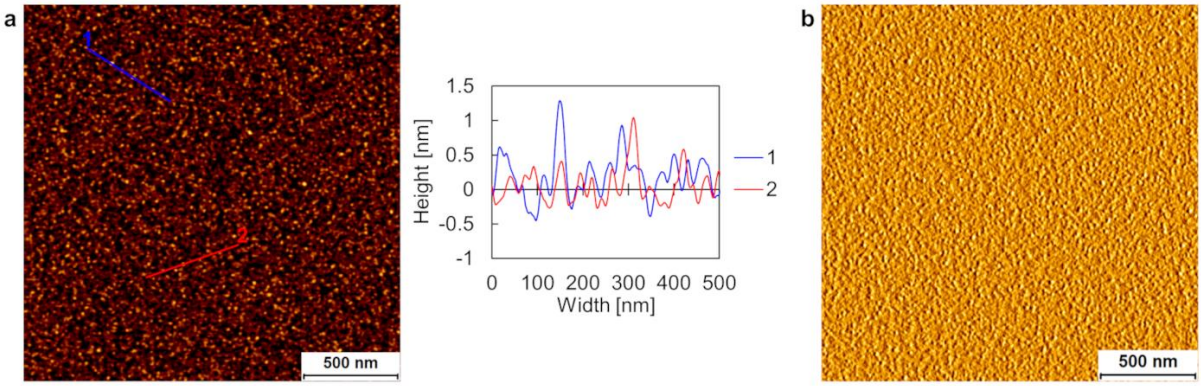

Figure 125. (**a**) AFM overview scan with corresponding cross sections and (**b**) deflection scan of assembled **ON5*ON11**. Conditions: 1 µM **ON5*ON11**, 10 mM sodium phosphate buffer pH 7.2, 0.1 mM spermine · 4 HCl, 20 vol% ethanol.

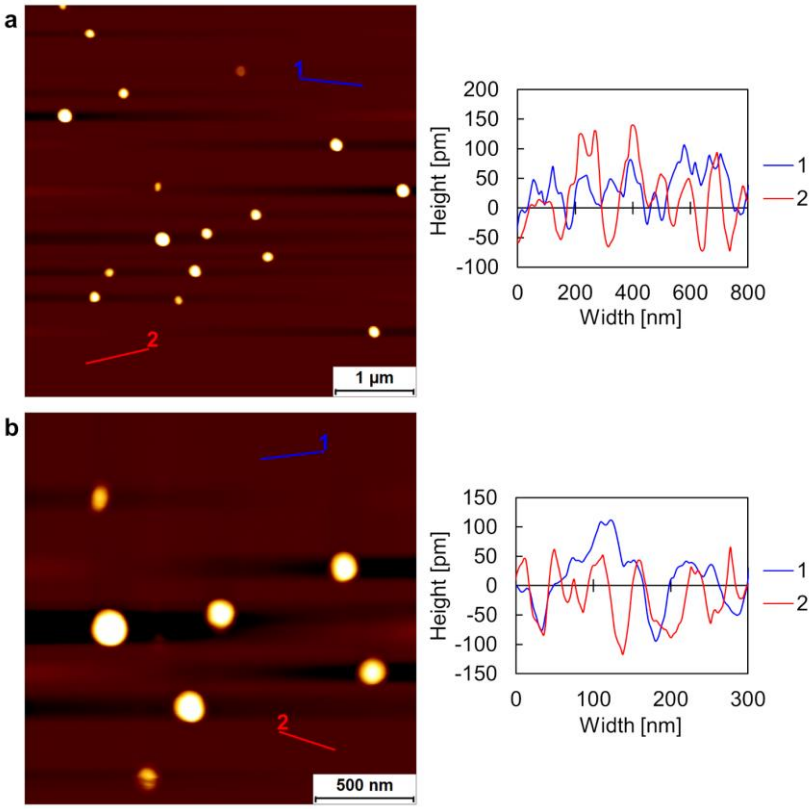

Figure 126. (**a**) AFM overview scan and (**b**) zoom image with corresponding cross sections measured apart from nanostructures, illustrating the mica surface roughness of the sample with self-assembled **ON5*ON9**. Conditions: 1 µM **ON5*ON9**, 10 mM sodium phosphate buffer pH 7.2, 0.1 mM spermine · 4 HCl, 30 vol% ethanol.

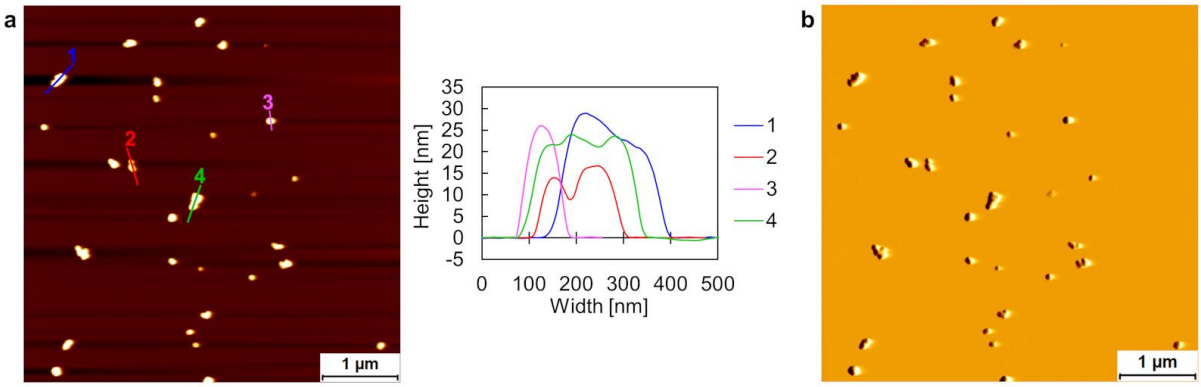

Figure 127. (**a**) AFM overview scan with corresponding cross sections and (**b**) deflection scan of assembled **ON12*ON13**. Conditions: 1 µM **ON12*ON13**, 10 mM sodium phosphate buffer pH 7.2, 0.1 mM spermine · 4 HCl, 20 vol% ethanol.

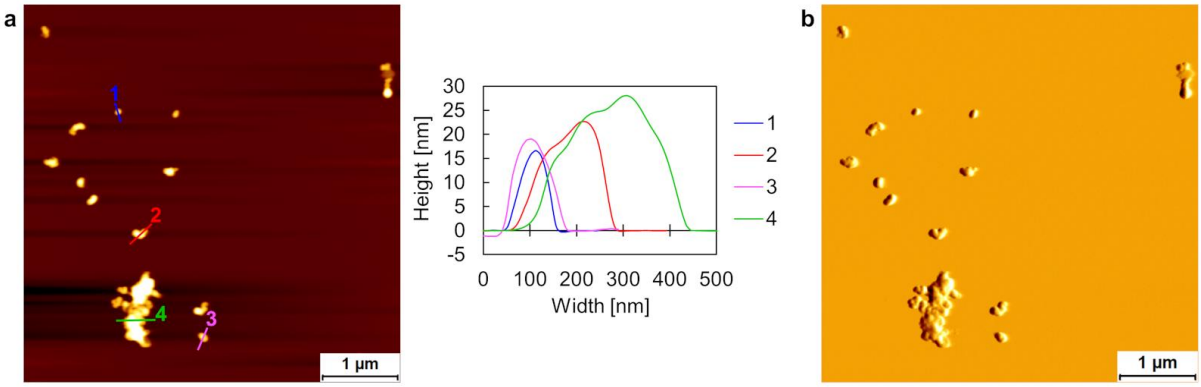

Figure 128. (**a**) AFM overview scan with corresponding cross sections and (**b**) deflection scan of assembled **ON14*ON15**. Conditions: 1 µM **ON14*ON15**, 10 mM sodium phosphate buffer pH 7.2, 0.1 mM spermine · 4 HCl, 20 vol% ethanol.

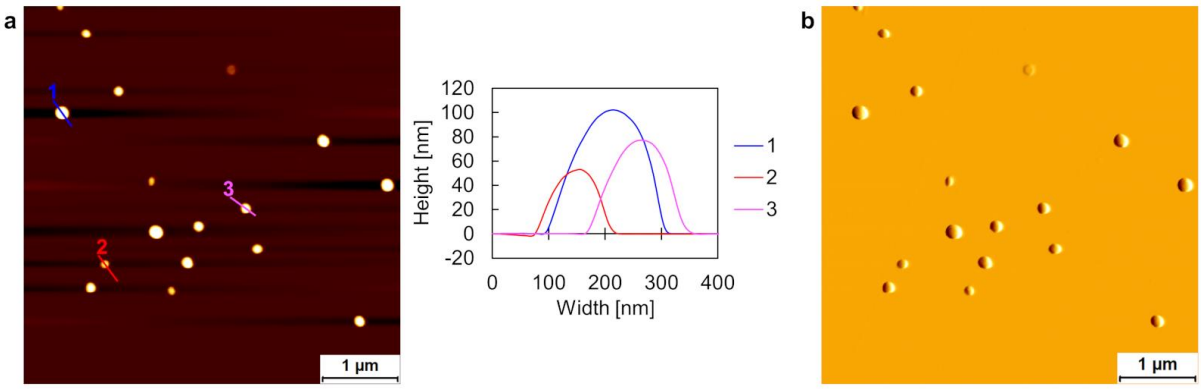

Figure 129. (**a**) AFM overview scan with corresponding cross sections and (**b**) deflection scan of assembled **ON5*ON9**. Conditions: 1 µM **ON5*ON9**, 10 mM sodium phosphate buffer pH 7.2, 0.1 mM spermine · 4 HCl, 30 vol% ethanol.

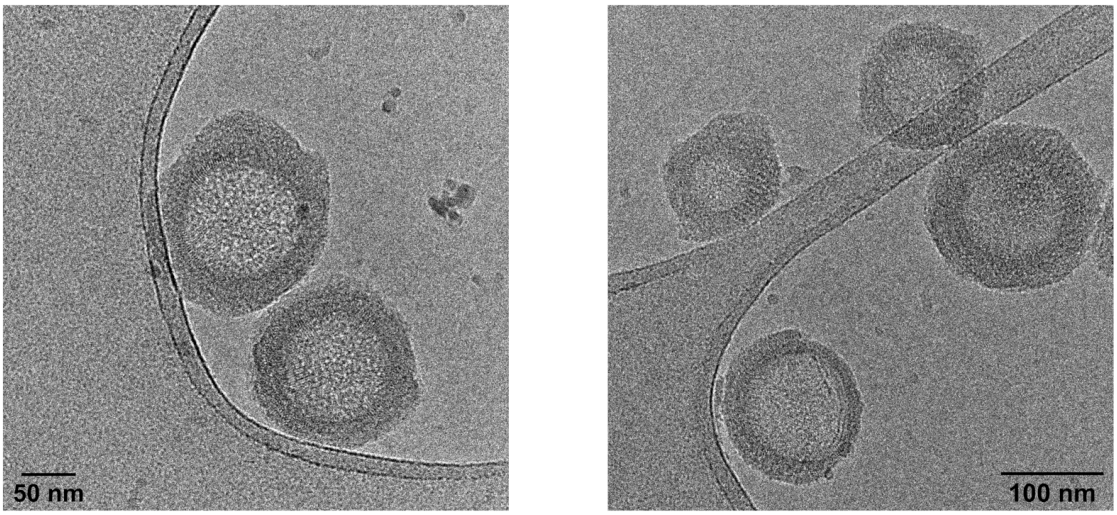

Figure 130. Additional cryo-EM images of type III vesicles of **ON5*ON9**. Conditions: 1 µM **ON5*ON9**, 10 mM sodium phosphate buffer pH 7.2, 0.1 mM spermine · 4 HCl, 30 vol% ethanol.

4.3.3 Cryo-EM Distance Measurements

Table 7. Summary of distance measurements. The reported distances are mean values with the corresponding standard deviation, along with the number of measurements in brackets.

Vesicular type	DNA length corresponding to type I vesicles	DNA length corresponding to type II vesicles	DNA width corresponding to type II vesicles
Type III	8.0 ± 0.5 nm (*n* = 39)	10.5 ± 0.6 nm (*n* = 37)	2.4 ± 0.5 nm (*n* = 40)

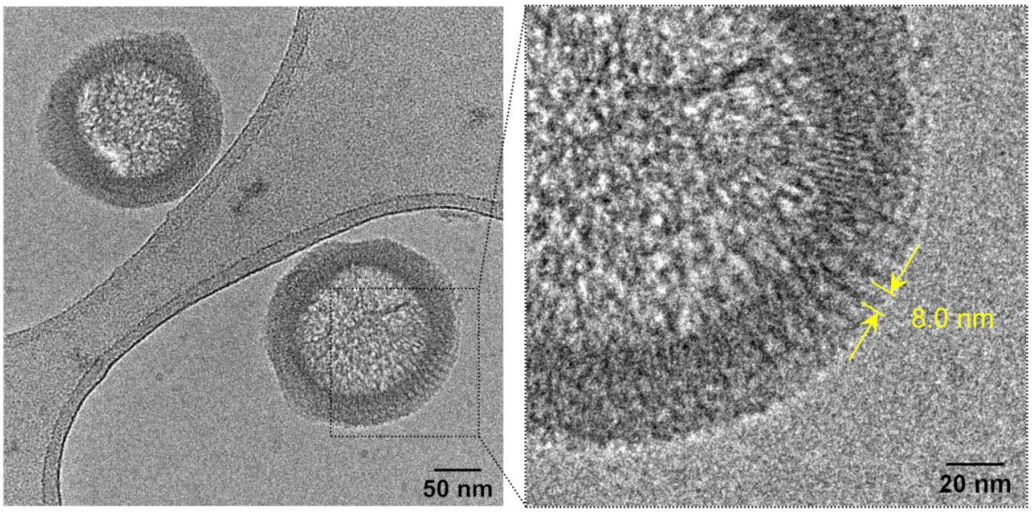

Figure 131. Representative DNA length measurement in a type III vesicle (corresponding to the DNA length of a type I vesicle) of self-assembled **ON5*ON9**. Conditions: 1 µM **ON5*ON9**, 10 mM sodium phosphate buffer pH 7.2, 0.1 mM spermine · 4 HCl, 30 vol% ethanol.

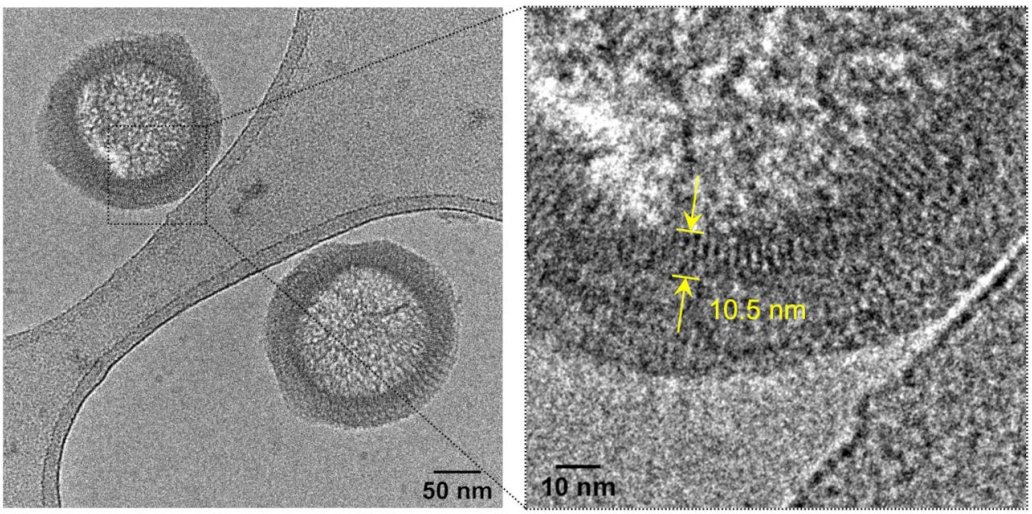

Figure 132. Representative DNA length measurement in a type III vesicle (corresponding to the DNA length of a type II vesicle) of self-assembled **ON5*ON9**. Conditions: 1 µM **ON5*ON9**, 10 mM sodium phosphate buffer pH 7.2, 0.1 mM spermine · 4 HCl, 30 vol% ethanol.

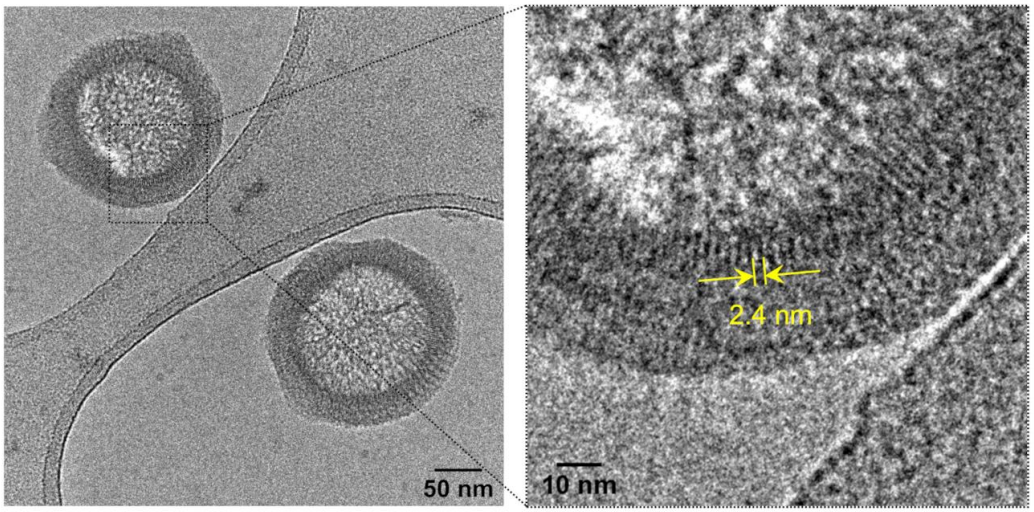

Figure 133. Representative DNA width measurement in a type III vesicle (corresponding to the DNA width of a type II vesicle) of self-assembled **ON5*ON9**. Conditions: 1 µM **ON5*ON9**, 10 mM sodium phosphate buffer pH 7.2, 0.1 mM spermine · 4 HCl, 30 vol% ethanol.

5 DNA Architectonics

The effect of a terminal functionality, present on the complementary DNA single strand hybridized to a 3'-/5'-end TPE-modified DNA single strand, on the resulting supramolecular morphology will be studied. The terminal functional group governs the assembly process and accounts for the observation of three distinct DNA architectures. A morphological change from vesicles to ribbons is demonstrated by increasing the length of linear PEG chains. Remarkably, a branched trivalent carbohydrate moiety results in an unprecedented star-shaped supramolecular morphology.

Part of this work has been published:

Complex DNA Architectonics – Self-Assembly of Amphiphilic Oligonucleotides into Ribbons, Vesicles, and Asterosomes

S. Rothenbühler, I. Iacovache, S. M. Langenegger, B. Zuber, R. Häner, *Bioconjugate Chemistry* **2022**, DOI: 10.1021/acs.bioconjchem.2c00077.

5.1 Results and Discussion

The 20-mer DNA single strands used in this study are shown in Figure 134. Oligonucleotide **ON5** has already been used in the previous chapters, as well as **ON9**. TPE-DNA conjugate **ON9** is modified at the 3’- and 5’-end with three phosphodiester-linked TPE units each (see section 4.3.1 for details about the synthesis). HPLC purified 5’-end modified polyethylene glycol (PEG) DNA conjugate **ON18** was purchased from Merck (Germany). PEG conjugated oligonucleotides **ON20**–**ON22** were prepared according to standard copper-catalyzed azide-alkyne cycloaddition (CuAAC) click chemistry conditions, starting with the 3’-end alkyne modified DNA single strand **ON19** (purchased from

Microsynth, Switzerland).[205] The synthesis and purification of these three oligomers is described in more detail in chapter 5.3.1. HPLC purified 3'-end *N*-acetylgalactosamine (GalNAc) modified **ON23** was purchased from Microsynth (Switzerland).

Hybridization of TPE-DNA conjugate **ON9** with any of the modified DNA single strands **ON18**–**ON23** affords duplexes with TPE sticky ends on both sides together with an additional terminal functionality derived from the complements. The terminal functionality was priamarily selected due to potential bio-related applications of the nanostructures that are for example already employed in drug delivery systems. The results obtained after supramolecular assembly of these DNA duplexes will be discussed hereinafter.

Strand	Sequence (5'→3')
ON5	CAA GGT CCG ATG CAA GGA AG
ON9	(***E*-TPE**)$_3$-CTT CCT TGC ATC GGA CCT TG-(***E*-TPE**)$_3$
ON18	**PEG$_6$**-CAA GGT CCG ATG CAA GGA AG
ON19	CAA GGT CCG ATG CAA GGA AG-**Alkyne**
ON20	CAA GGT CCG ATG CAA GGA AG-**PEG$_6$-L**
ON21	CAA GGT CCG ATG CAA GGA AG-**PEG2000**
ON22	CAA GGT CCG ATG CAA GGA AG-**PEG5000**
ON23	CAA GGT CCG ATG CAA GGA AG-**GalNAc**

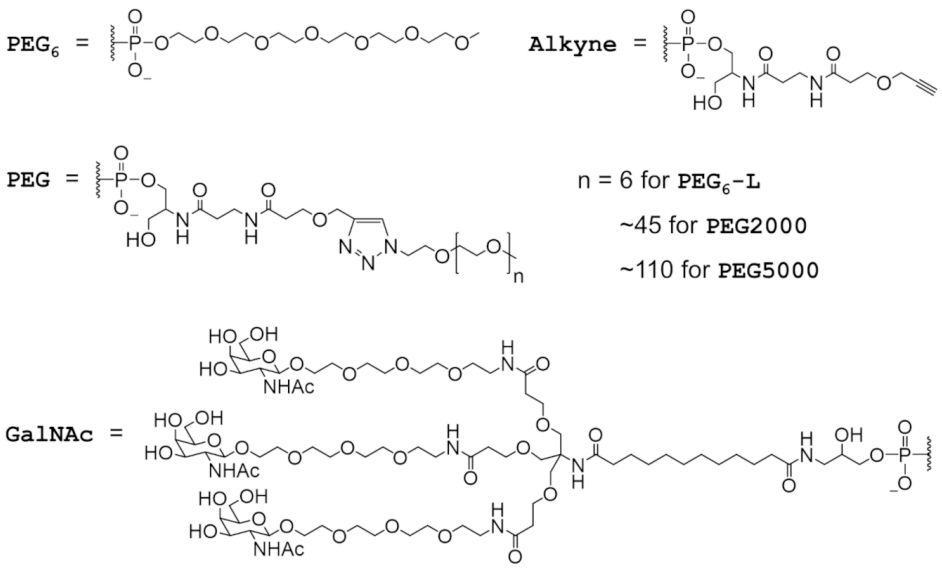

Figure 134. Summary of the DNA sequences used in this study. For the molecular structure of the *E*-TPE modification, see Figure 15a.

5.1.1 Effect of Short PEG_6 Conjugated DNA

Firstly, the influence of a sterically small terminal functionality on the self-assembly behavior was examined. Therefore, duplex **ON9*ON18** was investigated, which exhibits besides the TPE sticky ends also a PEG_6 unit (Figure 135). It is well documented that PEGylation of oligonucleotides improves the pharmacokinetic properties of therapeutic oligonucleotides.[206–208] This is mainly attributed to the stealth properties of PEG, which *e.g.*, protects the oligomers from nucleolytic degradation to some extent.[209,210]

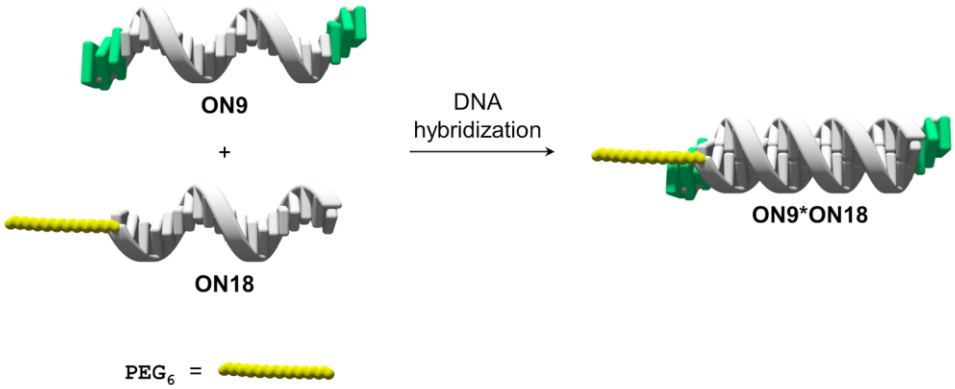

Figure 135. The two complementary single strands **ON9** and **ON18** hybridize to form duplex **ON9*ON18**.

The supramolecular assembly process was examined by fluorescence-monitored annealing curves (Figure 136). Compared to **ON5*ON9**, without any additional functional group, the shape of the annealing curve of **ON9*ON18** is very similar. The main difference resides in the nucleation temperature, which decreased by 3 °C. UV-Vis and fluorescence spectra of **ON9*ON18** are presented in Figure 169, which are comparable to the spectroscopic results obtained for **ON5*ON9** (Figure 93).

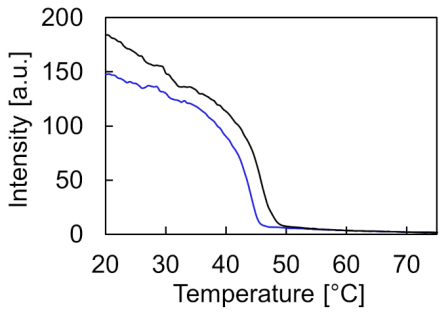

Duplex	T_{FL}(nucleation)[a] [°C]
ON5*ON9	49
ON9*ON18	46

Figure 136. Fluorescence-monitored annealing curves of **ON5*ON9** (black) and **ON9*ON18** (blue), as well as a summary of nucleation temperatures T_{FL}(nucleation). Conditions: 1 µM each single strand, 10 mM sodium phosphate buffer pH 7.2, 0.1 mM spermine · 4 HCl, 30 vol% ethanol, $\lambda_{ex.}$: 335 nm, $\lambda_{em.}$: 490 nm, gradient: 0.5 °C/min. [a] Nucleation temperature, determined by fluorescence onset temperature in annealing curve.

After thermal assembly, the nanostructures were visualized by cryo-EM imaging, which was conducted in collaboration with Prof. Dr. Benoît Zuber and Dr. Ioan Iacovache from the Institute of Anatomy of the University of Bern. Depicted in Figure 137a is a cryo-EM image of assembled **ON9*ON18**, which shows vesicular nanostructures. The diameter of the vesicles is in the range between 50–100 nm. In many areas of the structures, a rod-like pattern (perpendicular to the vesicular membrane, see section 5.3.3) with a distance between these parallel arranged rods of 2.5 ± 0.3 nm suggests a columnar DNA duplex packing. Additionally, a membrane thickness of the vesicles was measured to be 10.7 ± 0.6 nm. This distance agrees well with the length of **ON9*ON18** and is comparable to the thickness of type II vesicles assembled from **ON1*ON2** (10.9 ± 0.5 nm, Figure 22). In contrast to the type II vesicles constructed from **ON1*ON2**, duplexes **ON9*ON18** self-assemble predominantly into unilamellar vesicles, as illustrated schematically in Figure 137b (see also the cryo-EM images in Figure 175). It is believed that within the columnar duplex arrangement, the modified duplexes are oriented randomly, implying the presence of a thin PEG layer covering the in- and outside of the vesicles.

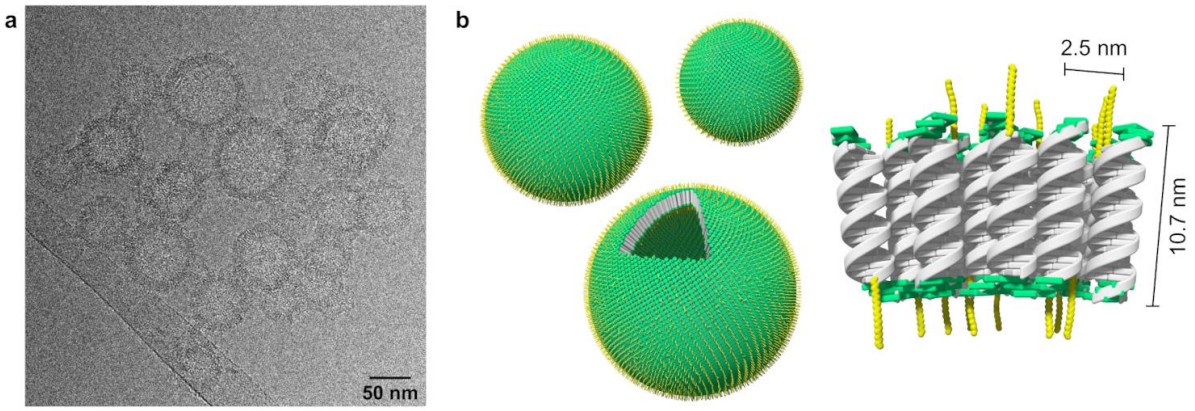

Figure 137. Cryo-EM image (**a**) and schematic illustration (**b**) of vesicular nanostructures assembled from **ON9*ON18**. Conditions: 1 µM **ON9*ON18**, 10 mM sodium phosphate buffer pH 7.2, 0.1 mM spermine · 4 HCl, 30 vol% ethanol.

AFM imaging confirms the spherical nature of the self-assemblies of **ON9*ON18** (Figure 138), with heights matching the size range observed by cryo-EM. However, the agglomeration of the vesicles obvious in the cryo-EM images indicates that the shielding properties of the PEG_6 units are too weak to prevent hydrophobic interactions between individual vesicles. Therefore, the preparation of PEG-DNA conjugates was envisioned that exhibit longer, linear PEG chains. Longer PEG chains should further minimize unwanted surface interactions due to the increased stealth properties of PEG. The corresponding results are discussed in the next subchapter.

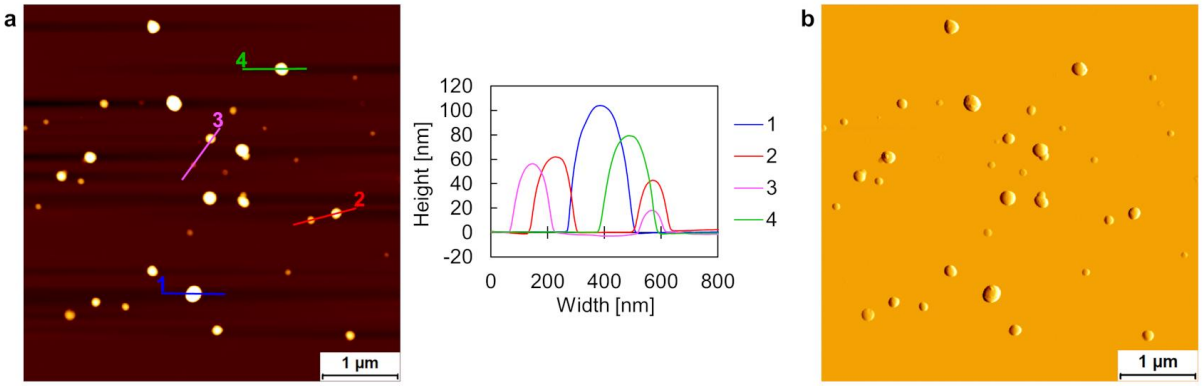

Figure 138. (**a**) AFM image with corresponding cross sections and (**b**) deflection scan of self-assembled **ON9*ON18**. Conditions: 1 µM **ON9*ON18**, 10 mM sodium phosphate buffer pH 7.2, 0.1 mM spermine · 4 HCl, 30 vol% ethanol.

5.1.2 Influence of DNA-PEGylation

Nanostructures assembled from DNA duplexes composed of TPE-modified **ON9** and complementary oligonucleotides conjugated to varied PEG chain lengths were investigated next. A representative DNA duplex, **ON9*ON22**, is illustrated schematically in Figure 139, which has a linear PEG5000 chain attached on one side. Temperature-dependent UV-Vis and fluorescence spectra of the duplexes **ON9*ON20**, **ON9*ON21**, and **ON9*ON22** are displayed in Figure 170–Figure 172.

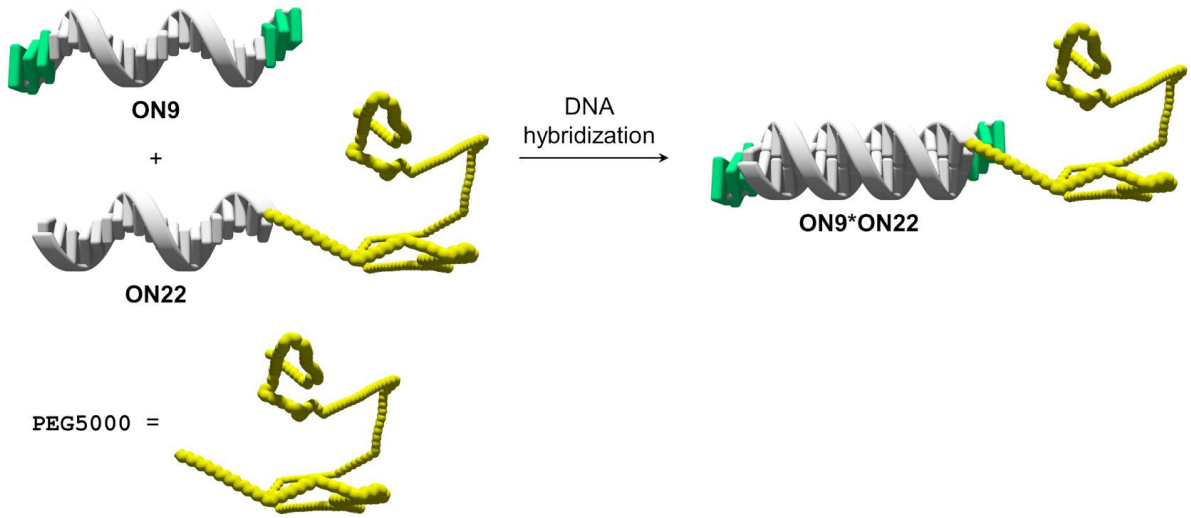

Figure 139. The two complementary single strands **ON9** and **ON22** hybridize to form duplex **ON9*ON22**.

Fluorescence-monitored annealing curves demonstrate a clear trend: the longer the attached PEG chain, the lower the measured nucleation temperature (Figure 140). Thus, for duplex **ON9*ON22**, with a PEG5000 moiety, a nucleation temperature of 35 °C was measured. This is a significant reduction by 14 °C, compared to the T_{FL}(nucleation) of duplex **ON5*ON9** without any additional functionality. Comparing duplexes **ON9*ON18** and **ON9*ON20**, they exhibit comparable nucleation temperatures. The difference between these two duplexes is that for **ON9*ON18**, the PEG_6 chain is linked *via* a phosphodiester at the 5'-end, while for **ON9*ON20**, the PEG_6 unit is attached at the 3'-end with a linker between the DNA and PEG_6 (Figure 134).

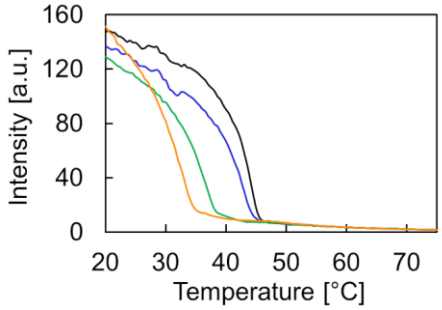

Duplex	T_{FL}(nucleation)[a] [°C]
ON9*ON18	46
ON9*ON20	45
ON9*ON21	38
ON9*ON22	35

Figure 140. Fluorescence-monitored annealing curves of **ON9*ON18** (black), **ON9*ON20** (blue), **ON9*ON21** (green), and **ON9*ON22** (orange), as well as a summary of nucleation temperatures T_{FL}(nucleation). Conditions: 1 µM each single strand, 10 mM sodium phosphate buffer pH 7.2, 0.1 mM spermine · 4 HCl, 30 vol% ethanol, $\lambda_{ex.}$: 335 nm, $\lambda_{em.}$: 490 nm, gradient: 0.5 °C/min. [a] Nucleation temperature, determined by fluorescence onset temperature in annealing curve.

Cryo-EM images of assembled **ON9*ON20** show spherical structures (Figure 141). However, compared to **ON9*ON18** (Figure 137), the vesicular constructs of **ON9*ON20** appear less defined and thus, no detailed distance measurements have been done.

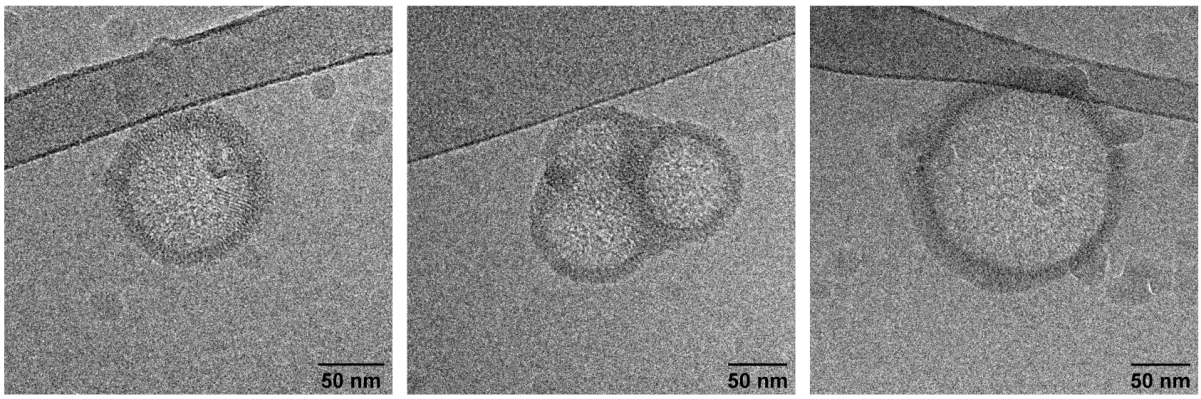

Figure 141. Cryo-EM images of self-assembled **ON9*ON20**. Conditions: 1 µM **ON9*ON20**, 10 mM sodium phosphate buffer pH 7.2, 0.1 mM spermine · 4 HCl, 30 vol% ethanol.

AFM experiments support the observations from cryo-EM imaging. The AFM image of self-assembled **ON9*ON20**, displayed in Figure 142, shows roundish objects with heights ranging from about 10 nm up to roughly 50 nm. Additionally, some smaller structures are visible as well, but they seem somehow to be collapsed on the APTES-modified mica surface.

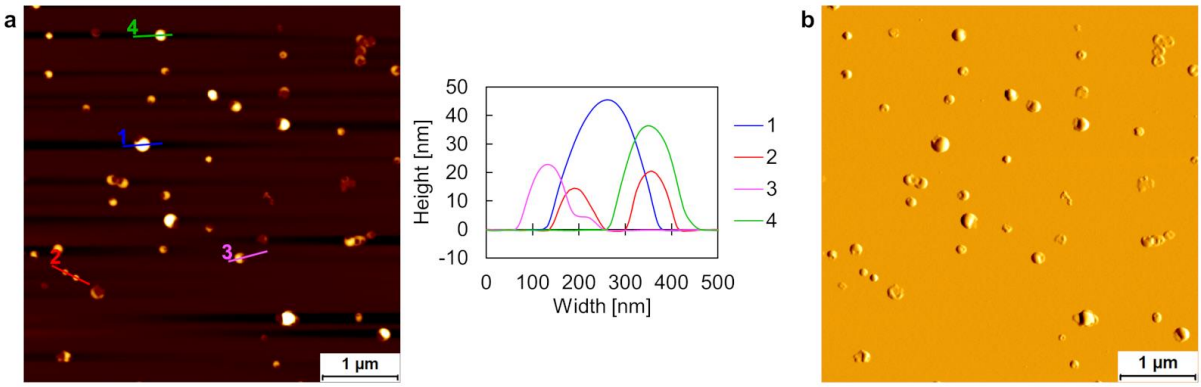

Figure 142. (**a**) AFM image with corresponding cross sections and (**b**) deflection scan of self-assembled **ON9*ON20**. Conditions: 1 µM **ON9*ON20**, 10 mM sodium phosphate buffer pH 7.2, 0.1 mM spermine · 4 HCl, 30 vol% ethanol.

It is likely that these less defined nanostructures were obtained due to the linker in **ON20** (Figure 134). The non-covalent interactions derived from the linker may contribute to a similar extent, as the PEG_6 subunit, to the self-assembly process. To test this hypothesis, duplex **ON9*ON19**, just with the alkyne linker was investigated. Cryo-EM images (Figure 143) and AFM imaging (Figure 144) of assembled **ON9*ON19** show comparable spherical nanostructures. Hence, the results support the previously mentioned assumption of the influence of the linker on the self-assembly behavior.

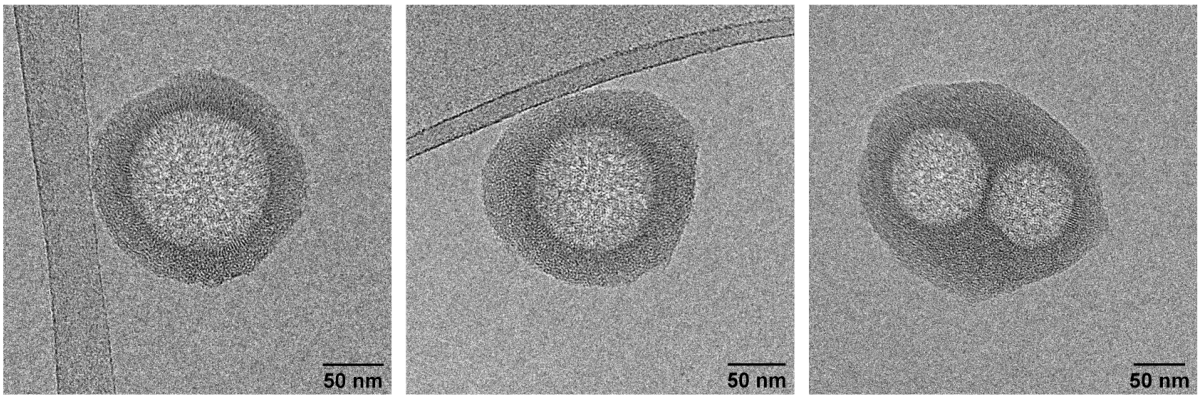

Figure 143. Cryo-EM images of self-assembled **ON9*ON19**. Conditions: 1 µM **ON9*ON19**, 10 mM sodium phosphate buffer pH 7.2, 0.1 mM spermine · 4 HCl, 30 vol% ethanol.

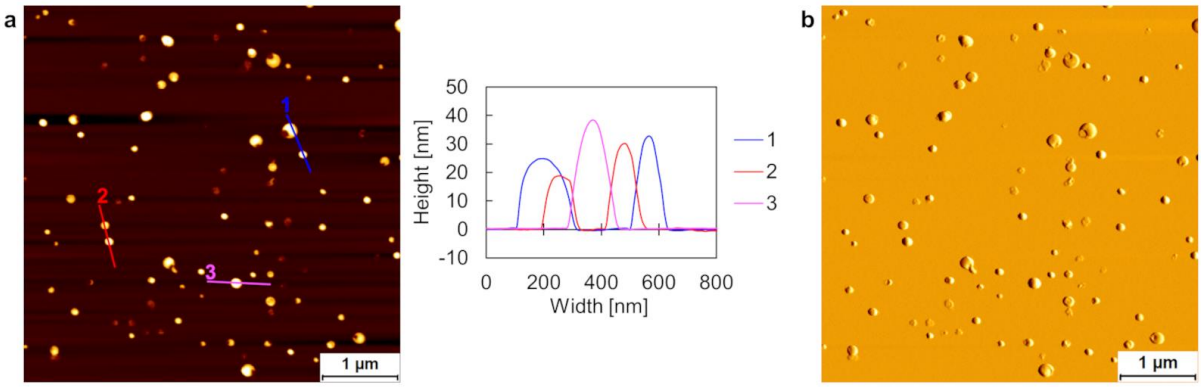

Figure 144. (**a**) AFM image with corresponding cross sections and (**b**) deflection scan of self-assembled **ON9*ON19**. Conditions: 1 µM **ON9*ON19**, 10 mM sodium phosphate buffer pH 7.2, 0.1 mM spermine · 4 HCl, 30 vol% ethanol.

In the case of **ON9*ON21**, which has a PEG2000 moiety (PEG average M_n 2000 Da, ~45 PEG units), the most prominent morphology changed to ribbon-like structures (Figure 145a). Vesicular constructs are rarely visible, which is further supported by the additional cryo-EM images in Figure 177. The distance measurements of the vesicles assembled from **ON9*ON21** (membrane thickness: 10.0 ± 0.5 nm; DNA width: 2.4 ± 0.3 nm) evince the same columnar DNA duplex alignment as it was described for the vesicles constructed from **ON9*ON18** (Figure 137). They mainly differ in the diameter only: the size range of the vesicles assembled from **ON9*ON21** increased to 100–200 nm in diameter.

Regarding the ribbons, the length reaches a few micrometers in certain cases. The apparent thickness of the ribbon-like structure was measured to be 10.1 ± 0.7 nm, which matches the duplex length of **ON9*ON21**. Hence, a side-by-side DNA arrangement is suggested, which is illustrated schematically in Figure 145b.

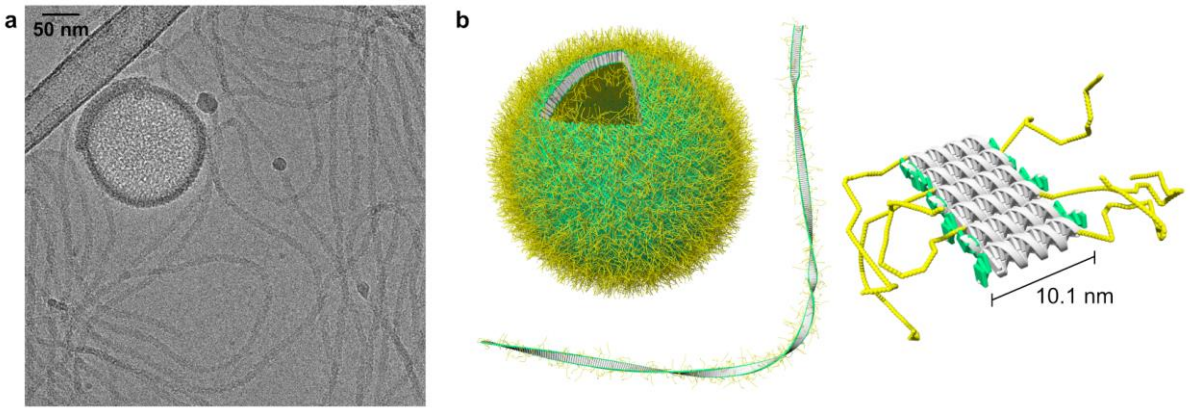

Figure 145. Cryo-EM image (**a**) and schematic illustration (**b**) of self-assemblies of **ON9*ON21**. Conditions: 1 µM **ON9*ON21**, 10 mM sodium phosphate buffer pH 7.2, 0.1 mM spermine · 4 HCl, 30 vol% ethanol.

Depicted in Figure 146 is an AFM image of self-assembled **ON9*ON21**, which confirms the ribbon-like structures. The height profiles show heights roughly around 1 nm, which is in fact, less than expected for a DNA duplex width. However, this observation is likely due to the tip convolution effect, which causes a flattening of the detected structures.[211] Interestingly, no vesicular assemblies were discernible by AFM. This might be explained by the fact that the longer PEG2000 chain in **ON9*ON21** prevents the vesicles from adsorbing onto the APTES-modified mica surface due to increased PEG stealth properties, which generally reduce surface interactions.

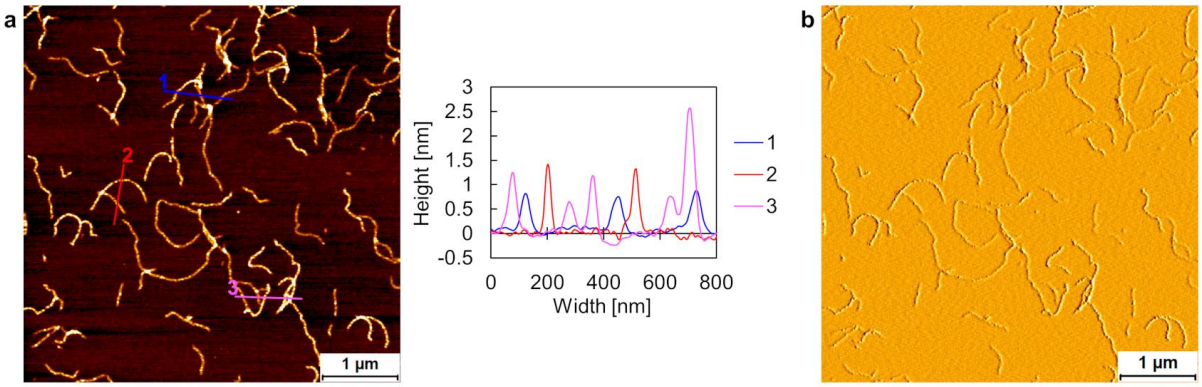

Figure 146. (**a**) AFM image with corresponding cross sections and (**b**) deflection scan of self-assembled **ON9*ON21**. Conditions: 1 µM **ON9*ON21**, 10 mM sodium phosphate buffer pH 7.2, 0.1 mM spermine · 4 HCl, 30 vol% ethanol.

The change of the main type from the vesicular morphology to ribbons by extending the PEG chain length guided us to investigate the even longer PEG5000 chain (PEG average M_n 5000 Da, ~110 PEG units), namely duplex **ON9*ON22**. The corresponding cryo-EM images (Figure 147a and Figure 179) exclusively show ribbons. A comparable thickness of 10.2 ± 0.7 nm was determined for these ribbons, which is comparable to the ribbons assembled from **ON9*ON21**. Thus, the same side-by-side DNA duplex alignment is suggested for the ribbons constructed from **ON9*ON22** and is presented schematically in Figure 147b.

Compared to the ribbons from **ON9*ON21**, the ribbons assembled from **ON9*ON22** are significantly shorter. They are typically less than 350 nm long. It could be imagined that the long PEG5000 chains are somehow wrapped around the DNA duplexes. This might lead to the impeding of the assembly of these duplexes into the supramolecular nanostructures. Experimental support of this hypothesis is the presence of numerous dark spots in the cryo-EM images, surrounding the ribbon structures (Figure 147a). With an average size of roughly 4 nm, these small dark spots may be assigned to single DNA duplexes **ON9*ON22**.

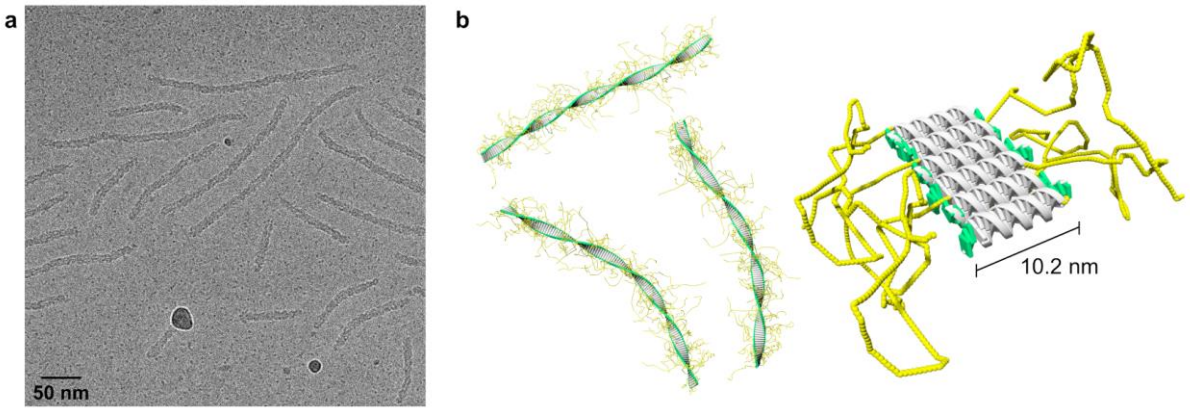

Figure 147. Cryo-EM image (**a**) and illustration (**b**) of ribbons assembled from **ON9*ON22**. Conditions: 1 µM **ON9*ON22**, 10 mM sodium phosphate buffer pH 7.2, 0.1 mM spermine · 4 HCl, 30 vol% ethanol.

AFM experiments of **ON9*ON22** also show a ribbon-like morphology (Figure 148). As described previously for **ON9*ON21**, the ribbons might be flattened to some extent, giving rise to the apparent heights of about 1 nm. A striking feature of the AFM image (Figure 148) is the obvious directionality of the ribbons. They seem to be aligned predominantly in one distinct orientation (from the top left to the bottom right corner of the AFM scan). To exclude possible imaging artefacts, the mica plate was rotated counterclockwise by about 60°, then imaged again (Figure 149). After rotation, the ribbons are oriented horizontally, which presumably eliminates the potential imaging artefacts. Notably, the directionality of the ribbons could be confirmed by directionality analyses done in Fiji.[212] Before the mica plate was rotated, a value of –60° was obtained, and +4° after rotation, proofing the preferential orientation of the ribbons on the mica plate. It is supposed that the ribbons are oriented during the AFM sample preparation. During the washing step, the ribbons may orient along the flow of the water. This is also based on the assumption that the ribbons are only weakly adsorbed on the APTES-modified mica plate due to the considerable stealth properties of PEG5000, as previously mentioned for **ON9*ON21**.

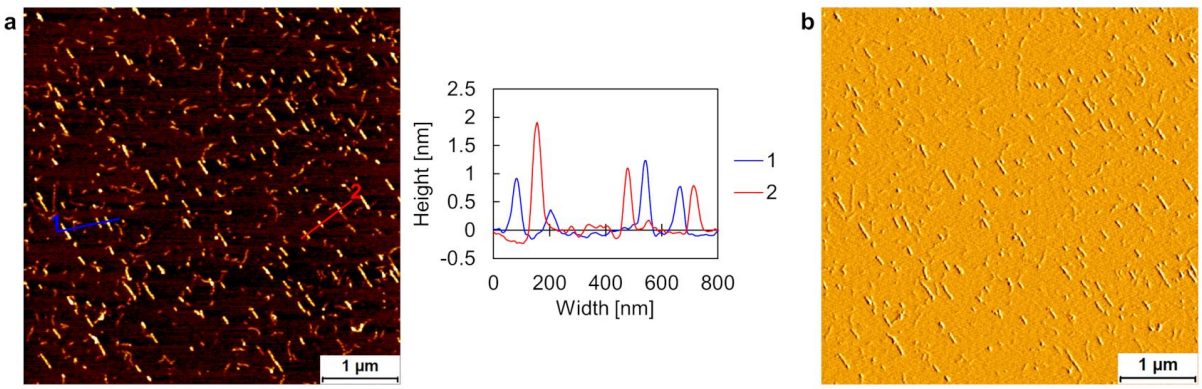

Figure 148. (**a**) AFM image with corresponding cross sections and (**b**) deflection scan of self-assembled **ON9*ON22**. Conditions: 1 µM **ON9*ON22**, 10 mM sodium phosphate buffer pH 7.2, 0.1 mM spermine · 4 HCl, 30 vol% ethanol.

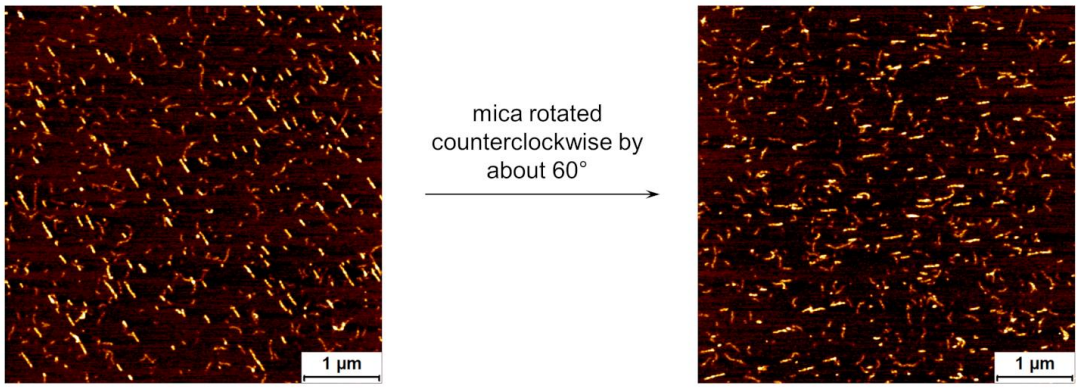

Figure 149. AFM images of self-assembled **ON9*ON22** before and after rotation of the mica. Conditions: 1 µM **ON9*ON22**, 10 mM sodium phosphate buffer pH 7.2, 0.1 mM spermine · 4 HCl, 30 vol% ethanol.

5.1.3 Impact of a Branched GalNAc Moiety

In contrast to the linear PEG chains, the branched trivalent GalNAc moiety is sterically more demanding. Surface crowding induced by sterically confined proteins on lipid membranes can, for example, promote membrane bending.[213–216] Therefore, the branched GalNAc component in duplex **ON9*ON23** (Figure 150) might also have a morphological impact on the self-assembled DNA nanostructures. Additionally, the triantennary GalNAc functional group was chosen because of the promising potential of targeted delivery applications of GalNAc modified nucleic acids to liver cells.[217–221] GalNAc, especially as a trivalent cluster, was shown to have an excellent binding affinity towards the asialoglycoprotein receptor (ASGR), which is abundantly expressed in hepatocytes.[222,223] GalNAc-conjugated substrates are internalized by receptor-mediated endocytosis, which accounts for the efficient and targeted delivery.[224]

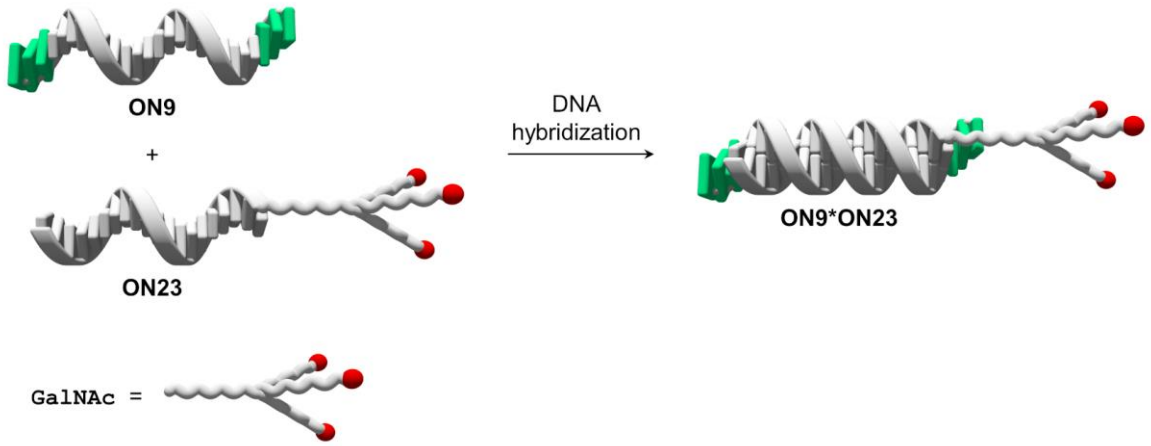

Figure 150. The two complementary single strands **ON9** and **ON23** hybridize to form duplex **ON9*ON23**.

The fluorescence-monitored annealing curve of the GalNAc modified duplex **ON9*ON23** is displayed in Figure 151. Compared to **ON5*ON9**, without any additional terminal functionality, the nucleation temperature was lowered to 40 °C in the case of **ON9*ON23**. Nonetheless, the overall shape of the two annealing curves is very similar.

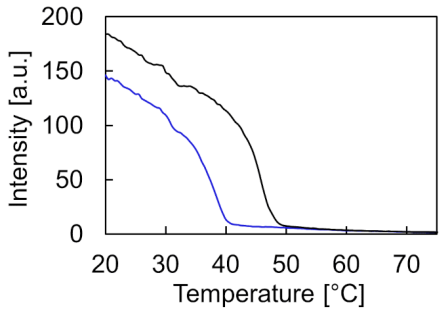

Duplex	T_{FL}(nucleation)[a] [°C]
ON5*ON9	49
ON9*ON23	40

Figure 151. Fluorescence-monitored annealing curves of **ON5*ON9** (black) and **ON9*ON23** (blue), as well as a summary of nucleation temperatures T_{FL}(nucleation). Conditions: 1 µM each single strand, 10 mM sodium phosphate buffer pH 7.2, 0.1 mM spermine · 4 HCl, 30 vol% ethanol, $\lambda_{ex.}$: 335 nm, $\lambda_{em.}$: 490 nm, gradient: 0.5 °C/min. [a] Nucleation temperature, determined by fluorescence onset temperature in annealing curve.

Strikingly, cryo-EM images in Figure 152a reveal a fundamentally different and novel morphology. A star-shaped nanostructure can be observed, which is constructed from multiple parabolic cones originating from a common center and point outwards of this center. Because these nanostructures appear star-like, these assemblies are referred to as *asterosomes*. Considering also the additional cryo-EM images presented in Figure 180, the number of the cone-shaped extensions differs between the *asterosomes*. In the case of twelve cones, the arrangement of these protrusions might be approximated by the small-stellated dodecahedron,[225] and an *asterosome* with such an arrangement is illustrated schematically in Figure 152b.

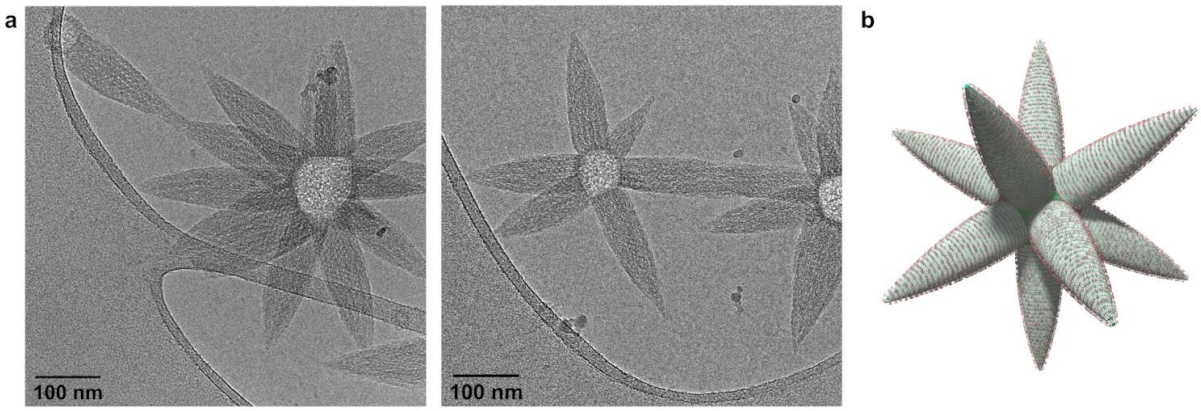

Figure 152. (**a**) Cryo-EM images and (**b**) schematic illustration of an *asterosome* assembled from **ON9*ON23**. Conditions: 1 µM **ON9*ON23**, 10 mM sodium phosphate buffer pH 7.2, 0.1 mM spermine · 4 HCl, 30 vol% ethanol.

At closer inspection, cryo-EM imaging reveals the DNA duplex alignment of **ON9*ON23** within the intriguing *asterosome* architecture. In the cones, the regular rod-like pattern with a distance between the rods of 2.5 ± 0.2 nm (Figure 153a) implies the DNA width and suggests an extended DNA duplex alignment, comparable to the DNA arrangement of type I vesicles assembled from **ON1*ON2** (Figure 21). The alignment of **ON9*ON23** in the cones is depicted schematically in Figure 153b. At the base of the cones, a width in the range between 50–75 nm was determined. The centers of the *asterosomes* appear spherical and for structures with only a few parabolic cones, a membrane is discernible around the base of these cones. This membrane has a thickness of 10.5 ± 0.5 nm (Figure 153a) and indicates for a columnar, unilamellar DNA duplex arrangement. Such an alignment has already been described for the vesicular architectures constructed from **ON1*ON2**, (type II vesicles, Figure 22), or from the PEG conjugated duplexes **ON9*ON18** (Figure 137) and **ON9*ON21** (Figure 145).

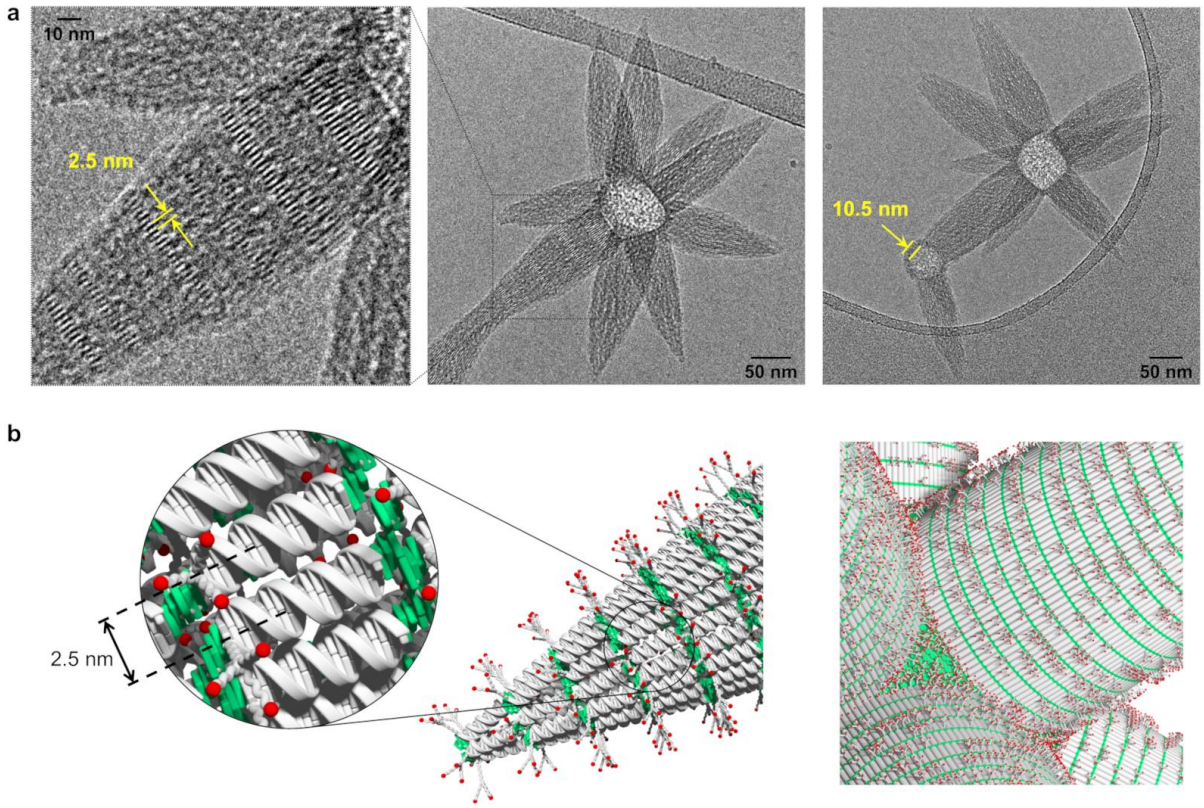

Figure 153. Additional cryo-EM images (**a**) and further schematic illustrations (**b**) of *asterosomes* assembled from **ON9*ON23**. Conditions: 1 µM **ON9*ON23**, 10 mM sodium phosphate buffer pH 7.2, 0.1 mM spermine · 4 HCl, 30 vol% ethanol.

The 3D nature of the *asterosomes* were supported with modeled shadow images, as displayed in Figure 154b. The shadow images should facilitate the interpretation of a 3D object, projected onto a 2D plane. This is of importance because cryo-EM images also represent such projections. In brief, the shadow

images were generated from a dodecahedral arranged 3D *asterosome* (as depicted in Figure 152b), created from light-absorbing medium. Then, the 3D object was rotated into an arbitrary orientation, before it was irradiated with parallel light, orthogonal to the shadow plane (Figure 154a). This yielded the shadow images presented in Figure 154b. The evident resemblance of the shadow images with the structures from cryo-EM imaging, the proposed model in Figure 152b can be reasonably assigned to the DNA architecture assembled from **ON9*ON23**. In addition, the cryo-EM images of the *asterosomes* might imply irregularly sized cones. However, the shadow images show that uniformly sized cones appear somewhat irregular or asymmetric, depending on the orientation of the 3D assembly.

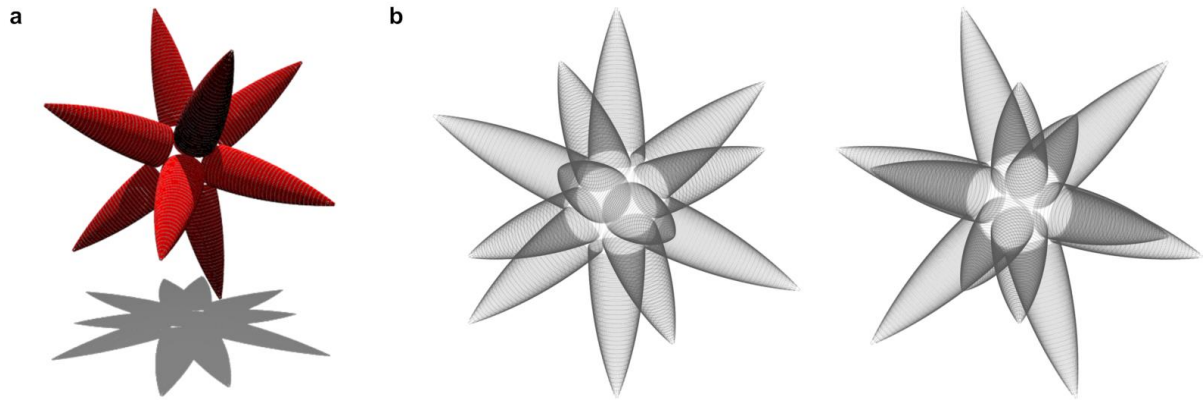

Figure 154. (**a**) Dodecahedral arranged 3D *asterosome* (red) incl. projected shadow (gray). (**b**) Shadow images of two *asterosomes* at arbitrary orientations.

Based on the structural characteristics of the *asterosome*, it is believed that this DNA architecture is formed *via* a two-step process. It is assumed that during the assembly process, vesicles of different sizes and with a columnar DNA alignment are assembled in a first step. This is mainly explained by the fact that no single cones (without a columnar packed vesicular membrane around the base of the cones) were observed. In the second step, further cooling of the solution might lead to a steric crowding on the surface of these vesicular constructs, induced by the branched, bulky triantennary GalNAc units in **ON9*ON23**. This steric crowding is reduced by the evolution of the cones, leading to the mace-like *asterosome* architecture. The reduction of the strain can be explained due to the change of the supramolecular organization of the DNA duplexes from columnar to the extended DNA alignment present in the cones. A telescopic slide-out process is hypothesized for the evolution of the cones, in which the DNA duplexes of the columnar packed vesicles slide along the surrounding duplexes until the extended DNA alignment is accomplished. This change involves a surface expansion and allows a redistribution of the sterically demanding GalNAc moieties over a larger surface area, thus resulting in a less crowded surface. Two

additional considerations support this assumption. Firstly, nanostructures with small vesicular centers exhibit generally less cones. The smaller the vesicle, the higher its surface curvature, which is attributed to a rather modest surface crowding of the GalNAc units only. And secondly, the number of individual duplexes **ON9*ON23** in a cone is roughly the same as the number of DNAs that would be assembled in the curved surface area of the vesicular membrane exhibiting a columnar DNA alignment.

The *asterosome* morphology was validated independently by AFM experiments. The AFM image in Figure 155 confirms the star-like appearance of the self-assemblies. However, the rather complex 3D architectures often seem to be disrupted, but the cones are still obvious in the deflection scan. The disruption of the *asterosomes* might occur during AFM sample preparation, either during the adsorption of the nanostructures onto the APTES-modified mica or during the subsequent drying step.

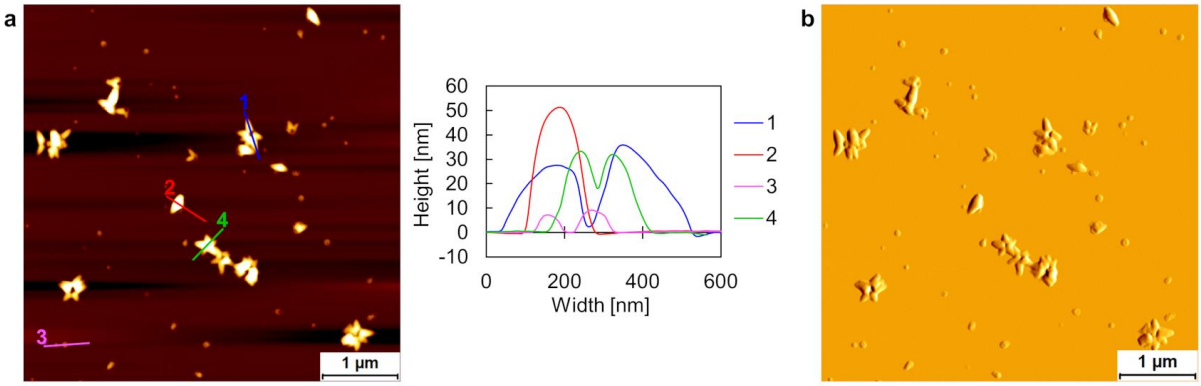

Figure 155. (**a**) AFM image with corresponding cross sections and (**b**) deflection scan of self-assembled **ON9*ON23**. Conditions: 1 µM **ON9*ON23**, 10 mM sodium phosphate buffer pH 7.2, 0.1 mM spermine · 4 HCl, 30 vol% ethanol.

The proposed model of an *asterosome* presented in Figure 152b illustrates that the supramolecular assembly is decorated on the surface with carbohydrate moieties. As mentioned previously, the triantennary GalNAc moiety effectively binds ASGR. In a next step, binding of ASGR to the *asterosomes* was envisioned to test the addressability of the GalNAc moieties. The structural division of the lectin ASGR is sketched in Figure 156a. Two subunits, H1 and H2, constitute the functional ASGR. The H1 subunit can be further divided into four different domains, namely a cytosolic, transmembrane, stalk, and carbohydrate recognition domain (CRD).[226] The CRD domain is illustrated in Figure 156b with the black arrow indicating the carbohydrate binding site.

However, to avoid denaturation of the protein, the aqueous conditions of the *asterosomes* had to be adjusted, *i.e.*, removal of the ethanol fraction by dialysis.

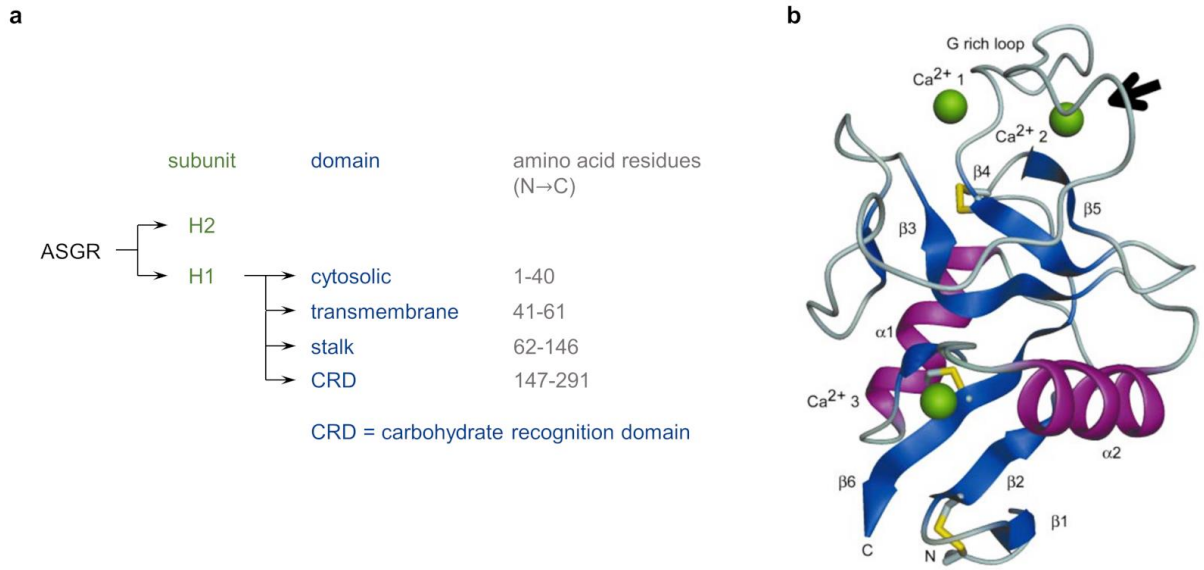

Figure 156. (**a**) Overview of the structural organization of the ASGR protein. (**b**) Illustration of the CRD domain (amino acid residues 147–290) of the H1 subunit of ASGR. Figure adapted from ref. [226].

Also in the case of the *asterosomes*, the ethanol fraction has been removed after the nanostructures have been formed by the thermal assembly process in the presence of 30 vol% ethanol (spectroscopic characterization after dialysis, see Figure 182). The cryo-EM images in Figure 157 prove that the *asterosome* architecture generally remains intact after dialysis. The most obvious difference resides in the number of cones present in the structures. It seems that after dialyzing off the ethanol fraction, less cones per *asterosome* are present. On the other hand, more vesicular structures are discernible. Hence, the change of the aqueous medium might induce some collapses of cones. But in general, the sizes of the *asterosomes* are comparable as before dialysis. AFM imaging further verifies star-shaped self-assemblies after dialysis (Figure 158).

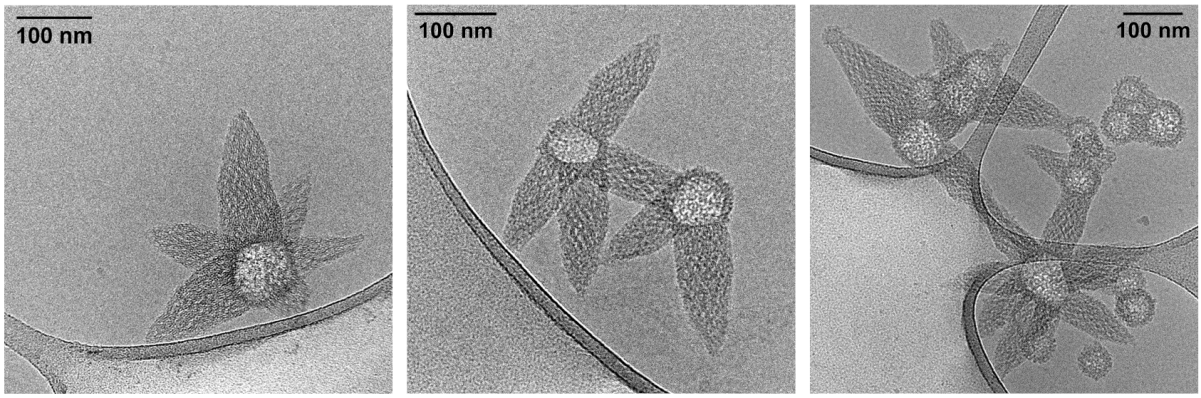

Figure 157. Cryo-EM images of assembled **ON9*ON23** after ethanol removal by dialysis. Conditions: 1 µM **ON9*ON23**, 10 mM sodium phosphate buffer pH 7.2, 0.1 mM spermine · 4 HCl, <0.5 vol% ethanol.

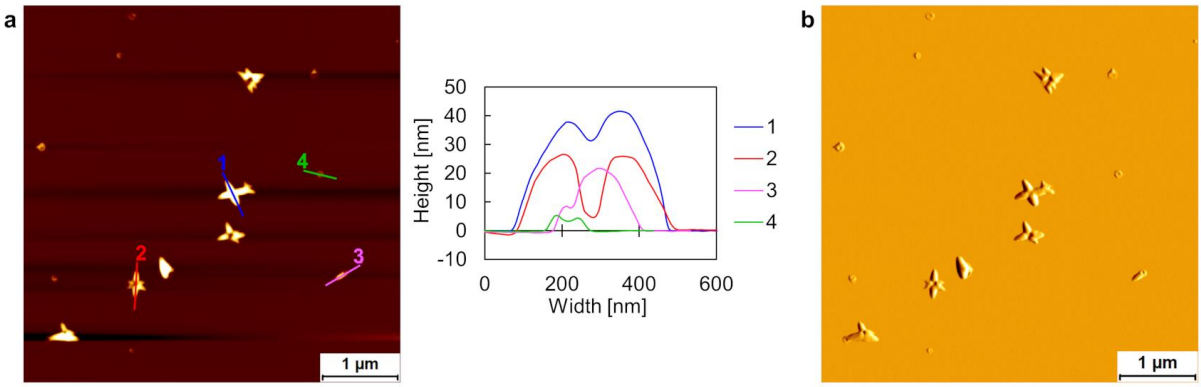

Figure 158. (**a**) AFM image with corresponding cross sections and (**b**) deflection scan of assembled **ON9*ON23** after dialyzing off the ethanol fraction. Conditions: 1 µM **ON9*ON23**, 10 mM sodium phosphate buffer pH 7.2, 0.1 mM spermine · 4 HCl, <0.5 vol% ethanol.

After validating the *asterosome* architecture after removal of the ethanol fraction, ASGR was added to the supramolecular DNA nanostructures. For these experiments, only a part of the recombinant human ASGR protein (amino acid residues 62–291, with a C-6His tag) was purchased from *antibodies-online GmbH* (Germany); additional information is provided in Table 9. For simplicity, amino acid residues 62–291, which comprise of the stalk and CRD domain, will be referred to as ASGR in the text. As illustrated in Figure 156b, two calcium ions are present very close to the sugar binding site. Hence, successful binding of the carbohydrates to the CRD domain of ASGR is efficient in the presence of calcium only.[227–230] Therefore, 0.4 mM $CaCl_2$ was added to the dialyzed *asterosomes*, together with ASGR. The cryo-EM images in Figure 159 show vesicular constructs with some cones. Again, it seems that the number of cones per *asterosome* is further reduced, compared to the nanostructures observed after removal of the ethanol fraction (Figure 157), probably due to the addition of $CaCl_2$.

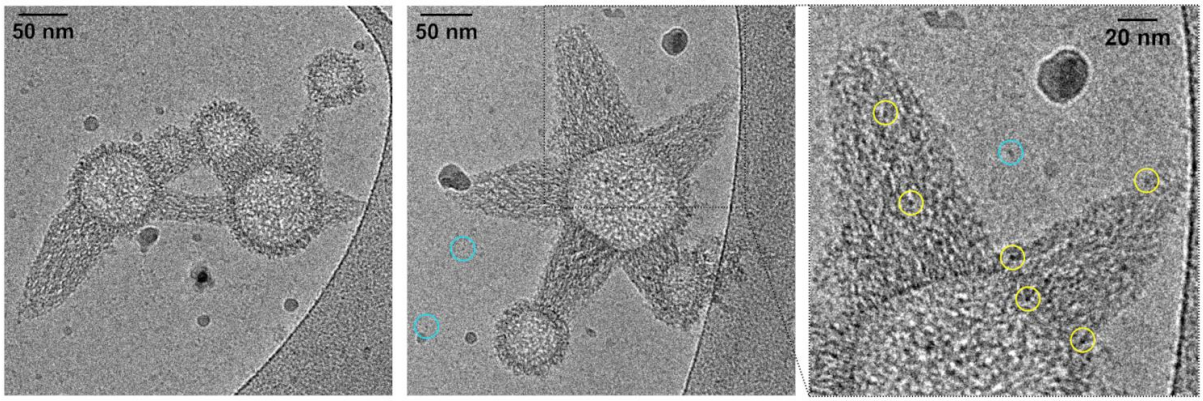

Figure 159. Cryo-EM images of **ON9*ON23** nanostructures in the presence of ASGR. Conditions: 1 µM **ON9*ON23**, 10 mM sodium phosphate buffer pH 7.2, 0.1 mM spermine · 4 HCl, <0.5 vol% ethanol, 0.4 mM $CaCl_2$, 1 µM ASGR. "Bound" ASGR encircled in yellow. Unbound ASGR/background noise encircled in blue.

The CRD domain exhibits a globular shape with dimensions of about 41 x 24 x 32 Å.[226] A zoom of one *asterosome* (inset Figure 159) shows spherical dots on the cones with diameters of roughly 3.5 nm (encircled yellow). This would match the size of ASGR and hence, these dots might be ascribed to proteins bound to the GalNAc moieties of the *asterosome*. However, the size of the protein is rather small and a distinctive discrimination between other dots that could be either unbound protein or simply background noise (encircled light blue) is nearly infeasible. Overall, the presented cryo-EM images do not provide solid evidence of ASGR binding to the supramolecular nanostructures, mainly due to the small size of the protein.

5.2 Conclusions and Outlook

In summary, distinct DNA architectures have been achieved *via* self-assembly of chemically modified DNA duplexes. These amphiphilic DNA duplexes comprise hydrophobic TPE residues on the 3'- and 5'-ends of one DNA single strand and an additional terminal moiety on the DNA complement. The nature of the terminal group governs the supramolecular assembly process and are responsible for the formation of the fundamentally different morphologies (Figure 160). Thus, DNA architectures such as vesicles, ribbons, or star-shaped *asterosomes* have been described.

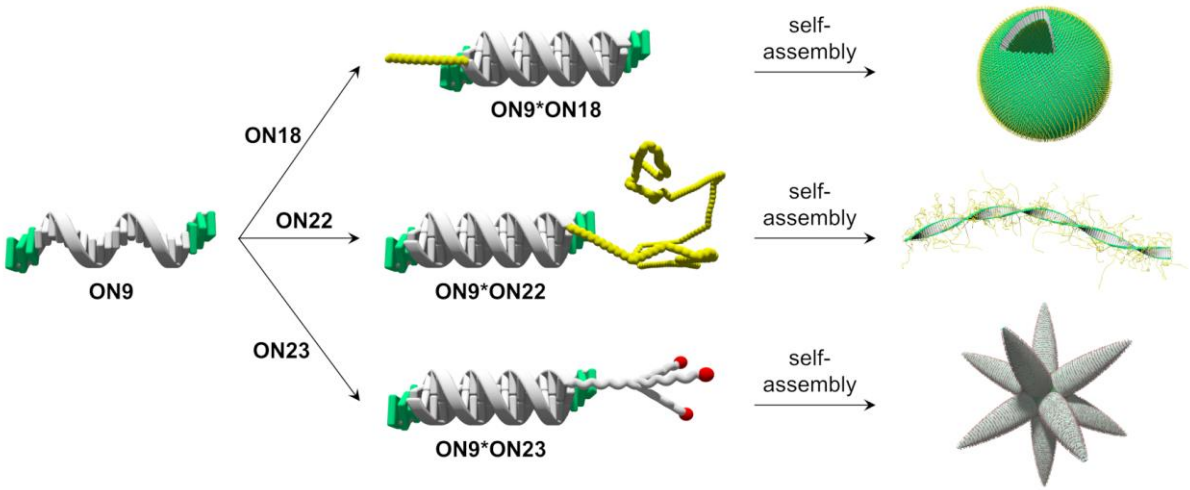

Figure 160. Diverse DNA architectures were accomplished after self-assembly of amphiphilic DNA.

Employing a short PEG_6 moiety in the duplexes leads to unilamellar vesicles with a columnar DNA duplex arrangement, as evidenced by cryo-EM imaging. Extending the linear PEG to PEG2000 chains, vesicles coexist with a ribbon morphology. These ribbons are characterized by a side-by-side DNA duplex alignment and range over long distances. Further increase of the length of PEG to PEG5000, short ribbons were detected only, which completes the morphological change from vesicles to ribbons.

Introducing a branched, triantennary GalNAc moiety in the amphiphilic DNA affords a novel type of DNA nanostructures, namely star-shaped *asterosomes*. In these constructs, parabolic cones emerge radially from a spherical center of the nanostructures. It is assumed that these cones evolve due to the influence of surface crowding. In this proposition, a change of the DNA duplex arrangement from a columnar to an extended DNA alignment is involved. This change results in the reduction of surface crowding, which is induced by the sterically demanding GalNAc moieties. Similar star-like nanostructures have only been described that are either based on nanoparticles[231,232] or colloidal clusters.[233,234]

The length of the ribbon architecture assembled from **ON9*ON21**, which ranges up to the micrometer scale, might allow to harvest light along these ribbons over very long distances. Therefore, replacement of one nucleobase in the middle of each complementary DNA single strand **ON9** and **ON21** with a donor chromophore could act as a light-harvesting antenna. Doping of such a system with a suitable energy acceptor (*e.g.*, a DNA single strand with another chromophore modification in the middle of the strand) would eventually lead to an artificial light-harvesting system. In this case, the energy would be transferred not along the helical axis of one DNA duplex as reported previously in our research group,[57,61,62] but across numerous DNA duplexes in the side-by-side duplex arrangement that is present in the ribbons.

The rather small size of ASGR rendered it difficult to unambiguously identify the protein by cryo-EM and hence, to study potential binding of the protein to the GalNAc decorated *asterosomes*. One may therefore envision to immobilize ASGR on gold nanoparticles, following described conjugation strategies.[235,236] Such ASGR conjugated gold nanoparticles would be clearly visible and distinguishable in cryo-EM experiments, which would facilitate the investigation of the addressability of the GalNAc moieties in the *asterosomes*.

5.3 Appendix – Chapter 5

5.3.1 Synthesis of Oligonucleotides

The synthesis of PEG conjugated oligomers **ON20**–**ON22** was carried out following standard CuAAC conditions, starting with alkyne-modified **ON19** and the respective mPEG azides (Scheme 4).[205] For **ON21** and **ON22**, conjugation with **mPEG2000N$_3$** (PEG average M_n 2000 Da) or **mPEG5000N$_3$** (PEG average M_n 5000 Da), yielded PEG-DNA conjugates with a distribution of different PEG chain lengths.

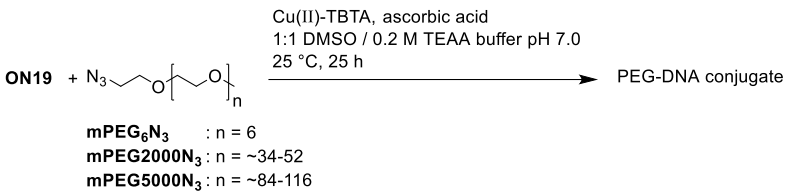

Scheme 4. Click reaction of **ON19** with mPEG azides.

Oligonucleotide ON20

The alkyne-modified oligonucleotide **ON19** was dissolved in Milli-Q H_2O (c: 229 µM). 2 M TEAA buffer pH 7.0 (28 µL) was added to **ON19** (76 µL) in an Eppendorf tube, followed by DMSO (122 µL). The reaction mixture was vortexed, before a 2.6 mM solution of **mPEG$_6$N$_3$** in DMSO (10 µL) was added. A solution of 5 mM ascorbic acid in Milli-Q H_2O (28 µL) was added. The reaction mixture was vortexed briefly, then degassed by bubbling argon in it for 30 s. A solution of 10 mM Cu(II)-TBTA in Milli-Q H_2O/DMSO 45:55 (14 µL) was added, before the Eppendorf tube was flushed with argon, sealed, vortexed thoroughly, and shaken in a ThermoMixer for 25 h (25 °C, 500 rpm). The reaction mixture was lyophilized.

The crude PEG$_6$ conjugated oligonucleotide **ON20** was purified by reversed-phase HPLC (Shimadzu LC-20AT, ReproSil 100 C18, 5 µm, 250 x 4 mm) at 40 °C with a flow rate of 1 mL/min, λ: 260 nm. Solvent A: 0.1 M aqueous TEAA buffer pH 7; solvent B: acetonitrile; B [%] (t_R [min]) = 0 (0), 0 (1), 45 (22). The purified oligomer was dissolved in Milli-Q H_2O (100 µL). The absorbance was measured at 260 nm to determine the concentration of the stock solution. The calculation was according to the Beer-Lambert law and the following molar absorptivities (at 260 nm) in [L/mol·cm] were used for the DNA nucleobases: ε_A: 15’300; ε_T: 9’000; ε_G: 11’700; ε_C: 7’400. The corresponding MS result of **ON20** is listed in Table 8, the HPLC trace is displayed in Figure 161, and the MS spectra are presented in Figure 162 and Figure 163.

Oligonucleotides ON21 and ON22

A general experimental procedure is described for the preparation of **ON21** and **ON22**. The alkyne-modified oligonucleotide **ON19** was dissolved in Milli-Q H_2O (c: 225 µM). 2 M TEAA buffer pH 7.0 (28 µL) was added to **ON19** (84 µL) in an Eppendorf tube, followed by DMSO (117 µL). The reaction mixture was vortexed, before a 3 mM solution of either **mPEG2000N$_3$** (PEG average M_n 2000 Da) in DMSO (9.5 µL) or **mPEG5000N$_3$** (PEG average M_n 5000 Da) in DMSO (9.5 µL) was added. A solution of 5 mM ascorbic acid in Milli-Q H_2O (28 µL) was added. The reaction mixture was vortexed briefly, then degassed by bubbling argon in it for 30 s. A solution of 10 mM Cu(II)-TBTA in Milli-Q H_2O/DMSO 45:55 (14 µL) was added, before the Eppendorf tube was flushed with argon, sealed, vortexed thoroughly, and shaken in a ThermoMixer for 25 h (25 °C, 500 rpm). Afterwards, the reaction mixture was lyophilized.

The crude oligonucleotides **ON21** and **ON22** were purified by reversed-phase HPLC (Shimadzu LC-20AT, ReproSil 100 C18, 5 µm, 250 x 4 mm) at 40 °C with a flow rate of 1 mL/min, λ: 260 nm. Solvent A: 0.1 M aqueous TEAA buffer pH 7; solvent B: acetonitrile; B [%] (t_R [min]) = 0 (0), 0 (1), 5 (2), 60 (22). The purified oligomers were dissolved in Milli-Q H_2O (130 µL). The concentration of the stock solution was calculated as described above for **ON20**. The corresponding MS results of **ON21** and **ON22** are listed in Table 8, the HPLC traces are displayed in Figure 161, and the MS spectra are presented in Figure 164–Figure 168.

Table 8: Oligomer sequences of **ON20**, **ON21**, and **ON22**; calculated and found masses by NSI-MS.

Oligomer	Sequence (5'→3')	Calc. mass	Found mass	n(PEG)
ON20	CAA GGT CCG ATG CAA GGA AG-**PEG$_6$-L**	6855.3780	6855.4056	6
ON21	CAA GGT CCG ATG CAA GGA AG-**PEG2000**	8616.4266	8616.4650	45
ON22	CAA GGT CCG ATG CAA GGA AG-**PEG5000**	11478.1306	11478.1212	110

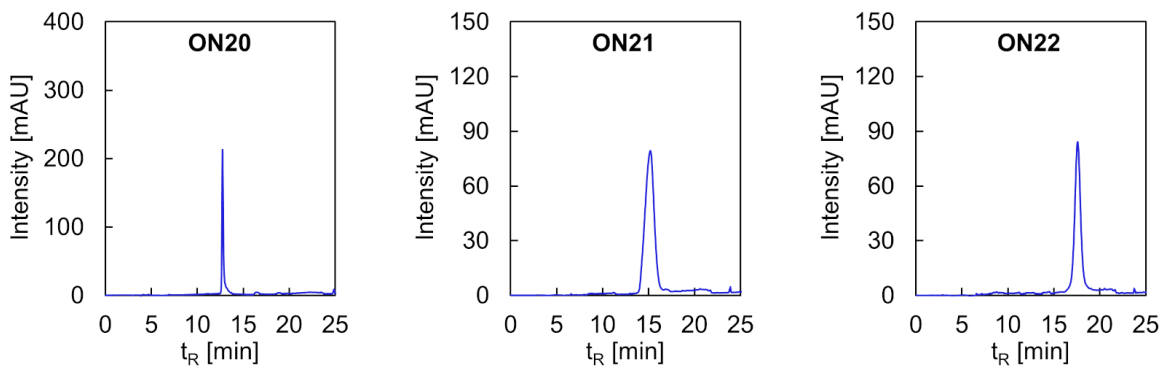

Figure 161. HPLC traces of PEG-modified DNA conjugates **ON20**, **ON21**, and **ON22**.

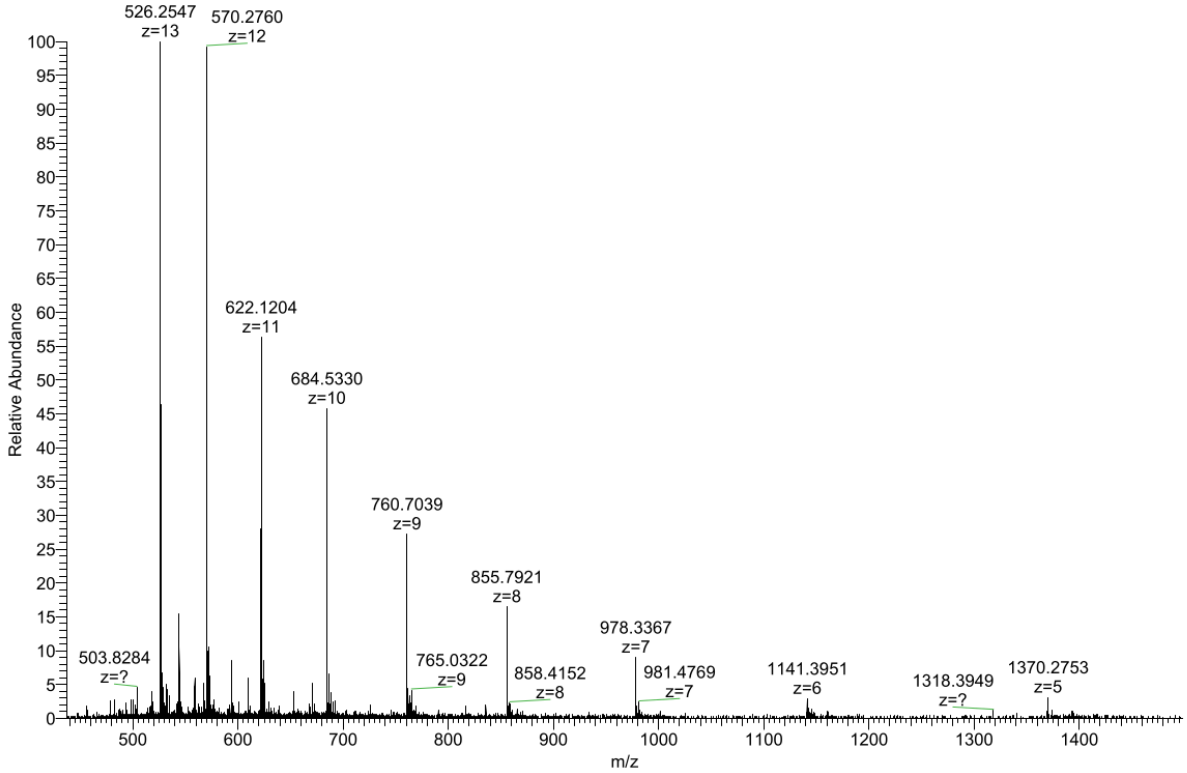

Figure 162. MS spectrum of **ON20**.

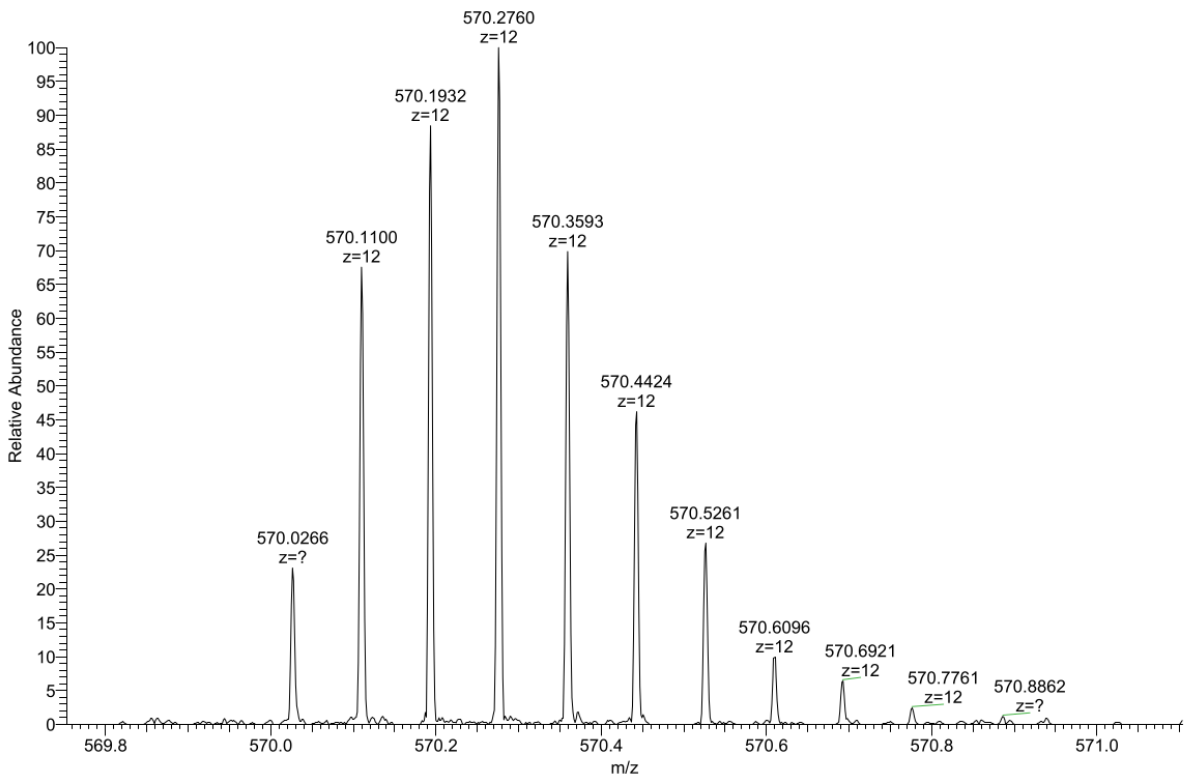

Figure 163. MS spectrum (zoom) of **ON20**.

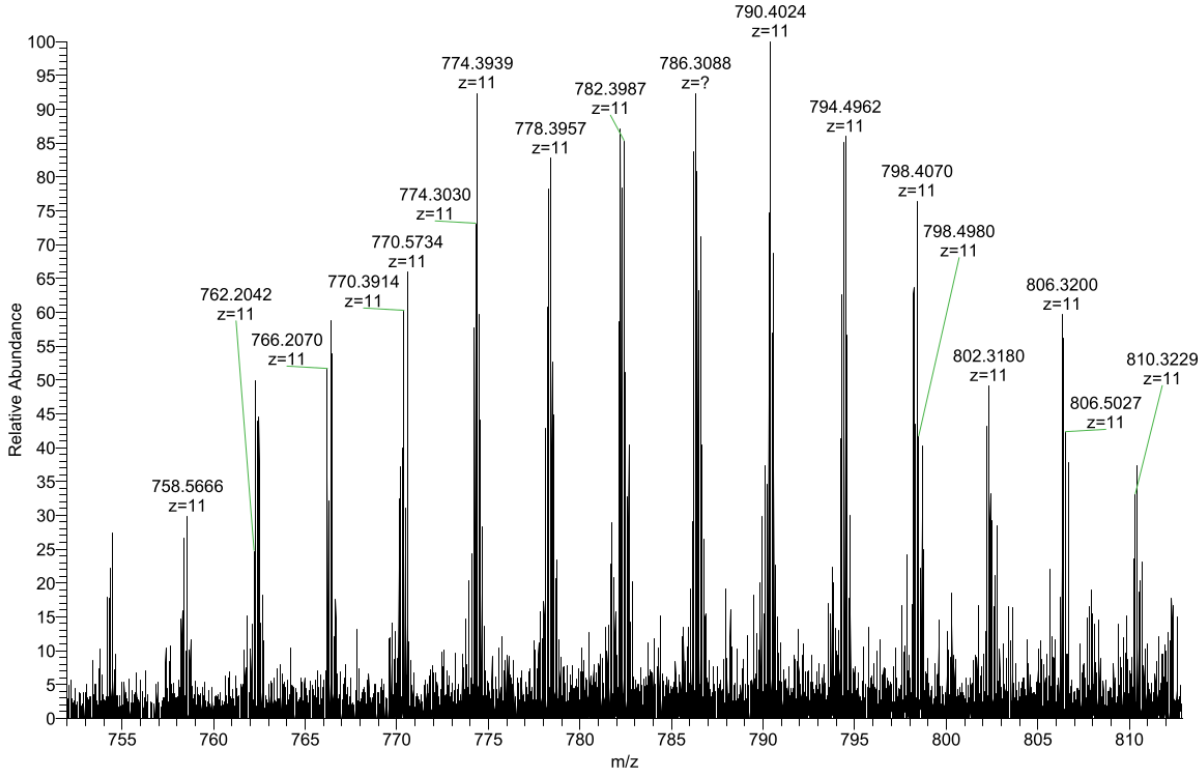

Figure 164. MS spectrum of **ON21**.

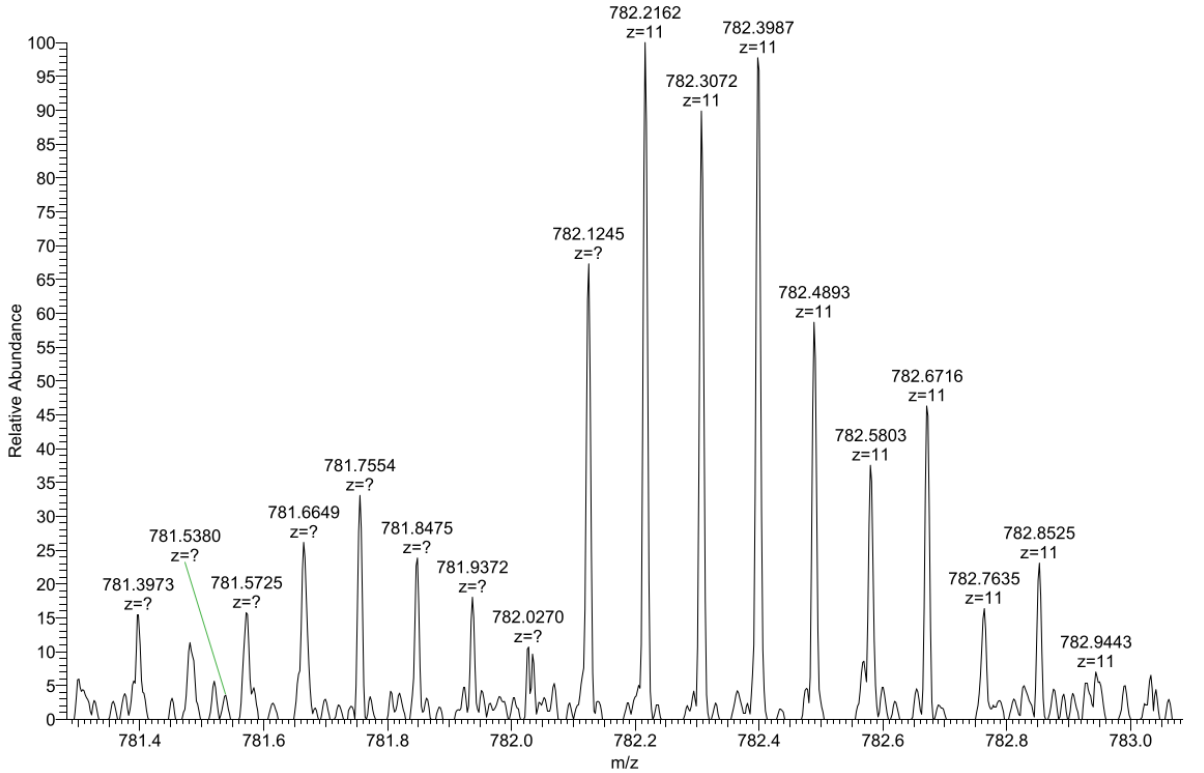

Figure 165. MS spectrum (zoom) of **ON21**.

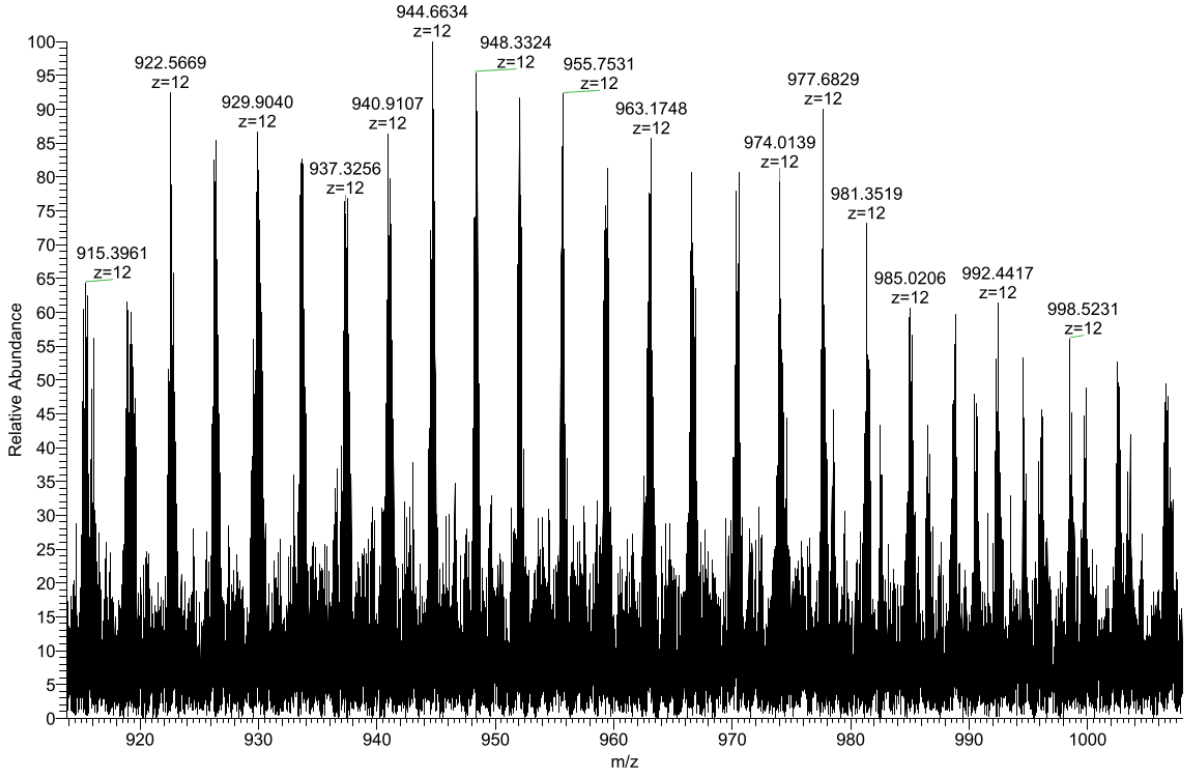

Figure 166. MS spectrum of **ON22**.

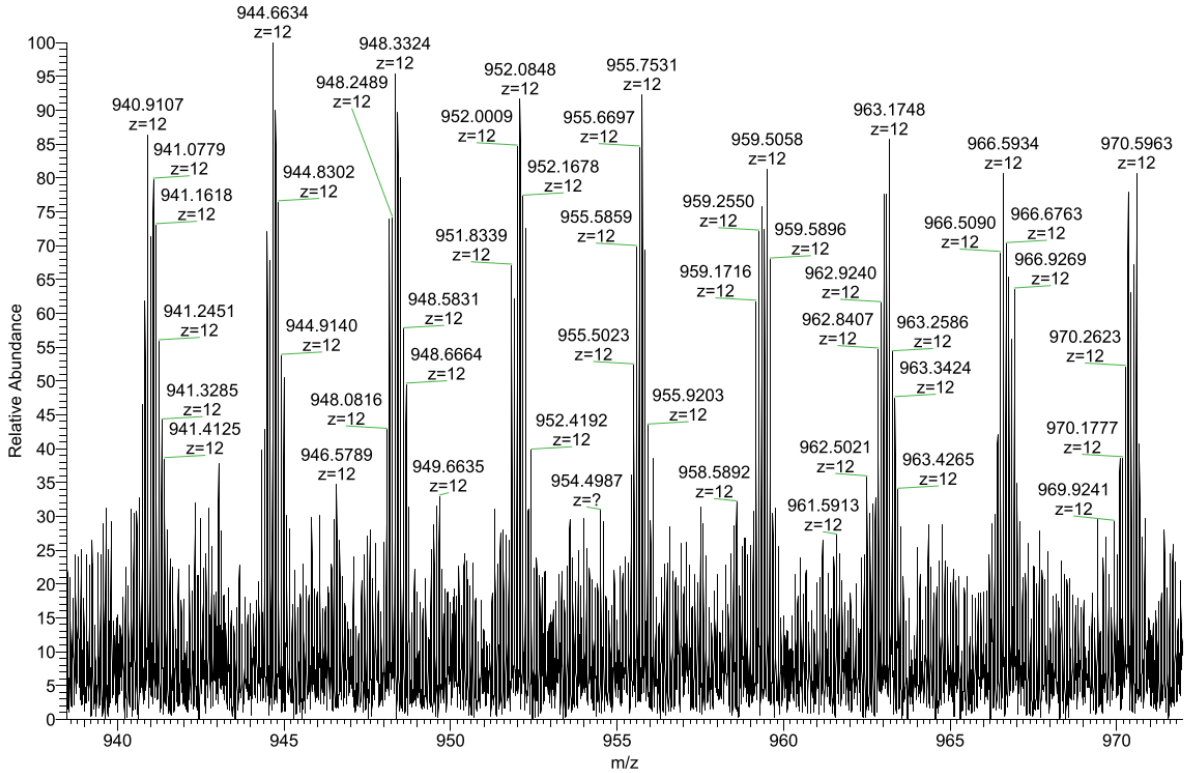

Figure 167. MS spectrum (zoom 1) of **ON22**.

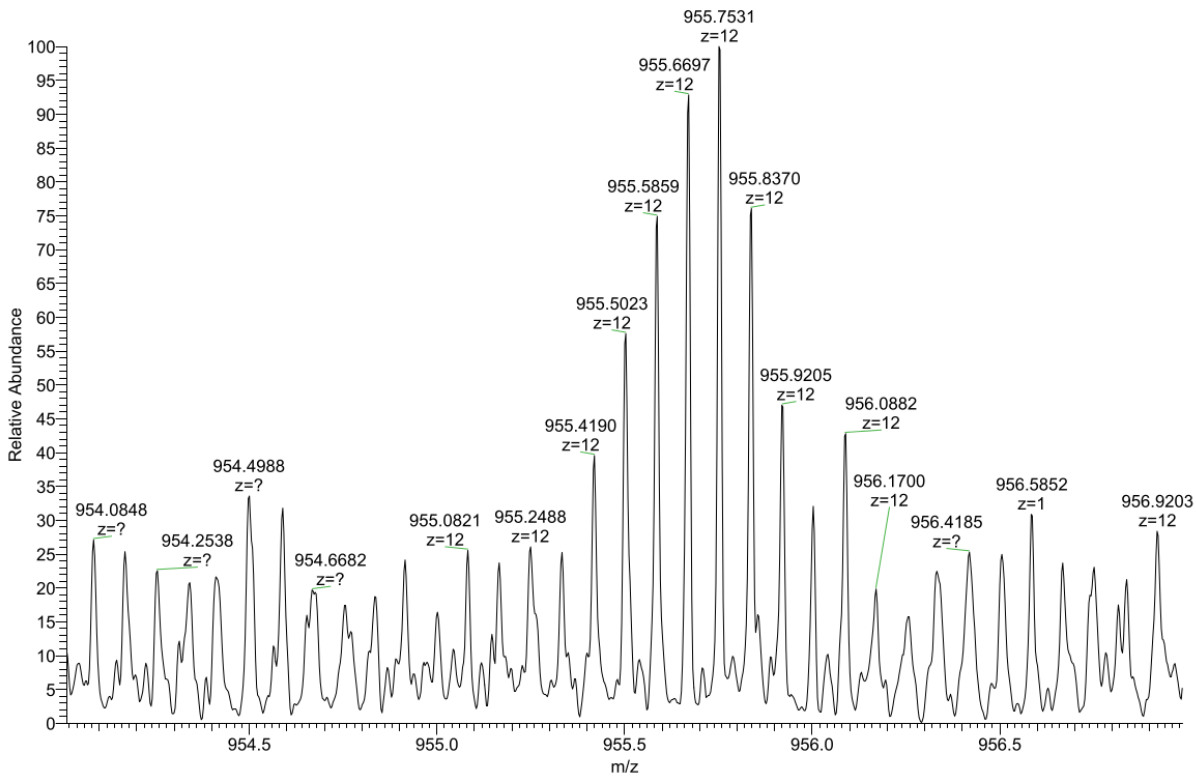

Figure 168. MS spectrum (zoom 2) of **ON22**.

5.3.2 Spectroscopic and Microscopic Measurements

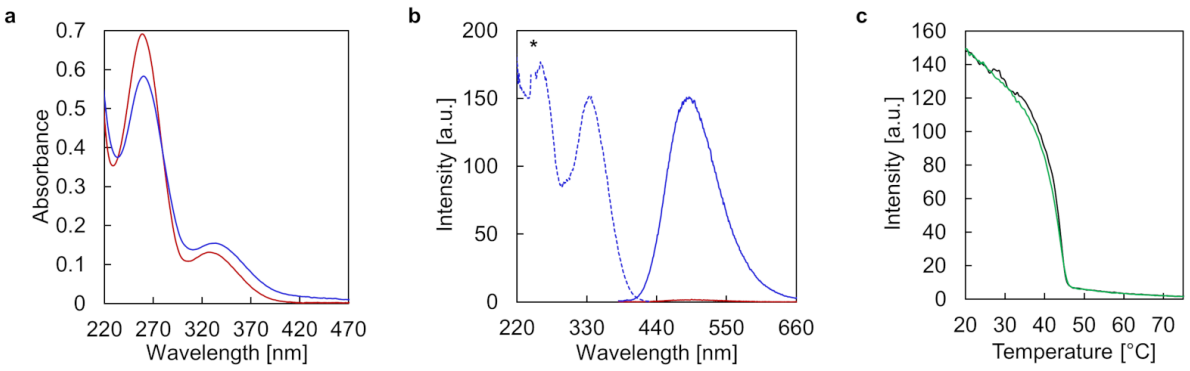

Figure 169. Temperature-dependent UV-Vis absorption (**a**), fluorescence emission (**b**, solid line) and excitation (**b**, dotted line) spectra of **ON9*ON18** at 75 °C (red) and at 20 °C (blue) after thermally controlled assembly (0.5 °C/min; * denotes second-order diffraction). (**c**) Fluorescence-monitored annealing (black) and melting (green) curves of **ON9*ON18**. Conditions: 1 µM **ON9*ON18**, 10 mM sodium phosphate buffer pH 7.2, 0.1 mM spermine · 4 HCl, 30 vol% ethanol, $\lambda_{ex.}$: 335 nm, $\lambda_{em.}$: 490 nm.

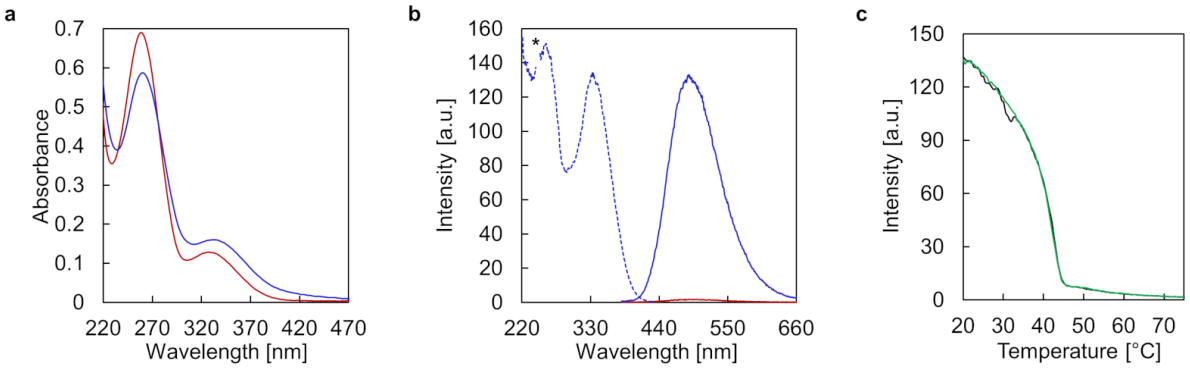

Figure 170. Temperature-dependent UV-Vis absorption (**a**), fluorescence emission (**b**, solid line) and excitation (**b**, dotted line) spectra of **ON9*ON20** at 75 °C (red) and at 20 °C (blue) after thermally controlled assembly (0.5 °C/min; * denotes second-order diffraction). (**c**) Fluorescence-monitored annealing (black) and melting (green) curves of **ON9*ON20**. Conditions: 1 µM **ON9*ON20**, 10 mM sodium phosphate buffer pH 7.2, 0.1 mM spermine · 4 HCl, 30 vol% ethanol, $\lambda_{ex.}$: 335 nm, $\lambda_{em.}$: 490 nm.

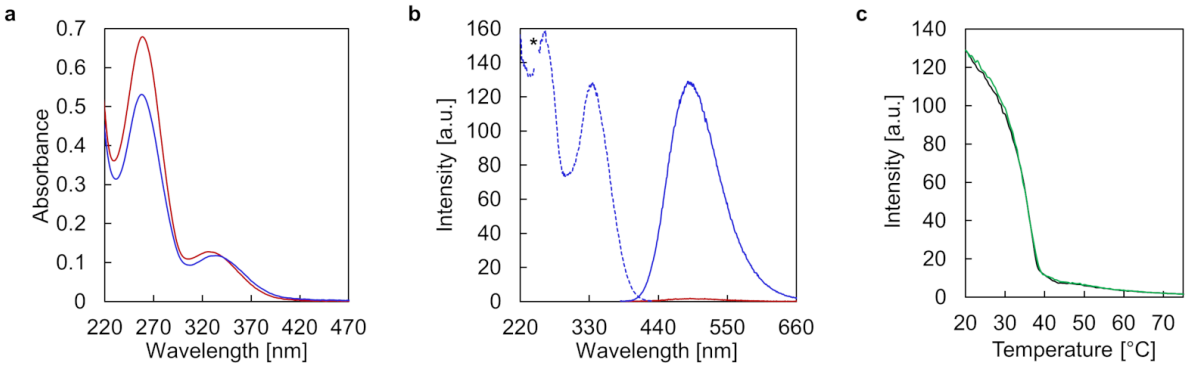

Figure 171. Temperature-dependent UV-Vis absorption (**a**), fluorescence emission (**b**, solid line) and excitation (**b**, dotted line) spectra of **ON9*ON21** at 75 °C (red) and at 20 °C (blue) after thermally controlled assembly (0.5 °C/min; * denotes second-order diffraction). (**c**) Fluorescence-monitored annealing (black) and melting (green) curves of **ON9*ON21**. Conditions: 1 µM **ON9*ON21**, 10 mM sodium phosphate buffer pH 7.2, 0.1 mM spermine · 4 HCl, 30 vol% ethanol, $\lambda_{ex.}$: 335 nm, $\lambda_{em.}$: 490 nm.

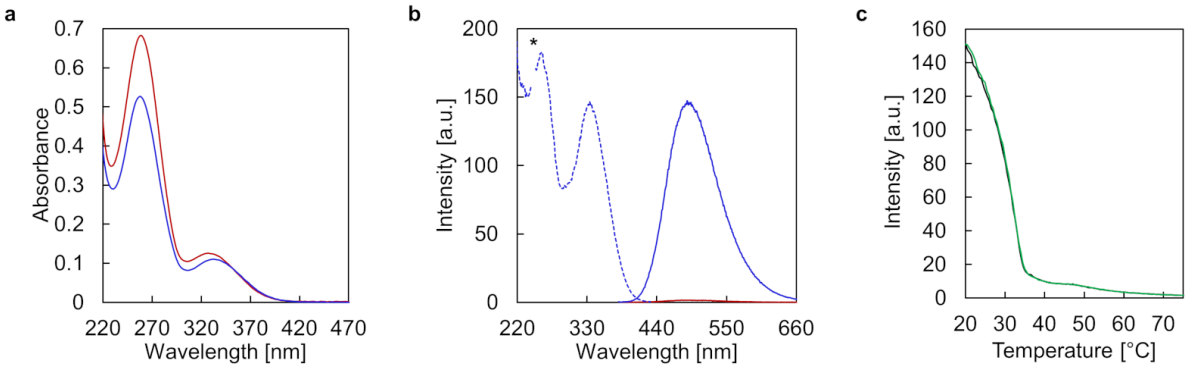

Figure 172. Temperature-dependent UV-Vis absorption (**a**), fluorescence emission (**b**, solid line) and excitation (**b**, dotted line) spectra of **ON9*ON22** at 75 °C (red) and at 20 °C (blue) after thermally controlled assembly (0.5 °C/min; * denotes second-order diffraction). (**c**) Fluorescence-monitored annealing (black) and melting (green) curves of **ON9*ON22**. Conditions: 1 µM **ON9*ON22**, 10 mM sodium phosphate buffer pH 7.2, 0.1 mM spermine · 4 HCl, 30 vol% ethanol, $\lambda_{ex.}$: 335 nm, $\lambda_{em.}$: 490 nm.

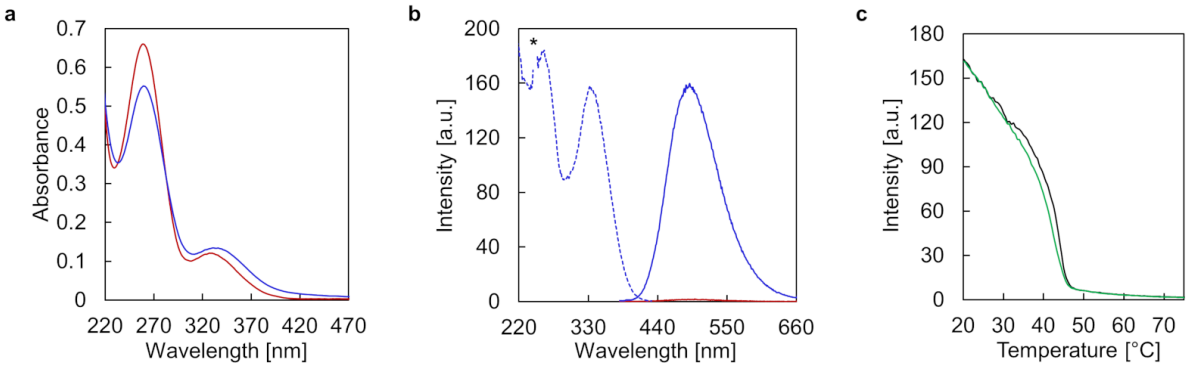

Figure 173. Temperature-dependent UV-Vis absorption (**a**), fluorescence emission (**b**, solid line) and excitation (**b**, dotted line) spectra of **ON9*ON19** at 75 °C (red) and at 20 °C (blue) after thermally controlled assembly (0.5 °C/min; * denotes second-order diffraction). (**c**) Fluorescence-monitored annealing (black) and melting (green) curves of **ON9*ON19**. Conditions: 1 µM **ON9*ON19**, 10 mM sodium phosphate buffer pH 7.2, 0.1 mM spermine · 4 HCl, 30 vol% ethanol, $\lambda_{ex.}$: 335 nm, $\lambda_{em.}$: 490 nm.

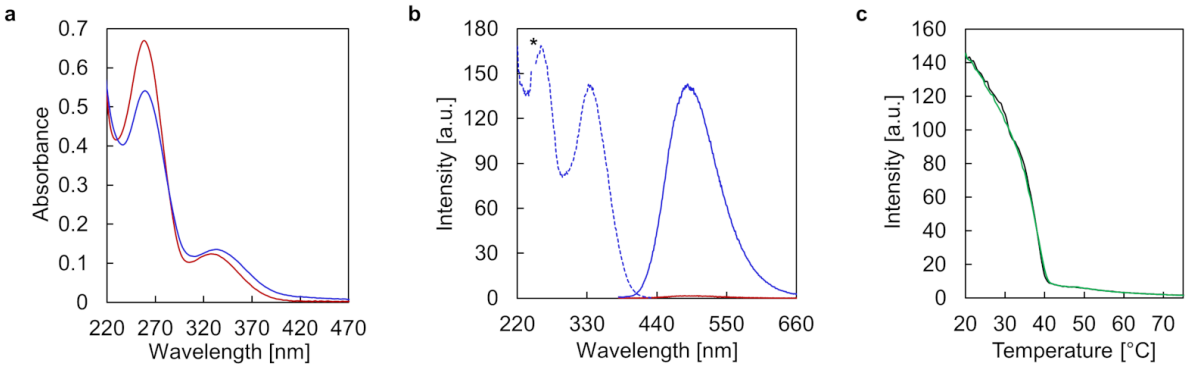

Figure 174. Temperature-dependent UV-Vis absorption (**a**), fluorescence emission (**b**, solid line) and excitation (**b**, dotted line) spectra of **ON9*ON23** at 75 °C (red) and at 20 °C (blue) after thermally controlled assembly (0.5 °C/min; * denotes second-order diffraction). (**c**) Fluorescence-monitored annealing (black) and melting (green) curves of **ON9*ON23**. Conditions: 1 µM **ON9*ON23**, 10 mM sodium phosphate buffer pH 7.2, 0.1 mM spermine · 4 HCl, 30 vol% ethanol, $\lambda_{ex.}$: 335 nm, $\lambda_{em.}$: 490 nm.

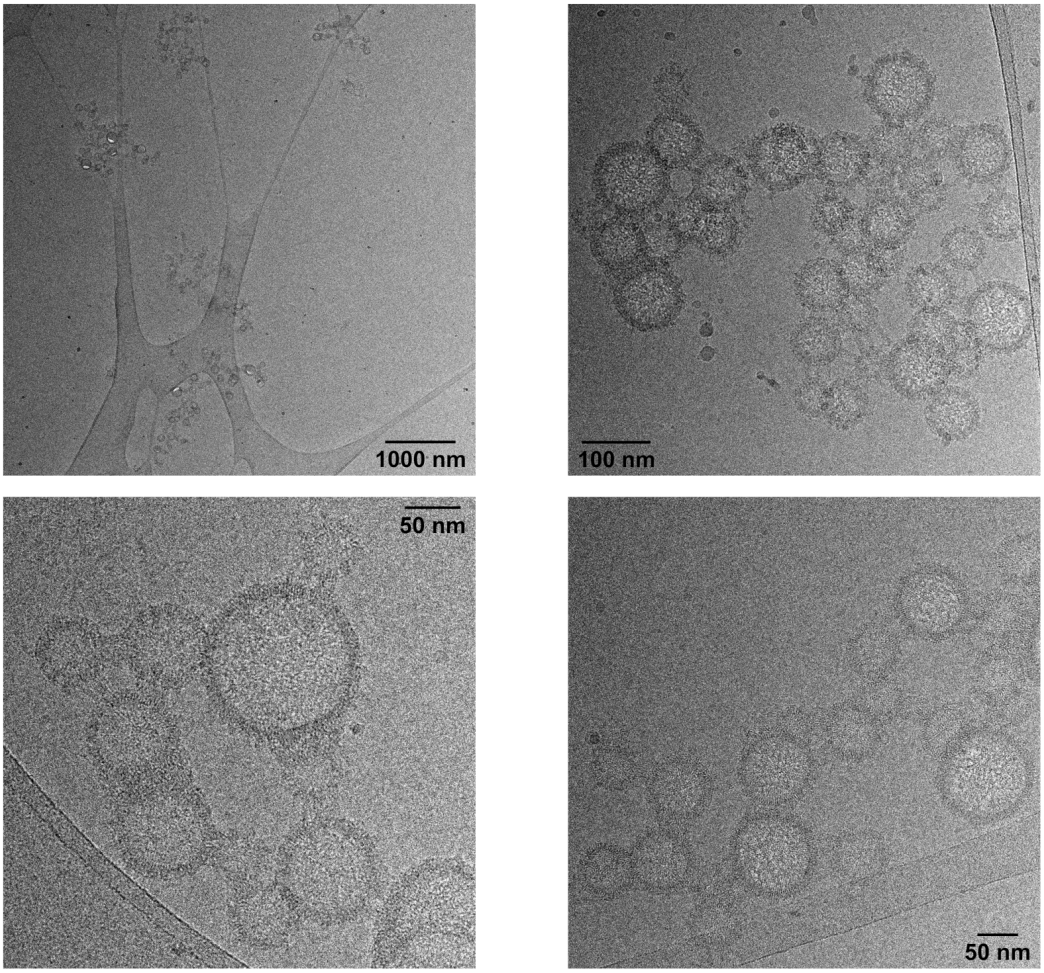

Figure 175. Additional cryo-EM images of self-assembled **ON9*ON18**. Conditions: 1 µM **ON9*ON18**, 10 mM sodium phosphate buffer pH 7.2, 0.1 mM spermine · 4 HCl, 30 vol% ethanol.

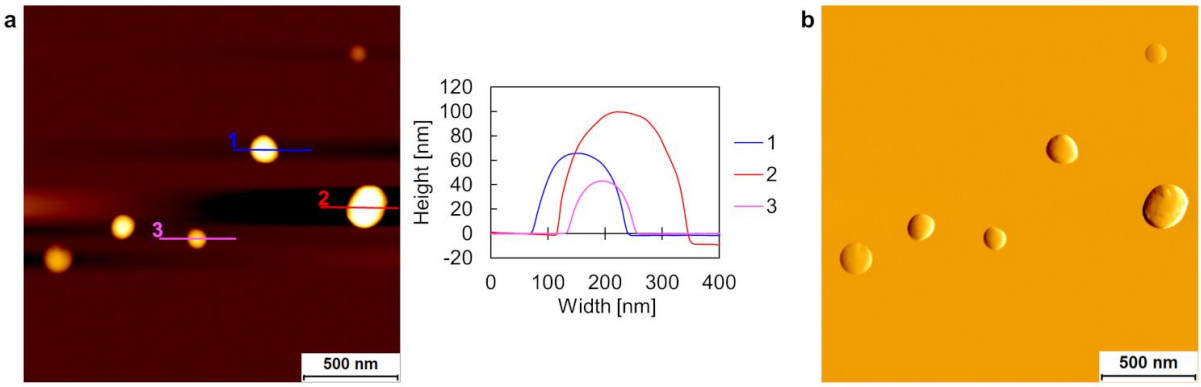

Figure 176. (**a**) Additional AFM image with corresponding cross sections and (**b**) deflection scan of aggregated **ON9*ON18**. Conditions: 1 µM **ON9*ON18**, 10 mM sodium phosphate buffer pH 7.2, 0.1 mM spermine · 4 HCl, 30 vol% ethanol.

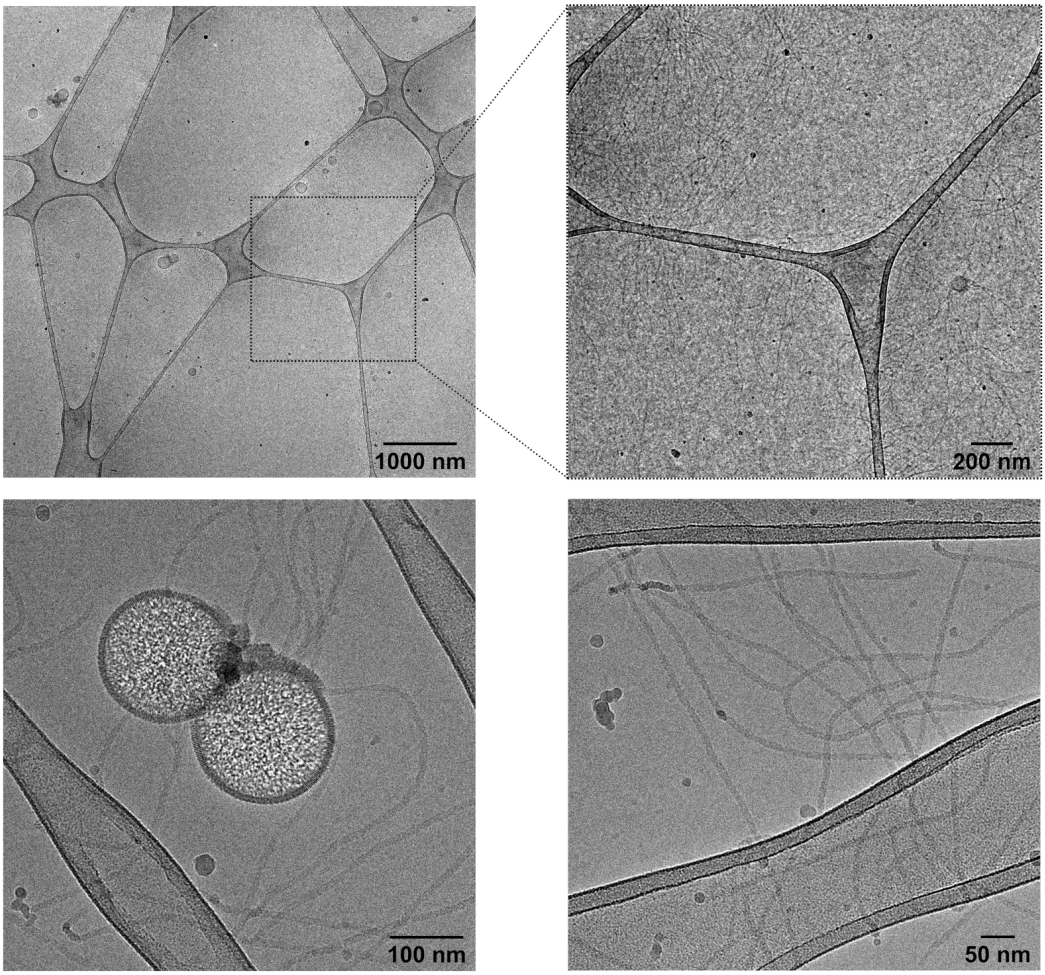

Figure 177. Additional cryo-EM images of self-assembled **ON9*ON21**. Conditions: 1 µM **ON9*ON21**, 10 mM sodium phosphate buffer pH 7.2, 0.1 mM spermine · 4 HCl, 30 vol% ethanol.

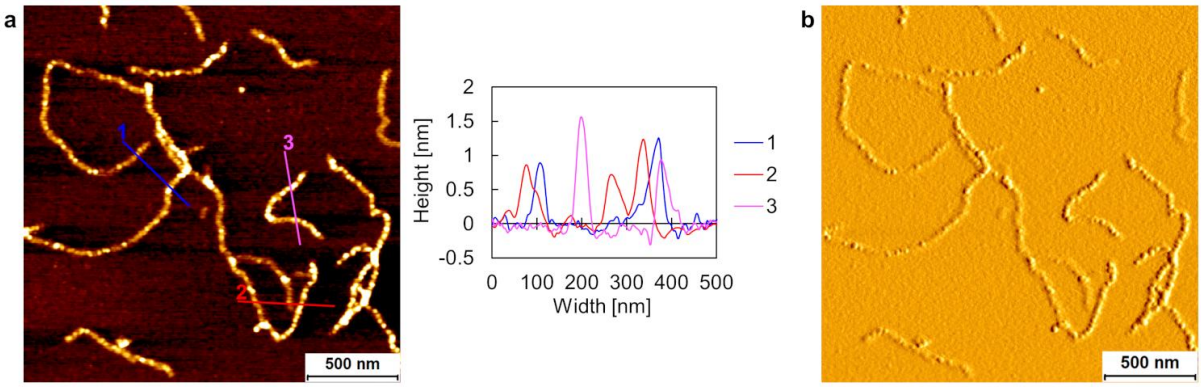

Figure 178. (**a**) Additional AFM image with corresponding cross sections and (**b**) deflection scan of aggregated **ON9*ON21**. Conditions: 1 µM **ON9*ON21**, 10 mM sodium phosphate buffer pH 7.2, 0.1 mM spermine · 4 HCl, 30 vol% ethanol.

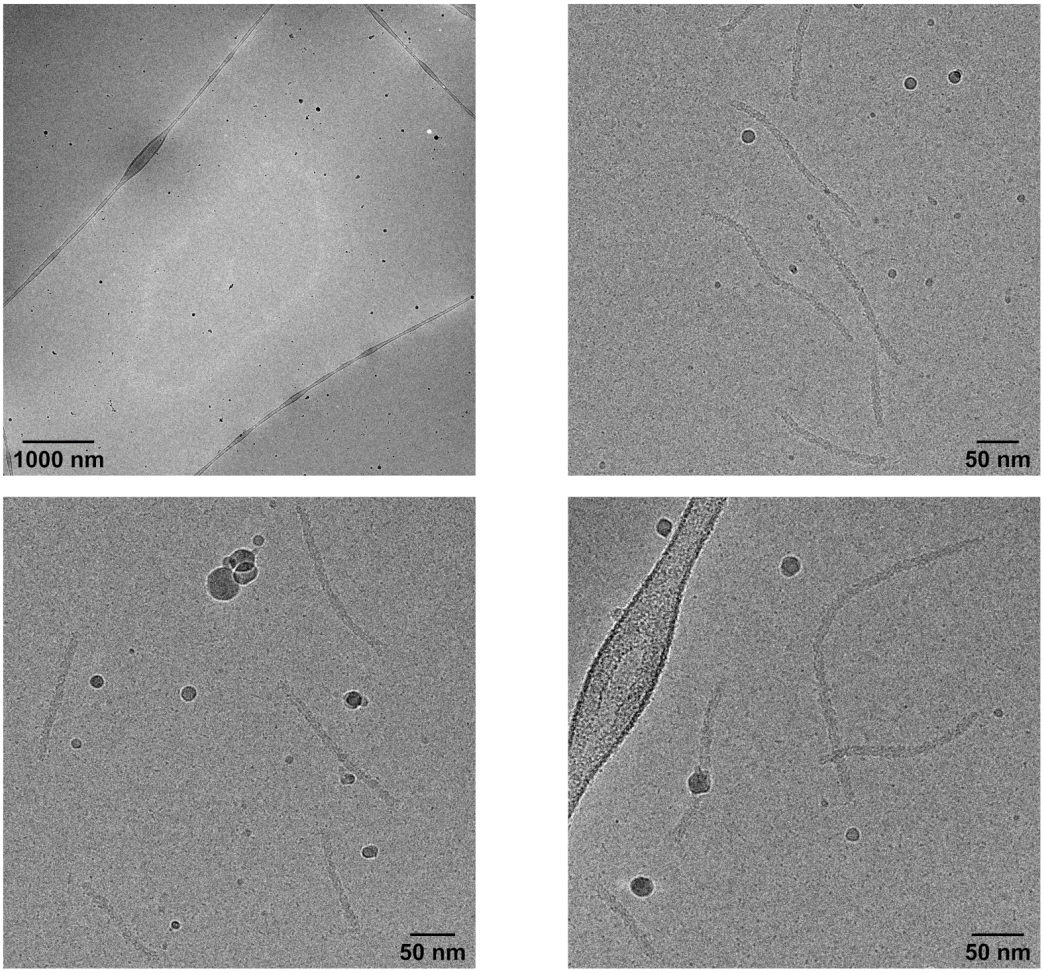

Figure 179. Additional cryo-EM images of self-assembled **ON9*ON22**. Conditions: 1 µM **ON9*ON22**, 10 mM sodium phosphate buffer pH 7.2, 0.1 mM spermine · 4 HCl, 30 vol% ethanol.

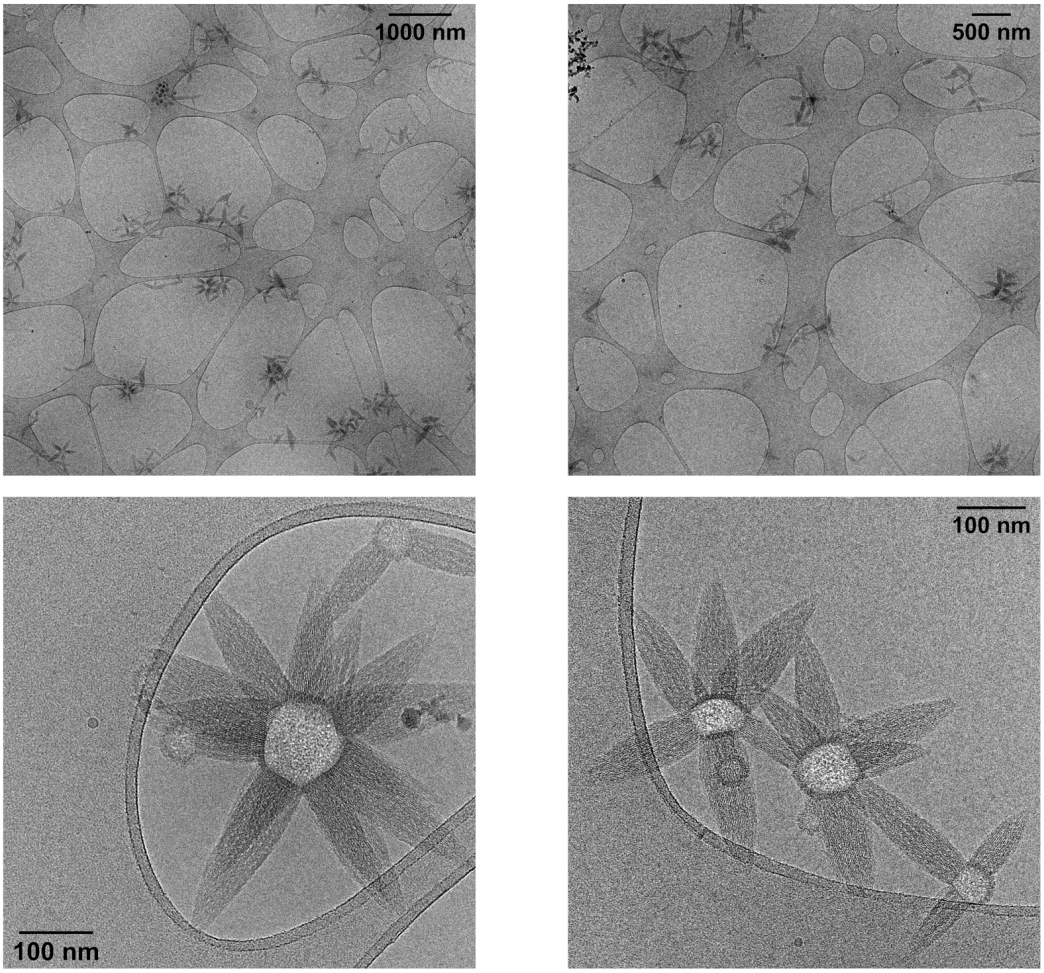

Figure 180. Additional cryo-EM images of self-assembled **ON9*ON23**. Conditions: 1 µM **ON9*ON23**, 10 mM sodium phosphate buffer pH 7.2, 0.1 mM spermine · 4 HCl, 30 vol% ethanol.

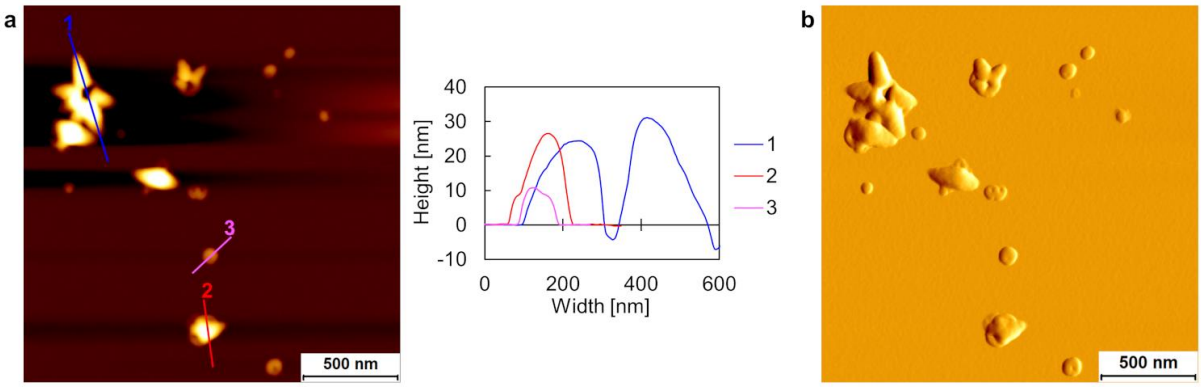

Figure 181. (**a**) Additional AFM image with corresponding cross sections and (**b**) deflection scan of aggregated **ON9*ON23**. Conditions: 1 µM **ON9*ON23**, 10 mM sodium phosphate buffer pH 7.2, 0.1 mM spermine · 4 HCl, 30 vol% ethanol.

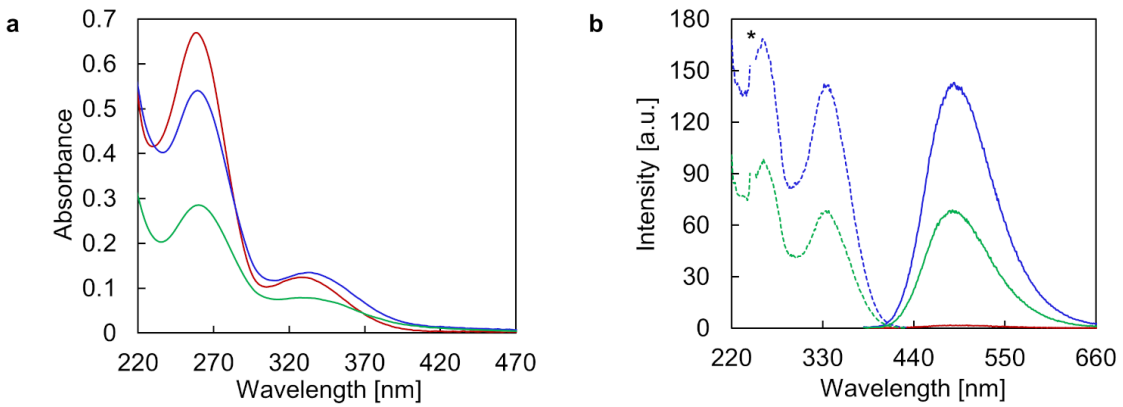

Figure 182. (**a**) UV-Vis absorption and (**b**) fluorescence emission (solid line) and excitation (dotted line) spectra of **ON9*ON23** at 75 °C (red), at 20 °C after thermally controlled assembly (blue), and at 20 °C after removal of the ethanol by dialysis (green). Conditions: 1 µM **ON9*ON23**, 10 mM sodium phosphate buffer pH 7.2, 0.1 mM spermine · 4 HCl, 30 resp. <0.5 vol% ethanol, $\lambda_{ex.}$: 335 nm, $\lambda_{em.}$: 490 nm, * denotes second-order diffraction.

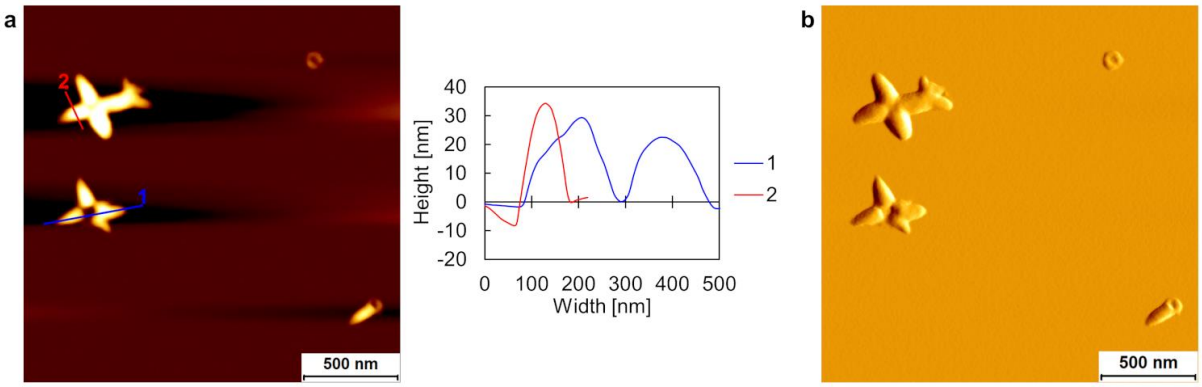

Figure 183. (**a**) Additional AFM image with corresponding cross sections and (**b**) deflection scan of aggregated **ON9*ON23** after dialyzing off the ethanol fraction. Conditions: 1 µM **ON9*ON23**, 10 mM sodium phosphate buffer pH 7.2, 0.1 mM spermine · 4 HCl, <0.5 vol% ethanol.

Table 9. Additional information about purchased ASGR.

Supplier	antibodies-online GmbH (catalog number: ABIN1096055)
UniProt entry	P07306
Sequence (N→C)	QNSQLQEELRGLRETFSNFTASTEAQVKGLSTQGGNVGRKMKSLESQLEKQQ KDLSEDHSSLLLHVKQFVSDLRSLSCQMAALQGNGSERTCCPVNWVEHERSC YWFSRSGKAWADADNYCRLEDAHLVVVTSWEEQKFVQHHIGPVNTWMGLH DQNGPWKWVDGTDYETGFKNWRPEQPDDWYGHGLGGGEDCAHFTDDGRW NDDVCQRPYRWVCETELDKASQEPPLLVDHHHHHH
Molecular weight	27.43 kDa

5.3.3 Cryo-EM Distance Measurements

Table 10. Summary of distance measurements. The reported distances are mean values with the corresponding standard deviation, along with the number of measurements in brackets.

Duplex	DNA length (vesicle)	DNA width	DNA length (ribbon)
ON9*ON18	10.7 ± 0.6 nm (*n* = 40)	2.5 ± 0.3 nm (*n* = 43)	–
ON9*ON21	10.0 ± 0.5 nm (*n* = 52)	2.4 ± 0.3 nm (*n* = 84)	10.1 ± 0.7 nm (*n* = 65)
ON9*ON22	–	–	10.2 ± 0.7 nm (*n* = 68)
ON9*ON23	10.5 ± 0.5 nm (*n* = 46)	2.5 ± 0.2 nm (*n* = 79)	–

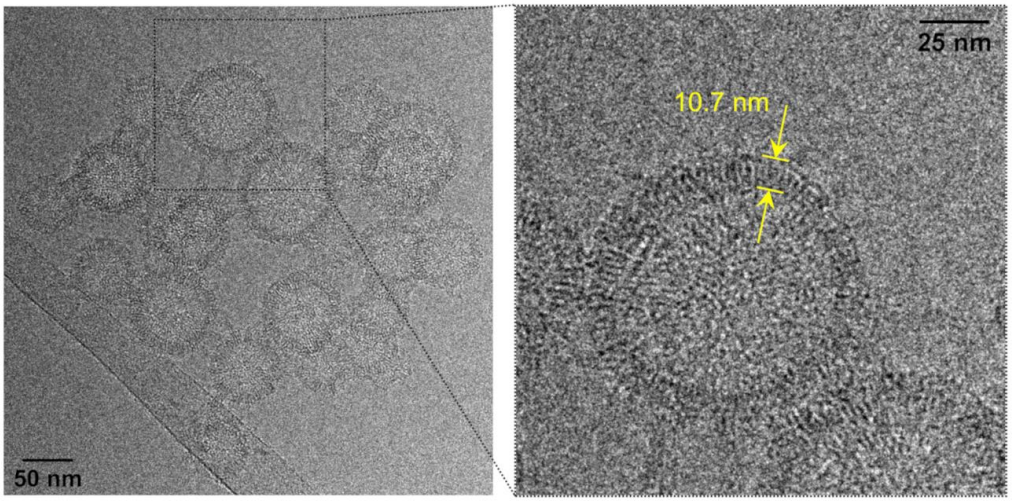

Figure 184. Representative DNA length (vesicle) measurement of self-assembled **ON9*ON18**. Conditions: 1 µM **ON9*ON18**, 10 mM sodium phosphate buffer pH 7.2, 0.1 mM spermine · 4 HCl, 30 vol% ethanol.

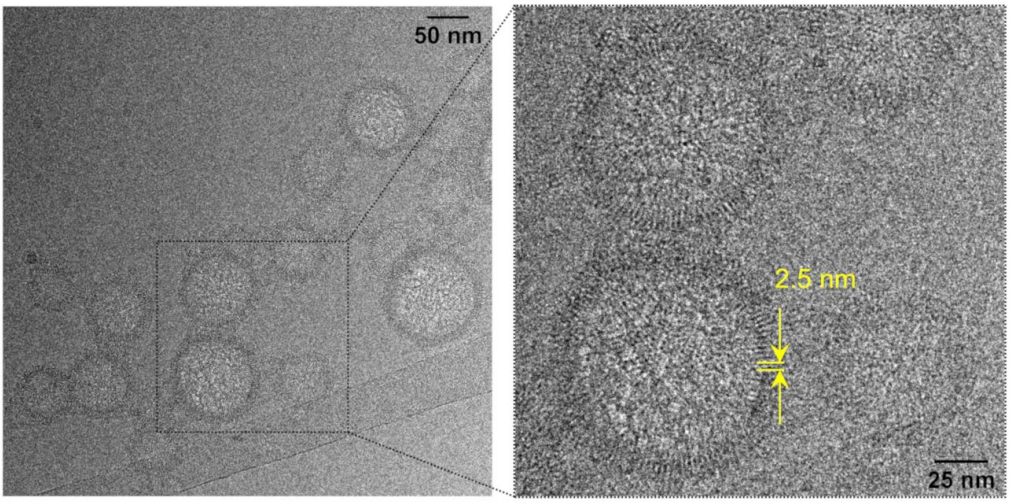

Figure 185. Representative DNA width measurement of self-assembled **ON9*ON18**. Conditions: 1 µM **ON9*ON18**, 10 mM sodium phosphate buffer pH 7.2, 0.1 mM spermine · 4 HCl, 30 vol% ethanol.

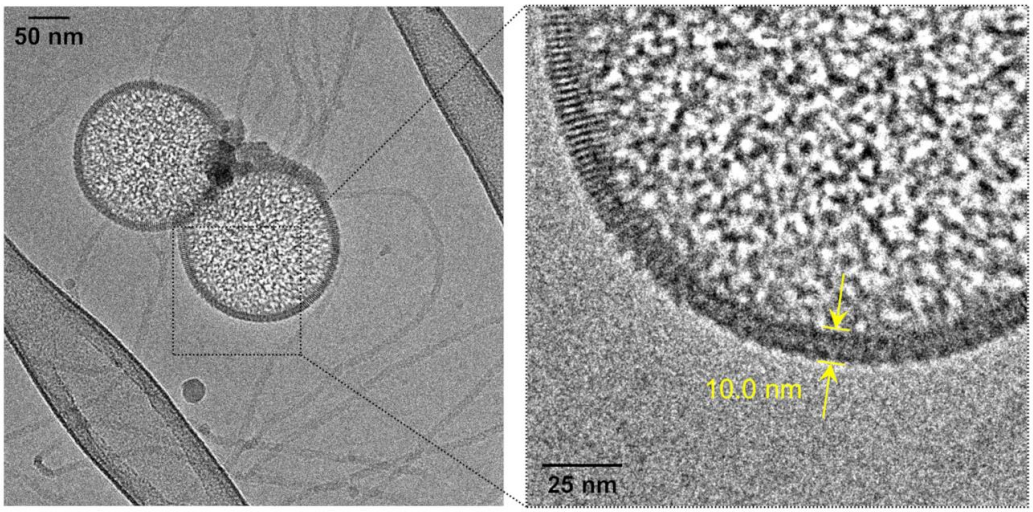

Figure 186. Representative DNA length (vesicle) measurement of self-assembled **ON9*ON21**. Conditions: 1 µM **ON9*ON21**, 10 mM sodium phosphate buffer pH 7.2, 0.1 mM spermine · 4 HCl, 30 vol% ethanol.

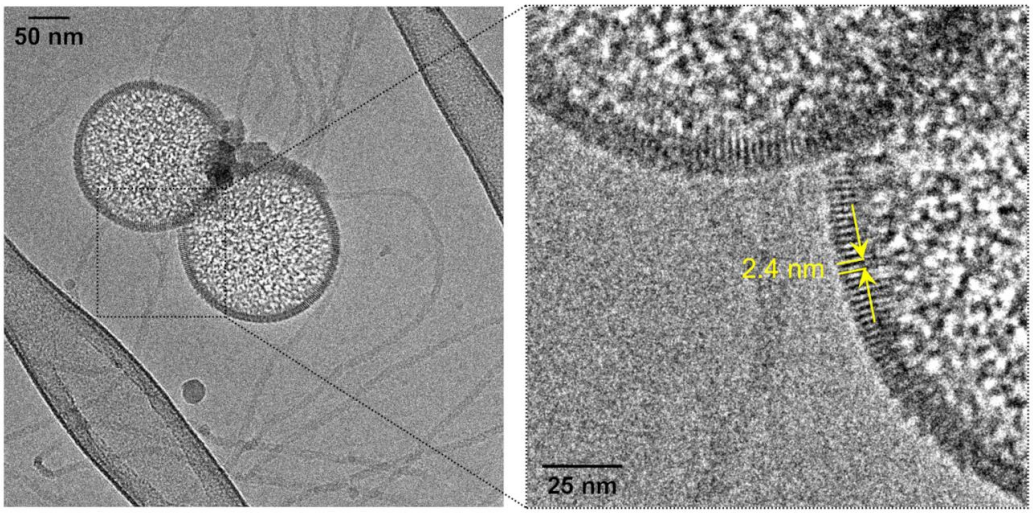

Figure 187. Representative DNA width measurement of self-assembled **ON9*ON21**. Conditions: 1 µM **ON9*ON21**, 10 mM sodium phosphate buffer pH 7.2, 0.1 mM spermine · 4 HCl, 30 vol% ethanol.

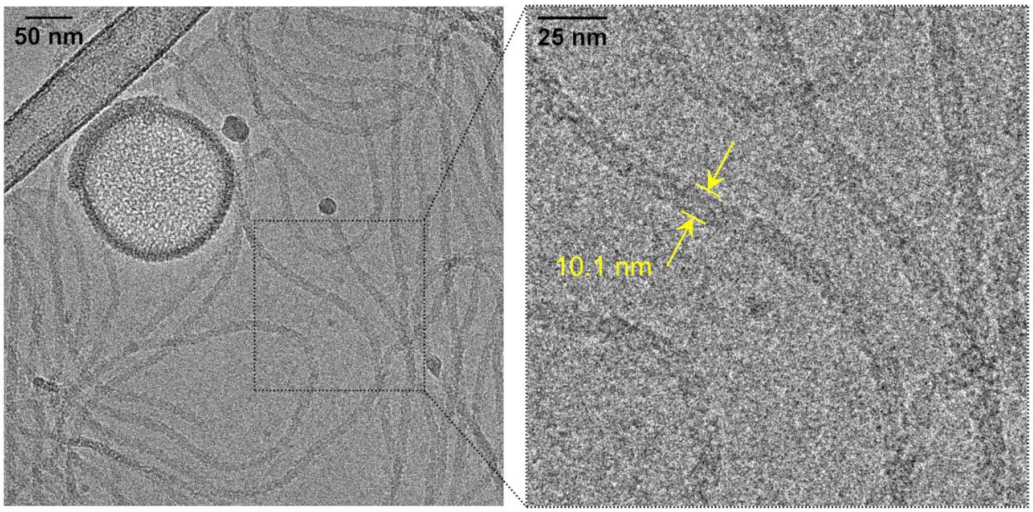

Figure 188. Representative DNA length (ribbon) measurement of self-assembled **ON9*ON21**. Conditions: 1 µM **ON9*ON21**, 10 mM sodium phosphate buffer pH 7.2, 0.1 mM spermine · 4 HCl, 30 vol% ethanol.

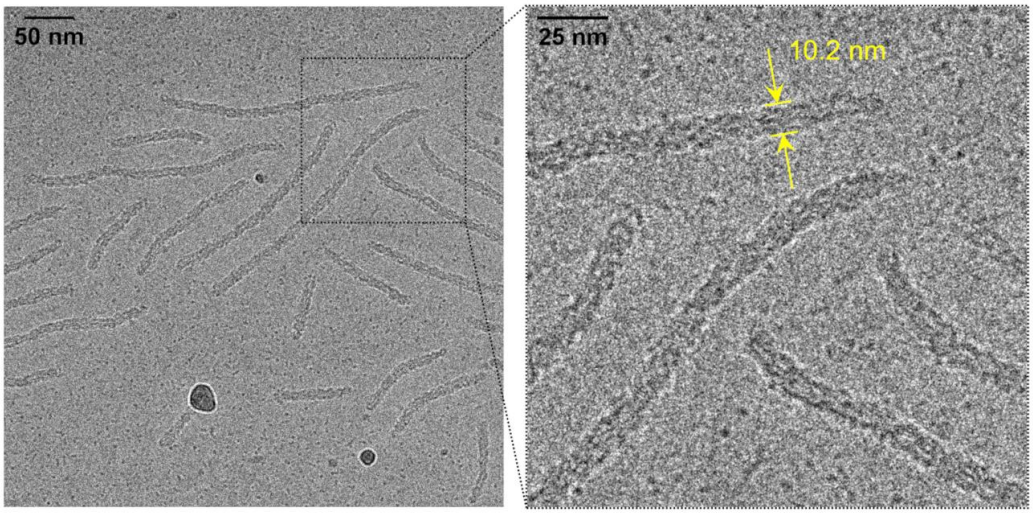

Figure 189. Representative DNA length (ribbon) measurement of self-assembled **ON9*ON22**. Conditions: 1 µM **ON9*ON22**, 10 mM sodium phosphate buffer pH 7.2, 0.1 mM spermine · 4 HCl, 30 vol% ethanol.

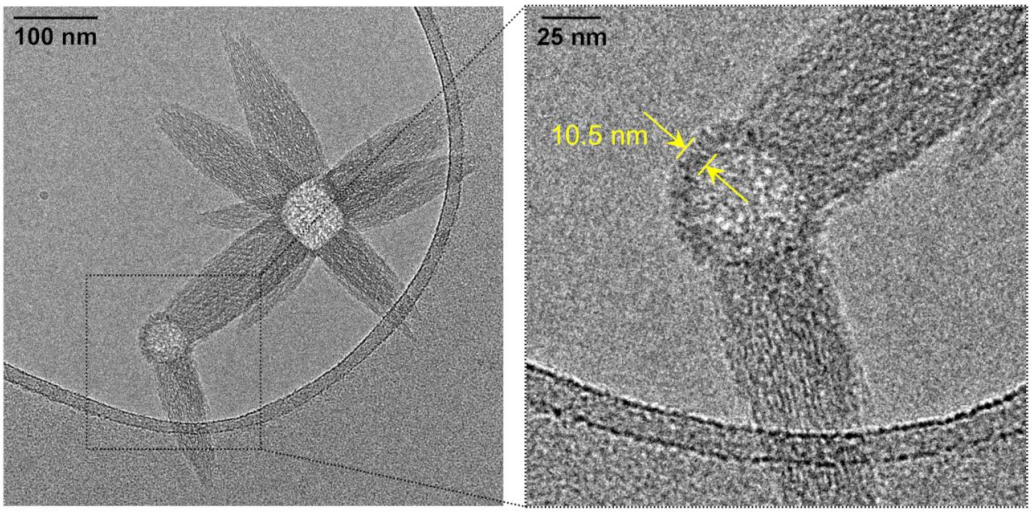

Figure 190. Representative DNA length (vesicle) measurement of self-assembled **ON9*ON23**. Conditions: 1 μM **ON9*ON23**, 10 mM sodium phosphate buffer pH 7.2, 0.1 mM spermine · 4 HCl, 30 vol% ethanol.

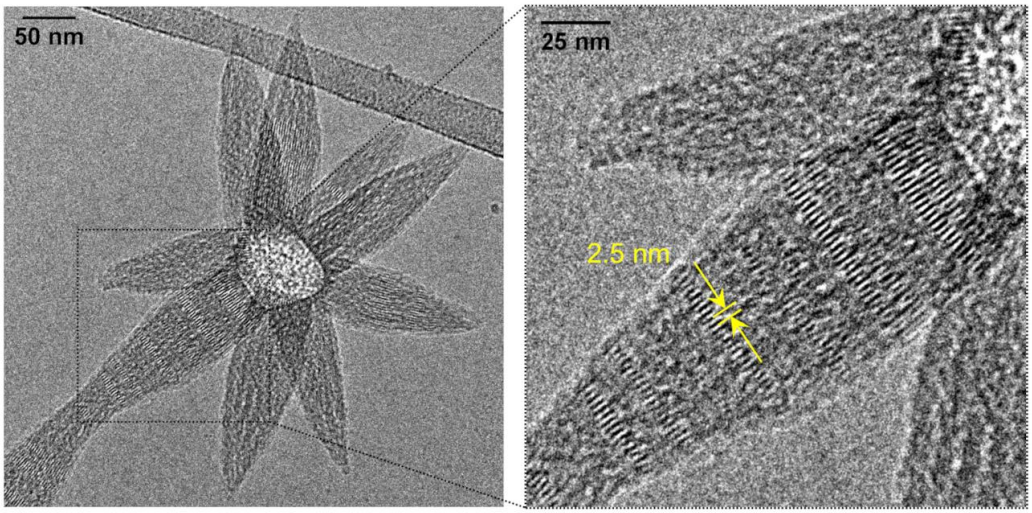

Figure 191. Representative DNA width measurement of self-assembled **ON9*ON23**. Conditions: 1 μM **ON9*ON23**, 10 mM sodium phosphate buffer pH 7.2, 0.1 mM spermine · 4 HCl, 30 vol% ethanol.

6 Supramolecular Assembly of a 40-mer DNA

The aim of this chapter is to investigate the supramolecular assembly behavior of an unmodified 40-mer DNA single strand hybridized to two 20 nucleotides long TPE-modified DNA single strands. The self-assembly behavior and thus, the resulting structural properties of the supramolecular constructs, was influenced by the number of TPE sticky ends. The approach presented herein advances the construction of DNA architectures, assembled from long, unmodified DNA single strands, stabilized by hydrophobic sticky end interactions rather than Watson-Crick base pairing only.

6.1 Results and Discussion

In this chapter, three different oligonucleotides were utilized, which are outlined in Figure 192a. Single-stranded TPE-DNA conjugates **ON2** and **ON9** consist of a 20-mer DNA, modified with three *E*-TPE units long overhangs either at the 3'-end only (**ON2**), or at the 3'-end as well as at the 5'-end (**ON9**). Thus, they only differ in the number of TPE sticky ends. The synthesis of these two oligomers is described in more detail in the chapters 3.3.3 and 4.3.1. HPLC purified, unmodified DNA single strand **ON24** was purchased from Microsynth (Switzerland). **ON24** is a 40-mer, which comprises two identical, repeating 20 nucleotides long sequences. This repeating 20-mer DNA sequence is complementary to the TPE-DNA conjugates **ON2** and **ON9**. Therefore, DNA duplexes as illustrated in Figure 192b can be formed in a 2:1 ratio between TPE-DNA conjugates and 40-mer DNA **ON24**. The two duplexes shown in Figure 192b are represented in a folded manner, where **ON24** reverses direction after 20 nucleotides. Like this, all TPE overhangs are located on the sides of the duplex, accessible for hydrophobic sticky end interactions. Alternatively, a straight 40-mer long DNA duplex could be formed, with the TPEs imagined being looped out of the double helix (this kind of duplex is not presented here). The effect of the number of sticky ends on the self-assembly behavior was investigated by spectroscopic measurements as well as AFM and cryo-EM imaging.

a

Strand	Sequence (5'→3')
ON2	CTT CCT TGC ATC GGA CCT TG-(*E*-TPE)$_3$
ON9	(*E*-TPE)$_3$-CTT CCT TGC ATC GGA CCT TG-(*E*-TPE)$_3$
ON24	CAA GGT CCG ATG CAA GGA AGC AAG GTC CGA TGC AAG GAA G

b

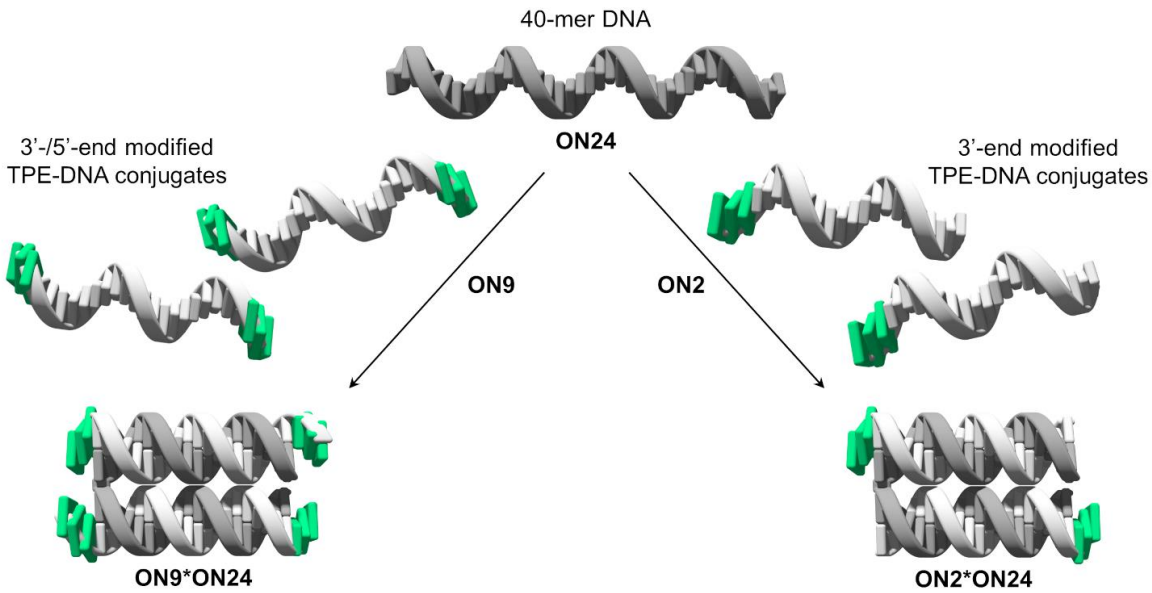

Figure 192. (**a**) Summary of the DNA sequences used in this study. For molecular structures of the modifications, see Figure 15a. (**b**) Two shorter TPE-modified DNA single strands hybridize to the 40-mer DNA single strand to form either **ON9*ON24** or **ON2*ON24** duplexes, represented in a folded manner.

The self-assembly behaviors of the two duplexes **ON9*ON24** and **ON2*ON24** were investigated under their respective optimized conditions. Accordingly, they differ in the ethanol fraction, which is 30 vol% for **ON9*ON24** and 20 vol% for **ON2*ON24**. Figure 193a and Figure 193b show the temperature-dependent UV-Vis absorption and fluorescence spectra, at 75 °C and at 20 °C after controlled cooling (0.5 °C/min). The spectroscopic changes upon cooling are in agreement with the observations described in chapter 3.1.3 for the 3'-end modified duplex **ON1*ON2**. The fluorescence-monitored annealing curves, displayed in Figure 193c, demonstrate the AIE behavior of **ON9*ON24** and **ON2*ON24**. Both of them suggest a cooperative nucleation-elongation supramolecular assembly process.[179–185] A nucleation temperature of 53 °C was determined for **ON9*ON24** and a T_{FL}(nucleation) of 55 °C for **ON2*ON24**. While **ON2*ON24** shows no apparent hysteresis between the annealing and melting curve, a slight hysteresis of about 1 °C is visible for **ON9*ON24**.

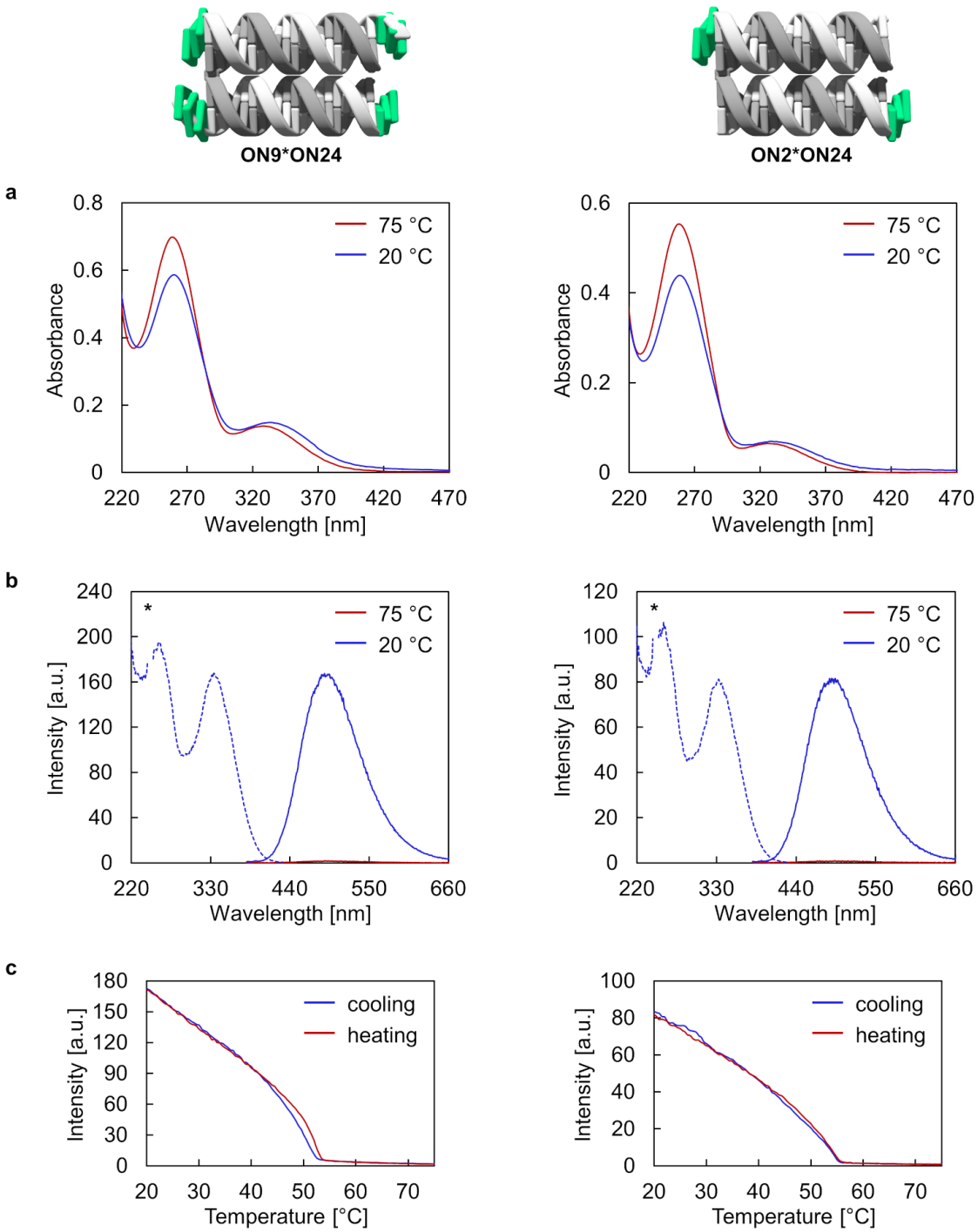

Figure 193. Temperature-dependent UV-Vis absorption spectra (**a**), temperature-dependent fluorescence emission (solid line) and excitation (dotted line) spectra (**b**), and fluorescence-monitored annealing and melting curves (**c**) of **ON9*ON24** (left) and **ON2*ON24** (right). Conditions: 1 µM TPE-modified DNA single strand, 0.5 µM **ON24**, 10 mM sodium phosphate buffer pH 7.2, 0.1 mM spermine · 4 HCl, 30 vol% ethanol (for **ON9*ON24**) resp. 20 vol% ethanol (for **ON2*ON24**), $\lambda_{ex.}$: 335 nm, $\lambda_{em.}$: 490 nm, gradient: 0.5 °C/min, * denotes second-order diffraction.

After conducting a thermal assembly process (cooling the sample solution from 75 °C to 20 °C, 0.5 °C/min), the nanostructures were imaged by AFM. Individual, spherical self-assemblies with varying sizes were detected in the overview scan of assembled **ON9*ON24** (Figure 194a). Together with the zoom image in Figure 194b, it seems that the vesicles can roughly be classified into two different size ranges. The smaller vesicular morphology exhibits heights around 10–20 nm, while the larger assemblies reach heights of up to 80 nm and diameters of about 100–150 nm. Hence, the vesicular assemblies are in a similar size range as previously described for the nanostructures assembled from the 20-mer DNA analogue **ON5*ON9** under identical conditions (see Figure 94).

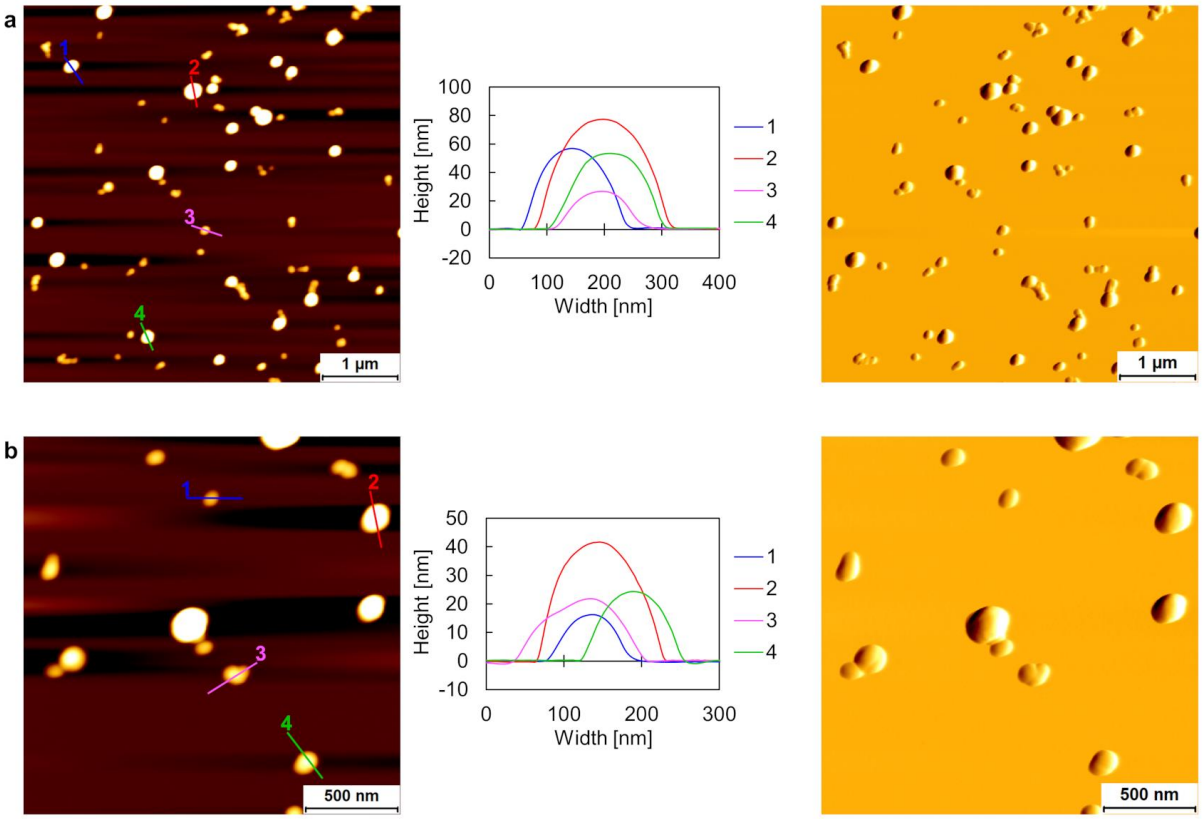

Figure 194. AFM overview scan (**a**) and zoom image (**b**) with corresponding cross sections and deflection scan of assembled **ON9*ON24**. Conditions: 1 µM **ON9**, 0.5 µM **ON24**, 10 mM sodium phosphate buffer pH 7.2, 0.1 mM spermine · 4 HCl, 30 vol% ethanol.

On the other hand, only small vesicular assemblies were found for aggregated **ON2*ON24** (Figure 195). These supramolecular arrays appear with an average height between 20–30 nm for single vesicles and slightly higher for agglomerated structures. Apart from the smaller size range of **ON2*ON24** compared to **ON9*ON24**, the second difference resides in the degree of agglomeration of the nanostructures. Assemblies of **ON2*ON24** tend to agglomerate into larger, undefined aggregates. Therefore, only the vesicles assembled from **ON9*ON24** were further analyzed by cryo-EM experiments.

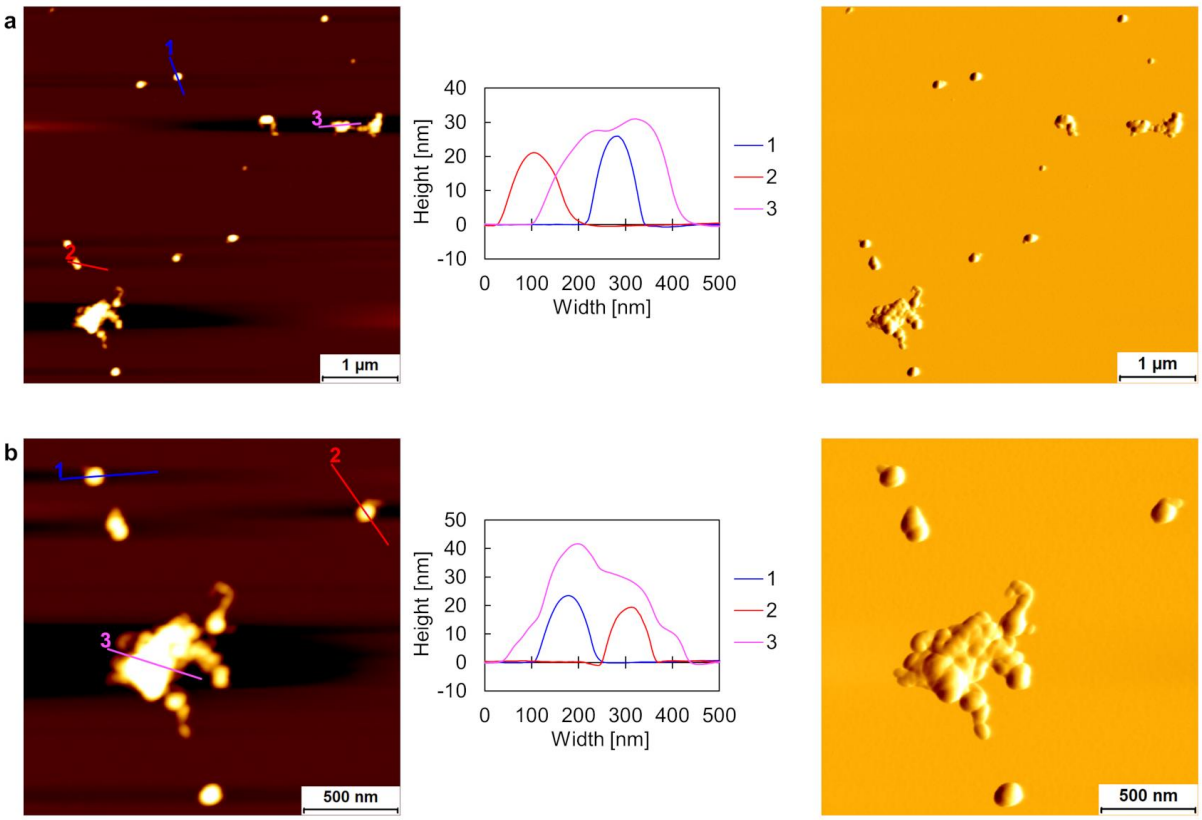

Figure 195. AFM overview scan (**a**) and zoom image (**b**) with corresponding cross sections and deflection scan of assembled **ON2*ON24**. Conditions: 1 µM **ON2**, 0.5 µM **ON24**, 10 mM sodium phosphate buffer pH 7.2, 0.1 mM spermine · 4 HCl, 20 vol% ethanol.

Cryo-EM experiments were performed in collaboration with Prof. Dr. Benoît Zuber and Dr. Ioan Iacovache from the Institute of Anatomy of the University of Bern. Depicted in Figure 196 are cryo-EM images of the nanostructures assembled from **ON9*ON24**. They show individual vesicular constructs with diameters in the range between 75 nm and 200 nm. The inset in Figure 196 discloses the duplex arrangement and demonstrates a columnar DNA alignment, classifying these nanostructures as type II vesicles (analogous to the architecture from **ON1*ON2**, Figure 22). The regular distance between the

rod-like pattern was measured to be 2.4 ± 0.3 nm (see section 6.3.1), which again correlates to the DNA width of the duplex **ON9*ON24**. A membrane thickness of 13.7 ± 1.6 nm was measured. Taking all the distance measurements of this thesis into account, the standard deviation of 1.6 nm is the largest standard deviation obtained, despite that a similar number of individual distance measurements have been considered. This restricts to some extent the unambiguous assignment of the exact DNA duplex alignment. Particularly, to answer the question if the duplexes are folded (as illustrated schematically in Figure 196) or entirely straight. Nonetheless, it is speculated that duplex **ON9*ON24** might be folded by different arbitrary angles between the two 20-mer DNA segments, that give eventually rise to the observed continuous thicknesses of the vesicular membrane. This is supported by the fact that no obvious staircase-like increase can be observed, which could correspond either to an additional layer of folded duplexes or the transition from a folded to a straight DNA duplex alignment.

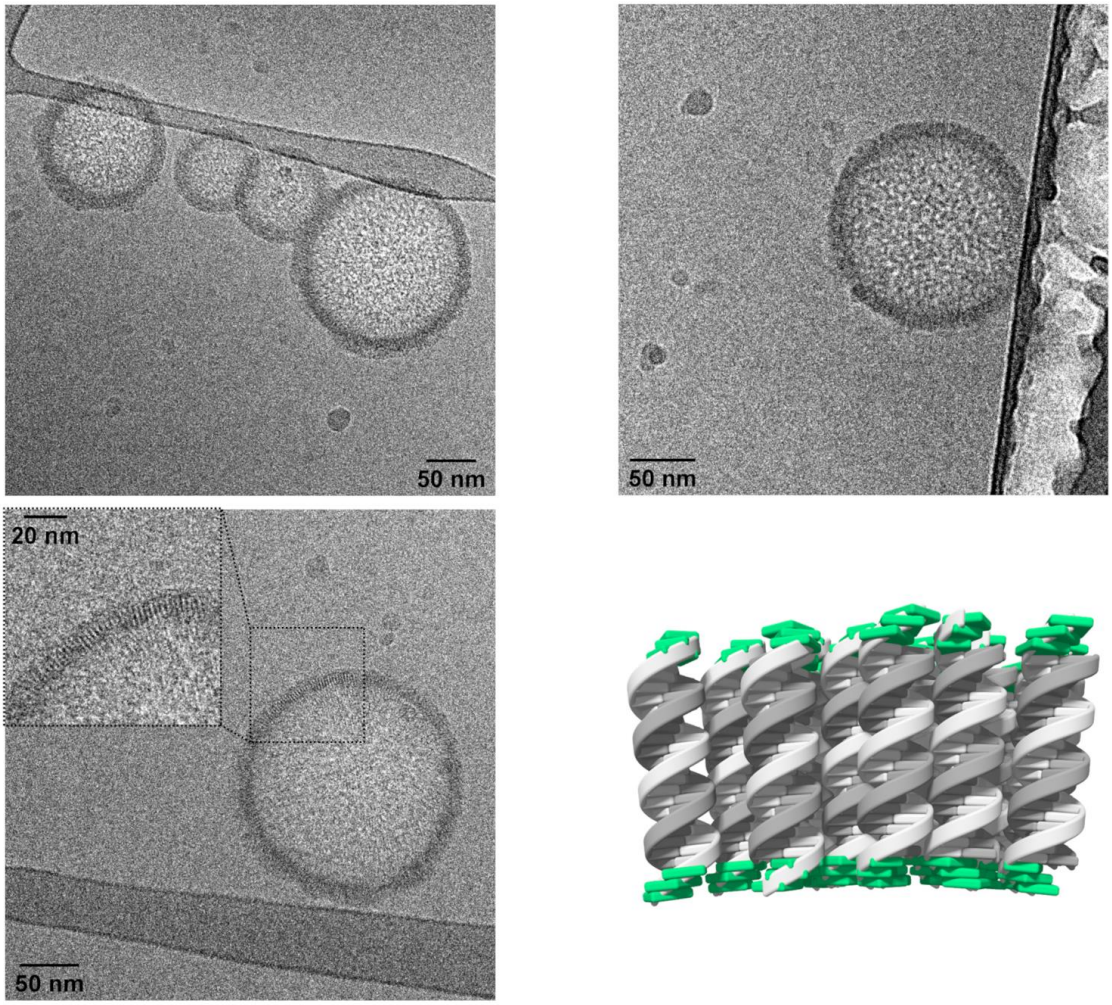

Figure 196. Supramolecular assemblies of **ON9*ON24** visualized by cryo-EM and schematic illustration of the vesicular morphology. Conditions: 1 µM **ON9**, 0.5 µM **ON24**, 10 mM sodium phosphate buffer pH 7.2, 0.1 mM spermine · 4 HCl, 30 vol% ethanol.

6.2 Conclusions and Outlook

In conclusion, well-defined, individual vesicular constructs were obtained in the case of **ON9*ON24** only, even though the spectroscopic measurements of both duplexes, **ON2*ON24** and **ON9*ON24**, showed similar characteristics under their respective optimized conditions (*i.e.*, fluorescence-monitored annealing curve). Duplex **ON2*ON24** self-assembles into smaller vesicles that have the tendency to further agglomerate into larger aggregates. This indicates that the overall number of TPE sticky ends significantly influence the self-assembly behavior. Based on AFM, the assemblies from **ON9*ON24** were in a comparable size range as the vesicles formed from the 20-mer DNA analogue **ON5*ON9**. Cryo-EM imaging disclosed the general type of architecture, which can be considered as type II-like vesicles. However, regarding the membrane thickness, cryo-EM could not unambiguously answer the question on how the DNA duplexes are assembled within the nanostructures (*i.e.*, folded or straight).

The approach described in this chapter, could allow the design of various other systems for the assembly of a long, unmodified single-stranded DNA into supramolecular nanostructures. One possibility would be to use an even longer DNA single strand, *e.g.*, a 50-mer DNA. The ten additional nucleotides could be inserted between the complementary 20 nucleotides long complementary sequences of the TPE-DNA conjugates. This strategy is schematically illustrated in Figure 197a.
Another approach is to use also a 40-mer DNA single strand, but in this case, the TPE-DNA conjugates would be hybridized to two separate complements that connect the two unmodified DNA single strands (Figure 197b).
Extending this method and by appropriate sequence design, one could omit the TPE-DNA conjugates that are fully hybridized to the complement (light gray shaded duplexes in Figure 197b). This would result somehow in a combination of the two approaches outlined in Figure 197.

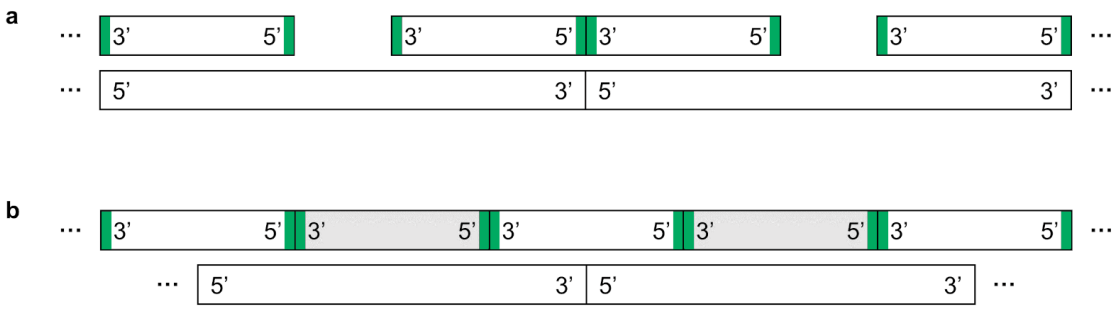

Figure 197. (**a**, **b**) Schematic representations of two alternative approaches for the construction of supramolecular nanostructures. TPE sticky ends are illustrated in green.

6.3 Appendix – Chapter 6

6.3.1 Cryo-EM Distance Measurements

Table 11. Summary of distance measurements. The reported distances are mean values with the corresponding standard deviation, along with the number of measurements in brackets.

Duplex	Vesicle membrane thickness	DNA width
ON9*ON24	13.7 ± 1.6 nm (*n* = 63)	2.4 ± 0.3 nm (*n* = 44)

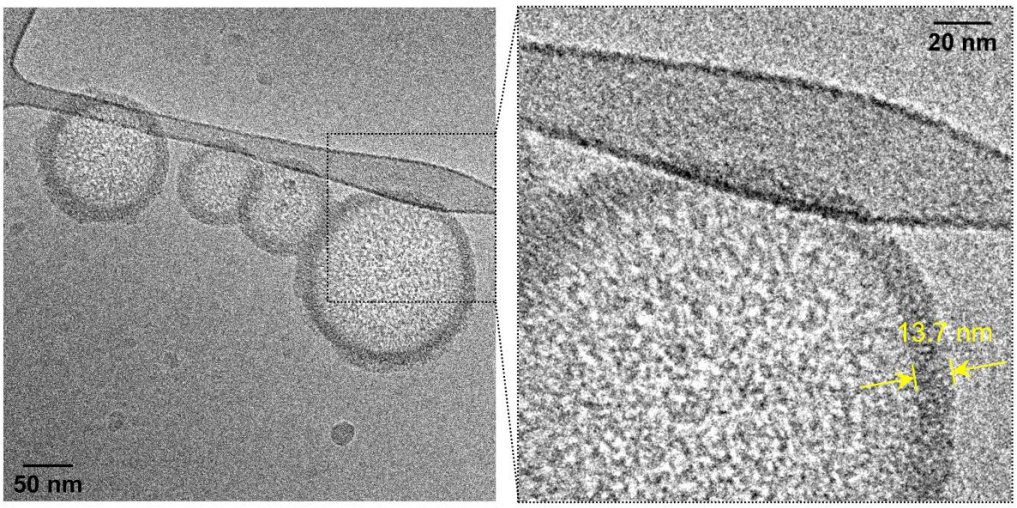

Figure 198. Representative vesicle membrane thickness measurement of self-assembled **ON9*ON24**. Conditions: 1 µM **ON9*ON24**, 10 mM sodium phosphate buffer pH 7.2, 0.1 mM spermine · 4 HCl, 30 vol% ethanol.

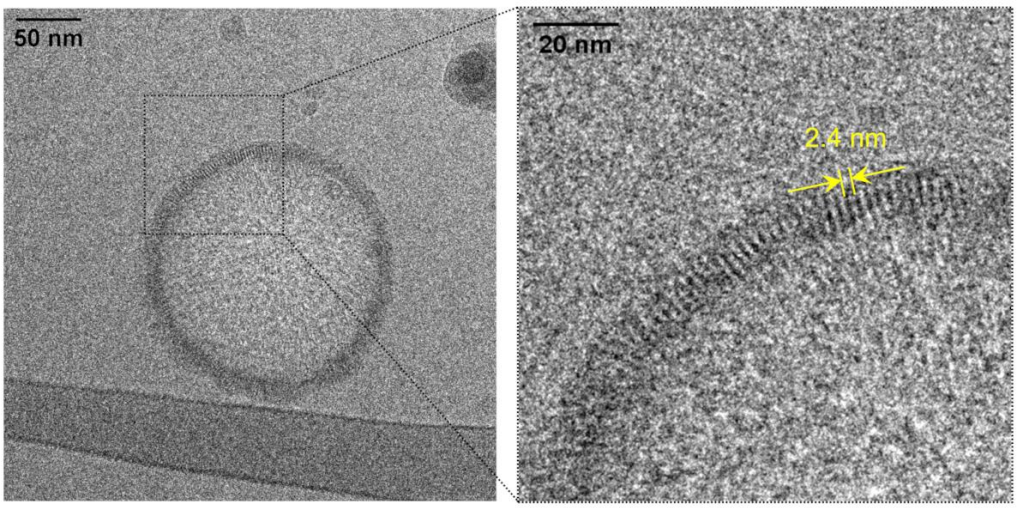

Figure 199. Representative DNA width measurement of self-assembled **ON9*ON24**. Conditions: 1 µM **ON9*ON24**, 10 mM sodium phosphate buffer pH 7.2, 0.1 mM spermine · 4 HCl, 30 vol% ethanol.

7 Self-Assembly of TPE Trimers

It has been shown previously that constitution isomers of phosphodiester-linked trimers lead to contrasting supramolecular morphologies. For example, 2,7-phosphodiester-linked phenanthrene trimers self-assemble into tubes, while the 3,6-phosphodiester-linked analogs form fibers.[26,27] Supramolecular assembly of different stereoisomers even result in two distinct nanostructures, as demonstrated by *E*-/*Z*-isomers of phosphodiester-linked azobenzene trimers.[237] Here, the self-assembly of *E*-/*Z*-isomers of phosphodiester-linked TPE trimers in aqueous medium is described, leading to AIE-active supramolecular arrays. Characteristic self-assembly behaviors were observed for the two TPE stereoisomers. Well-defined vesicular structures have been obtained only for *E*-TPE trimers in the presence of guanidine hydrochloride.

7.1 Synthetic Pathway for the Preparation of TPE Trimers

Outlined in Scheme 5 is the synthetic approach for the synthesis of *E*-TPE trimer (*E*-TPE)$_3$ **15**. In our research group, the synthesis of phosphodiester-linked trimers was commonly achieved *via* solid-phase synthesis using an automated DNA synthesizer. In contrast, the coupling of *E*-TPE trimer (formation of compound **14**) was performed in solution. The experimental procedure was adapted from a published procedure, describing the introduction of terminal phosphate groups onto a cyclopenta[*hi*]aceanthrylene core.[238] Therefore, two appropriate building blocks have been prepared for this coupling reaction, starting with diol **2**: the mono-acetylated compound **12** and bis-phosphoramidite **13**. After the coupling reaction and affording the phosphite triester linkages, the intermediate was oxidized into the corresponding phosphate triester **14** in the presence of *tert*-butyl hydroperoxide (^{t}BuOOH). Deprotection of the base-labile cyanoethyl and acetyl groups was accomplished by treatment with methanolic ammonia. The *E*-TPE trimer counter ion was exchanged by an ion exchange chromatography to obtain the final (*E*-TPE)$_3$ **15** as an ammonium salt. However, excessive ammonium acetate could not be fully evaporated by repeated lyophilization cycles as observed by ^{1}H NMR (singlet at 1.88 ppm, Figure 221).

Nonetheless, the amount of excessive ammonium acetate is neglectable for the subsequent experiments, considering that all the experiments were done in an aqueous 10 mM sodium phosphate buffer pH 7.2 solution.

The same synthetic approach was followed for the synthesis of *Z*-TPE trimer (*Z*-TPE)$_3$ **19** (Scheme 6), as it was previously described for the synthesis of *E*-TPE trimer **15** (Scheme 5).

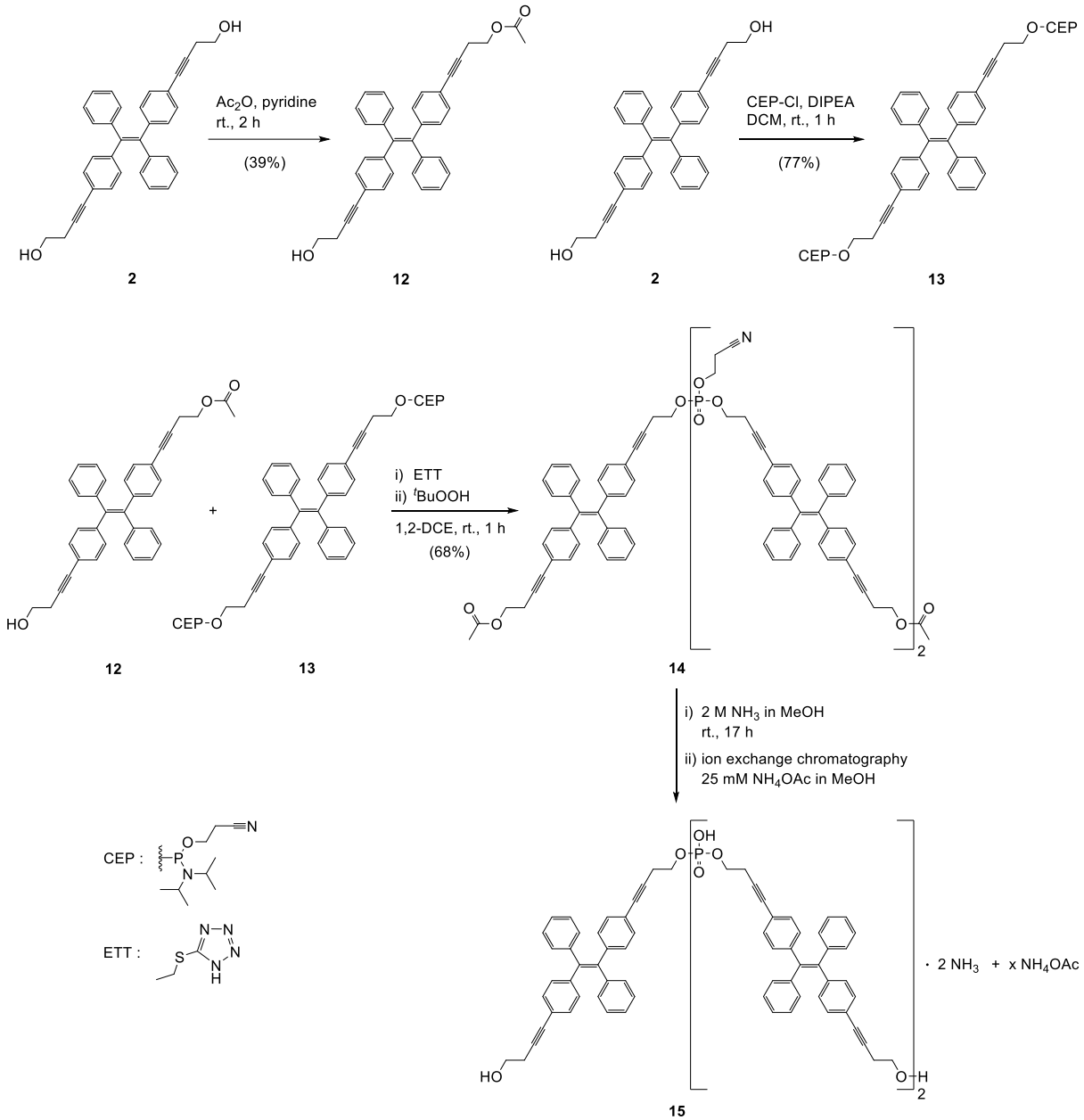

Scheme 5. Synthesis of *E*-TPE trimer (*E*-TPE)$_3$ **15**.

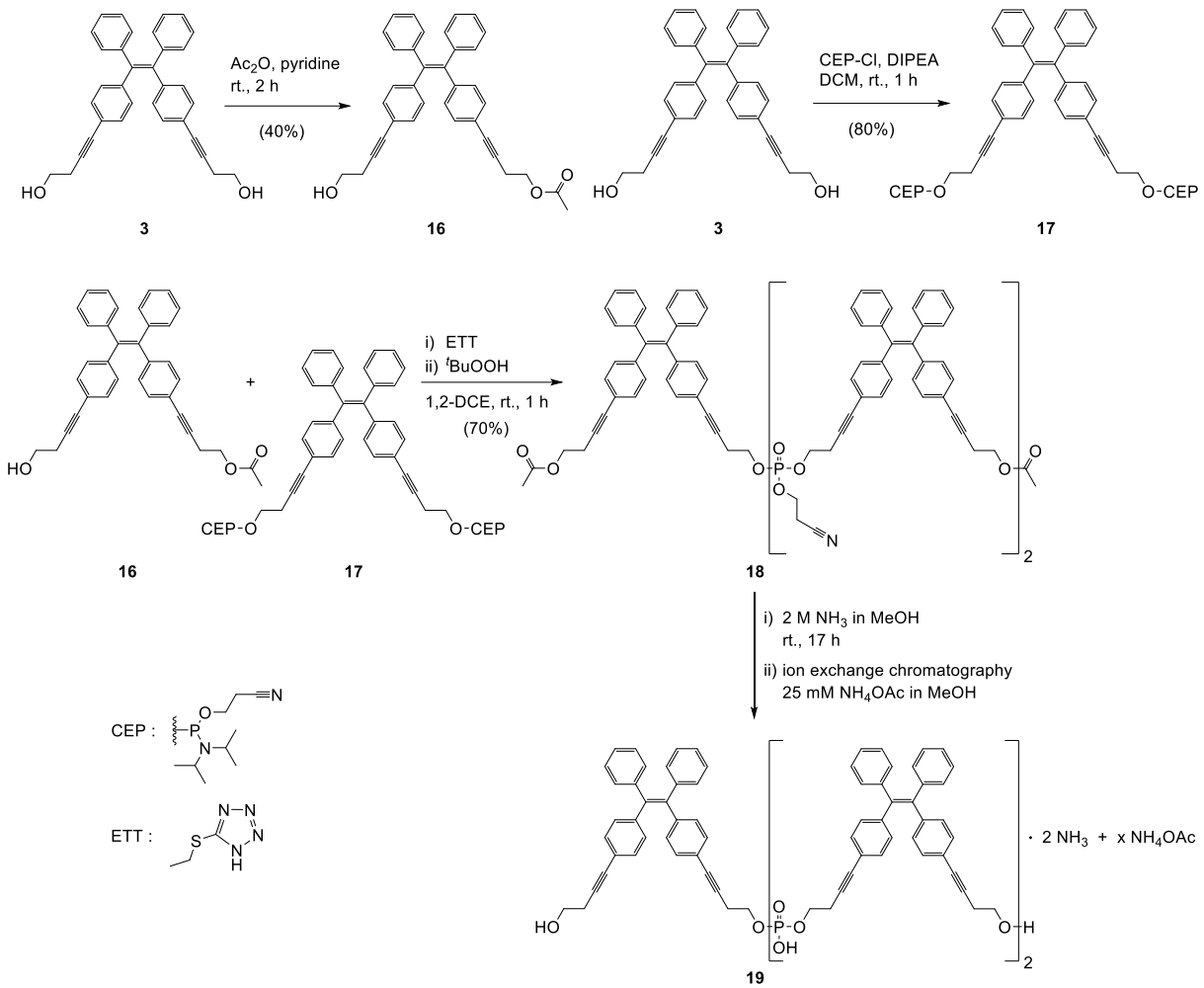

Scheme 6. Synthesis of *Z*-TPE-trimer (*Z*-TPE)$_3$ **19**.

7.2 Results and Discussion

7.2.1 Spectroscopic Characterization of (*E*-TPE)$_3$ and (*Z*-TPE)$_3$ in Ethanol

UV-Vis absorption spectra of (*E*-TPE)$_3$ **15** and (*Z*-TPE)$_3$ **19** in ethanol at 20 °C are displayed in Figure 200a. (*E*-TPE)$_3$ **15** exhibits a maximum at 261 nm and a second one at 329 nm, while (*Z*-TPE)$_3$ **19** features the first maximum at 265 nm and the second one also at 329 nm. The fluorescence emission intensity is close to zero, which is a clear evidence that the TPE trimers are not aggregated in ethanol (Figure 200b). Comparable to the emission spectra of TPE diol **2** and **3** in ethanol (Figure 14b), the emission is centered roughly around 500 nm.

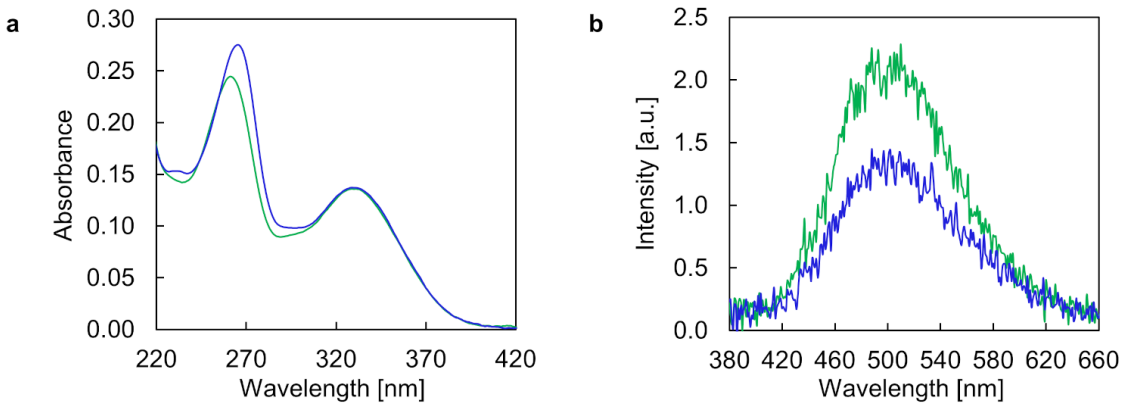

Figure 200. (**a**) UV-Vis absorption and (**b**) fluorescence emission spectra of (*E*-TPE)$_3$ **15** (green) and (*Z*-TPE)$_3$ **19** (blue). Conditions: 2 µM (TPE)$_3$ in ethanol, 20 °C, $\lambda_{ex.}$: 335 nm.

7.2.2 Self-Assembly of (*E*-TPE)$_3$ and (*Z*-TPE)$_3$ in Aqueous Medium

In a first step, various aqueous conditions were tested for (*E*-TPE)$_3$ **15**, aiming to find optimized conditions that indicate for a complete disassembly of **15** at 75 °C and imply for aggregation at 20 °C by means of optical spectroscopy. Complete disassembly of the trimers was assumed when the spectra in aqueous medium at 75 °C resembled the spectra obtained in ethanol (Figure 200). The influence of the ethanol fraction on the supramolecular assembly behavior was investigated first. The sample containing 10 vol% ethanol exhibits an absorption maximum at 332 nm at 75 °C (Figure 201a). Together with the obvious fluorescence emission signal at 75 °C (Figure 201b), it is assumed that (*E*-TPE)$_3$ **15** is not entirely disassembled at this temperature.

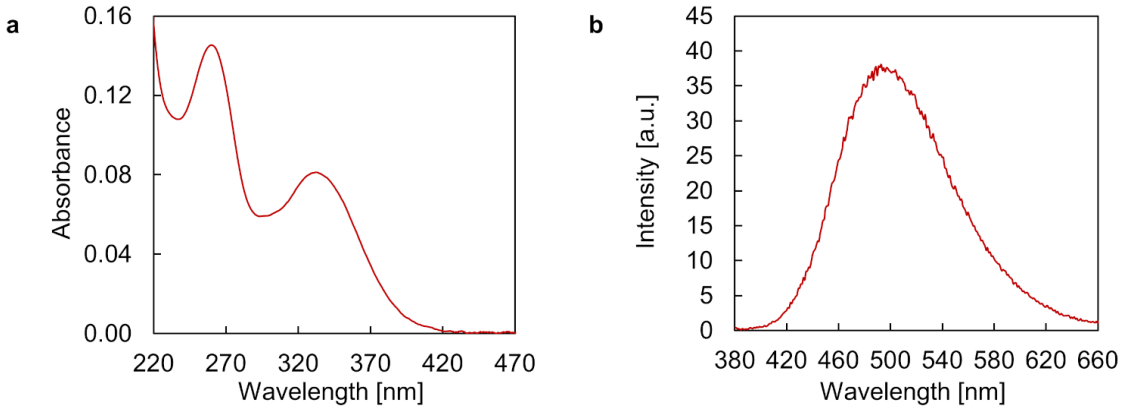

Figure 201. (**a**) UV-Vis absorption and (**b**) fluorescence emission spectra of (*E*-TPE)$_3$ **15**. Conditions: 2 µM (*E*-TPE)$_3$ **15**, 10 mM sodium phosphate buffer pH 7.2, 10 vol% ethanol, 75 °C, $\lambda_{ex.}$: 335 nm.

Hence, to achieve complete disassembly in aqueous medium at 75 °C, the ethanol fraction was increased to 20 vol%. Under these conditions, the fluorescence emission at 75 °C is close to zero (Figure 202b). The low emission is comparable to the emission intensity of (*E*-TPE)$_3$ **15** in ethanol (Figure 200b), where it is assumed that no aggregates are present in solution. This confirms the complete disassembly of (*E*-TPE)$_3$ **15** in aqueous medium with an ethanol fraction of 20 vol% at 75 °C. Hypochromicity at 260 nm, a bathochromic shift from 329 nm to 336 nm, and strong fluorescence emission enhancement was observed upon cooling (Figure 202). The temperature-dependent fluorescence emission intensities exemplify the AIE properties of the TPE trimers. The shape of the annealing curve (Figure 202c) suggests a cooperative nucleation-elongation assembly process with a fluorescence onset temperature of 42 °C.[23] Therefore, after performing the thermal assembly process, AFM experiments were conducted of this sample to visualize the potential nanostructures that were formed under these conditions.

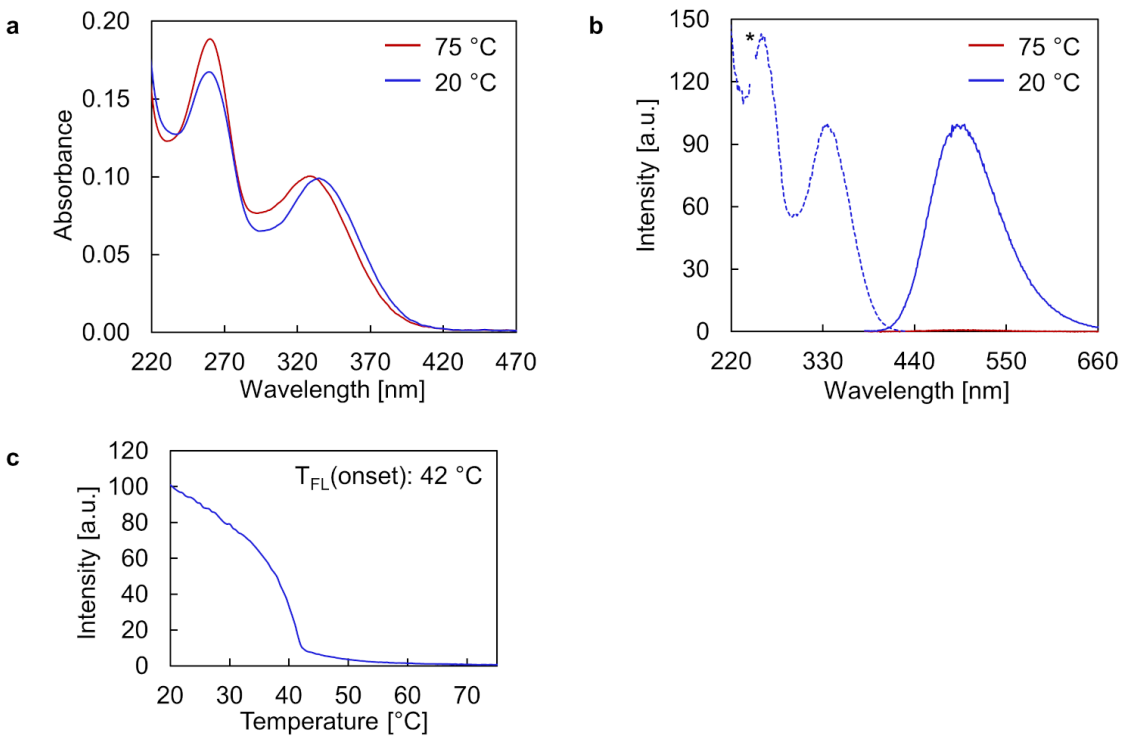

Figure 202. (**a**) UV-Vis absorption spectra, (**b**) fluorescence emission (solid line) and excitation (dotted line) spectra, and (**c**) fluorescence-monitored annealing curve of (*E*-TPE)$_3$ **15**. Conditions: 2 µM (*E*-TPE)$_3$ **15**, 10 mM sodium phosphate buffer pH 7.2, 20 vol% ethanol, $\lambda_{ex.}$: 335 nm, $\lambda_{em.}$: 490 nm, gradient: 0.5 °C/min, * denotes second-order diffraction.

Depicted in Figure 203 are the corresponding AFM images of aggregated (*E*-TPE)$_3$ **15** (20 vol% ethanol), which show small and ill-defined aggregates. The size of the observed nanostructures is not uniform, and the height range is from about 1 nm to 7 nm. As (*E*-TPE)$_3$ **15** does not self-assemble into regular assemblies under these conditions, additional conditions have been tested.

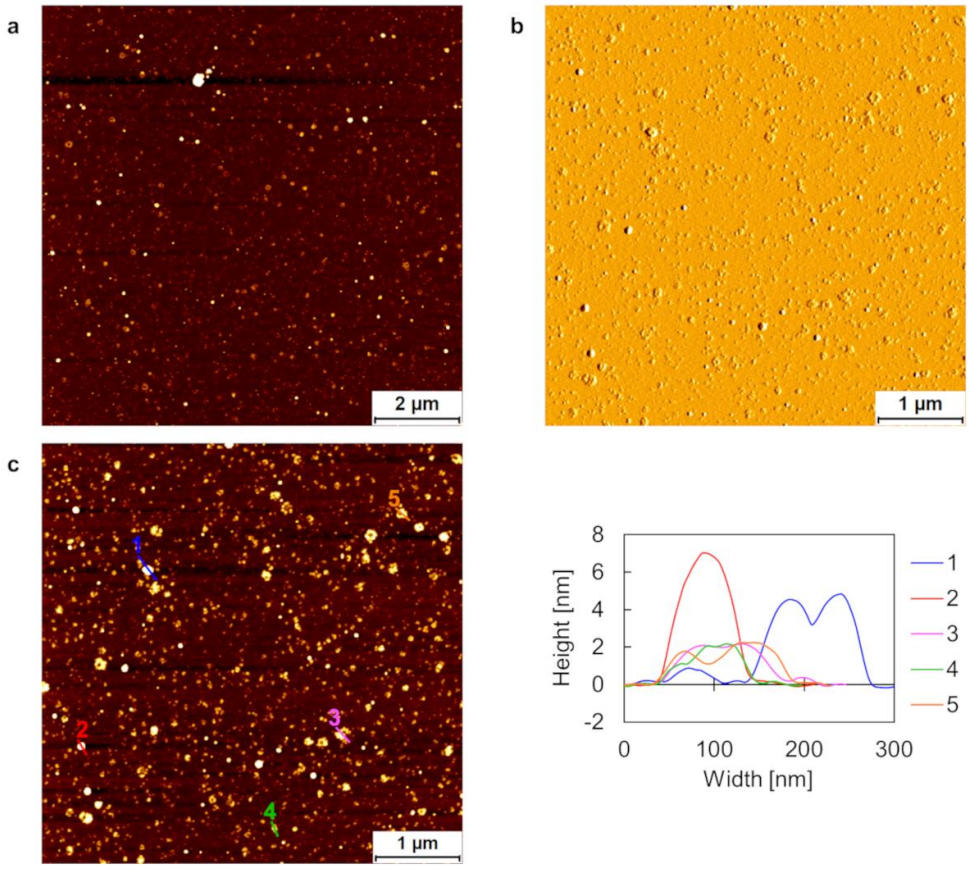

Figure 203. (**a**) AFM overview scan, (**b**) deflection scan, and (**c**) zoom with corresponding cross sections of assembled (*E*-TPE)$_3$ **15**. Conditions: 2 µM (*E*-TPE)$_3$ **15**, 10 mM sodium phosphate buffer pH 7.2, 20 vol% ethanol.

Two different salts (NaCl and guanidine hydrochloride) were added, intending to increase the ionic strength of the aqueous medium. The addition of salts intensifies the hydrophobic forces between the TPE units, seeking more defined assemblies. The ethanol fraction was kept constant at 20 vol%, promoting complete disassembly at 75 °C.

In the presence of an additional salt (50 mM NaCl), a red-shift from 329 nm to 336 nm was observed in the UV-Vis absorption spectrum after controlled cooling of the sample solution (Figure 204a). In contrast to the sample containing no NaCl (Figure 202a), the sample with 50 mM NaCl suggests hyperchromicity upon cooling. However, this observation might be explained by scattering effects that contribute to a significant extent to the observed absorption profile at 20 °C. Displayed in Figure 204b is the fluorescence emission spectra at 75 °C, which demonstrates complete disassembly, even after the addition of 50 mM NaCl. The fluorescence-monitored annealing curve shown in Figure 204c indicates two distinct onset temperatures. It is hypothesized that around 61 °C, small aggregates may be formed first, which further agglomerate around 25 °C, explaining the two different transitions.

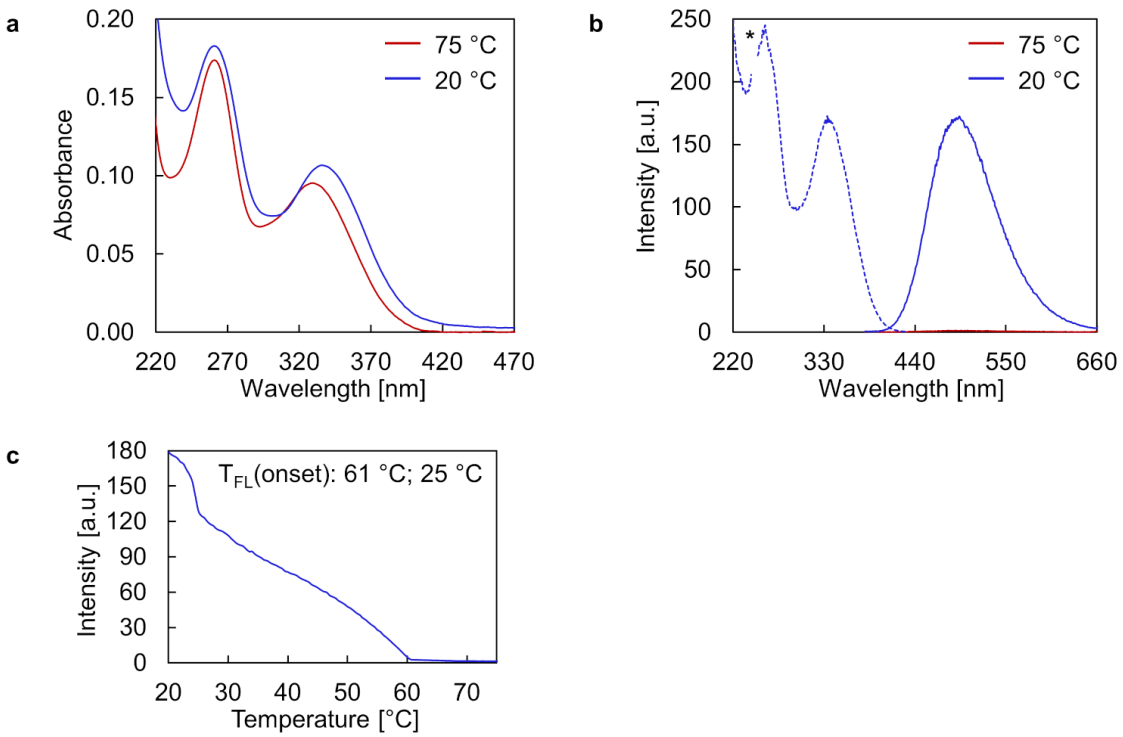

Figure 204. (**a**) UV-Vis absorption spectra, (**b**) fluorescence emission (solid line) and excitation (dotted line) spectra, and (**c**) fluorescence-monitored annealing curve of (*E*-TPE)$_3$ **15**. Conditions: 2 µM (*E*-TPE)$_3$ **15**, 10 mM sodium phosphate buffer pH 7.2, 50 mM NaCl, 20 vol% ethanol, $\lambda_{ex.}$: 335 nm, $\lambda_{em.}$: 490 nm, gradient: 0.5 °C/min, * denotes second-order diffraction.

Nevertheless, this hypothesis is only partly supported by AFM experiments (Figure 205). Roundish objects with heights of up to 25 nm are visible while larger aggregates are missing. However, not so many structures are present on the mica. Hence, larger aggregates indeed may have been formed in solution, but they probably did not adsorb strongly enough on the mica and thus, were washed away during sample preparation (*i.e.*, washing step with water).

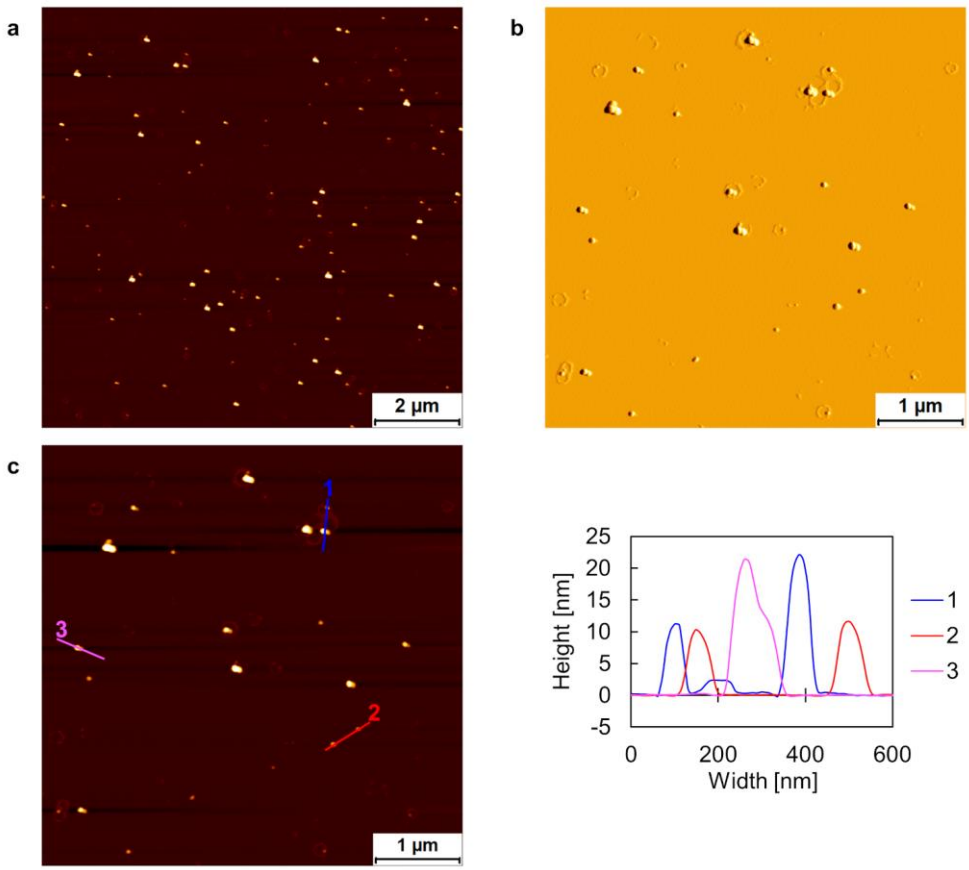

Figure 205. (**a**) AFM overview scan, (**b**) deflection scan, and (**c**) zoom with corresponding cross sections of assembled (*E*-TPE)$_3$ **15**. Conditions: 2 µM (*E*-TPE)$_3$ **15**, 10 mM sodium phosphate buffer pH 7.2, 50 mM NaCl, 20 vol% ethanol.

After changing the salt from NaCl (50 mM) to guanidine hydrochloride (10 mM), similar spectroscopic characteristics were observed, which are depicted in Figure 206. Under these conditions, the most pronounced bathochromic shift was noticed when cooling the solution from 75 °C to 20 °C, namely from 329 nm to 338 nm. The fluorescence-monitored annealing curve shows mainly one apparent onset temperature at 60 °C.

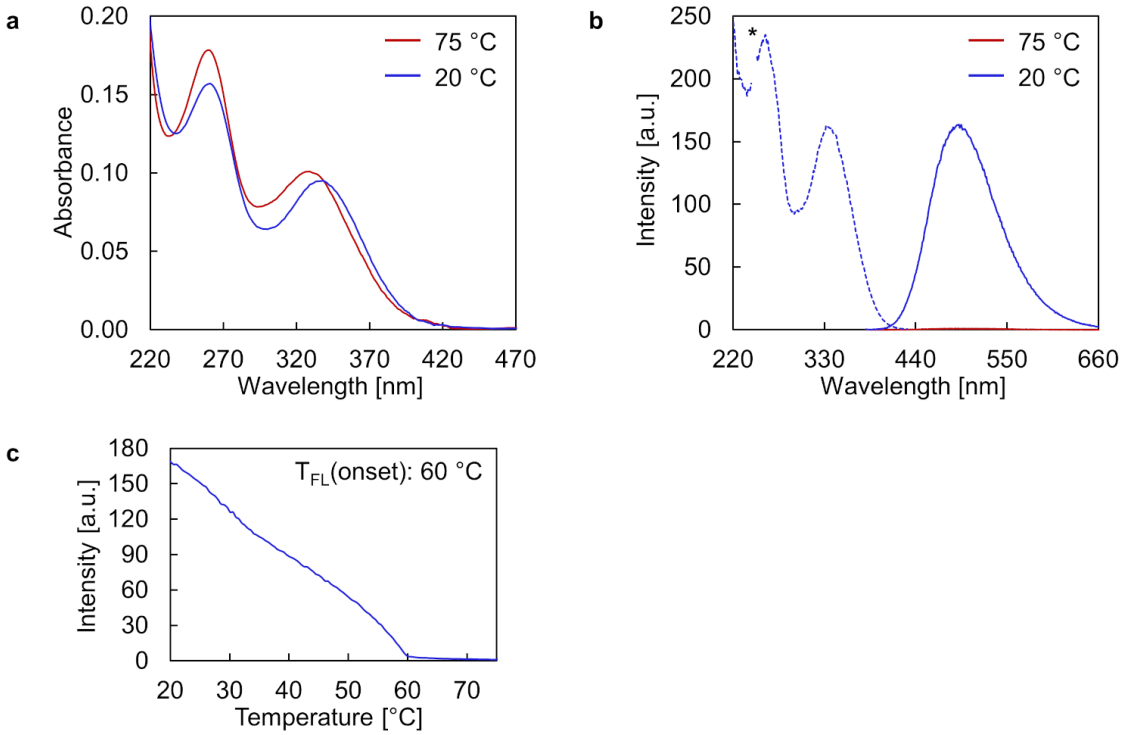

Figure 206. (**a**) UV-Vis absorption spectra, (**b**) fluorescence emission (solid line) and excitation (dotted line) spectra, and (**c**) fluorescence-monitored annealing curve of (*E*-TPE)$_3$ **15**. Conditions: 2 µM (*E*-TPE)$_3$ **15**, 10 mM sodium phosphate buffer pH 7.2, 10 mM guanidine · HCl, 20 vol% ethanol, $\lambda_{ex.}$: 335 nm, $\lambda_{em.}$: 490 nm, gradient: 0.5 °C/min, * denotes second-order diffraction.

AFM imaging showed in terms of size and morphology the most promising results (Figure 207). Besides some small aggregates, large, spherical nanostructures with a well-defined shape are present. The size range of these larger assemblies range roughly between 20 nm and 50 nm.

After these attempts of conditions optimization for (*E*-TPE)$_3$ **15**, the results were compared with the experiments conducted with (*Z*-TPE)$_3$ **19**. This was done to find out the potential influence of the different stereoisomers on the self-assembly behavior and the morphology of the supramolecular assemblies.

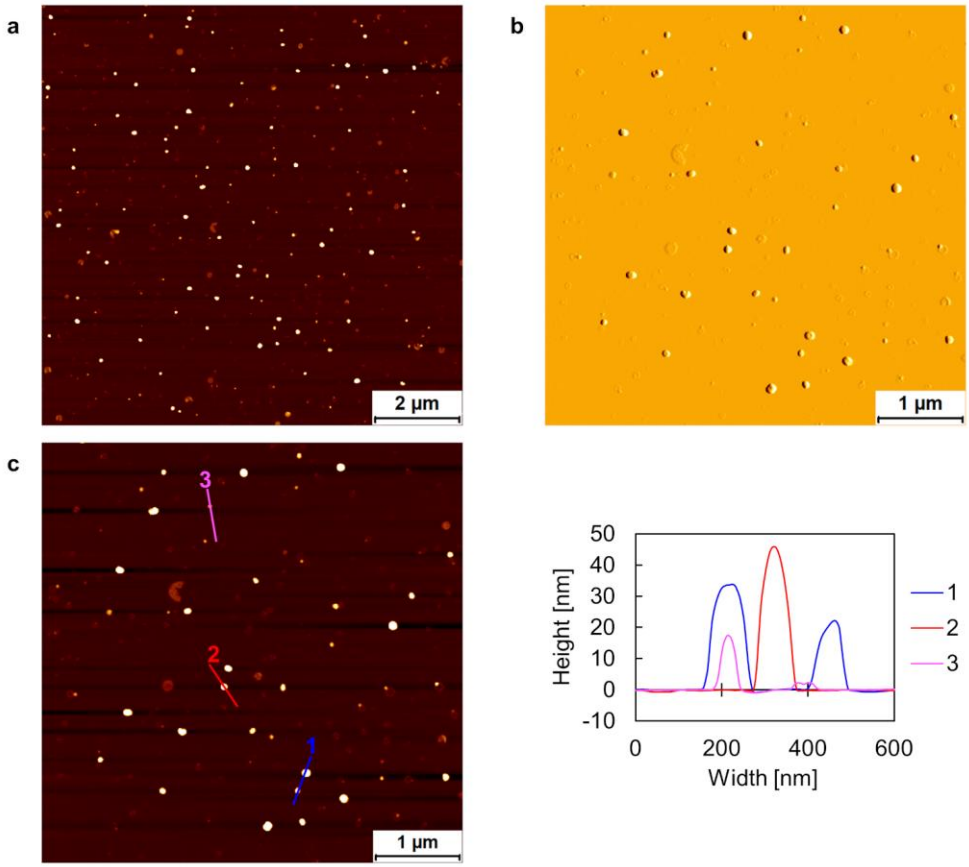

Figure 207. (**a**) AFM overview scan, (**b**) deflection scan, and (**c**) zoom with corresponding cross sections of assembled (*E*-TPE)$_3$ **15**. Conditions: 2 µM (*E*-TPE)$_3$ **15**, 10 mM sodium phosphate buffer pH 7.2, 10 mM guanidine · HCl, 20 vol% ethanol.

Displayed in Figure 208, Figure 210, and Figure 212 are the temperature-dependent UV-Vis and fluorescence spectra of (*Z*-TPE)$_3$ **19** in aqueous medium under different conditions. Comparable spectroscopic characteristics were observed for (*E*-TPE)$_3$ **15** and (*Z*-TPE)$_3$ **19** under the respective conditions, except the presumable hyperchromicity around 260 nm of (*E*-TPE)$_3$ **15** in the presence of 50 mM NaCl. In the case of (*Z*-TPE)$_3$ **19**, hypochromicity is observed in the absorption band around 260 nm upon cooling the sample solution under these conditions (Figure 210a).

Comparing the fluorescence onset temperatures between (*E*-TPE)$_3$ **15** and (*Z*-TPE)$_3$ **19** (Table 12), the temperatures for the (*Z*-TPE)$_3$ **19** isomer are always lower. The largest difference is in the presence of guanidine hydrochloride. While (*E*-TPE)$_3$ **15** shows under these conditions a fluorescence onset temperature of 60 °C, this temperature was significantly lowered by 16 °C to 44 °C for (*Z*-TPE)$_3$ **19**.

Differences are also apparent regarding the shape of the fluorescence-monitored annealing curves. Only in the absence of any additional salt, a nucleation-elongation polymerization pathway[23] can be assumed for (*Z*-TPE)$_3$ **19**, as displayed in Figure 208c. However, already a considerable fluorescence increase is observed above the T_{FL}(onset). For the other two samples of this isomer, a fluorescence onset temperature is discernible, but after the sharp onset, the emission increases rather linearly (Figure 210c and Figure 212c). This indicates that the two TPE stereoisomers exhibit a different self-assembly behavior.

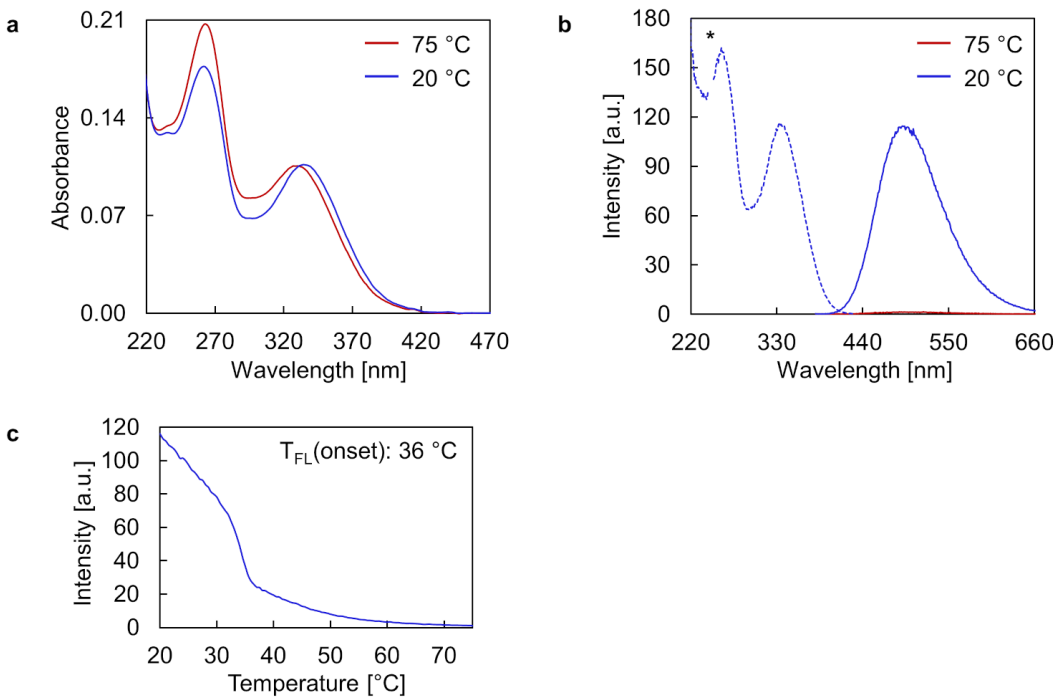

Figure 208. (**a**) UV-Vis absorption spectra, (**b**) fluorescence emission (solid line) and excitation (dotted line) spectra, and (**c**) fluorescence-monitored annealing curve of (*Z*-TPE)$_3$ **19**. Conditions: 2 µM (*Z*-TPE)$_3$ **19**, 10 mM sodium phosphate buffer pH 7.2, 20 vol% ethanol, $\lambda_{ex.}$: 335 nm, $\lambda_{em.}$: 490 nm, gradient: 0.5 °C/min, * denotes second-order diffraction.

AFM imaging was utilized to visualize the nanostructures of self-assembled (*Z*-TPE)$_3$ **19** after performing the thermal assembly process under the three different conditions. In Figure 209 are the AFM images depicted, when no additional salt was added to the sample solution. A similar result was obtained as already described for (*E*-TPE)$_3$ **15** under the same conditions (Figure 203). Only very small aggregates are visible that cover the entire surface.

After the addition of 50 mM NaCl (Figure 211), although some larger, ill-defined assemblies were formed with a height of up to 30 nm, the sample appears rather inhomogeneous and many structures with heights below 10 nm are present as well.

In the presence of 10 mM guanidine hydrochloride (Figure 213), the shape of the structures could not be improved significantly. Assemblies with maximum heights of about 5 nm are visible and larger aggregates are missing completely. This underpins the divergent self-assembly behavior of the two stereoisomers, because in the presence of 10 mM guanidine hydrochloride, well-defined nanostructures with heights of nearly 50 nm were found for (*E*-TPE)$_3$ **15** (Figure 207).

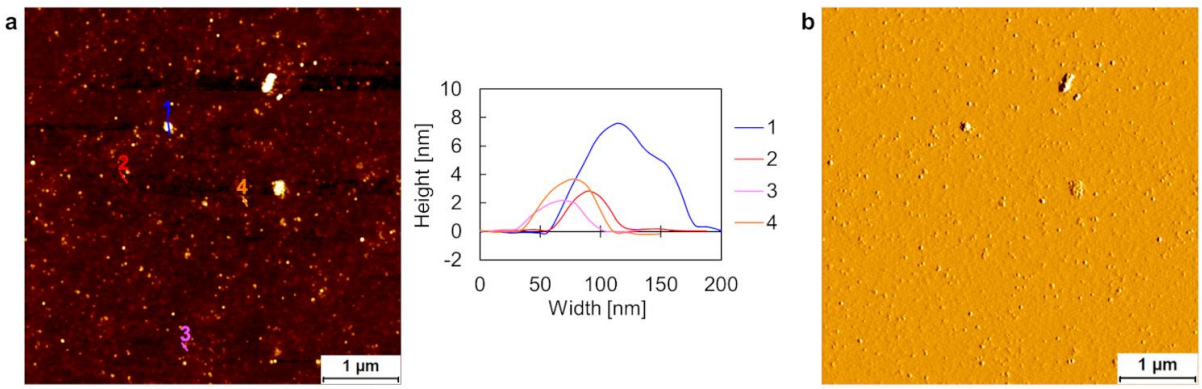

Figure 209. (**a**) AFM scan with corresponding cross sections and (**b**) deflection scan of assembled (*Z*-TPE)$_3$ **19**. Conditions: 2 µM (*Z*-TPE)$_3$ **19**, 10 mM sodium phosphate buffer pH 7.2, 20 vol% ethanol.

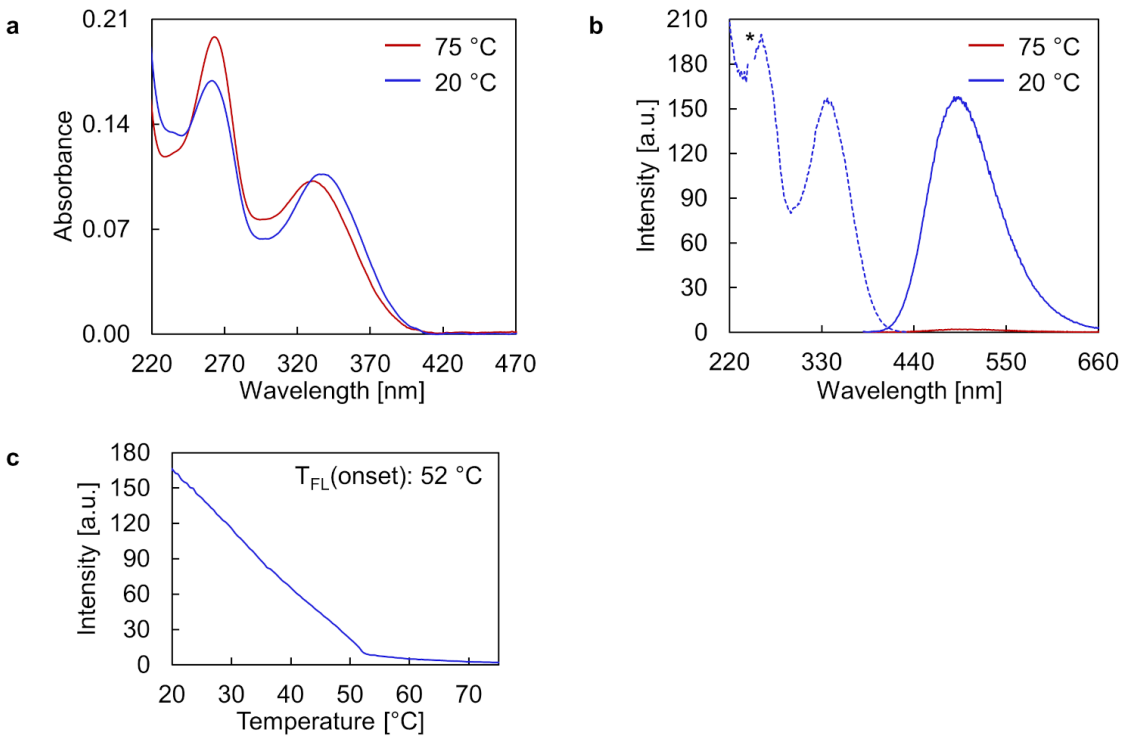

Figure 210. (**a**) UV-Vis absorption spectra, (**b**) fluorescence emission (solid line) and excitation (dotted line) spectra, and (**c**) fluorescence-monitored annealing curve of (*Z*-TPE)$_3$ **19**. Conditions: 2 µM (*Z*-TPE)$_3$ **19**, 10 mM sodium phosphate buffer pH 7.2, 50 mM NaCl, 20 vol% ethanol, $\lambda_{ex.}$: 335 nm, $\lambda_{em.}$: 490 nm, gradient: 0.5 °C/min, * denotes second-order diffraction.

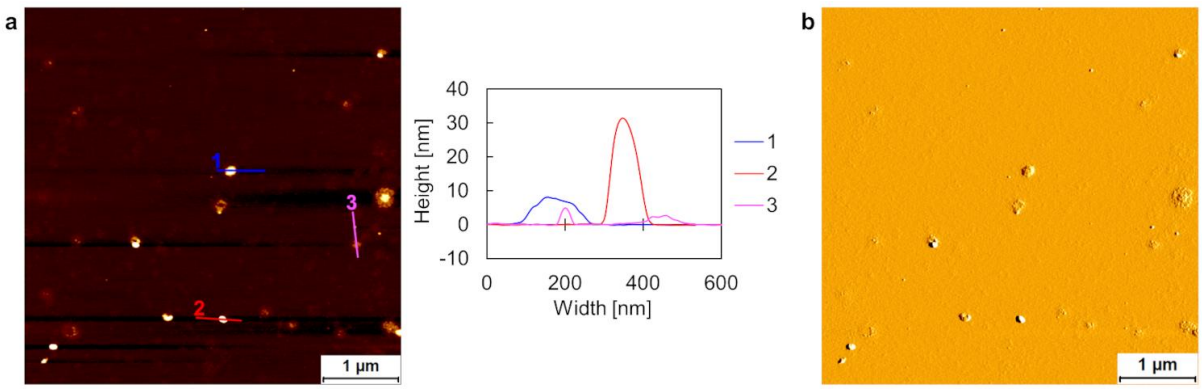

Figure 211. (**a**) AFM scan with corresponding cross sections and (**b**) deflection scan of assembled (*Z*-TPE)$_3$ **19**. Conditions: 2 µM (*Z*-TPE)$_3$ **19**, 10 mM sodium phosphate buffer pH 7.2, 50 mM NaCl, 20 vol% ethanol.

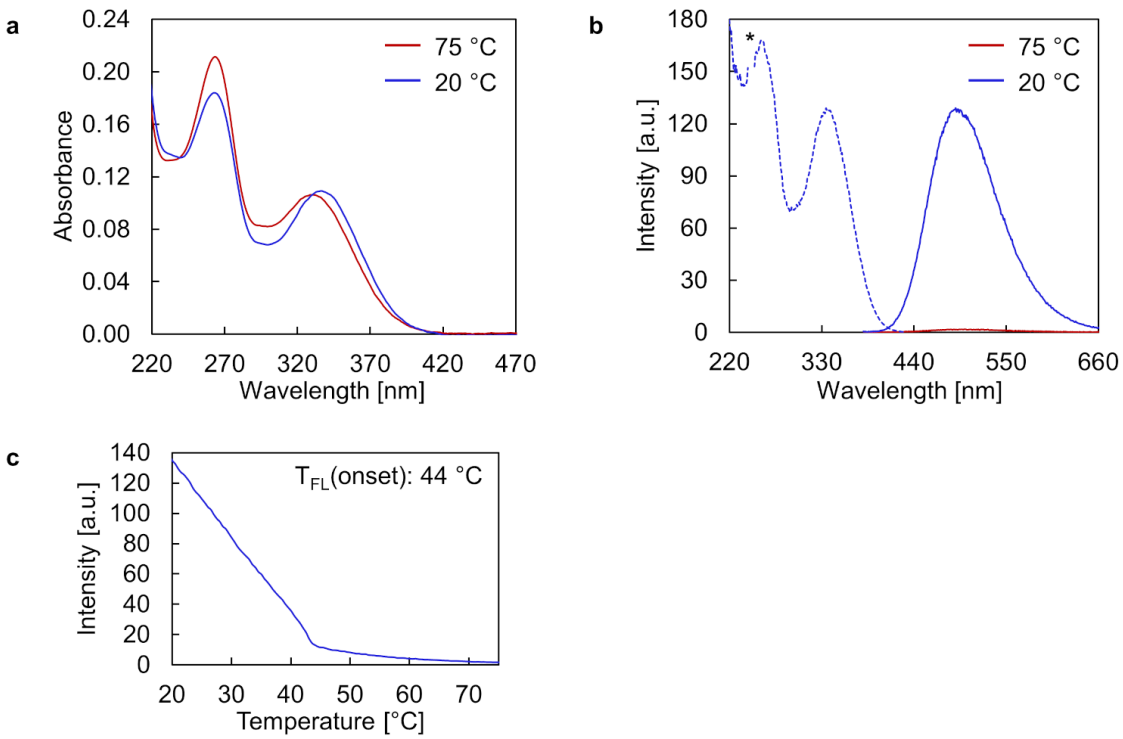

Figure 212. (**a**) UV-Vis absorption spectra, (**b**) fluorescence emission (solid line) and excitation (dotted line) spectra, and (**c**) fluorescence-monitored annealing curve of (*Z*-TPE)$_3$ **19**. Conditions: 2 µM (*Z*-TPE)$_3$ **19**, 10 mM sodium phosphate buffer pH 7.2, 10 mM guanidine · HCl, 20 vol% ethanol, $\lambda_{ex.}$: 335 nm, $\lambda_{em.}$: 490 nm, gradient: 0.5 °C/min, * denotes second-order diffraction.

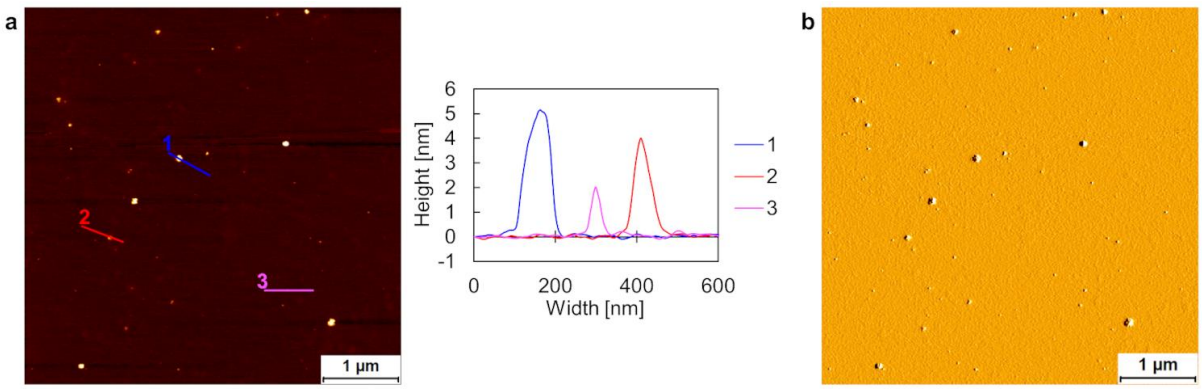

Figure 213. (**a**) AFM scan with corresponding cross sections and (**b**) deflection scan of assembled (*Z*-TPE)$_3$ **19**. Conditions: 2 µM (*Z*-TPE)$_3$ **19**, 10 mM sodium phosphate buffer pH 7.2, 10 mM guanidine · HCl, 20 vol% ethanol.

Table 12. Summary of onset temperatures [T_{FL}(onset)] of (*E*-TPE)$_3$ **15** and (*Z*-TPE)$_3$ **19** under the tested conditions, based on fluorescence-monitored annealing curves.

Conditions	**T_{FL}(onset) [°C]**	
	(*E*-TPE)$_3$ **15**	(*Z*-TPE)$_3$ **19**
2 µM (TPE)$_3$, 10 mM sodium phosphate buffer pH 7.2, 20 vol% ethanol	42	36
2 µM (TPE)$_3$, 10 mM sodium phosphate buffer pH 7.2, 20 vol% ethanol, 50 mM NaCl	61; 25	52
2 µM (TPE)$_3$, 10 mM sodium phosphate buffer pH 7.2, 20 vol% ethanol, 10 mM guanidine · HCl	60	44

7.3 Conclusions and Outlook

In summary, AIE-active supramolecular assemblies composed of TPE trimers have been described. Various aqueous conditions for the self-assembly of TPE trimers have been tested. Within the scope of this study, well-defined supramolecular arrays assembled from (*E*-TPE)$_3$ **15** have been afforded only after the addition of guanidine hydrochloride. In contrast, no suitable conditions have been found for the self-assembly of (*Z*-TPE)$_3$ **19** into large, regular nanostructures. Therefore, the *E*- and *Z*-TPE stereoisomers demonstrate a contrasting self-assembly behavior. This is evidenced by AFM imaging as well as the differences in nucleation temperatures, based on fluorescence-monitored annealing curves. Under some conditions, the fluorescence-monitored annealing curve suggested a nucleation-elongation polymerization pathway.[23] In these cases, it may well be that regular supramolecular polymers have been formed in solution. However, these structures might have been disrupted during AFM sample preparation. It has been described, that *e.g.*, vesicles collapse upon surface adsorption or drying.[239–241] Thus, a solution-based method like DLS, NTA, or cryo-EM imaging could be employed to test this possibility.

To potentially increase the stability (*i.e.*, nucleation temperature) of the supramolecular polymers, the TPE oligomers might be elongated to tetramers or even pentamers. Alternatively, one might test other salts, such as spermine · 4 HCl, which afforded well-defined nanostructures assembled from TPE-DNA conjugates that were described in the previous chapters.

In collaboration with the research group of Prof. Dr. Dirk M. Guldi, both TPE trimers **15** and **19** will be investigated for exfoliation of graphite and the preparation of other carbon-based nanomaterials. Promising results along this line have already been reported with the use of a phosphodiester-linked anthanthrene trimer.[242]

7.4 Appendix – Chapter 7

7.4.1 Organic Synthesis

The organic synthesis of (*E*-TPE)$_3$ **15** and (*Z*-TPE)$_3$ **19** followed the synthetic pathways outlined in Scheme 5 and Scheme 6, respectively.

(*E*)-4-(4-(2-(4-(4-hydroxybut-1-yn-1-yl)phenyl)-1,2-diphenylvinyl)phenyl)but-3-yn-1-yl acetate (12)
Compound **2** (168 mg, 0.36 mmol) was dissolved in pyridine (3.5 mL), before a 2 M solution of acetic anhydride in pyridine (0.2 mL) was added dropwise at rt. over a period of 10 min. The reaction mixture was stirred at rt. for 2 h. The reaction mixture was diluted with EtOAc (20 mL), and the organic phase was washed three times with aq. 0.5 M HCl (3x20 mL), twice with aq. sat. $NaHCO_3$ (2x20 mL), once with brine (20 mL), dried over $MgSO_4$, filtered, and concentrated *in vacuo*. The residue was purified by flash column chromatography on silica gel (hexane/EtOAc 7:3 → 1:1) to afford compound **12** as a yellowish foam (71 mg, 0.14 mmol, 39%). R_f = 0.28 (hexane/EtOAc 6:4); ^{1}H NMR (400 MHz, CD_3CN) δ 7.16–7.11 (m, 10H), 7.04–7.00 (m, 4H), 6.97–6.94 (m, 4H), 4.16 (t, *J* = 6.6 Hz, 2H), 3.63 (q, *J* = 6.5 Hz, 2H), 2.93 (t, *J* = 6.1 Hz, 1H), 2.69 (t, *J* = 6.6 Hz, 2H), 2.53 (t, *J* = 6.6 Hz, 2H), 2.01 (s, 3H); ^{13}C NMR (101 MHz, CD_3CN) δ 171.51, 144.48, 144.21, 144.06, 142.06, 141.95, 132.05, 132.01, 131.95, 131.75, 131.72, 128.88, 127.83, 122.84, 122.42, 89.26, 87.67, 82.13, 81.92, 63.02, 61.35, 24.27, 21.02, 20.39; HRMS-NSI (*m/z*): $[M+H]^+$ calcd for $C_{36}H_{31}O_3$, 511.2268; found, 511.2262.

(*E*)-bis(2-cyanoethyl) (((1,2-diphenylethene-1,2-diyl)bis(4,1-phenylene))bis(but-3-yne-4,1-diyl)) bis(diisopropylphosphoramidite) (13)
Compound **2** (119 mg, 0.25 mmol) was dissolved in DCM (2.5 mL) and DIPEA (0.3 mL), before CEP-Cl (122 mg, 0.52 mmol) was added dropwise at rt. The reaction mixture was stirred at rt. for 1 h, then concentrated *in vacuo*. The residue was purified by a short silica gel flash column chromatography (hexane/EtOAc 7:3 + 1% Et_3N) to obtain compound **13** as a yellowish solid (169 mg, 0.19 mmol, 77%). R_f = 0.46 (hexane/EtOAc 7:3 + 1% Et_3N); ^{1}H NMR (400 MHz, DCM-d_2) δ 7.15–7.10 (m, 10H), 7.03–6.99 (m, 4H), 6.95–6.91 (m, 4H), 3.87–3.72 (m, 8H), 3.66–3.57 (m, 4H), 2.68 (t, *J* = 6.8 Hz, 4H), 2.61 (q, *J* = 6.2 Hz, 4H), 1.18 (dd, *J* = 6.8, 2.4 Hz, 24H); ^{13}C NMR (101 MHz, DCM-d_2) δ 143.86, 143.77, 141.51, 131.80, 131.73, 131.38, 128.40, 127.32, 122.27, 118.39, 87.79, 82.02, 62.55, 62.36, 59.22, 59.03, 43.80, 43.67, 25.00, 24.96, 24.93, 24.89, 22.96, 22.89, 21.00, 20.93; ^{31}P NMR (162 MHz, DCM-d_2) δ 148.14; HRMS-NSI (*m/z*): $[M+H]^+$ calcd for $C_{52}H_{63}O_4N_4P_2$, 869.4319; found, 869.4308.

***E*-TPE trimer (*E*-TPE)$_3$ (15)**

Compound **12** (44 mg, 0.09 mmol) was placed in a flask and a 0.15 M solution of compound **13** in 1,2-DCE (0.2 mL, 0.03 mmol) was added at rt., followed by a 0.25 M solution of ETT in 1,2-DCE (0.4 mL). The reaction mixture was stirred at rt. for 30 min., before ^{t}BuOOH hydroperoxide solution (24 µL, 70% in H_2O) was added. The reaction mixture was stirred at rt. for further 30 min., then diluted with $CHCl_3$ (10 mL). The organic phase was washed three times with aq. sat. $NaHCO_3$ (3x10 mL), once with brine (10 mL), dried over $MgSO_4$, filtered, and concentrated *in vacuo*. The residue was purified by flash column chromatography on silica gel ($CHCl_3$ → $CHCl_3$/MeOH 98:2) to yield the protected *E*-TPE trimer **14** as a yellowish foam (35 mg, 0.02 mmol, 68%). R_f = 0.07 ($CHCl_3$/MeOH 99:1); ^{1}H NMR (400 MHz, $CDCl_3$, 323 K) δ 7.14–7.07 (m, 30H), 7.01–6.97 (m, 12H), 6.95–6.90 (m, 12H), 4.27–4.20 (m, 16H), 2.78 (t, *J* = 6.7 Hz, 8H), 2.71 (t, *J* = 6.9 Hz, 4H), 2.66 (t, *J* = 6.3 Hz, 4H), 2.07 (s, 6H); ^{31}P NMR (162 MHz, $CDCl_3$, 323 K) δ –2.20; HRMS-NSI (*m/z*): $[M–e]^+$ calcd for $C_{112}H_{92}O_{12}N_2P_2$, 1718.6125; found, 1718.6321.

The protected *E*-TPE trimer **14** (33 mg, 0.02 mmol) was dissolved in a 2 M solution of NH_3 in MeOH (15 mL) and the reaction mixture was stirred at rt. for 17 h. The solvent was removed *in vacuo* to yield a yellowish solid (31 mg). 7 mg of this yellowish solid was dissolved in 25 mM ammonium acetate in MeOH pH 6 (5 mL) and the counter ion of *E*-TPE trimer was exchanged to ammonium by ion exchange chromatography (resin: Dowex 50WX8 hydrogen form, 50–100 mesh; eluent: 25 mM ammonium acetate in MeOH pH 6). After repeated lyophilization cycles (MeOH/H_2O 1:1), the final (*E*-TPE)$_3$ **15** was isolated as a yellow solid. A stock solution was prepared by dissolving some of (*E*-TPE)$_3$ **15** in ethanol. The concentration of this stock solution was determined according to the Beer-Lambert law: the absorbance was measured at 260 nm at 75 °C, using the following molar absorptivity ε: 107’925 L/mol·cm for (*E*-TPE)$_3$ **15**. ^{1}H NMR (400 MHz, CD_3OD, 328 K) δ 7.16–6.80 (m, 54H), 4.01 (q, *J* = 6.6 Hz, 8H), 3.69 (t, *J* = 6.8 Hz, 4H), 2.69 (q, *J* = 6.7 Hz, 8H), 2.57 (t, *J* = 6.8 Hz, 4H), 1.88 (s); ^{31}P NMR (162 MHz, CD_3OD, 328 K) δ 0.01; HRMS-NSI (*m/z*): $[M–2H]^{2–}$ calcd for $C_{102}H_{80}O_{10}P_2$, 763.2619; found, 763.2622.

(*Z*)-4-(4-(2-(4-(4-hydroxybut-1-yn-1-yl)phenyl)-1,2-diphenylvinyl)phenyl)but-3-yn-1-yl acetate (16)

Compound **3** (161 mg, 0.34 mmol) was dissolved in pyridine (3.3 mL), before a 2 M solution of acetic anhydride in pyridine (0.2 mL) was added dropwise at rt. over a period of 10 min. The reaction mixture was stirred at rt. for 2 h. The reaction mixture was diluted with EtOAc (20 mL), and the organic phase was washed three times with aq. 0.5 M HCl (3x20 mL), twice with aq. sat. $NaHCO_3$ (2x20 mL), once with brine (20 mL), dried over $MgSO_4$, filtered, and concentrated *in vacuo*. The residue was purified by flash column chromatography on silica gel (hexane/EtOAc 7:3 → 1:1) to afford compound **16** as a yellowish foam (71 mg, 0.14 mmol, 40%). R_f = 0.21 (hexane/EtOAc 6:4); ^{1}H NMR (400 MHz, CD_3CN) δ 7.16–7.11 (m, 10H), 7.05–7.01 (m, 4H), 6.97–6.94 (m, 4H), 4.17 (t, *J* = 6.6 Hz, 2H), 3.64 (q, *J* = 6.4 Hz, 2H), 2.94 (t, *J* = 6.1 Hz, 1H), 2.70 (t, *J* = 6.6 Hz, 2H), 2.54 (t, *J* = 6.6 Hz, 2H), 2.02 (s, 3H); ^{13}C NMR (101 MHz, CD_3CN) δ 171.52, 144.46, 144.19, 144.08, 142.07, 141.96, 132.07, 132.03, 131.93, 131.82, 131.80, 128.81, 127.76, 122.92, 122.50, 89.31, 87.72, 82.14, 81.93, 63.04, 61.36, 24.29, 21.03, 20.41; HRMS-NSI (*m/z*): $[M–e]^+$ calcd for $C_{36}H_{30}O_3$, 510.2189; found, 510.2196.

(*Z*)-bis(2-cyanoethyl) (((1,2-diphenylethene-1,2-diyl)bis(4,1-phenylene))bis(but-3-yne-4,1-diyl)) bis(diisopropylphosphoramidite) (17)

Compound **3** (43 mg, 0.09 mmol) was dissolved in DCM (0.9 mL) and DIPEA (0.1 mL), before CEP-Cl (50 mg, 0.21 mmol) was added dropwise at rt. The reaction mixture was stirred at rt. for 1 h, then concentrated *in vacuo*. The residue was purified by a short silica gel flash column chromatography (hexane/EtOAc 7:3 + 1% Et_3N) to obtain compound **17** as a yellowish solid (64 mg, 0.07 mmol, 80%). R_f = 0.78 (hexane/EtOAc 4:6 + 1% Et_3N); ^{1}H NMR (400 MHz, DCM-d_2) δ 7.15–7.09 (m, 10H), 7.03–6.99 (m, 4H), 6.95–6.92 (m, 4H), 3.88–3.74 (m, 8H), 3.66–3.58 (m, 4H), 2.69 (t, *J* = 6.9 Hz, 4H), 2.62 (td, *J* = 6.3, 4.6 Hz, 4H), 1.19 (dd, *J* = 6.8, 1.6 Hz, 24H); ^{13}C NMR (101 MHz, DCM-d_2) δ 143.83, 143.79, 141.49, 131.79, 131.75, 131.49, 128.28, 127.21, 122.39, 118.40, 87.81, 82.02, 62.56, 62.38, 59.23, 59.04, 43.80, 43.68, 25.01, 24.97, 24.94, 24.90, 22.97, 22.90, 21.01, 20.94; ^{31}P NMR (162 MHz, DCM-d_2) δ 148.15; HRMS-NSI (*m/z*): $[M+H]^+$ calcd for $C_{52}H_{63}O_4N_4P_2$, 869.4319; found, 869.4309.

***Z*-TPE trimer (*Z*-TPE)$_3$ (19)**

Compound **16** (45 mg, 0.09 mmol) was placed in a flask and a 0.15 M solution of compound **17** in 1,2-DCE (0.2 mL, 0.03 mmol) was added at rt., followed by a 0.25 M solution of ETT in 1,2-DCE (0.4 mL). The reaction mixture was stirred at rt. for 30 min., before ^{t}BuOOH hydroperoxide solution (24 µL, 70% in H_2O) was added. The reaction mixture was stirred at rt. for further 30 min., then diluted with $CHCl_3$ (10 mL). The organic phase was washed three times with aq. sat. $NaHCO_3$ (3x10 mL), once with brine (10 mL), dried over $MgSO_4$, filtered, and concentrated *in vacuo*. The residue was purified by flash column chromatography on silica gel ($CHCl_3$ → $CHCl_3$/MeOH 98:2) to yield the protected *Z*-TPE trimer **18** as a yellowish foam (36 mg, 0.02 mmol, 70%). R_f = 0.06 ($CHCl_3$/MeOH 99:1); ^{1}H NMR (400 MHz, $CDCl_3$, 323 K) δ 7.15–7.07 (m, 30H), 7.00–6.96 (m, 12H), 6.95–6.92 (m, 12H), 4.28–4.21 (m, 16H), 2.80 (t, *J* = 6.7 Hz, 8H), 2.73–2.68 (m, 8H), 2.07 (s, 6H); ^{31}P NMR (162 MHz, $CDCl_3$, 323 K) δ –2.20; HRMS-NSI (*m/z*): $[M–e]^+$ calcd for $C_{112}H_{92}O_{12}N_2P_2$, 1718.6125; found, 1718.6309.

The protected *Z*-TPE trimer **18** (31 mg, 0.02 mmol) was dissolved in a 2 M solution of NH_3 in MeOH (15 mL) and the reaction mixture was stirred at rt. for 17 h. The solvent was removed *in vacuo* to yield a yellowish solid (29 mg). 6 mg of this yellowish solid was dissolved in 25 mM ammonium acetate in MeOH pH 6 (4 mL) and the counter ion of *Z*-TPE trimer was exchanged to ammonium by ion exchange chromatography (resin: Dowex 50WX8 hydrogen form, 50–100 mesh; eluent: 25 mM ammonium acetate in MeOH pH 6). After repeated lyophilization cycles (MeOH/H_2O 1:1), the final (*Z*-TPE)$_3$ **19** was isolated as a yellow solid. A stock solution was prepared by dissolving some of (*Z*-TPE)$_3$ **19** in ethanol. The concentration of this stock solution was determined according to the Beer-Lambert law: the absorbance was measured at 260 nm at 75 °C, using the following molar absorptivity ε: 122’364 L/mol·cm for (*Z*-TPE)$_3$ **19**. ^{1}H NMR (400 MHz, CD_3OD, 328 K) δ 7.12–6.82 (m, 54H), 4.02 (q, *J* = 6.9 Hz, 8H), 3.69 (t, *J* = 6.8 Hz, 4H), 2.70 (t, *J* = 6.7 Hz, 8H), 2.57 (t, *J* = 6.8 Hz, 4H), 1.88 (s); ^{31}P NMR (162 MHz, CD_3OD, 328 K) δ –0.08; HRMS-NSI (*m/z*): $[M–2H]^{2–}$ calcd for $C_{102}H_{80}O_{10}P_2$, 763.2619; found, 763.2626.

7.4.2 NMR Spectra

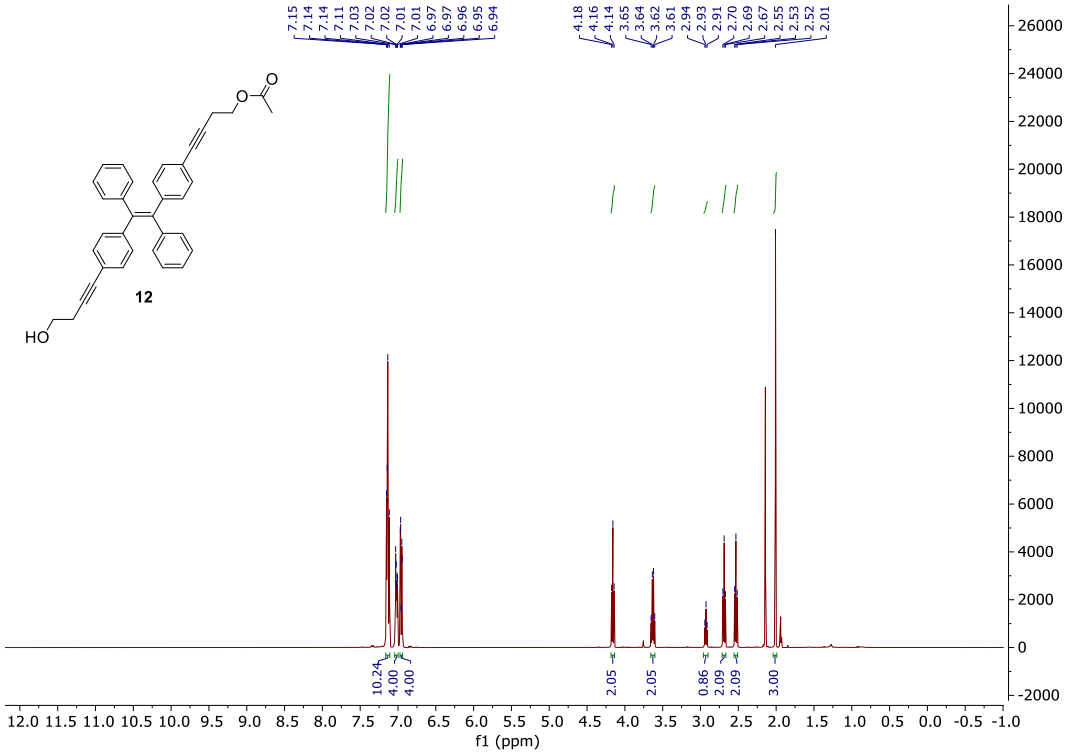

Figure 214. ^{1}H NMR of compound **12** in CD_3CN.

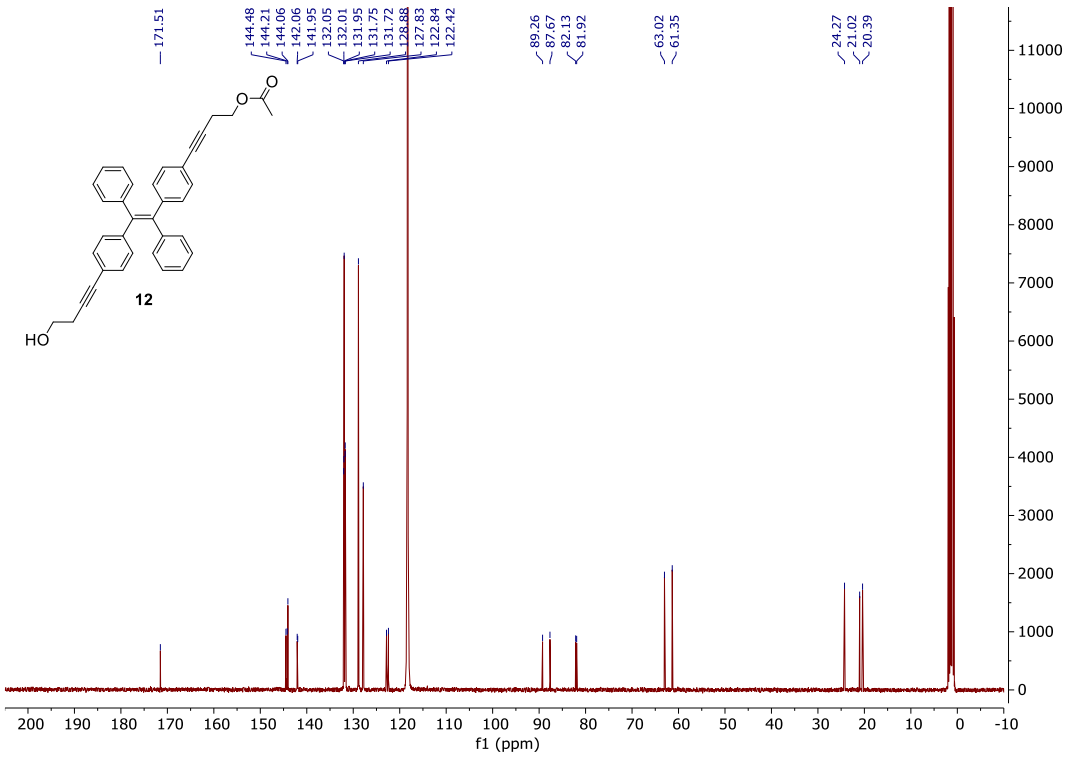

Figure 215. ^{13}C NMR of compound **12** in CD_3CN.

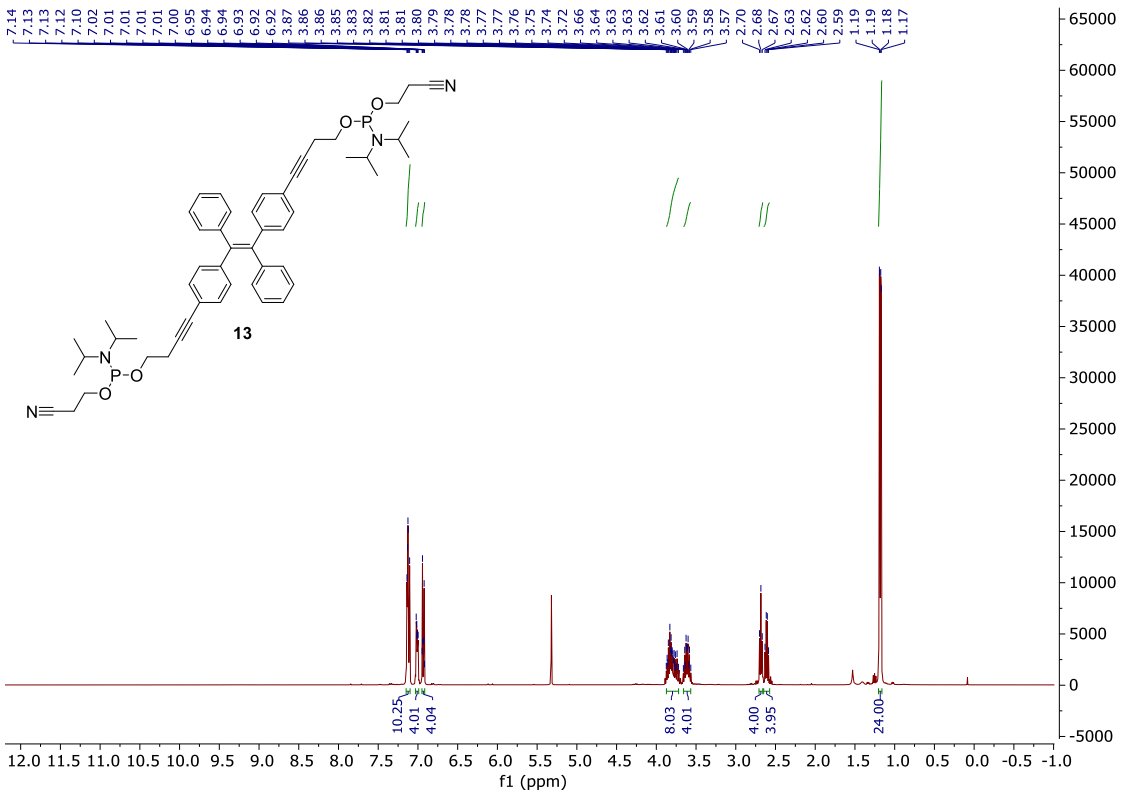

Figure 216. ^{1}H NMR of compound **13** in DCM-d_2.

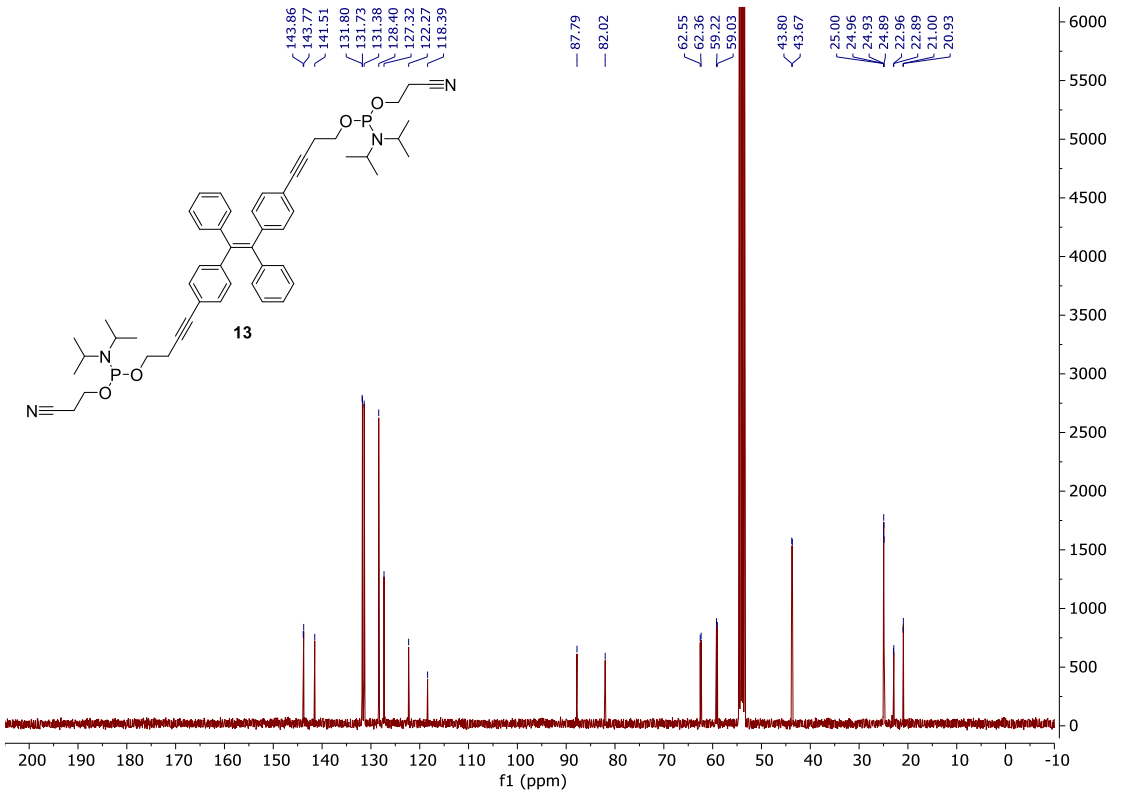

Figure 217. ^{13}C NMR of compound **13** in DCM-d_2.

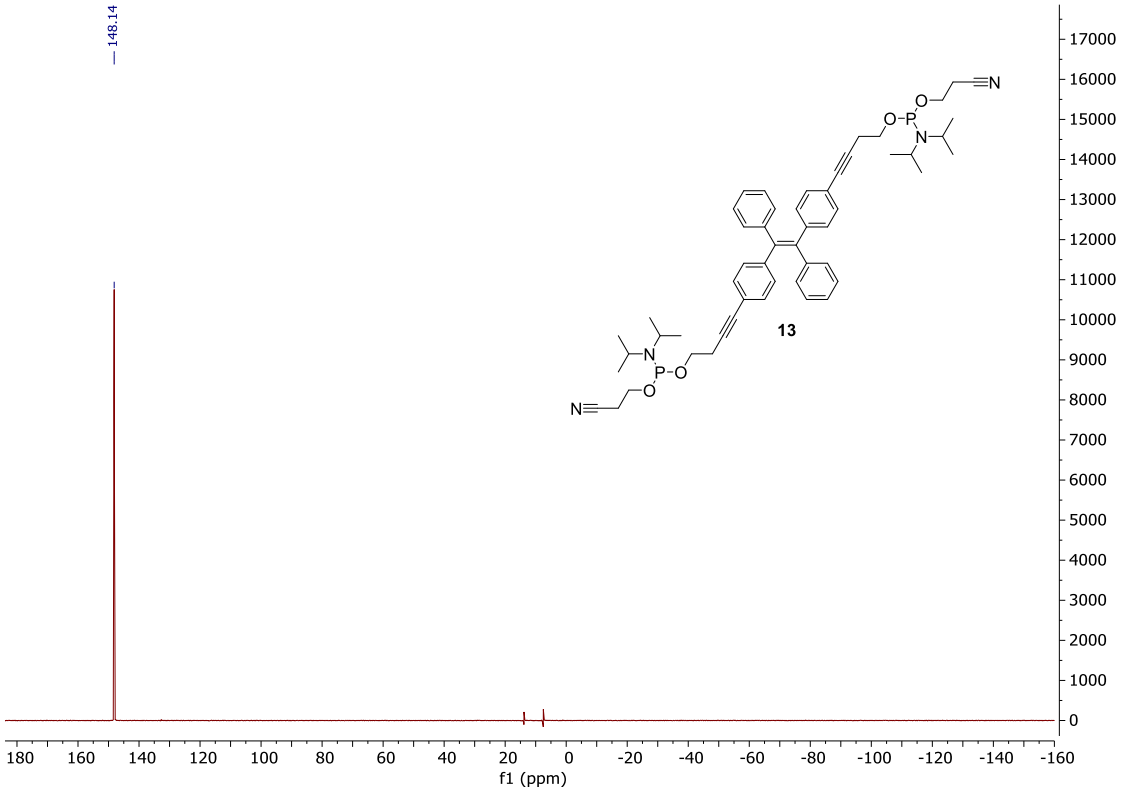

Figure 218. ^{31}P NMR of compound **13** in DCM-d_2.

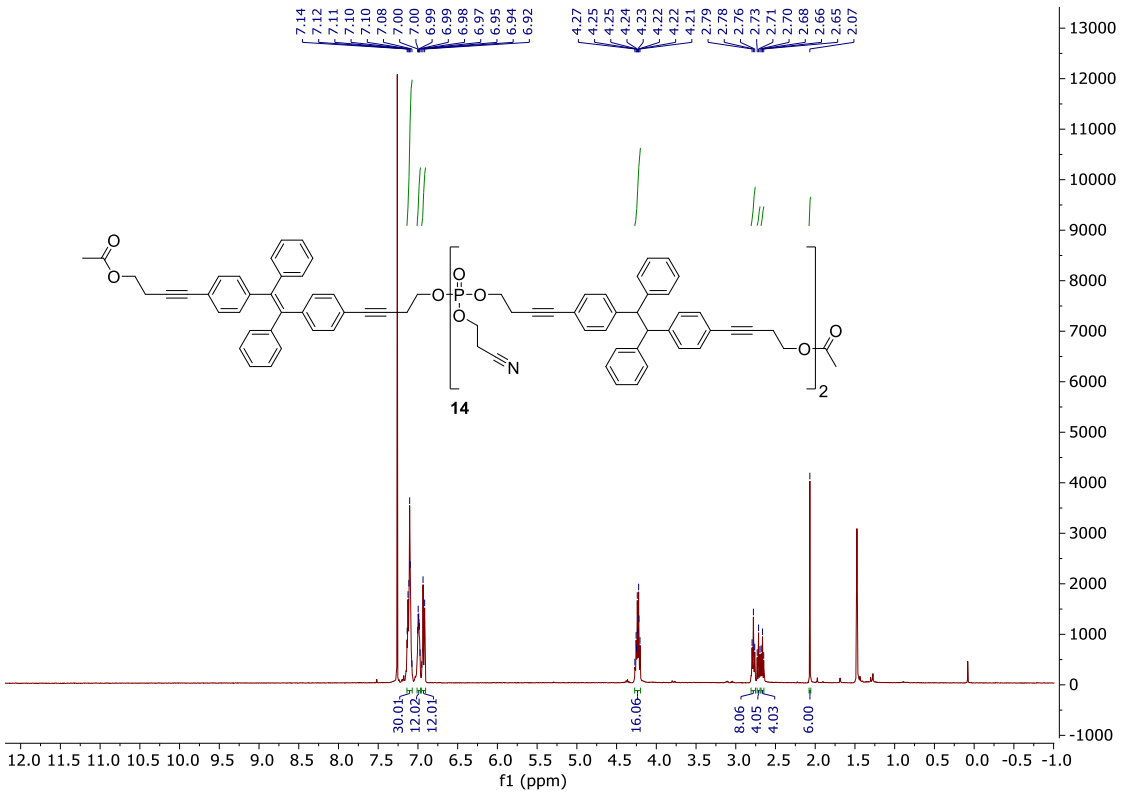

Figure 219. ^{1}H NMR of compound **14** in $CDCl_3$ at 323 K.

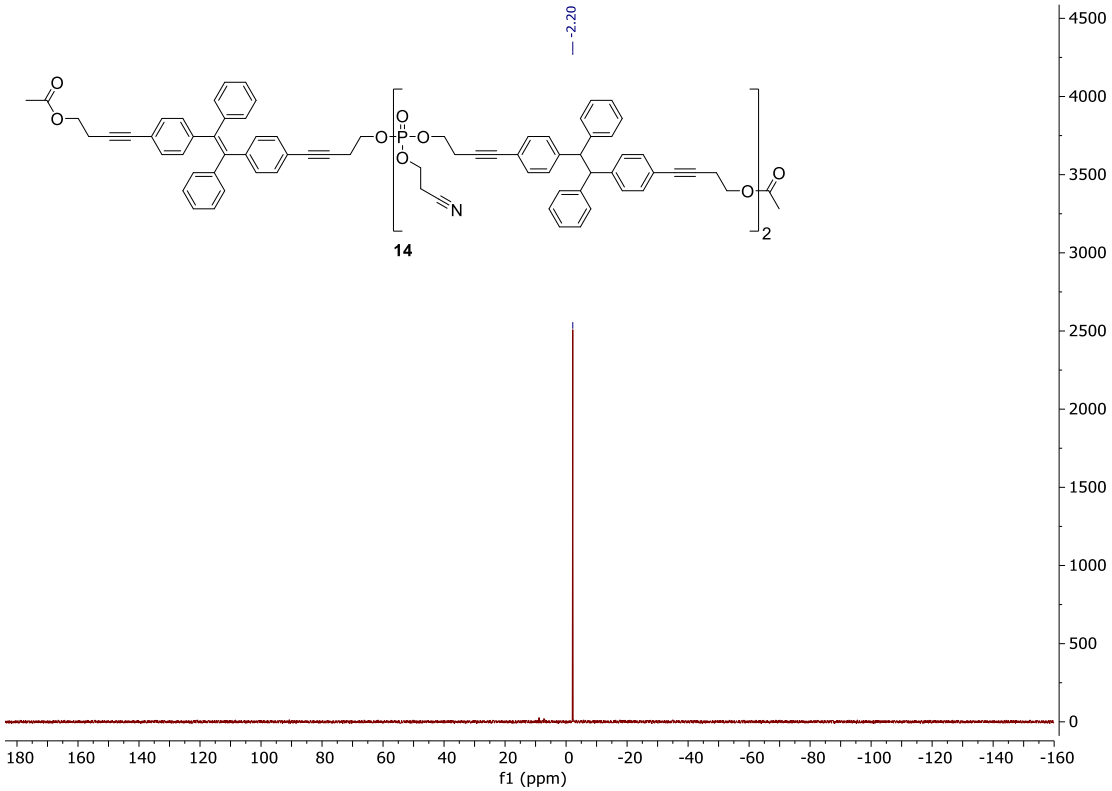

Figure 220. ^{31}P NMR of compound **14** in $CDCl_3$ at 323 K.

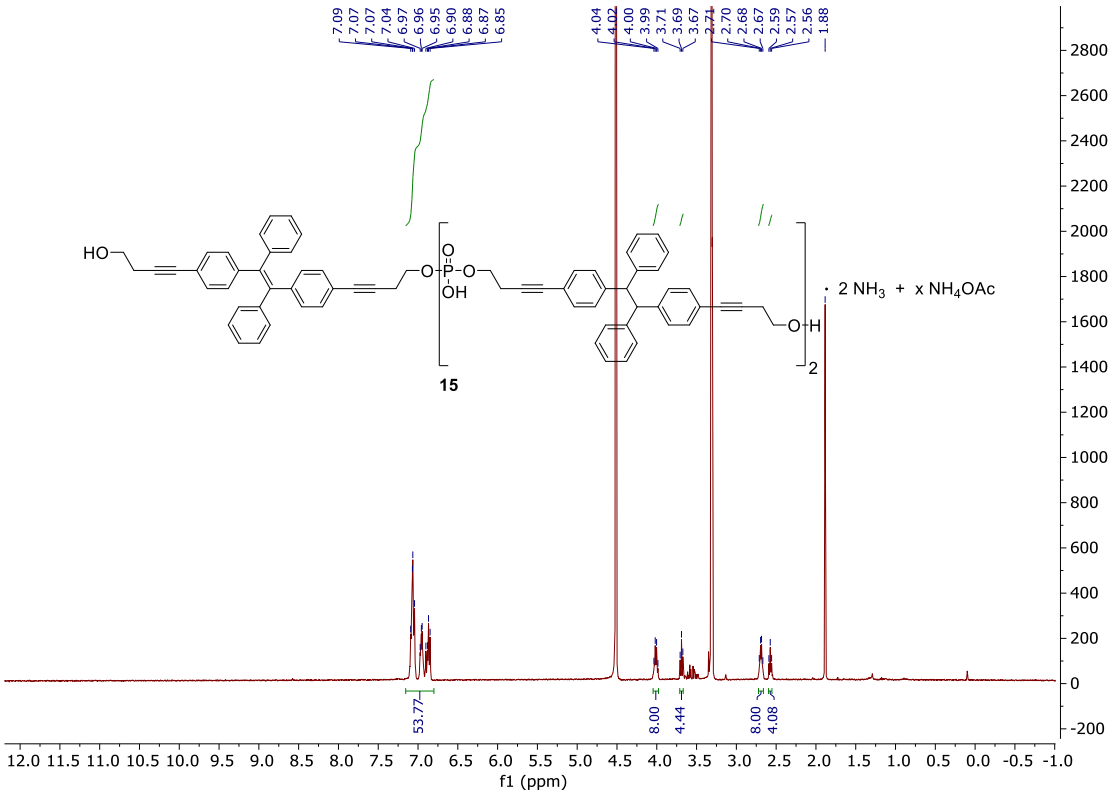

Figure 221. ^{1}H NMR of compound **15** in CD_3OD at 328 K.

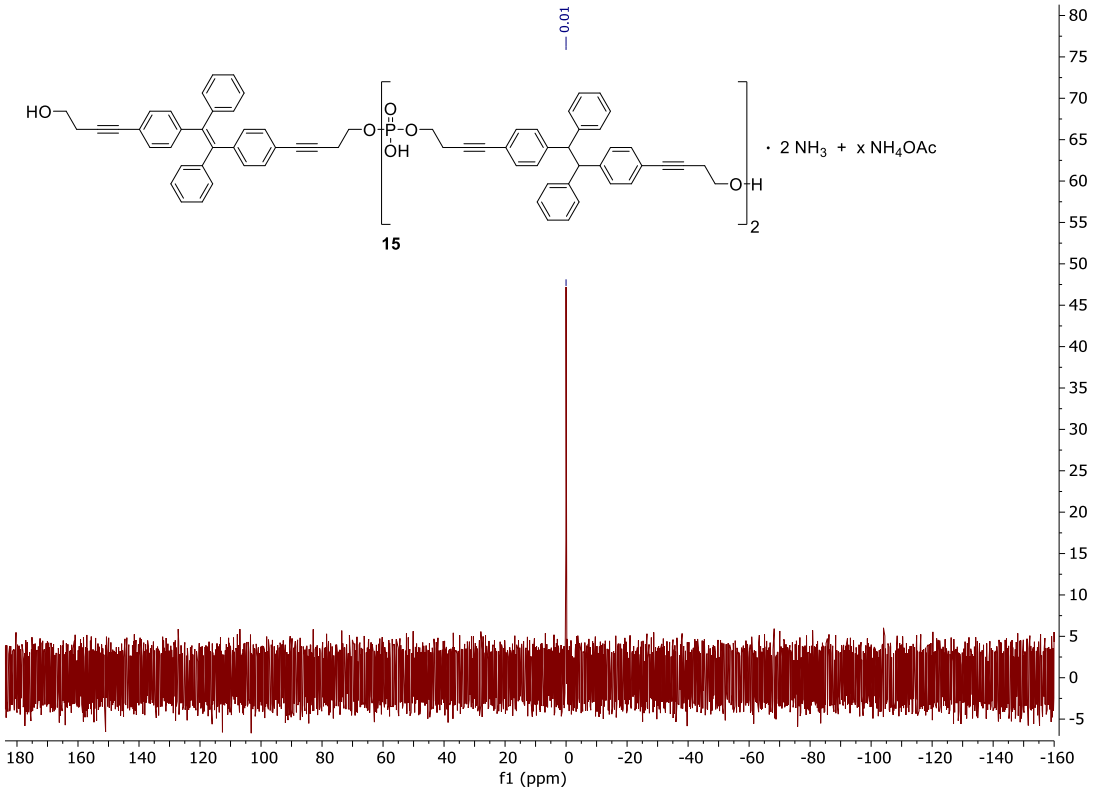

Figure 222. ^{31}P NMR of compound **15** in CD_3OD at 328 K.

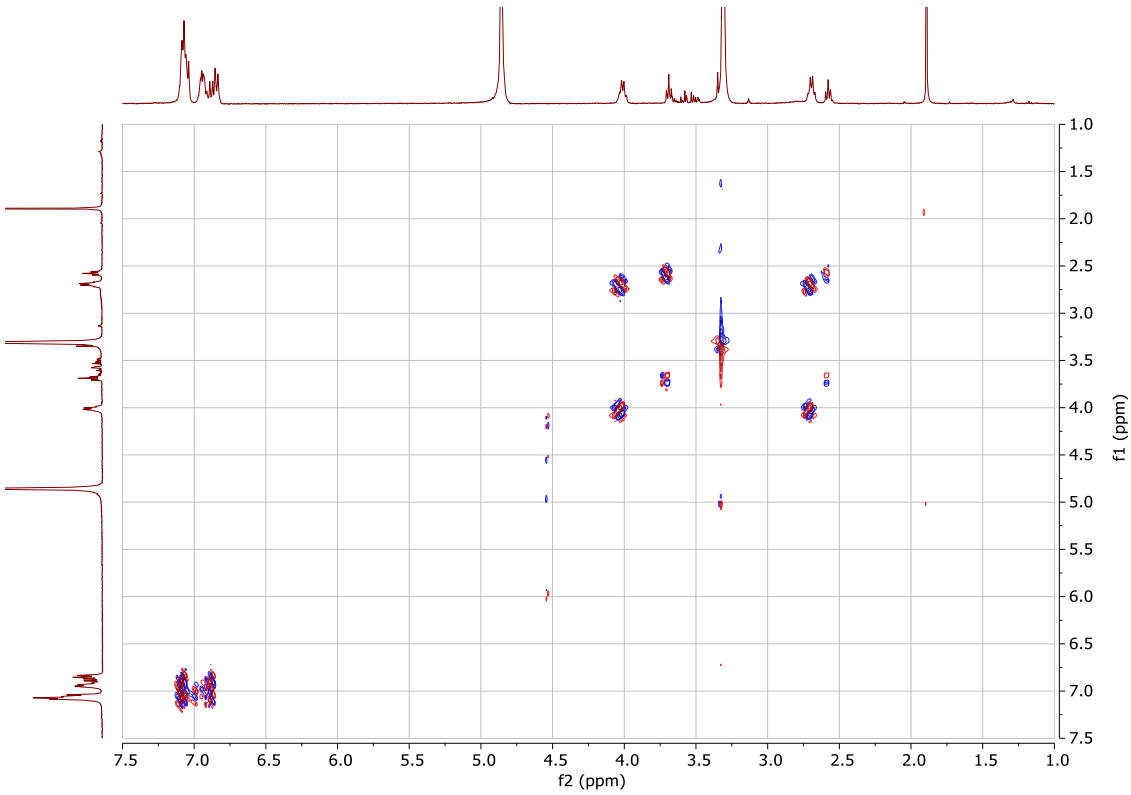

Figure 223. ^{1}H/^{1}H-COSY NMR of compound **15** in CD_3OD at 328 K.

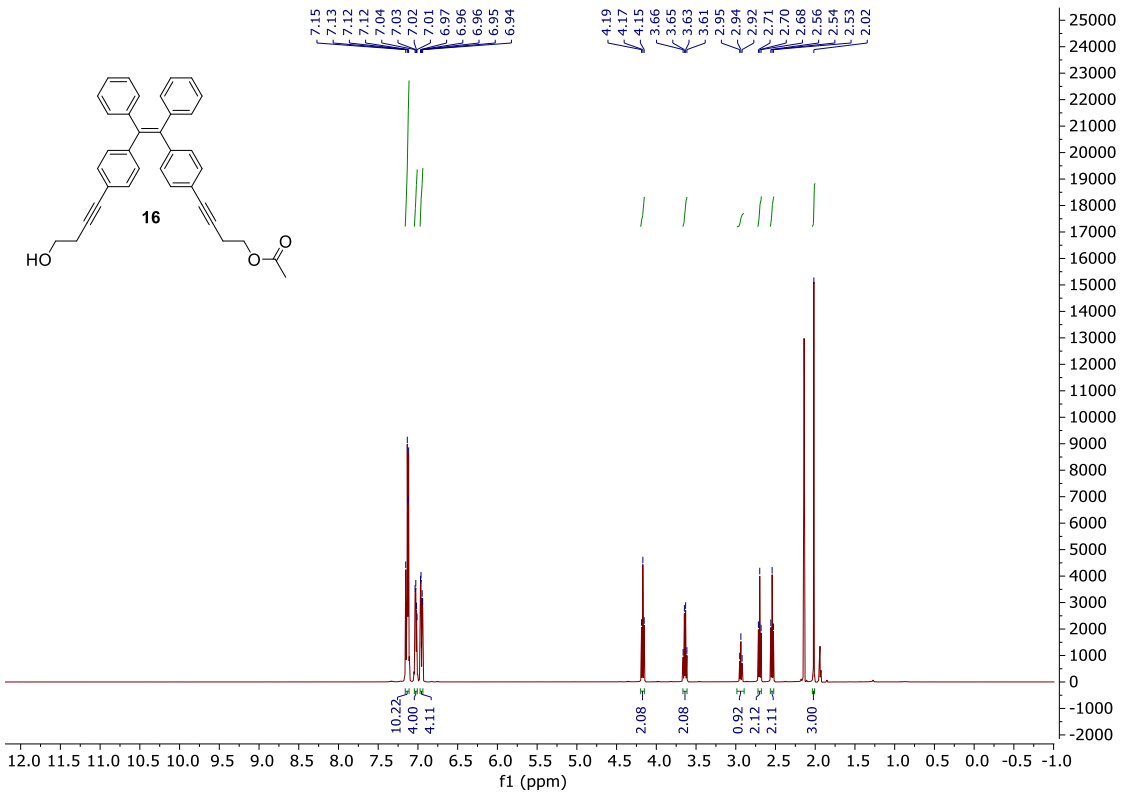

Figure 224. ^{1}H NMR of compound **16** in CD_3CN.

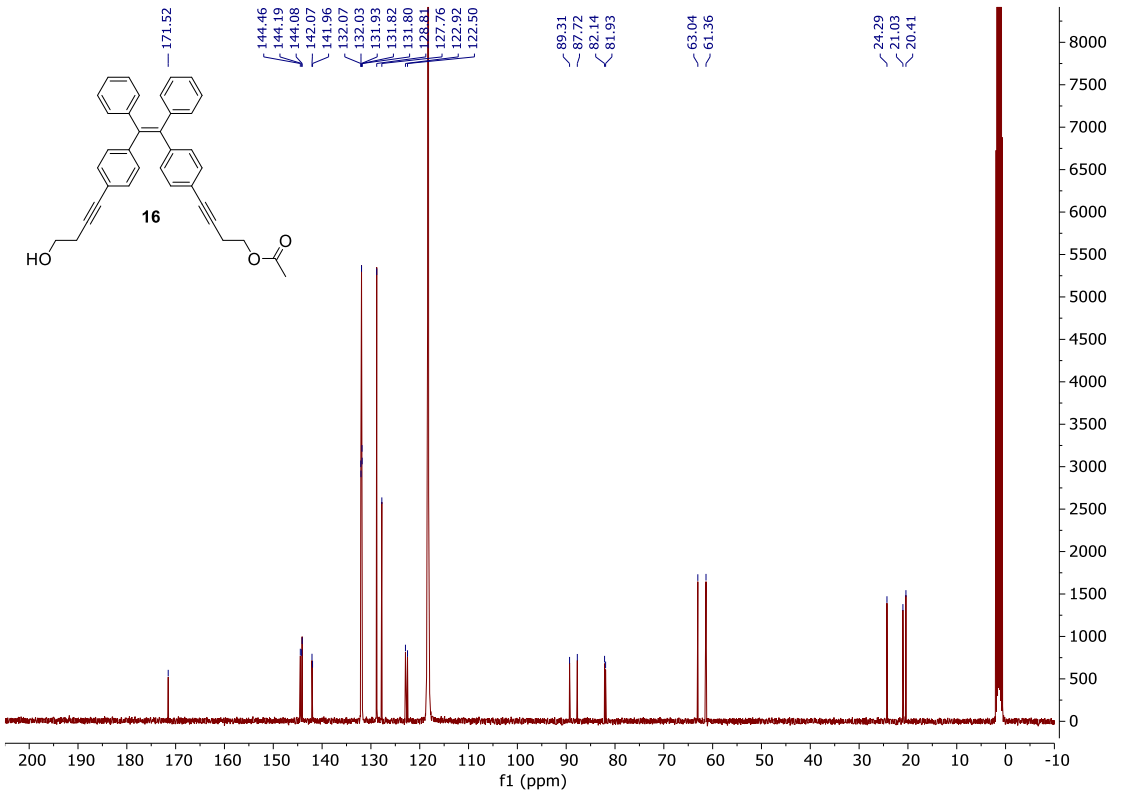

Figure 225. ^{13}C NMR of compound **16** in CD_3CN.

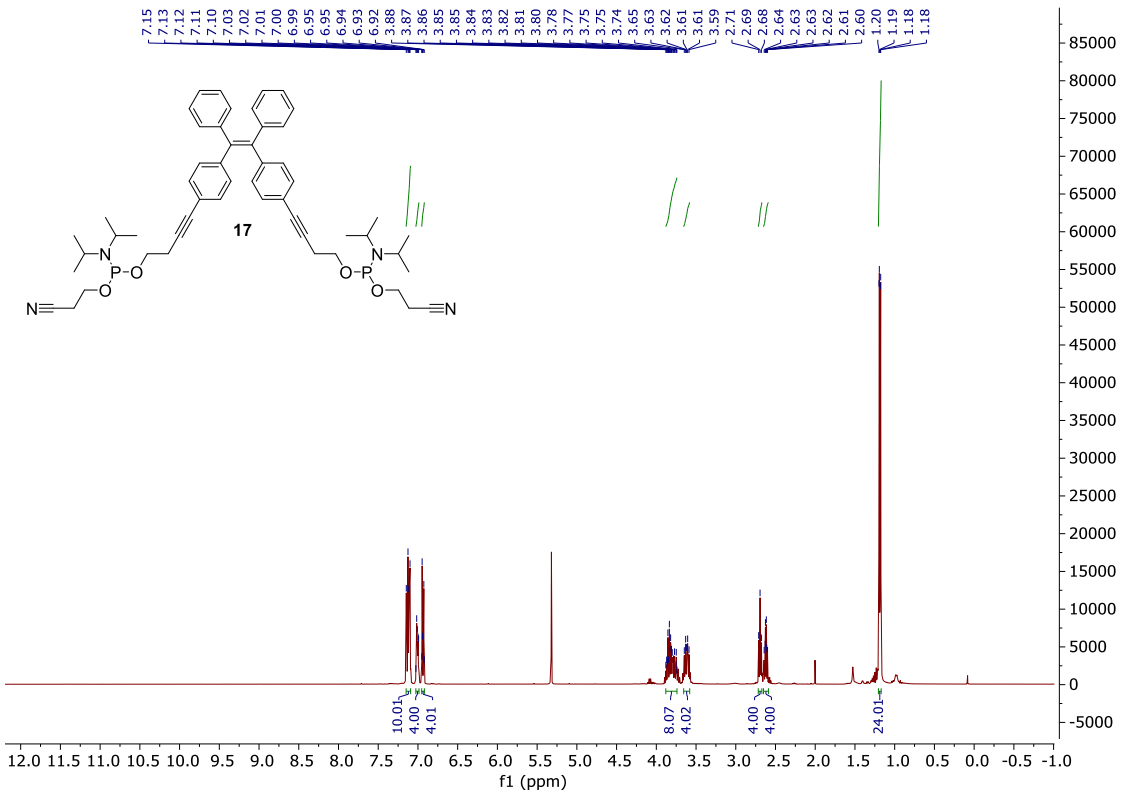

Figure 226. ^{1}H NMR of compound **17** in DCM-d_2.

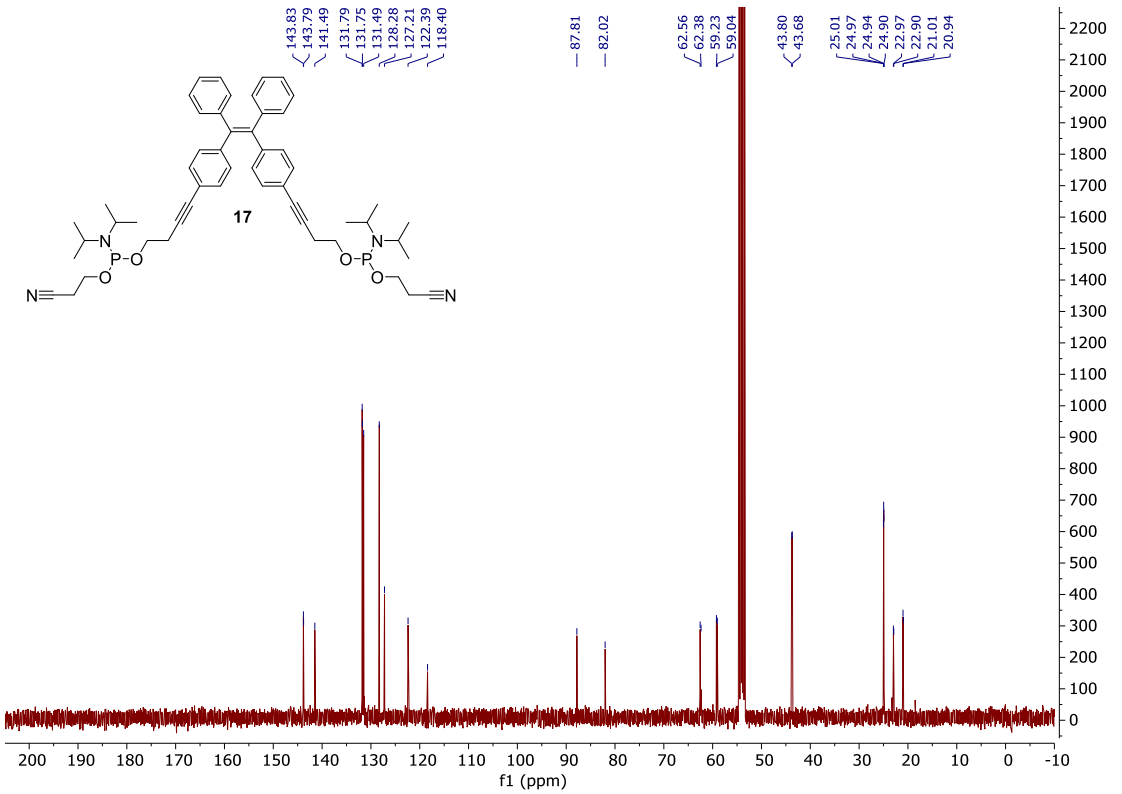

Figure 227. ^{13}C NMR of compound **17** in DCM-d_2.

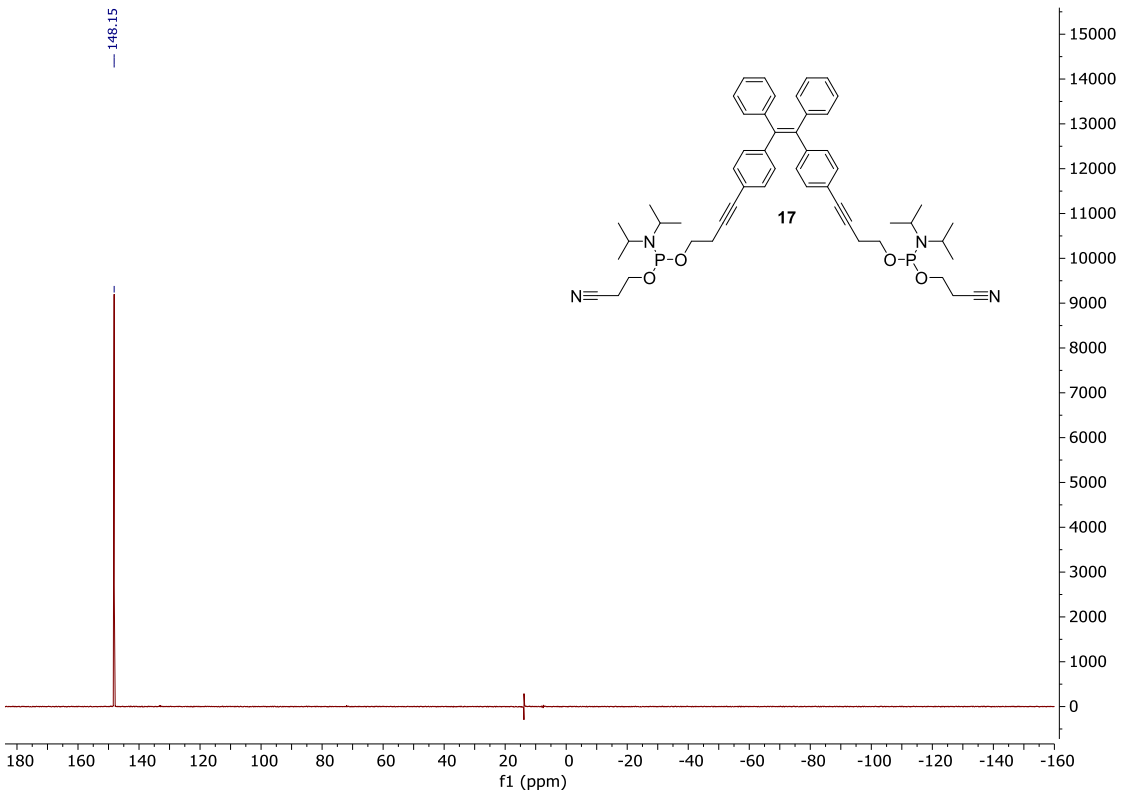

Figure 228. ^{31}P NMR of compound **17** in DCM-d_2.

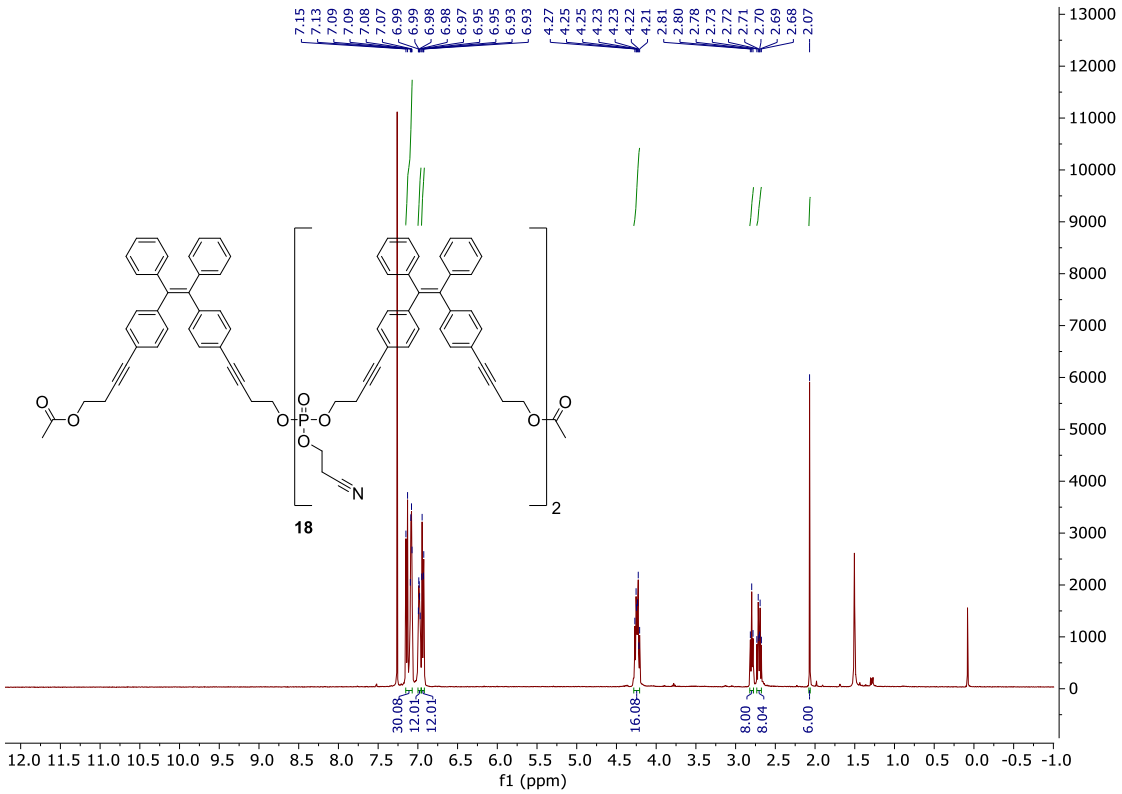

Figure 229. ^{1}H NMR of compound **18** in $CDCl_3$ at 323 K.

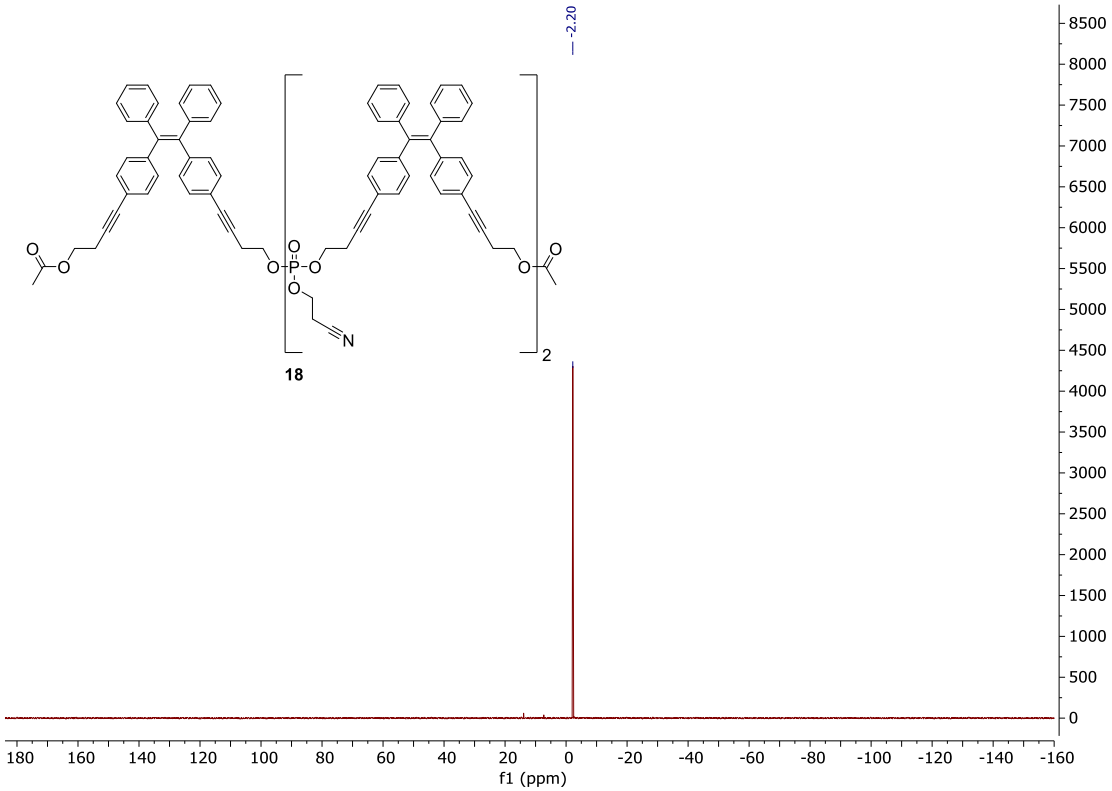

Figure 230. ^{31}P NMR of compound **18** in $CDCl_3$ at 323 K.

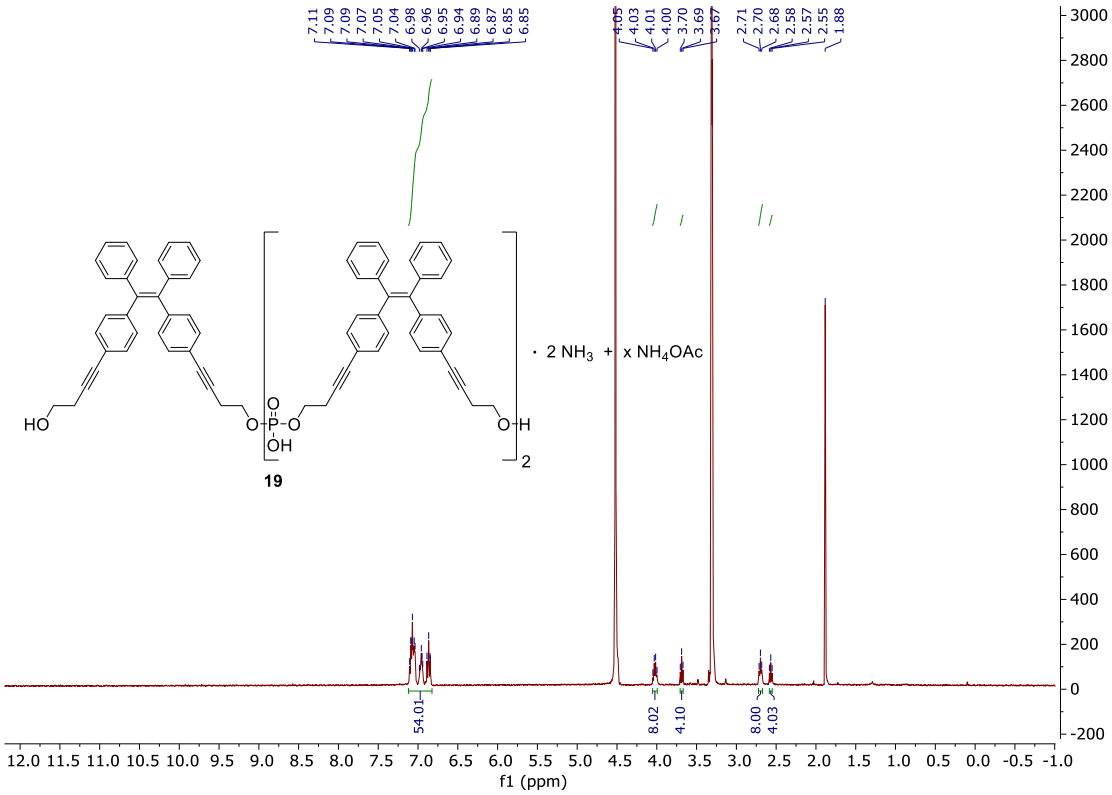

Figure 231. ^{1}H NMR of compound **19** in CD_3OD at 328 K.

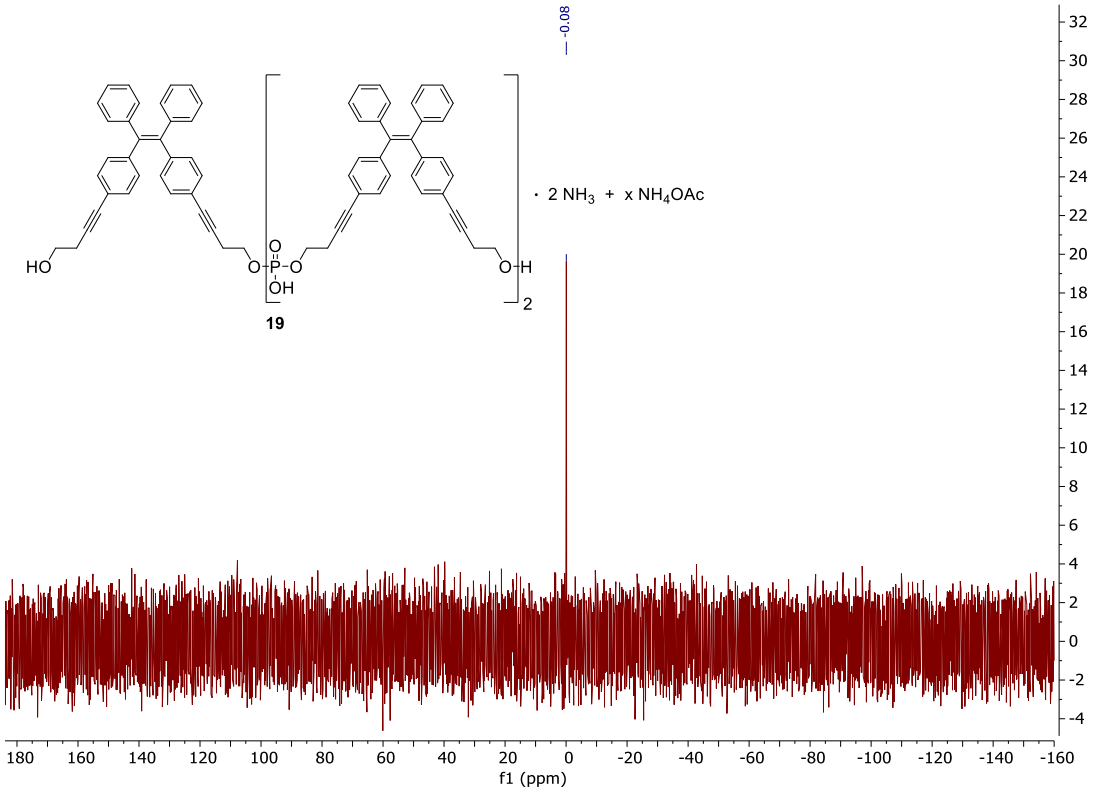

Figure 232. ^{31}P NMR of compound **19** in CD_3OD at 328 K.

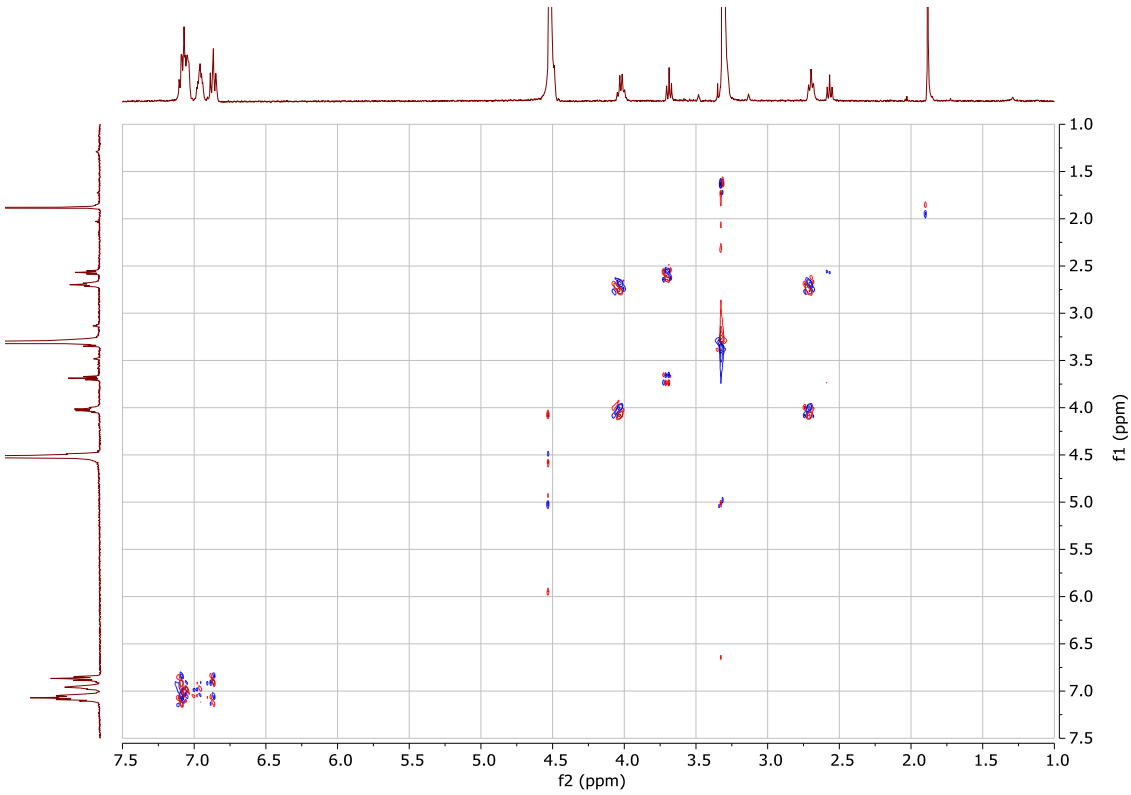

Figure 233. ^{1}H/^{1}H-COSY NMR of compound **19** in CD_3OD at 328 K.

7.4.3 MS Spectra

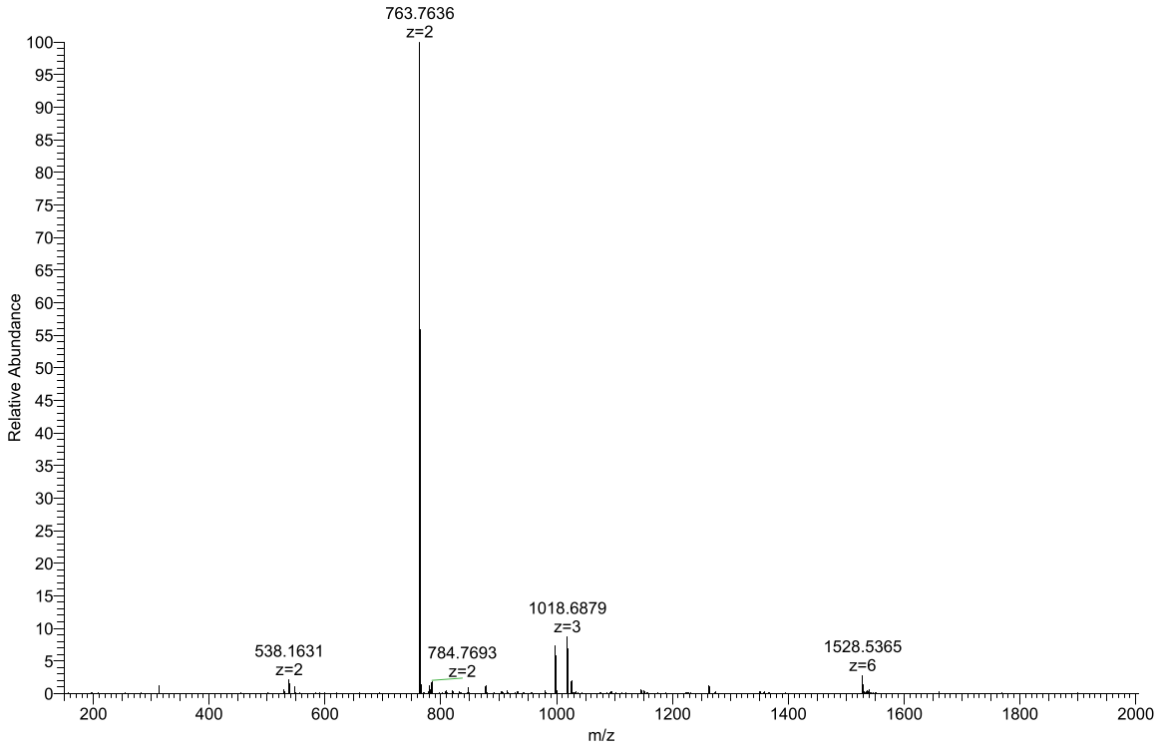

Figure 234. MS spectrum of (*E*-TPE)$_3$ **15**.

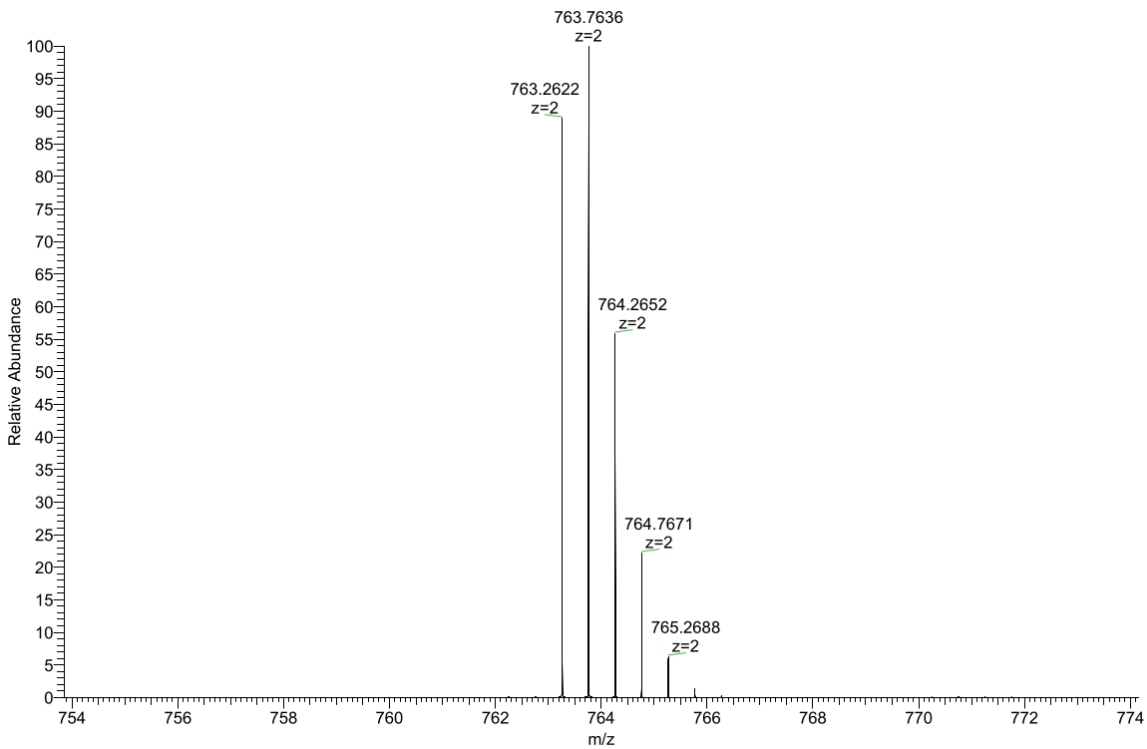

Figure 235. MS spectrum (zoom) of (*E*-TPE)$_3$ **15**.

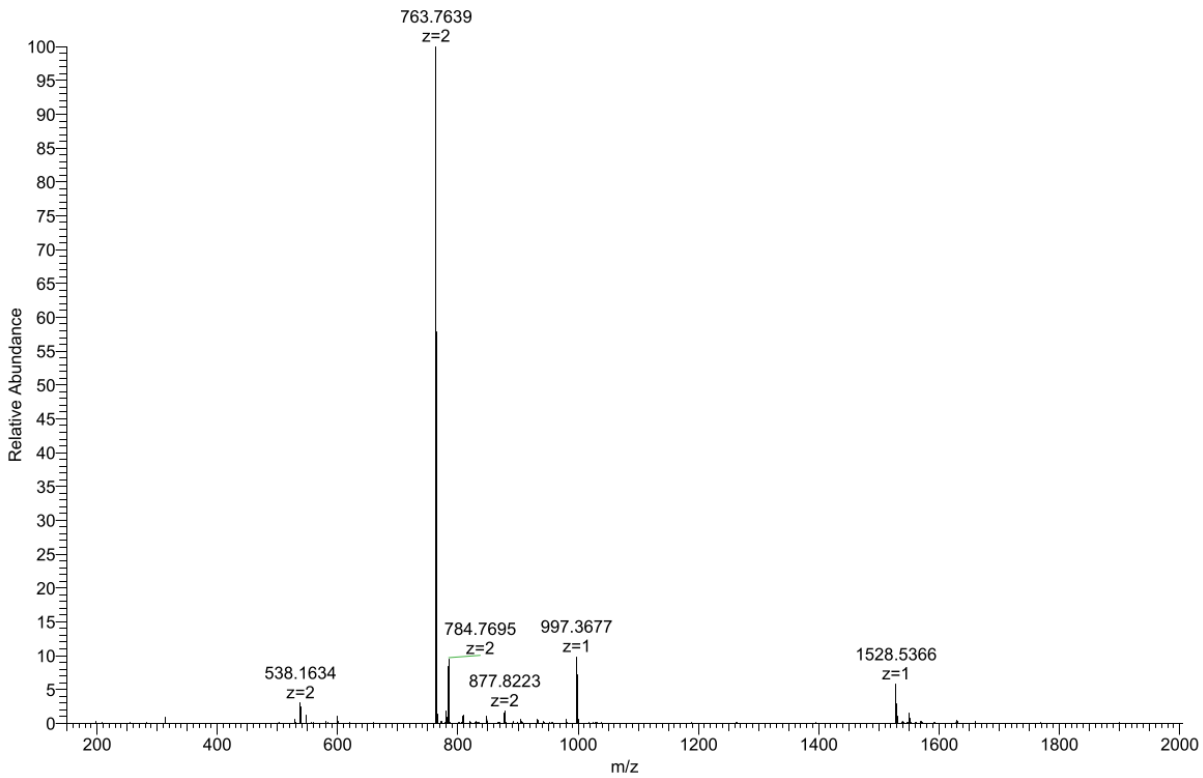

Figure 236. MS spectrum of (*Z*-TPE)$_3$ **19**.

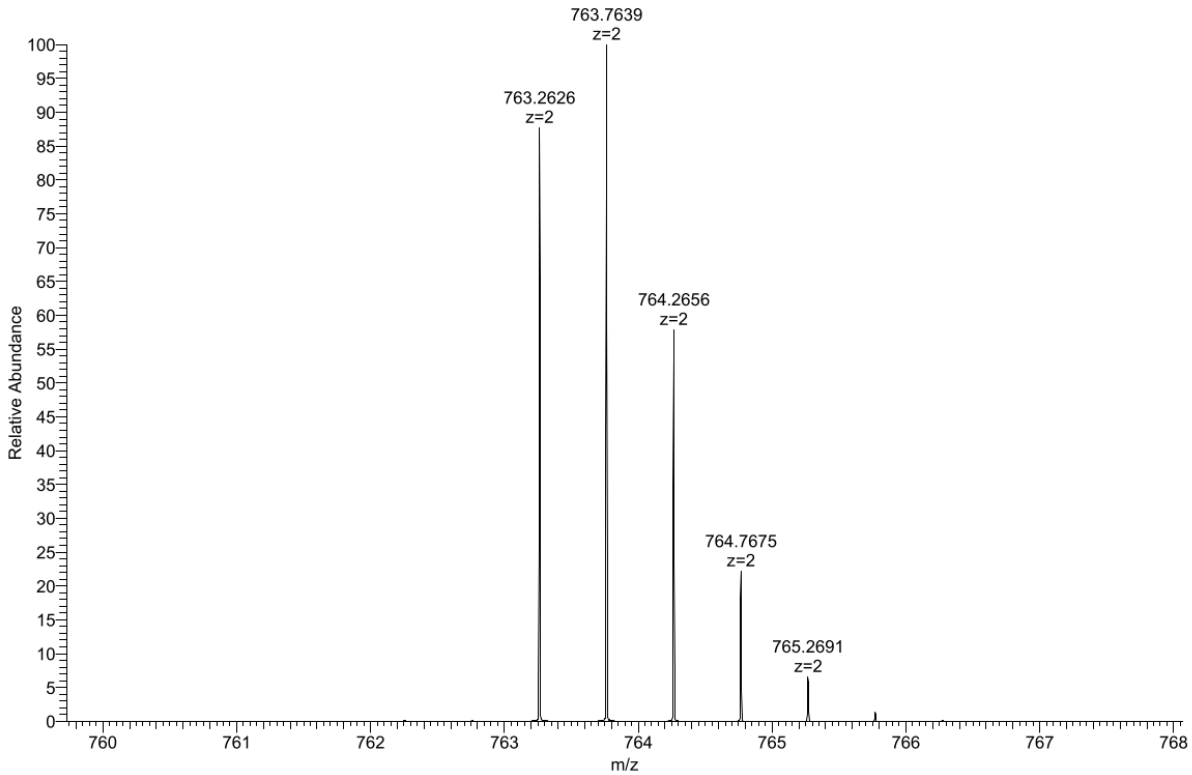

Figure 237. MS spectrum (zoom) of (*Z*-TPE)$_3$ **19**.

8 On-Surface Chemistry

The synthesis of two molecular precursors, either derived from cyclopenta[*hi*]aceanthrylene or pyrene, for subsequent on-surface polymerization reactions *via* Ullmann couplings is described. In addition, the synthesis of terpyridine-modified DNA single strands is reported. The mechanical properties of these chemically modified oligonucleotides, adsorbed on a gold surface, is intended to be investigated by cryo-force spectroscopy.

This entire chapter describes collaborative work with the research group of Prof. Dr. Ernst Meyer from the Department of Physics of the University of Basel. My contribution comprised the synthesis of the desired target compounds.

8.1 Introduction

On-surface synthesis of carbon-based nanomaterials and the study of the resulting mechanical properties between these carbon nanostructures and metal surfaces, is of importance for a variety of technological applications.[243,244] The on-surface synthesis of such carbon-based nanomaterials can be accomplished by surface-assisted Ullmann couplings between aryl halide precursors.[245–247] Figure 238 shows an example of a linear poly(2,7-pyrenylene) chain, formed by Ullmann couplings starting with 2,7-dibromopyrene as precursor molecule. Subsequently, mechanical forces at the nanoscale can be studied for example by cryo-force spectroscopy.[248,249]

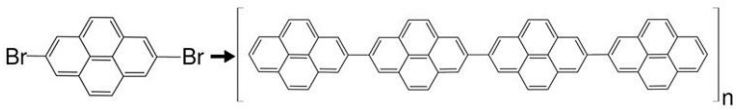

Figure 238. Ullmann coupling of 2,7-dibromopyrene, forming poly(2,7-pyrenylene). Figure adapted from ref. [250].

The Meyer group investigated such poly(2,7-pyrenylene) chains adsorbed on Au(111) surfaces by cryo-force spectroscopy under ultrahigh vacuum (UHV) conditions. Figure 239 displays some AFM and STM images of either the 2,7-dibromopyrene precursor or the poly(2,7-pyrenylene) chains adsorbed on Au(111). In the case of brominated nitrogen-containing precursors, nitrogen-doped nanomaterials with interesting electronic properties could be achieved.[251,252] In general, the observed mechanical and electronic properties depend on the precursors used, thus, two other dibromo-functionalized precursors were envisioned to employ for on-surface polymerization and cryo-force spectroscopy experiments, namely 2,7-dibromocyclopenta[*hi*]aceanthrylene **21** and 2,7-dibromopyrene-4,5,9,10-tetraone **23** (see sections 8.2.1 and 8.2.2).

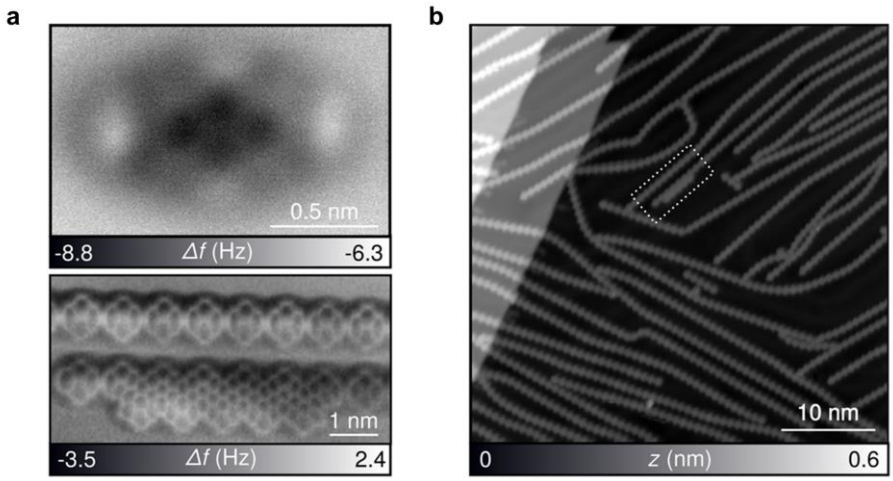

Figure 239. (**a**) AFM scan of 2,7-dibromopyrene imaged with a CO-functionalized tip (top) and AFM image of single and fused poly(2,7-pyrenylene) adsorbed on Au(111) (bottom). (**b**) STM overview image of poly(2,7-pyrenylene) chains. Figure adapted from ref. [250].

Beside the analysis of flat PAHs adsorbed on metal surfaces, the Meyer group also investigated mechanical properties of single-stranded DNA under UHV conditions.[253] For this purpose, 20-mer cytosine single strands were electrospray-deposited on Au(111). Afterwards, the DNA was lifted with the AFM tip vertically from the surface (Figure 240a). Lifting of the DNA resulted in repeating sharp dips in the retraction trace every 2–3 Å, which was attributed to the detachment of individual nucleotides (Figure 240b). However, the substantial folding of the DNA single strands on the surface limited the complete lifting. To overcome this limitation, DNA single strands with a terminal modification that could act as an anchoring group for a stronger DNA-tip interaction, *i.e.*, terpyridine, was proposed.[253]

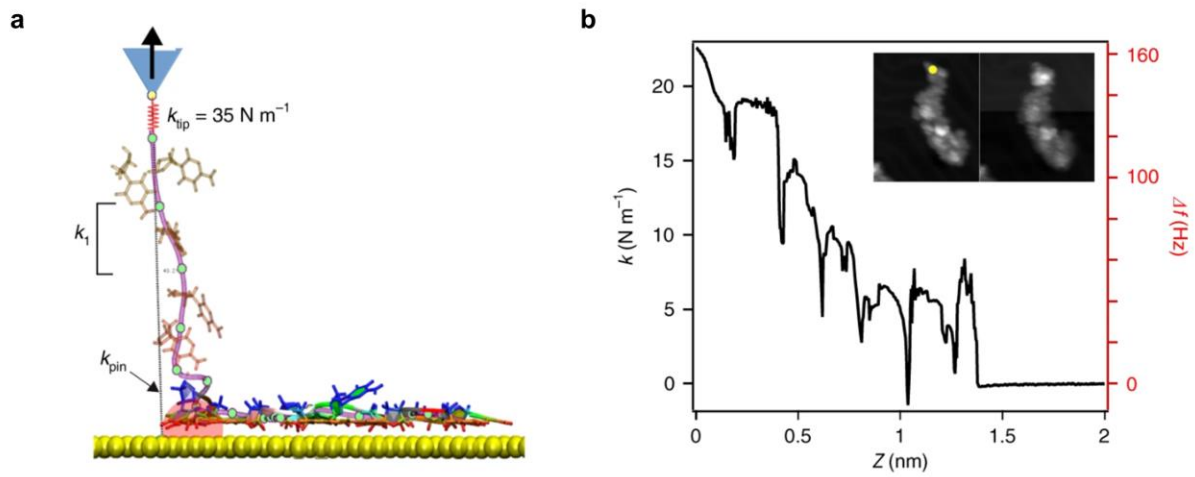

Figure 240. (**a**) Schematic representation of single-stranded DNA partially lifted and partially adsorbed on Au(111). (**b**) Retraction trace of single-stranded DNA. The yellow dot in the inset denotes the point, at which the lifting process of the single-stranded DNA was started. Figure adapted from ref. [253].

8.2 Results and Discussion

8.2.1 2,7-Dibromocyclopenta[*hi*]aceanthrylene

For the on-surface polymerization and characterization, 2,7-dibromocyclopenta[*hi*]aceanthrylene **21** was used (Scheme 7). This molecule was selected due to its exceptional electronic properties, which are mainly ascribed to the fact that cyclopenta[*hi*]aceanthrylene represents a fragment of the C_{70} fullerene.[254,255] Thus, compared to fullerenes, similar electronic properties have been reported for cyclopenta[*hi*]aceanthrylene derivatives, such as a low-lying lowest-energy unoccupied molecular orbital (LUMO) and a promising electron acceptor behavior, *e.g.*, relevant for organic photovoltaic applications.[256–259]

The synthesis of the target compound **21** was performed during the course of my Master's thesis (Simon Rothenbühler, *Water-Soluble, Supramolecular Polymers Based on the C_{70} Fullerene Subunit Cyclopenta[hi]aceanthrylene*, Master's thesis, University of Bern, 2018). However, the collaborative work for the on-surface polymerization of 2,7-dibromocyclopenta[*hi*]aceanthrylene **21** and the subsequent characterization of the polymeric chains was initiated in the beginning of my PhD thesis.

Outlined in Scheme 7 is the synthesis of 2,7-dibromocyclopenta[*hi*]aceanthrylene **21**, which followed published procedures.[255] Therefore, the commercially available 9,10-dibromoanthracene was transformed into 2,7-bis(trimethylsilyl)cyclopenta[*hi*]aceanthrylene **20**, which was further reacted with NBS to afford the desired compound **21**.

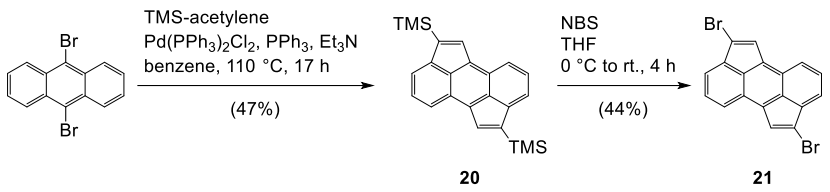

Scheme 7. Synthesis of 2,7-dibromocyclopenta[*hi*]aceanthrylene **21**.

8.2.2 2,7-Dibromopyrene-4,5,9,10-tetraone

2,7-Dibromopyrene-4,5,9,10-tetraone **23** was intended for on-surface experiments because adatoms, *i.e.*, iron, could be incorporated into the polymer chains *via* coordination of the metal adatoms to the oxygen lone pairs from compound **23**.[260] The introduction of adatoms into such polymer chains may result in materials with tailored nanotechnological properties.[261]

Depicted in Scheme 8 is the synthesis of 2,7-dibromopyrene-4,5,9,10-tetraone **23**, which was adapted from published procedures.[262,263] In a first step, pyrene was oxidized to obtain pyrene-4,5,9,10-tetraone **22**, before it was brominated in the presence of NBS to yield target compound **23**.

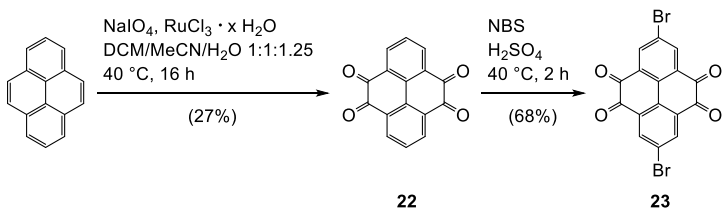

Scheme 8. Synthesis of 2,7-dibromopyrene-4,5,9,10-tetraone **23**.

8.2.3 TerPy-Modified DNA

As outlined in chapter 8.1, the adsorbed DNA single strand could not be lifted completely from the surface. This was mainly attributed to a too weak interaction between the AFM tip and the DNA itself. To enhance this AFM tip-DNA interaction, an anchoring group was proposed to install at the end of the DNA single strand, such as a terminal 2,2':6',2''-terpyridine (TerPy) moiety (Figure 241). This terminal TerPy group should then act as the attachment point for the lifting experiments. TerPy was selected because the tridentate ligand readily coordinates with different metals. The linker between the TerPy moiety and DNA was kept short (*i.e.*, rigid), to avoid perturbances during the lifting experiments. Listed in Figure 241 are the two DNA sequences, which are modified at the 5'-end with one TerPy unit each.

Strand	Sequence (5'→3')
ON25	TerPy-CAA GGT CCG ATG CAA GGA AG
ON26	TerPy-CTT CCT TGC ATC GGA CCT TG

TerPy =

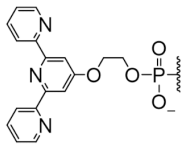

Figure 241. Summary of DNA sequences and molecular structure of the 2,2':6',2''-terpyridine modification.

The synthetic approach for the synthesis of TerPy phosphoramidite **25**, required for the subsequent solid-phase synthesis of the final TerPy-modified oligonucleotides **ON25** and **ON26**, is presented in Scheme 9. 4'-Chloro-2,2':6',2''-terpyridine was reacted in the presence of a base with ethylene glycol in excess to afford TerPy-OH **24**. Phosphitylation of TerPy-OH **24** yielded TerPy phosphoramidite **25**. Oligomers **ON25** and **ON26** were prepared *via* solid-phase synthesis and purified by HPLC (see section 8.4.4).

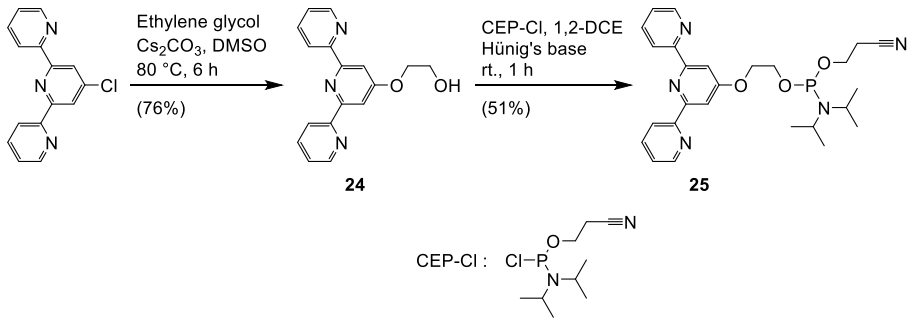

Scheme 9. Synthetic approach for TerPy phosphoramidite **25**.

8.3 Conclusions and Outlook

In summary, the desired target compounds, 2,7-dibromocyclopenta[*hi*]aceanthrylene **21**, 2,7-dibromopyrene-4,5,9,10-tetraone **23**, and TerPy-modified DNA single strands **ON25** and **ON26** have been successfully synthesized.

Ongoing experiments focus on the on-surface polymerization of compounds **21** and **23** as well as subsequent characterization, *e.g.*, lifting experiments to study desorption and re-adsorption of the polymerized molecules on the surface, or to measure mechanical forces, such as friction between the adsorbed molecules and the surface.

Regarding the TerPy-modified DNA single strands **ON25** and **ON26**, the addressability of the TerPy moiety with the tip would need to be studied. Additionally, if the TerPy unit can be specifically addressed with the tip, the strength of the TerPy-tip interaction should be investigated in future experiments. Achieving these challenging tasks among others, the vision towards successful single-base recognition in short DNA single strands by cryo-force spectroscopy can be imagined.[253]

The metal complexation properties of TerPy units or similar metal coordinating ligands render them as useful functionalities in DNA nanotechnology, *i.e.*, for the construction of metallo-supramolecular assemblies.[264–268] Hence, one could explore the supramolecular assembly behavior of the TerPy-modified DNA duplex **ON25*ON26** under comparable aqueous conditions (namely in the presence of spermine) as used previously for the TPE-modified DNA duplexes. In this case, one would replace the hydrophobic TPE sticky ends with TerPy units on both sides of the duplex that could form nanostructures mediated through TerPy-metal complexation interactions.

8.4 Appendix – Chapter 8

8.4.1 Organic Synthesis of 2,7-Dibromopyrene-4,5,9,10-tetraone

Pyrene-4,5,9,10-tetraone (22)

Pyrene (509 mg, 2.5 mmol) was dissolved in DCM (10 mL) and MeCN (10 mL). Sodium periodate (4.24 g, 19.8 mmol), H_2O (12 mL) and $RuCl_3 \cdot x\ H_2O$ (64 mg) was added. The resulting dark-brown reaction mixture was refluxed at 40 °C for 16 h. The reaction mixture was diluted with H_2O (20 mL) and the organic phase was separated. The remaining aqueous layer was extracted twelve times with DCM (10 mL), before all organic layers were combined and washed once with brine (50 mL). The organic layer was dried over $MgSO_4$, filtered and concentrated *in vacuo*. The crude product was purified by flash column chromatography on silica gel (DCM 100% → DCM/EtOAc 95:5) to yield product **22** as a yellowish solid (175 mg, 0.67 mmol, 27%). R_f = 0.09 (DCM); ^{1}H NMR (300 MHz, DMSO-d_6) δ 8.33 (d, J = 7.7 Hz, 4H), 7.74 (t, J = 7.7 Hz, 2H); HRMS-NSI (*m/z*): $[M+Na]^+$ calcd for $C_{16}H_6O_4Na$, 285.0158; found, 285.0159.

2,7-Dibromopyrene-4,5,9,10-tetraone (23)

Compound **22** (392 mg, 1.5 mmol) was dissolved in conc. H_2SO_4 (6 mL), before NBS (587 mg, 3.3 mmol) was added all at once. The reaction mixture was heated to 40 °C for 2 h. The orange/brown reaction mixture was quenched inversely with H_2O (195 mL) and the forming solid was filtered off. The filter cake was washed with H_2O, EtOH, and DCM. Product **23** was isolated as a bright yellow powder (426 mg, 1 mmol, 68%). R_f = 0.54 (DCM/EtOAc 95:5); ^{1}H NMR (300 MHz, THF-d_8) δ 8.49 (s, 4H); HRMS-NSI (*m/z*): $[M+Na]^+$ calcd for $C_{16}H_4O_4Br_2Na$, 440.8369; found, 440.8374.

8.4.2 Organic Synthesis of TerPy Phosphoramidite

2-([2,2':6',2''-Terpyridin]-4'-yloxy)ethan-1-ol (24)

Ethylene glycol (291 mg, 4.69 mmol) was dissolved in DMSO (4.7 mL), before Cs_2O_3 (1.52 g, 4.67 mmol) was added. The reaction mixture was heated to 80 °C and stirred at this temperature for 10 min. 4'-Chloro-2,2':6',2"-terpyridine (251 mg, 0.94 mmol) was added at 80 °C and the reaction mixture was stirred for further 6 h. After cooling the reaction mixture to rt., it was precipitated into ice-cold water (25 mL) and the precipitate was filtered off. The filter cake was washed thoroughly with ice-cold water. After drying the filter cake *in vacuo*, product **24** was afforded as an off-white solid (210 mg, 0.72 mmol, 76%). R_f = 0.05 (DCM/MeOH 98:2); ^{1}H NMR (400 MHz, DMSO-d_6) δ 8.72 (ddd, J = 4.7, 1.6, 0.8 Hz, 2H), 8.62 (dt, J = 7.9, 1.1 Hz, 2H), 8.03–7.97 (m, 4H), 7.50 (ddd, J = 7.5, 4.7, 1.2 Hz, 2H), 4.98 (t, J = 5.5 Hz, 1H), 4.27 (t, J = 4.8 Hz, 2H), 3.80 (q, J = 5.1 Hz, 2H); ^{13}C NMR (101 MHz, DMSO-d_6) δ 166.85, 156.67, 154.86, 149.24, 137.35, 124.48, 120.88, 106.80, 69.95, 59.30; HRMS-NSI (*m/z*): $[M+H]^+$ calcd for $C_{17}H_{16}O_2N_3$, 294.1237; found, 294.1228.

2-([2,2':6',2''-Terpyridin]-4'-yloxy)ethyl (2-cyanoethyl) diisopropylphosphoramidite (25)

Starting material **24** (150 mg, 0.51 mmol) was suspended in 1,2-dichloroethane (6.4 mL) and Hünig's base (0.3 mL). CEP-Cl (126 mg, 0.53 mmol) was added dropwise and the reaction mixture was stirred at rt. for 1 h. The reaction mixture was concentrated *in vacuo*, before the crude product (383 mg) was purified by a short flash column chromatography on silica gel (hexane/EtOAc 4:6 + 1% Et_3N). Product **25** was isolated as an off-white solid (128 mg, 0.26 mmol, 51%). R_f = 0.50 (hexane/EtOAc 4:6 + 1% Et_3N); ^{1}H NMR (400 MHz, DMSO-d_6) δ 8.72 (ddd, J = 4.8, 1.8, 0.9 Hz, 2H), 8.61 (dt, J = 8.0, 1.0 Hz, 2H), 8.03–7.97 (m, 4H), 7.50 (ddd, J = 7.5, 4.8, 1.2 Hz, 2H), 4.48–4.38 (m, 2H), 4.07–3.93 (m, 2H), 3.82–3.69 (m, 2H), 3.63–3.52 (m, 2H), 2.76 (t, J = 5.9 Hz, 2H), 1.12 (dd, J = 6.8, 3.8 Hz, 12H); ^{13}C NMR (101 MHz, DMSO-d_6) δ 166.68, 156.71, 154.83, 149.23, 137.35, 124.50, 120.89, 118.94, 106.81, 68.31, 68.24, 61.70, 61.53, 58.41, 58.23, 42.57, 42.45, 24.38, 24.34, 24.31, 24.26, 19.82, 19.75; ^{31}P NMR (162 MHz, DMSO-d_6) δ 147.92; HRMS-NSI (*m/z*): $[M+H]^+$ calcd for $C_{26}H_{33}O_3N_5P$, 494.2316; found, 494.2300.

8.4.3 NMR Spectra

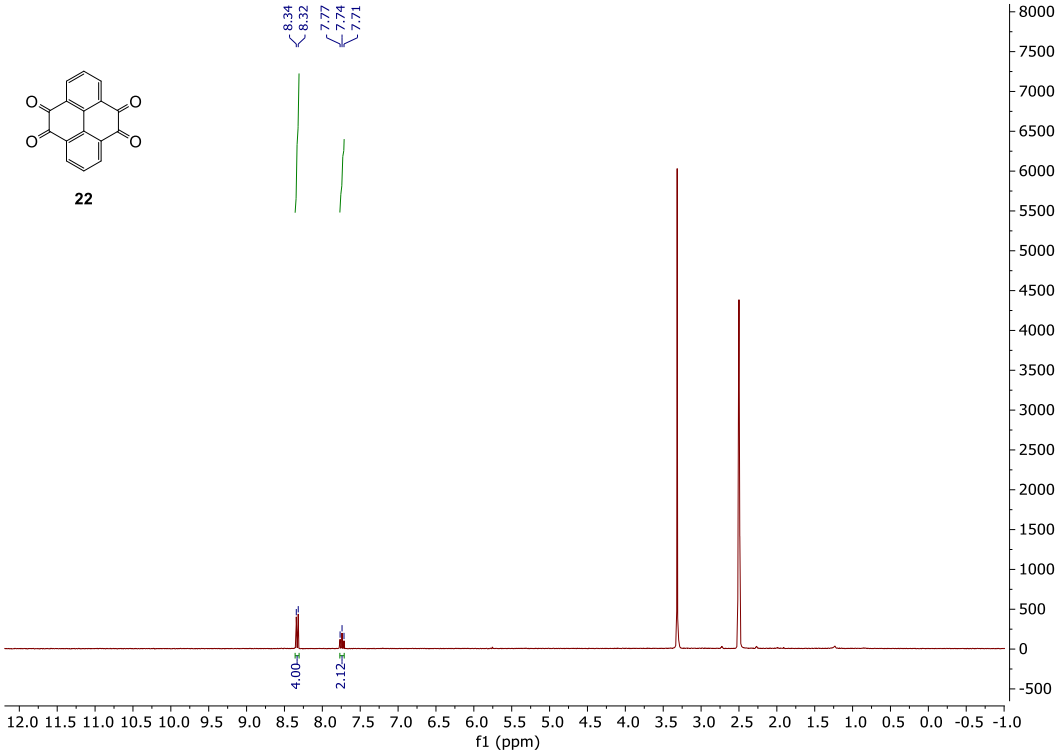

Figure 242. ^{1}H NMR of compound **22** in DMSO-d_6.

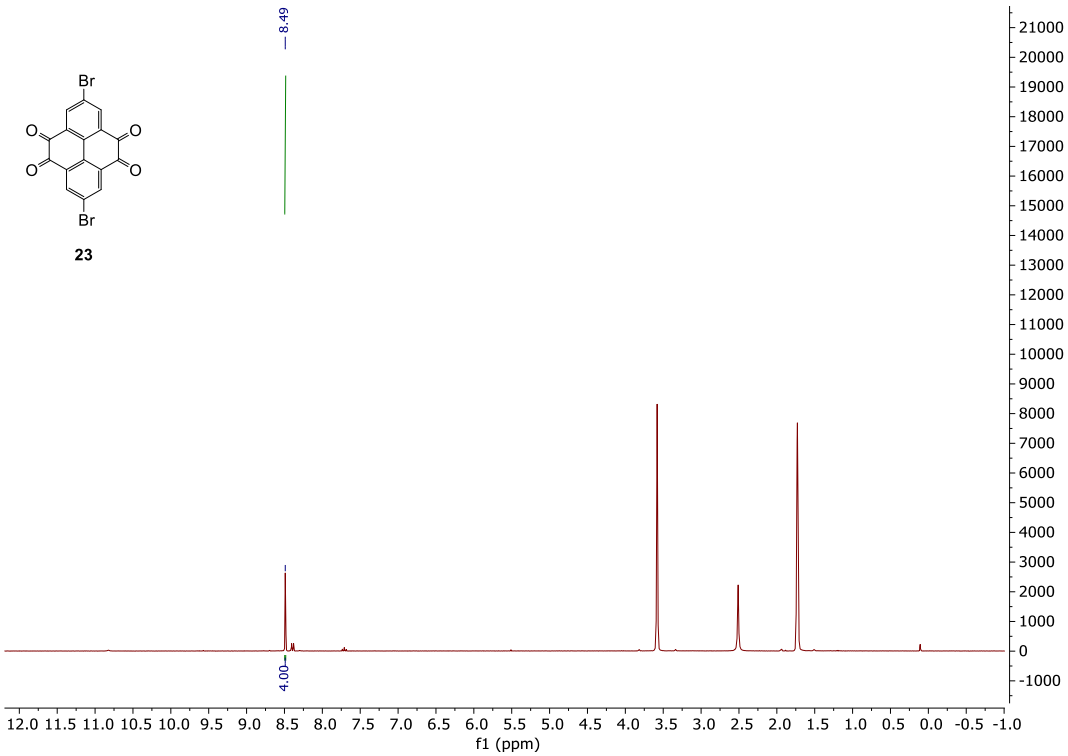

Figure 243. ^{1}H NMR of compound **23** in THF-d_8.

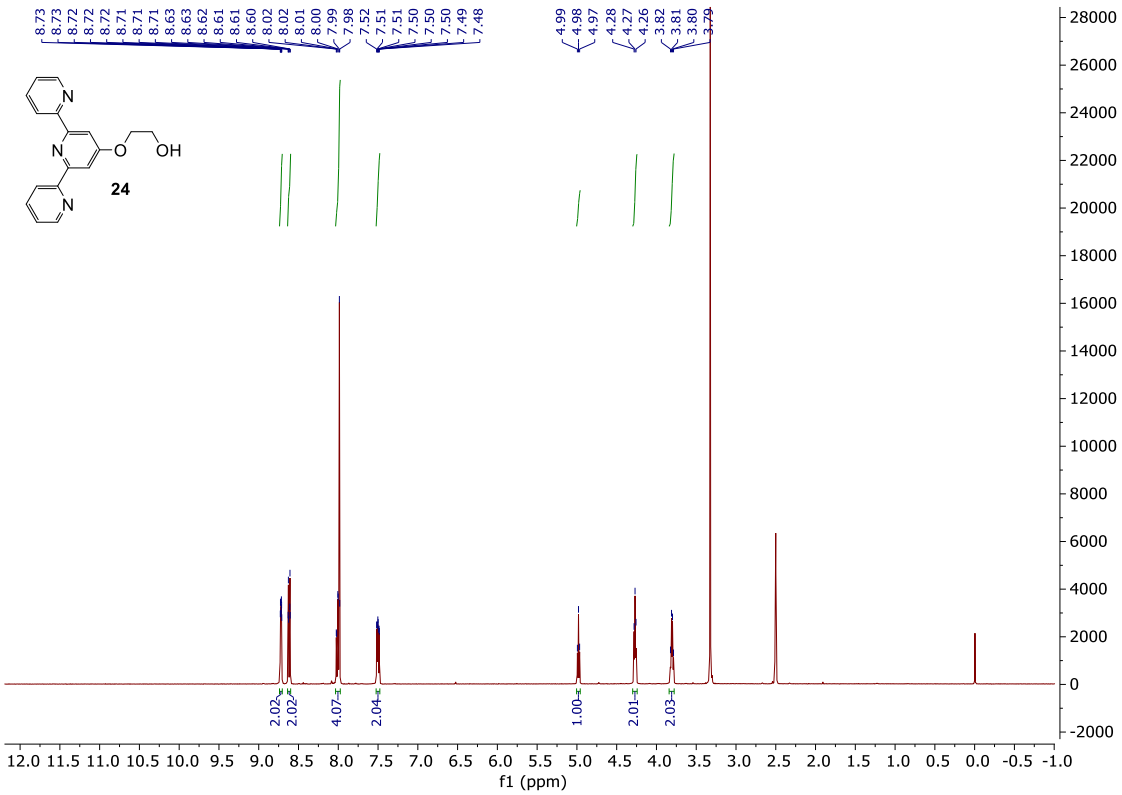

Figure 244. ^{1}H NMR of compound **24** in DMSO-d_6.

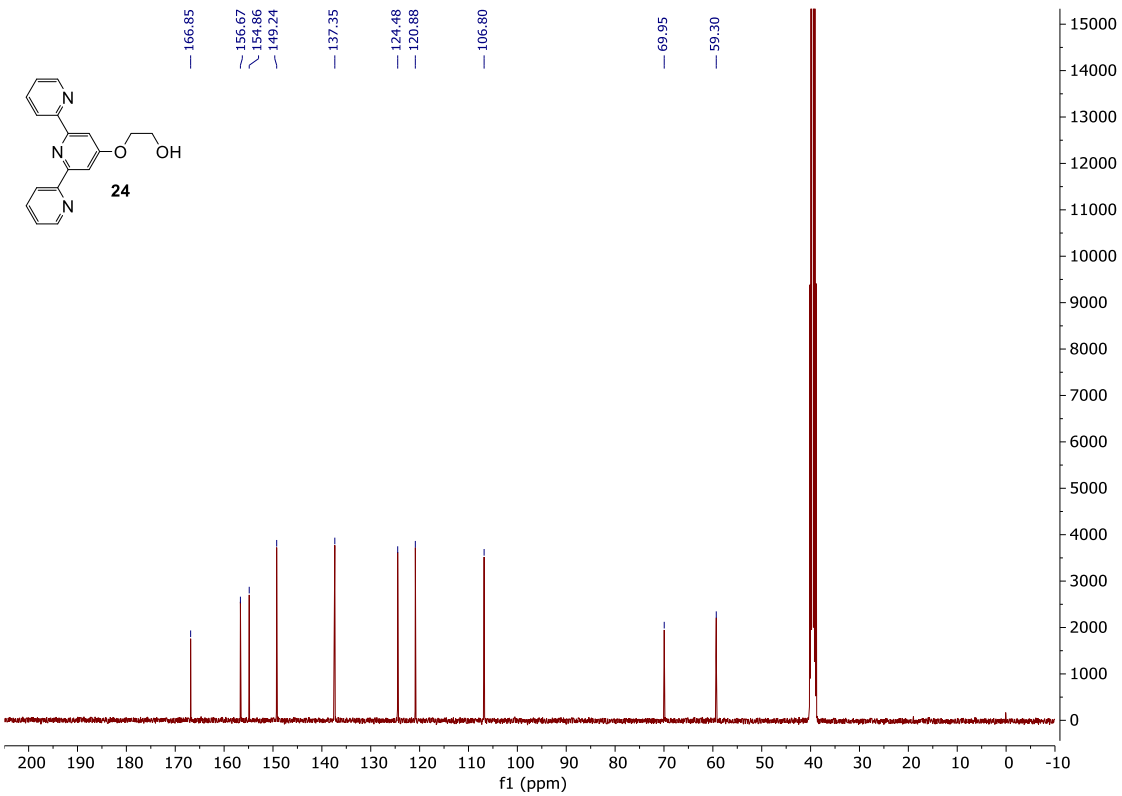

Figure 245. ^{13}C NMR of compound **24** in DMSO-d_6.

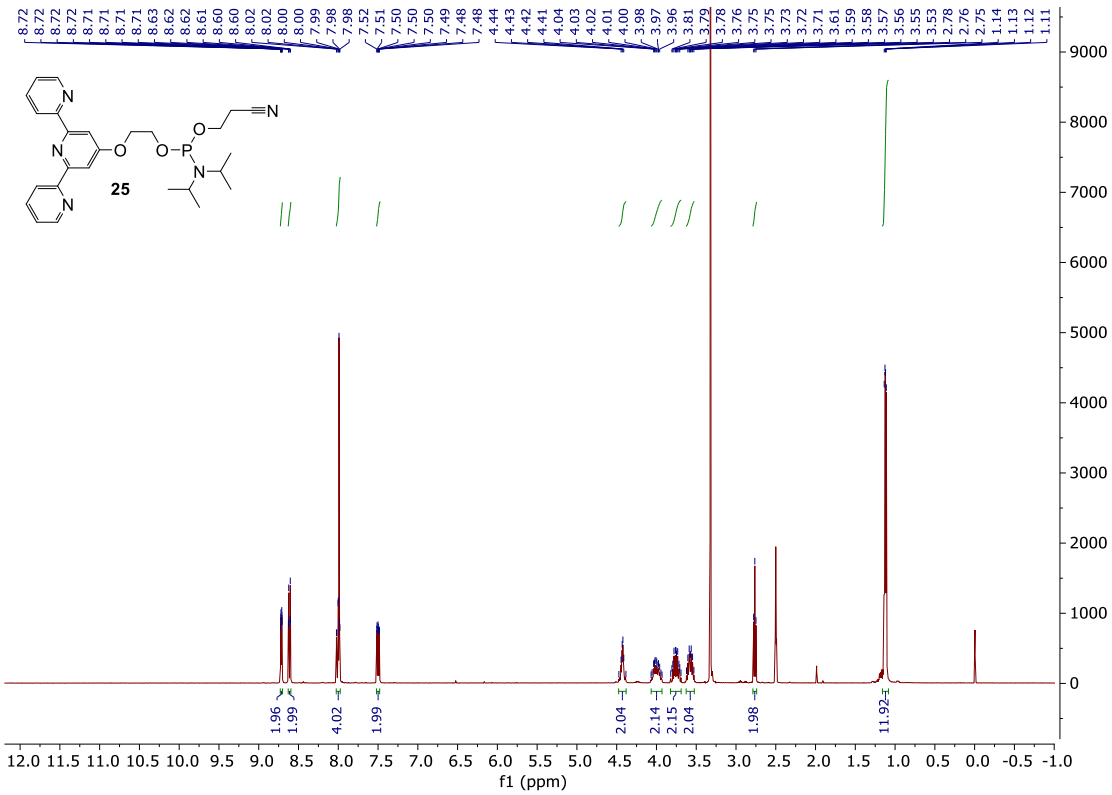

Figure 246. ^{1}H NMR of compound **25** in DMSO-d_6.

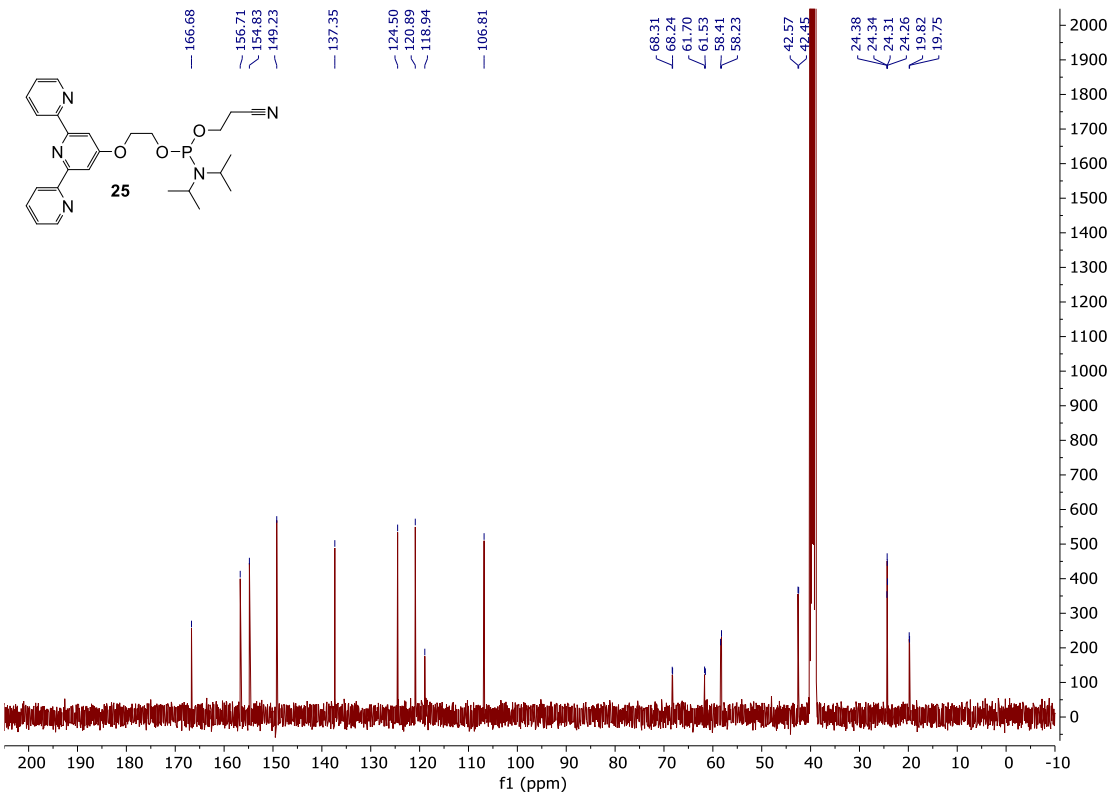

Figure 247. ^{13}C NMR of compound **25** in DMSO-d_6.

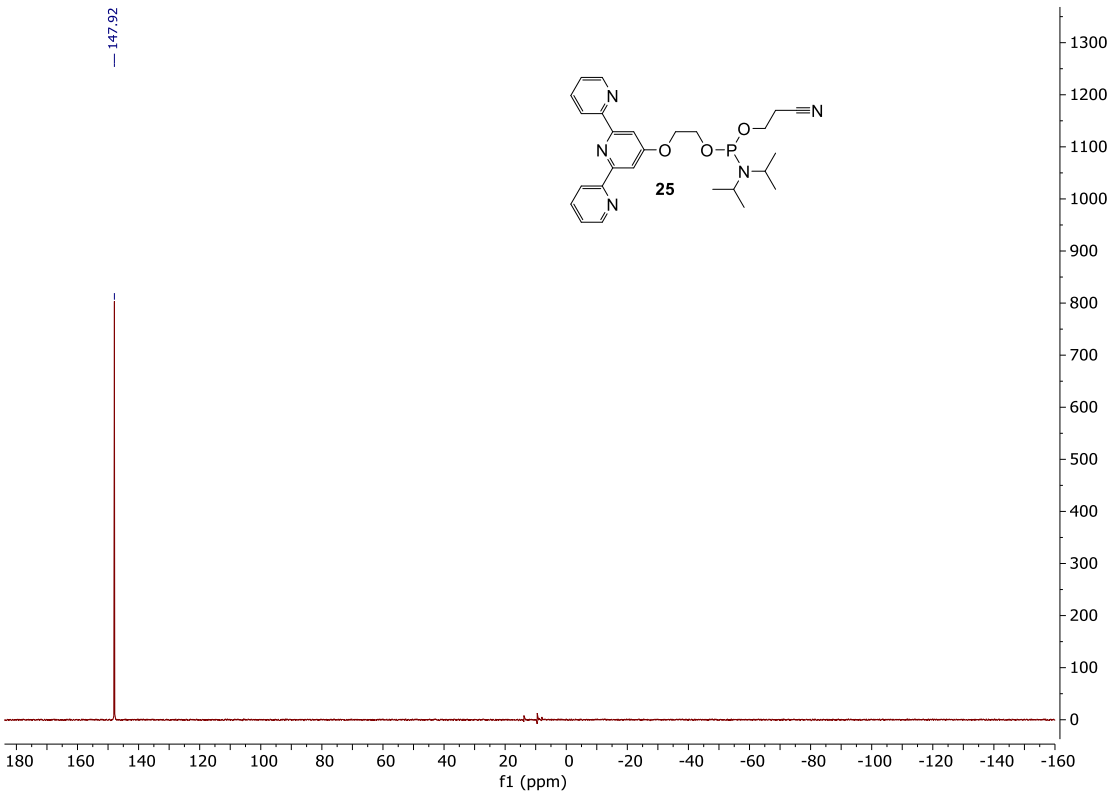

Figure 248. ^{31}P NMR of compound **25** in DMSO-d_6.

8.4.4 Synthesis of Oligonucleotides

TerPy-modified DNA oligomers **ON25** and **ON26** were synthesized on an Applied Biosystems 394 DNA/RNA synthesizer applying a standard cyanoethyl phosphoramidite coupling protocol on a 1 µmol scale. A coupling time of 30 s was employed for the DNA nucleobases and 2 min for the TerPy modification. TerPy phosphoramidite **25** was dissolved in 1,2-DCE to create a 0.1 M solution. The synthesis was started with dG-CPG (500 Å) solid-support. After the solid-phase synthesis, the oligomers were cleaved and deprotected by treatment with aqueous NH_4OH (28-30%) at 55 °C overnight. The supernatants were collected, and the solid-supports were washed three times with a solution of ethanol and Milli-Q H_2O (1:1, 3x1 mL), before the crude oligomers were lyophilized.

The crude TerPy-modified DNA oligomers were purified by reversed-phase HPLC (Shimadzu LC-20AT, ReproSil 100 C18, 5 µm, 250 x 4 mm) at 40 °C with a flow rate of 1 mL/min, λ: 300 nm. Solvent A: aqueous 2.1 mM triethylamine (TEA) / 25 mM 1,1,1,3,3,3-hexafluoropropan-2-ol (HFIP) pH 8; solvent B: acetonitrile; B [%] (t_R [min]) = 0 (0), 20 (20). The purified oligomers were dissolved in Milli-Q H_2O (1 mL). The absorbance was measured at 260 nm to determine the concentration of the

stock solutions and the yields of the oligomers. The calculation was according to the Beer-Lambert law. The following molar absorptivities (at 260 nm) in [L/mol·cm] were used for the DNA nucleobases: ε_A: 15’300; ε_T: 9’000; ε_G: 11’700; ε_C: 7’400. A molar absorptivity of ε_{TerPy}: 15’693 was used for the TerPy modification. The corresponding HPLC traces of **ON25** and **ON26** are displayed in Figure 249, the MS results are listed in Table 13, and the MS spectra are presented in Figure 250–Figure 255.

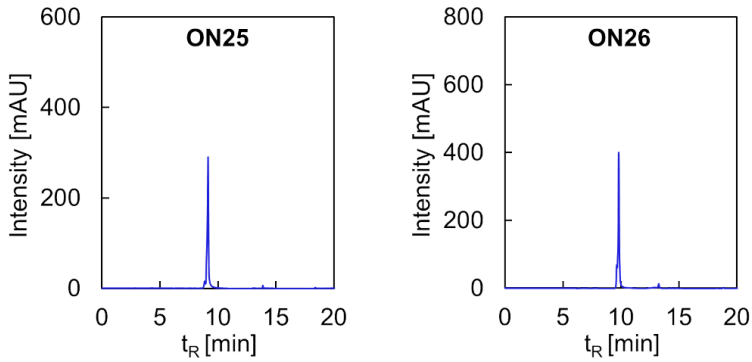

Figure 249: HPLC traces of TerPy-modified DNA oligomers **ON25** and **ON26**.

Table 13: Oligomer sequences of **ON25** and **ON26**; calculated and found masses by NSI-MS, and yields.

Oligomer	Sequence (5’→3’)	Calc. mass	Found mass	Yield [%]
ON25	**TerPy**-CAA GGT CCG ATG CAA GGA AG	6555.3766	6555.1730	33
ON26	**TerPy**-CTT CCT TGC ATC GGA CCT TG	6390.2364	6390.1090	39

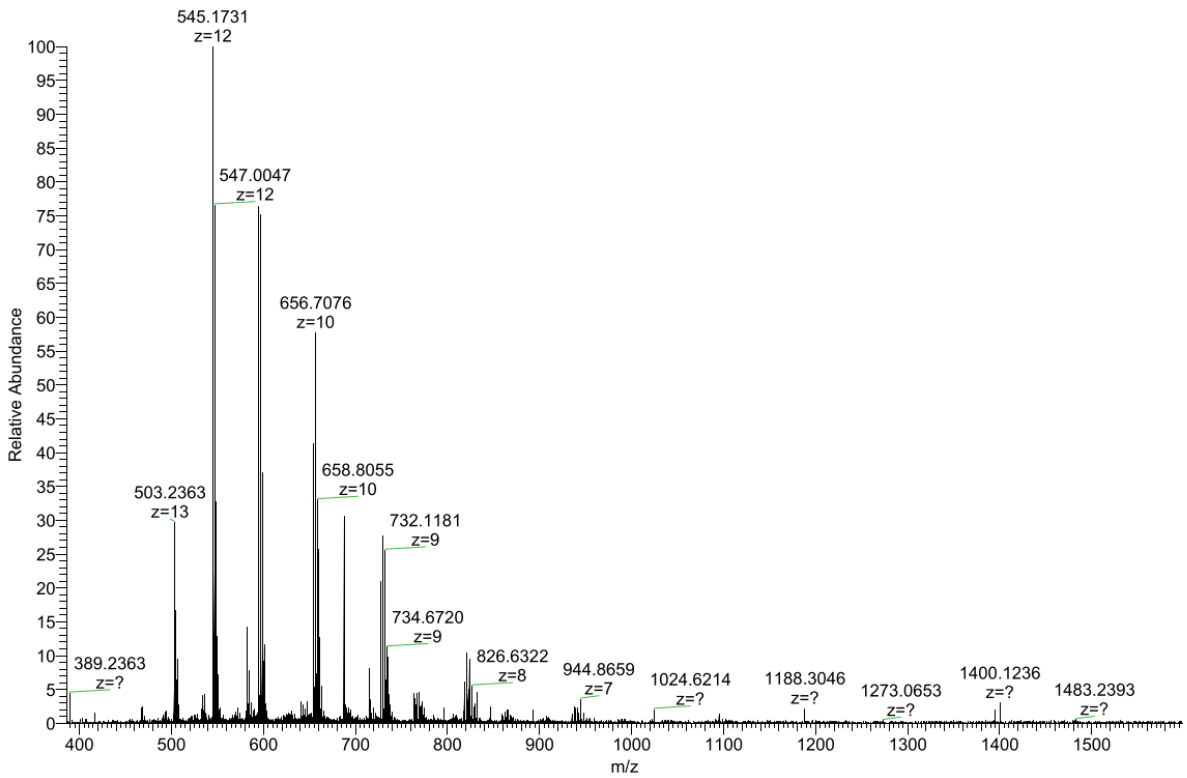

Figure 250. MS spectrum of **ON25**.

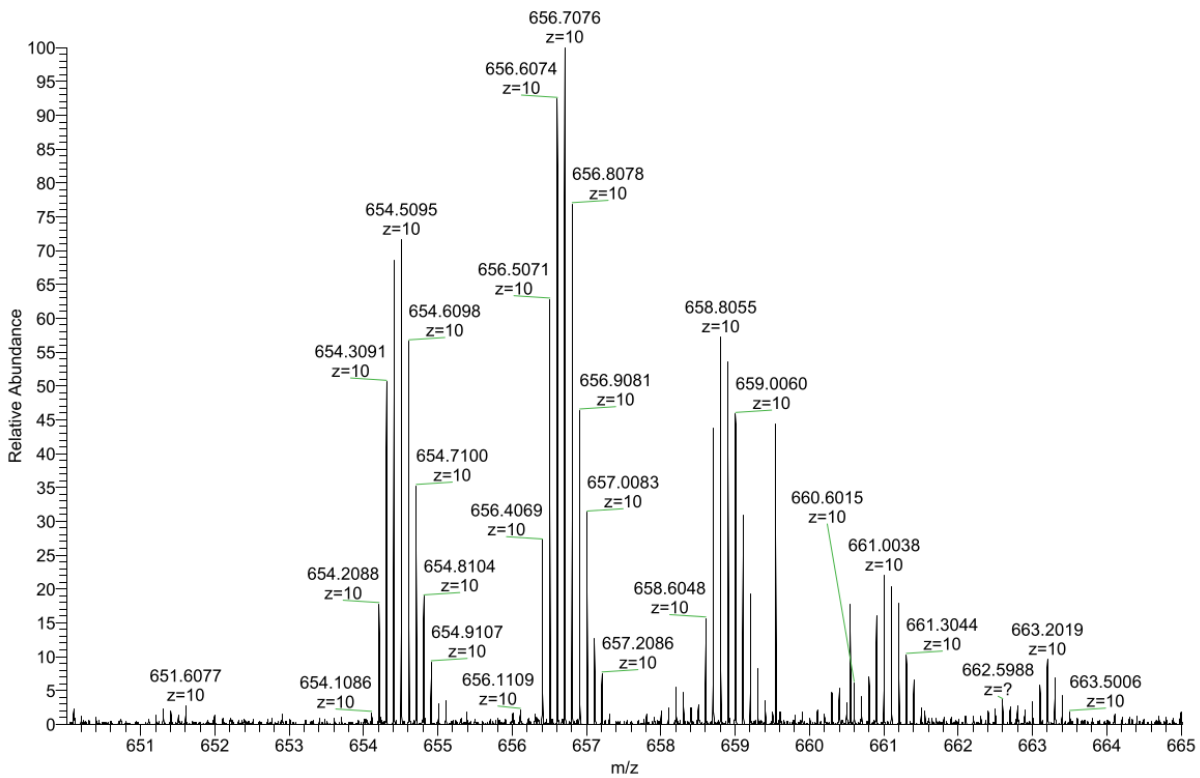

Figure 251. MS spectrum (zoom 1) of **ON25**.

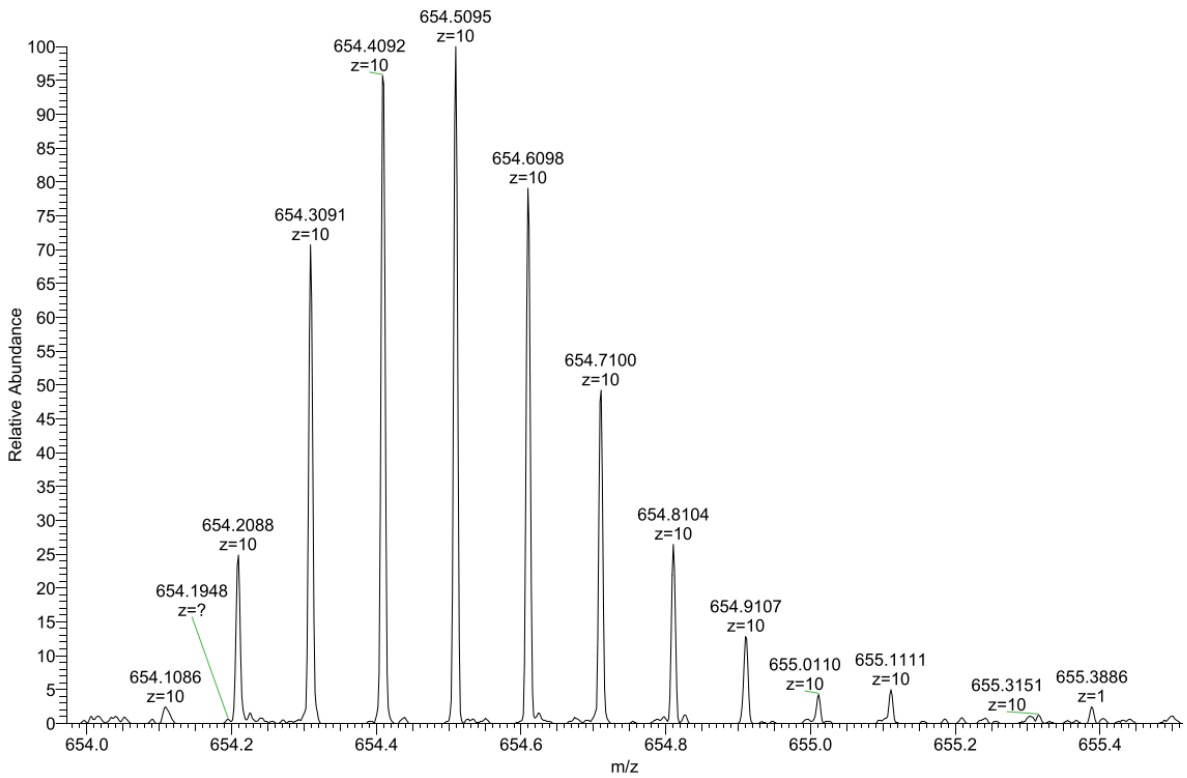

Figure 252. MS spectrum (zoom 2) of **ON25**.

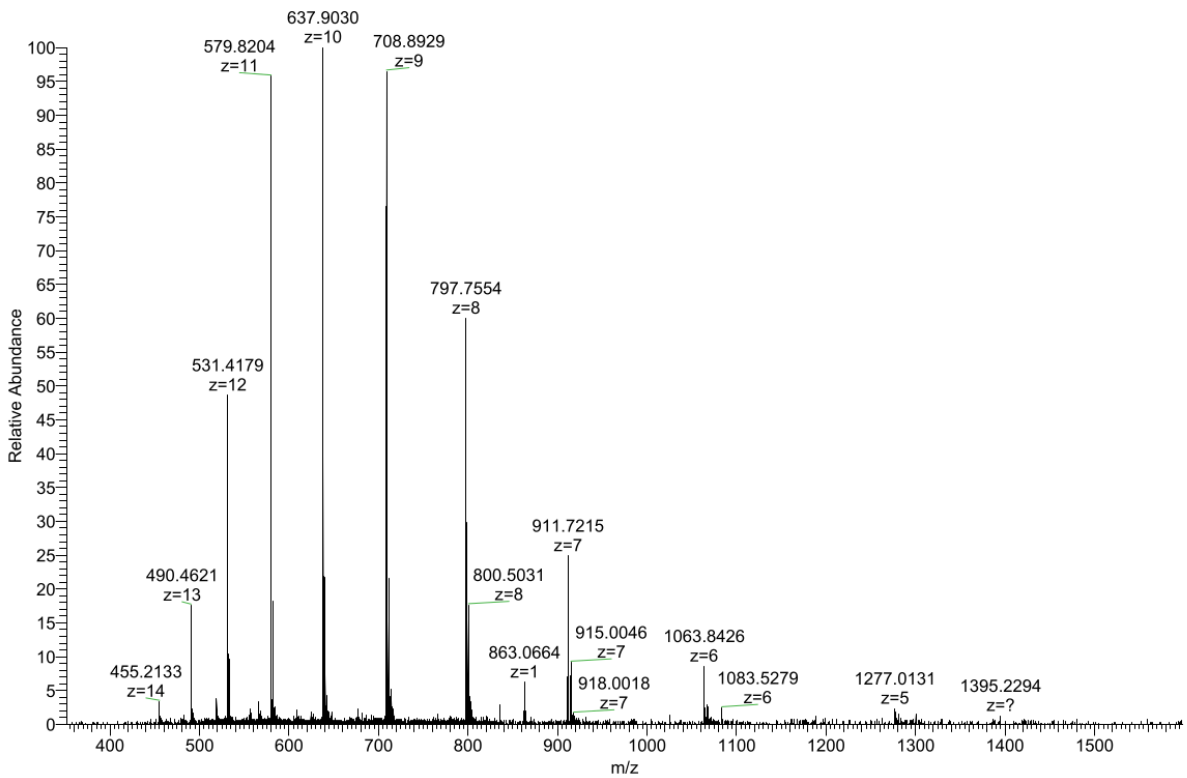

Figure 253. MS spectrum of **ON26**.

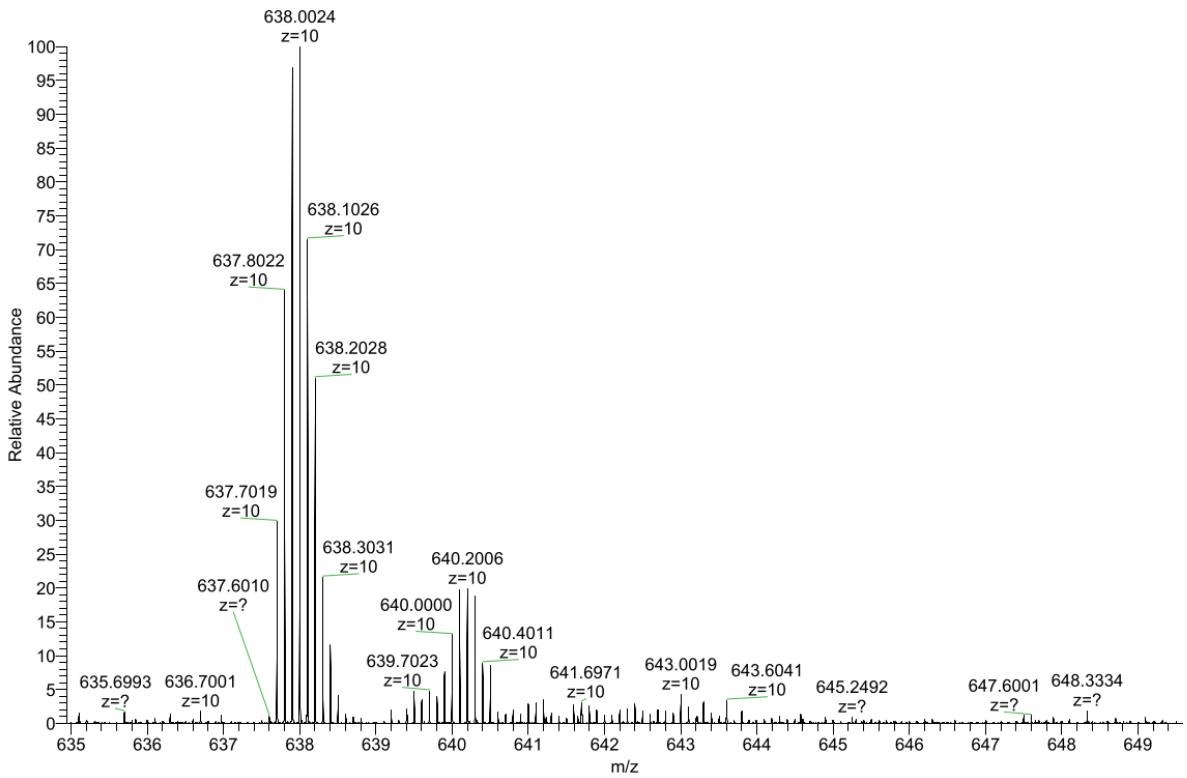

Figure 254. MS spectrum (zoom 1) of **ON26**.

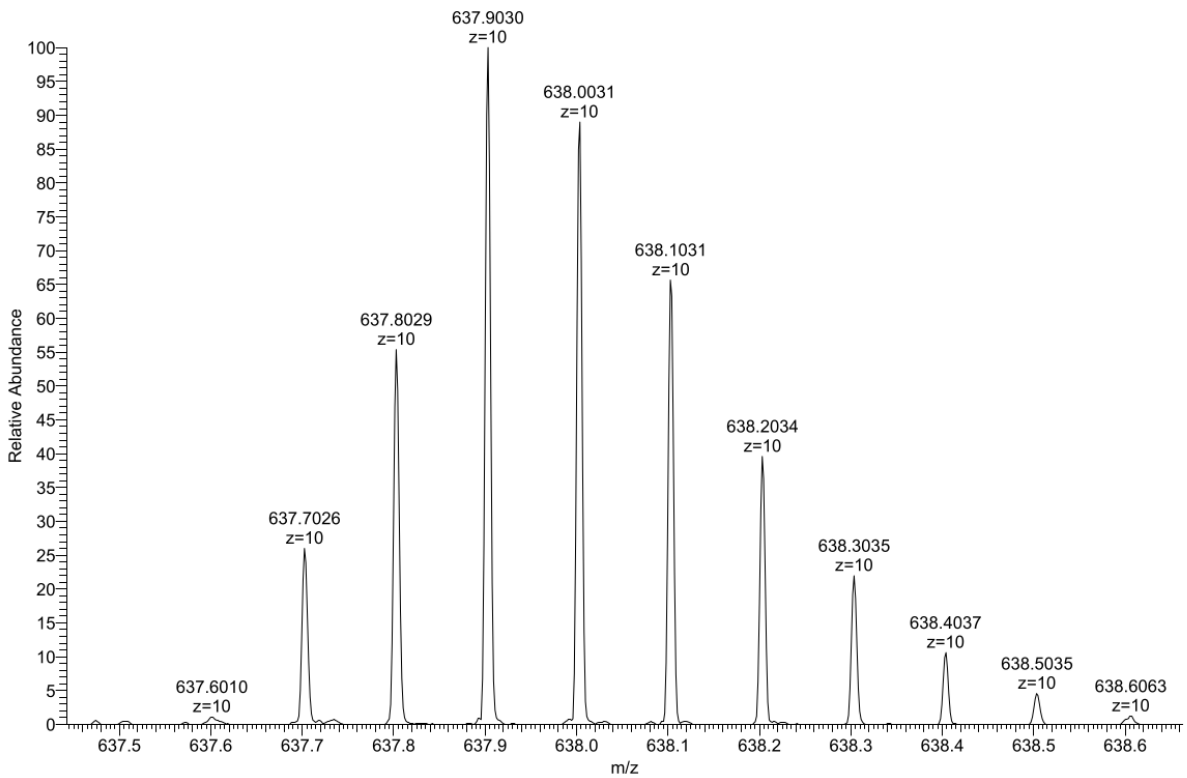

Figure 255. MS spectrum (zoom 2) of **ON26**.

8.4.5 UV-Vis Measurement

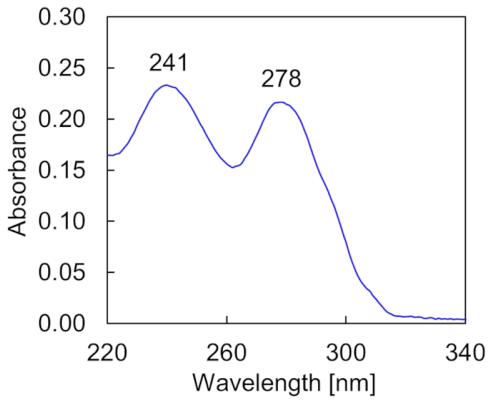

Figure 256. UV-Vis absorption spectra of TerPy-OH **24**. Conditions: 10 µM **24** in ethanol, 20 °C.

9 Overall Conclusions and Future Perspectives

Overall, modification of DNA single strands with TPE sticky ends allows the assembly of the resulting amphiphilic DNA duplexes into DNA-constructed, supramolecular morphologies. The polycation spermine is required for the construction of these DNA architectures, together with hydrophobic interactions derived from the TPE residues. Compared to previously reported supramolecular assemblies from phenanthrene-DNA conjugates,[158] similar vesicular nanostructures were observed. This may hint to a universal use of such amphiphilic DNA duplexes for the self-assembly into DNA constructs under given aqueous conditions. Cryo-EM imaging proofed to be an excellent method for the characterization of the well-defined DNA architectures and detailed insights into the DNA duplex arrangement could be attained. It was shown that a 3'-/5'-end modified TPE-DNA single strand can serve as a *scaffolding assembly unit*, owing to orthogonal non-covalent interactions, compared to DNA hybridization. Depending on a certain subunit of the complementary DNA single strand, *i.e.*, terminal functionality, diverse DNA architectures have been achieved.

Cryo-EM tomography of the nanostructures could further support the 3D shape of the DNA architectures. Preliminary attempts have already been done by Dr. Ioan Iacovache, however, mainly two factors precluded successful cryo-EM tomography. Firstly, the concentration of the self-assemblies was too low and secondly, the high vulnerability of the samples towards the electron dose.

So far, DNA architectures have not been further functionalized after supramolecular assembly. The unilamellar vesicles assembled from **ON9*ON18**, exhibiting a short PEG_6 terminal moiety, could be a suitable starting point for this aim. One might replace the methoxy-PEG_6 by a propargyl-PEG_6 moiety, which could be accessible for a post-assembly click reaction, to covalently attach *e.g.*, a bio-relevant tag to the vesicles.

3'-/5'-End modified TPE-DNA conjugates provide the required cohesive interactions between individual building blocks (double-stranded DNA), for the self-assembly into nanostructures. Thus, the described DNA nanostructures are constructed and supported by the DNA itself, *i.e.*, they require no

other framework like a nanoparticle. Therefore, such DNA architectures might be explored as drug carriers, or even for the delivery of DNA themselves. Additionally, the current developments of mRNA-based vaccines are extremely exciting and present a remarkable advancement of a therapeutic use of RNA. One could therefore envision to hybridize a complementary RNA single strand, instead of DNA, to the TPE-DNA conjugates and assemble these DNA-RNA hybrids into supramolecular nanostructures. It is believed that the assembled nucleic acids would be protected from nucleolytic degradation to some extent within the supramolecular nanostructures. Future efforts along this line would certainly shed new light on such applications in this unexplored field of research.

Abbreviations

1,2-DCE	1,2-Dichloroethane
2D	Two-dimensional
3D	Three-dimensional
AFM	Atomic force microscopy
APTES	(3-Aminopropyl)triethoxysilane
aq.	Aqueous
ASGR	Asialoglycoprotein receptor
BOP	(Benzotriazol-1-yloxy)tris(dimethylamino)phosphonium hexafluorophosphate
CCK-8	Cell Counting Kit-8
CEP-Cl	2-Cyanoethyl *N*,*N*-diisopropylchlorophosphoramidite
$CHCl_3$	Chloroform
CRD	Carbohydrate recognition domain
Cryo-EM	Cryo-electron microscopy
CuAAC	Copper-catalyzed azide-alkyne cycloaddition
Cy	Cyanine
DCM	Dichloromethane
DIPA	Diisopropylamine
DIPEA	Hünig's base
DLS	Dynamic light scattering
DMAP	*N*,*N*-Dimethylpyridin-4-amine
DMSO	Dimethyl sulfoxide
DMT-Cl	4,4'-Dimethoxytrityl chloride
DNA	Deoxyribonucleic acid
Et_3N	Triethylamine
EthBr	Ethidium bromide
EtOAc	Ethyl acetate
ETT	5-(Ethylthio)-1*H*-tetrazole
FRET	Förster resonance energy transfer

GalNAc	*N*-Acetylgalactosamine
HPLC	High performance liquid chromatography
^{i}PrOH	Propan-2-ol
LCAA-CPG	Long-chain alkyl-amino controlled pore glass
LUMO	Lowest-energy unoccupied molecular orbital
MeOH	Methanol
mRNA	Messenger ribonucleic acid
MS	Mass spectrometry
MWCO	Molecular weight cut-off
NBS	*N*-Bromosuccinimide
n_D^{20}	Refractive index
NMR	Nuclear magnetic resonance
NTA	Nanoparticle tracking analysis
PSD	Particle size distribution
PBS	Phosphate-buffered saline
PEG	Polyethylene glycol
RNA	Ribonucleic acid
rt.	Room temperature
sat.	Saturated
SAXS	Small angle X-ray scattering
SEM	Scanning electron microscopy
STM	Scanning tunneling microscopy
TBTA	Tris[(1-benzyl-1*H*-1,2,3-triazol-4-yl)methyl]amine
^{t}BuOOH	*Tert*-butyl hydroperoxide
TEAA	Triethylammonium acetate
TEM	Transmission electron microscopy
TerPy	2,2’:6’,2’’-Terpyridine
THF	Tetrahydrofuran
TLC	Thin-layer chromatography
T_m	Melting temperature
TMS	Trimethylsilyl
TPE	Tetraphenylethylene
UHV	Ultrahigh vacuum
UV-Vis	Ultraviolet-visible

General Methods

All reagents and solvents were purchased from commercial suppliers and used without further purification. All reactions were accomplished under argon atmosphere using anhydrous solvents. TLCs were conducted on silica gel SIL G UV_{254} glass plates (Macherey-Nagel). Flash column chromatography was performed on Sigma Aldrich silica gel, pore size 60 Å, 230–400 mesh particle size. Water was used from a Milli-Q system.

NMR, MS

NMR spectra were obtained on a Bruker Avance III HD (300 MHz or 400 MHz) spectrometer at 298 K (unless noted otherwise) from the Analytical Research and Services (ARS) of the University of Bern, Switzerland. Mass spectra were obtained on a Thermo Fisher LTQ Orbitrap XL using Nano Electrospray Ionization (NSI) from the ARS.

UV-Vis and Fluorescence Spectroscopy

Spectroscopic data were measured from at least five min thermally equilibrated samples at the corresponding temperature. UV-Vis spectra were recorded on an Agilent Cary 100 spectrophotometer using quartz cuvettes with an optical path of 1 cm. Fluorescence spectra were collected on a Cary Eclipse fluorescence spectrophotometer using an excitation slit of 2.5 nm and an emission slit of 5 nm (unless noted otherwise).

Supramolecular Assembly Procedure (Thermal Assembly Process)

Supramolecular assembly proceeded *via* thermal disassembly and reassembly: the sample solution was heated to 75 °C, followed by a controlled cooling of 0.5 °C/min to 20 °C in a Cary Eclipse fluorescence spectrophotometer equipped with a Peltier thermostat.

AFM

AFM experiments were conducted on a Nanosurf FlexAFM instrument in tapping mode under ambient conditions. Tap190Al-G cantilevers from Budget-Sensors, Innovative Solutions Bulgaria Ltd. were used. AFM samples were prepared on APTES-modified mica sheets (Glimmer "V1", 20 mm x 20 mm, G250-7, Plano GmbH) according to published procedures.[27] Therefore, mica sheets were freshly cleaved and mounted with tape on top of a desiccator (3 L), before the desiccator was purged with argon. APTES (30 µL) was pipetted into an Eppendorf tube cap and Hünig's base (10 µL) was added into a second cap. Both Eppendorf tube caps were placed at the bottom of the desiccator below the mica sheets, then the desiccator was closed. The chemicals were allowed to evaporate for 2 h, before the caps were removed, and the desiccator was flushed with argon. The mica sheets were left overnight in the desiccator. Afterwards, the corresponding sample solution (20 µL) was pipetted onto the APTES-modified mica sheet. After an adsorption time of either 7 min or 10 min, the mica sheet was rinsed with Milli-Q water (2 mL), then dried under a stream of argon.

SEM

SEM images were acquired on a Zeiss Gemini 450 instrument. 5 µL of the sample solution was pipetted onto a hydrophilized silicon nitride grid (5 nm atomic layer deposited hydroxylated aluminum oxide, Plano GmbH, 21555-10). After an adsorption time of 10 min, the solution was blotted. The grid was dipped into Milli-Q H_2O (30 µL) and blotted again. This washing step was repeated once.

SAXS

SAXS measurements were performed on a BRUKER NanoStar instrument with a sample to detector distance (SDD) of 107 cm. The samples were exposed at room temperature for 10 h in total, but after each hour of exposure time, the measuring location has been changed.

TEM

5 µL of the sample solution was pipetted on copper holey carbon grids (300 mesh, Agar Scientific). After 2 min of adsorption, the solution was blotted. Then, the grid was dipped into 30 µL of H_2O, before the solution was blotted. This washing step was repeated once. Afterwards, the grid was dipped into UA-Zero staining solution (Agar Scientific) and blotted. The grid was dipped again into the staining solution and blotted after 30 s. TEM images were recorded on a Tecnai Spirit using an operating voltage of 80 kV and with either an Olympus-SIS Veleta CCD camera or FEI Eagle CCD camera.

Cryo-EM

Samples for cryo-EM were plunge frozen using the FEI Vitrobot Mark 4 at room temperature and 100% humidity. In brief, quantifoil 2/1 copper grids (for images presented in chapter 3) or copper lacey carbon grids (for images presented in chapters 4–6) were glow discharged (air – 10 mA for 20 s). 3 µL of the sample solution was pipetted on the girds and blotted for 3 s before plunging into liquid ethane. Sample grids were stored in liquid nitrogen. Images were acquired using a Gatan 626 cryo holder on a Falcon III equipped FEI Tecnai F20 in nanoprobe mode. Due to the nature of the sample, acquisition settings had to be adjusted for a low total electron dose (less than 20 $e^-/Å^2$) using EPU software. Distance measurements were done in Fiji[212,269] using the multi-point tool to set marks. After the read-out of the x- and y-values, the distances between the marks were calculated. The reported distances are mean values with the corresponding standard deviation.

Dialysis

Dialysis buttons (Hampton research, HR3-332) and regenerated cellulose dialysis tubing (Spectra/Por 4, 12–14 kDa MWCO, 132 700) was utilized for dialysis. The samples were dialyzed against 200 mL of 10 mM sodium phosphate buffer pH 7.2, 0.1 mM spermine · 4 HCl dialysate buffer for at least 3 h to remove the ethanol (<0.5 vol%). The successful removal of the ethanol fraction was confirmed by measuring the refractive index of a control, that was treated identically to the respective sample and compared against a calibration curve. Refractive index measurements were conducted on a Reichert Abbe Mark III refractometer in the automatic temperature correction mode.

NTA

NTA measurements were conducted on a ParticleMetrix ZetaView instrument at 25 °C. After performing the thermal assembly process (1 µM each strand), the samples were diluted shortly before the NTA measurements 1:200 with aqueous medium (10 mM sodium phosphate buffer pH 7.2, 0.1 mM spermine · 4 HCl, 20 vol% ethanol).

Cytotoxicity Assay

In brief, 5000 cells/well were seeded into 96-well plates and cultured for 24 h at 37 °C, 5% CO_2. The cells were washed once with PBS buffer (Carl Roth), before the incubation solutions (200 µL/well) were added into the wells. The respective dilutions were prepared in cell culture medium (Carl Roth, RPMI-1640, without phenol red, 9104.1). After incubation for 24 h at 37 °C, 5% CO_2, the supernatant was removed, and the cells were washed with PBS buffer (Carl Roth). Cell culture medium (190 µL; Carl Roth, RPMI-1640, without phenol red, 9104.1), followed by CCK-8 solution (10 µL; Merck, 96992) were added into the wells, then incubated for 2 h, before the cells were evaluated in the plate reader ($\lambda_{abs.}$: 460 nm). The cell viability of a sample was determined relative to the viability of the cells treated with cell medium only. The reported cell viabilities are mean values with the corresponding standard deviation (n = 3).

Ultrafiltration

Vesicle concentration by ultrafiltration was accomplished using Amicon Ultra-0.5 centrifugal filter units with a regenerated cellulose membrane (100 kDa MWCO). 500 µL sample solution was pipetted into the filter device, before the sample was centrifuged for 2 min at 12000 g in an Eppendorf centrifuge 5415D, fixed angle rotor (F45-24-11, radius: 8.3 cm). This yielded about a tenfold concentration of the sample (verified by weight).

DLS

DLS experiments were performed on a Malvern Zetasizer Nano Series instrument (λ = 633 nm) in particle size distribution (PSD) mode (number value) at 25 °C.

Bibliography

[1] J.-M. Lehn, *Science* **2002**, *295*, 2400–2403.

[2] D. A. Uhlenheuer, K. Petkau, L. Brunsveld, *Chem. Soc. Rev.* **2010**, *39*, 2817–2826.

[3] L. Brunsveld, B. J. B. Folmer, E. W. Meijer, R. P. Sijbesma, *Chem. Rev.* **2001**, *101*, 4071–4097.

[4] E. Krieg, M. M. C. Bastings, P. Besenius, B. Rybtchinski, *Chem. Rev.* **2016**, *116*, 2414–2477.

[5] M. Hartlieb, E. D. H. Mansfield, S. Perrier, *Polym. Chem.* **2020**, *11*, 1083–1110.

[6] T. Aida, E. W. Meijer, S. I. Stupp, *Science* **2012**, *335*, 813–817.

[7] J. Boekhoven, W. E. Hendriksen, G. J. M. Koper, R. Eelkema, J. H. van Esch, *Science* **2015**, *349*, 1075–1079.

[8] J. Schill, B. J. H. M. Rosier, B. G. Audenis, E. M. Estirado, T. F. A. de Greef, L. Brunsveld, *Angew. Chem. Int. Ed.* **2021**, *60*, 7612–7616.

[9] O. Dumele, J. Chen, J. V. Passarelli, S. I. Stupp, *Adv. Mater.* **2020**, *32*, 1907247.

[10] J.-F. Lutz, J.-M. Lehn, E. W. Meijer, K. Matyjaszewski, *Nat. Rev. Mater.* **2016**, *1*, 16024.

[11] R. Freeman, M. Han, Z. Álvarez, J. A. Lewis, J. R. Wester, N. Stephanopoulos, M. T. McClendon, C. Lynsky, J. M. Godbe, H. Sangji, et al., *Science* **2018**, *362*, 808–813.

[12] K. Liu, Y. Kang, Z. Wang, X. Zhang, *Adv. Mater.* **2013**, *25*, 5530–5548.

[13] P. Cordier, F. Tournilhac, C. Soulié-Ziakovic, L. Leibler, *Nature* **2008**, *451*, 977–980.

[14] M. Vázquez-González, I. Willner, *Angew. Chem. Int. Ed.* **2020**, *59*, 15342–15377.

[15] E. M. Estirado, A. F. Mason, M. Á. A. García, J. C. M. van Hest, L. Brunsveld, *J. Am. Chem. Soc.* **2020**, *142*, 9106–9111.

[16] P. Ball, *Chem. Rev.* **2008**, *108*, 74–108.

[17] K. Petkau-Milroy, L. Brunsveld, *Org. Biomol. Chem.* **2013**, *11*, 219–232.

[18] T. Kim, J. Y. Park, J. Hwang, G. Seo, Y. Kim, *Adv. Mater.* **2020**, *32*, 2002405.

[19] A. S. Weingarten, R. V. Kazantsev, L. C. Palmer, M. McClendon, A. R. Koltonow, A. P. S. Samuel, D. J. Kiebala, M. R. Wasielewski, S. I. Stupp, *Nat. Chem.* **2014**, *6*, 964–970.

[20] A. L. Nussbaumer, D. Studer, V. L. Malinovskii, R. Häner, *Angew. Chem. Int. Ed.* **2011**, *50*, 5490–5494.

[21] V. L. Malinovskii, A. L. Nussbaumer, R. Häner, *Angew. Chem. Int. Ed.* **2012**, *51*, 4905–4908.

[22] A. V. Rudnev, V. L. Malinovskii, A. L. Nussbaumer, A. Mishchenko, R. Häner, T. Wandlowski, *Macromolecules* **2012**, *45*, 5986–5992.

[23] M. Vybornyi, A. V. Rudnev, S. M. Langenegger, T. Wandlowski, G. Calzaferri, R. Häner, *Angew. Chem. Int. Ed.* **2013**, *52*, 11488–11493.

[24] M. Vybornyi, A. Rudnev, R. Häner, *Chem. Mater.* **2015**, *27*, 1426–1431.

[25] M. Vybornyi, Y. Bur-Cecilio Hechevarria, M. Glauser, A. V. Rudnev, R. Häner, *Chem. Commun.* **2015**, *51*, 16191–16193.

[26] C. B. Winiger, S. Li, G. R. Kumar, S. M. Langenegger, R. Häner, *Angew. Chem. Int. Ed.* **2014**, *53*, 13609–13613.

[27] C. D. Bösch, S. M. Langenegger, R. Häner, *Angew. Chem. Int. Ed.* **2016**, *55*, 9961–9964.

[28] H. Yu, R. Häner, *Chem. Commun.* **2016**, *52*, 14396–14399.

[29] H. Yu, M. Sabetti, R. Häner, *Chem. - Asian J.* **2018**, *13*, 968–971.

[30] J. Jevric, S. M. Langenegger, R. Häner, *Eur. J. Org. Chem.* **2020**, *2020*, 4677–4680.

[31] M. Kownacki, S. M. Langenegger, S.-X. Liu, R. Häner, *Angew. Chem. Int. Ed.* **2019**, *58*, 751–755.

[32] T. Förster, *Ann. Phys.* **1948**, *437*, 55–75.

[33] T. Förster, *Zeitschrift für Naturforschung A* **1949**, *4*, 321–327.

[34] K. E. Sapsford, L. Berti, I. L. Medintz, *Angew. Chem. Int. Ed.* **2006**, *45*, 4562–4589.

[35] H. Sahoo, *J. Photochem. Photobiol. C Photochem. Rev.* **2011**, *12*, 20–30.

[36] P. Rajdev, S. Ghosh, *J. Phys. Chem. B* **2019**, *123*, 327–342.

[37] R. R. Sinden, C. E. Pearson, V. N. Potaman, D. W. Ussery, *DNA: Structure and Function*, Volume 5, JAI Press, Greenwich (Connecticut), **1998**.

[38] D. L. Nelson, M. M. Cox, *Lehninger Principles of Biochemistry*, 6th Edition, W. H. Freeman And Company, New York, **2013**.

[39] G. M. Blackburn, M. J. Gait, D. Loakes, D. M. Williams, *Nucleic Acids in Chemistry and Biology*, 3rd Edition, Royal Society of Chemistry, Cambridge, **2006**.

[40] J. D. Watson, F. H. Crick, *Nature* **1953**, *171*, 737–738.

[41] M. A. Fuertes, V. Cepeda, C. Alonso, J. M. Pérez, *Chem. Rev.* **2006**, *106*, 2045–2064.

[42] R. Wing, H. Drew, T. Takano, C. Broka, S. Tanaka, K. Itakura, R. E. Dickerson, *Nature* **1980**, *287*, 755–758.

[43] B. Hartmann, R. Lavery, *Q. Rev. Biophys.* **1996**, *29*, 309–368.

[44] M. Egli, V. Tereshko, M. Teplova, G. Minasov, A. Joachimiak, R. Sanishvili, C. M. Weeks, R. Miller, M. A. Maier, H. An, et al., *Biopolymers* **1998**, *48*, 234–252.

[45] V. L. Malinovskii, D. Wenger, R. Häner, *Chem. Soc. Rev.* **2010**, *39*, 410–422.

[46] F. Garo, R. Häner, *Angew. Chem. Int. Ed.* **2012**, *51*, 916–919.

[47] M. Vybornyi, A. L. Nussbaumer, S. M. Langenegger, R. Häner, *Bioconjugate Chem.* **2014**, *25*, 1785–1793.

[48] O. Khorev, C. D. Bösch, M. Probst, R. Häner, *Chem. Sci.* **2014**, *5*, 1506–1512.

[49] C. B. Winiger, S. M. Langenegger, G. Calzaferri, R. Häner, *Angew. Chem. Int. Ed.* **2015**, *54*, 3643–3647.

[50] P. Ensslen, H.-A. Wagenknecht, *Acc. Chem. Res.* **2015**, *48*, 2724–2733.

[51] M. Nakamura, Y. Matsui, T. Takada, K. Yamana, *ChemistrySelect* **2019**, *4*, 1525–1529.

[52] X. Zhou, S. Mandal, S. Jiang, S. Lin, J. Yang, Y. Liu, D. G. Whitten, N. W. Woodbury, H. Yan, *J. Am. Chem. Soc.* **2019**, *141*, 8473–8481.

[53] Y. N. Teo, E. T. Kool, *Chem. Rev.* **2012**, *112*, 4221–4245.

[54] J. Gorman, S. R. E. Orsborne, A. Sridhar, R. Pandya, P. Budden, A. Ohmann, N. A. Panjwani, Y. Liu, J. L. Greenfield, S. Dowland, et al., *J. Am. Chem. Soc.* **2022**, *144*, 368–376.

[55] J. R. Burns, J. W. Wood, E. Stulz, *Front. Chem.* **2020**, *8*, 113.

[56] S. M. Hart, W. J. Chen, J. L. Banal, W. P. Bricker, A. Dodin, L. Markova, Y. Vyborna, A. P. Willard, R. Häner, M. Bathe, et al., *Chem* **2021**, *7*, 752–773.

[57] F. Garo, R. Häner, *Bioconjugate Chem.* **2012**, *23*, 2105–2113.

[58] M. Probst, S. M. Langenegger, R. Häner, *Chem. Commun.* **2014**, *50*, 159–161.

[59] P. Ensslen, S. Gärtner, K. Glaser, A. Colsmann, H.-A. Wagenknecht, *Angew. Chem. Int. Ed.* **2016**, *55*, 1904–1908.

[60] H. Bui, S. A. Díaz, J. Fontana, M. Chiriboga, R. Veneziano, I. L. Medintz, *Adv. Opt. Mater.* **2019**, *7*, 1900562.

[61] C. D. Bösch, E. Abay, S. M. Langenegger, M. Nazari, A. Cannizzo, T. Feurer, R. Häner, *Helv. Chim. Acta* **2019**, *102*, e1900148.

[62] N. Bürki, E. Grossenbacher, A. Cannizzo, T. Feurer, S. M. Langenegger, R. Häner, *Org. Biomol. Chem.* **2020**, *18*, 6818–6822.

[63] O. A. Mass, C. K. Wilson, S. K. Roy, M. S. Barclay, L. K. Patten, E. A. Terpetschnig, J. Lee, R. D. Pensack, B. Yurke, W. B. Knowlton, *J. Phys. Chem. B* **2020**, *124*, 9636–9647.

[64] M. Madsen, K. V. Gothelf, *Chem. Rev.* **2019**, *119*, 6384–6458.

[65] N. Appukutti, C. J. Serpell, *Polym. Chem.* **2018**, *9*, 2210–2226.

[66] H. Ramezani, H. Dietz, *Nat. Rev. Genet.* **2020**, *21*, 5–26.

[67] G. Marth, A. M. Hartley, S. C. Reddington, L. L. Sargisson, M. Parcollet, K. E. Dunn, D. D. Jones, E. Stulz, *ACS Nano* **2017**, *11*, 5003–5010.

[68] O. I. Wilner, I. Willner, *Chem. Rev.* **2012**, *112*, 2528–2556.

[69] M. H. Caruthers, *Science* **1985**, *230*, 281–285.

[70] M. H. Caruthers, *Acc. Chem. Res.* **1991**, *24*, 278–284.

[71] S. L. Beaucage, R. P. Iyer, *Tetrahedron* **1993**, *49*, 6123–6194.

[72] M. Vybornyi, Y. Vyborna, R. Häner, *Chem. Soc. Rev.* **2019**, *48*, 4347–4360.

[73] T. J. Bandy, A. Brewer, J. R. Burns, G. Marth, T. Nguyen, E. Stulz, *Chem. Soc. Rev.* **2011**, *40*, 138–148.

[74] S. Li, S. M. Langenegger, R. Häner, *Chem. Commun.* **2013**, *49*, 5835–5837.

[75] J. Luo, Z. Xie, J. W. Y. Lam, L. Cheng, H. Chen, C. Qiu, H. S. Kwok, X. Zhan, Y. Liu, D. Zhu, et al., *Chem. Commun.* **2001**, 1740–1741.

[76] Y. Chen, J. W. Y. Lam, R. T. K. Kwok, B. Liu, B. Z. Tang, *Mater. Horiz.* **2019**, *6*, 428–433.

[77] Y. Cai, L. Du, K. Samedov, X. Gu, F. Qi, H. H. Y. Sung, B. O. Patrick, Z. Yan, X. Jiang, H. Zhang, et al., *Chem. Sci.* **2018**, *9*, 4662–4670.

[78] K. Kokado, K. Sada, *Angew. Chem. Int. Ed.* **2019**, *58*, 8632–8639.

[79] Z. Zhou, S. Xie, X. Chen, Y. Tu, J. Xiang, J. Wang, Z. He, Z. Zeng, B. Z. Tang, *J. Am. Chem. Soc.* **2019**, *141*, 9803–9807.

[80] A. Prlj, N. Došlić, C. Corminboeuf, *Phys. Chem. Chem. Phys.* **2016**, *18*, 11606–11609.

[81] Y. Hong, H. Xiong, J. W. Y. Lam, M. Häußler, J. Liu, Y. Yu, Y. Zhong, H. H. Y. Sung, I. D. Williams, K. S. Wong, et al., *Chem. - Eur. J.* **2010**, *16*, 1232–1245.

[82] Y. Dong, J. W. Y. Lam, A. Qin, J. Liu, Z. Li, B. Z. Tang, J. Sun, H. S. Kwok, *Appl. Phys. Lett.* **2007**, *91*, 011111.

[83] W. Lu, P. Xiao, J. Gu, J. Zhang, Y. Huang, Q. Huang, T. Chen, *Sens. Actuators, B* **2016**, *228*, 551–556.

[84] H. Liu, L. H. Xiong, R. T. K. Kwok, X. He, J. W. Y. Lam, B. Z. Tang, *Adv. Opt. Mater.* **2020**, *8*, 2000162.

[85] J. Jing, Y.-R. Xue, Y.-X. Liu, B. Xu, H.-W. Li, L. Liu, Y. Wu, W. Tian, *Nanoscale* **2020**, *12*, 5501–5506.

[86] X. Zhang, T. Liu, Q. Li, M. Li, L. Du, *Front. Chem.* **2019**, *7*, 54.

[87] X. Min, T. Fang, L. Li, C. Li, Z.-P. Zhang, X.-E. Zhang, F. Li, *Nanoscale* **2020**, *12*, 2340–2344.

[88] Y.-X. Hu, W.-J. Li, P.-P. Jia, X.-Q. Wang, L. Xu, H.-B. Yang, *Adv. Opt. Mater.* **2020**, *8*, 2000265.

[89] C. Li, J. Zhang, S. Zhang, Y. Zhao, *Angew. Chem. Int. Ed.* **2019**, *58*, 1643–1647.

[90] J. J. Li, Y. Chen, J. Yu, N. Cheng, Y. Liu, *Adv. Mater.* **2017**, *29*, 1701905.

[91] J. L. Banal, K. P. Ghiggino, W. W. H. Wong, *Phys. Chem. Chem. Phys.* **2014**, *16*, 25358–25363.

[92] J. Mei, N. L. C. Leung, R. T. K. Kwok, J. W. Y. Lam, B. Z. Tang, *Chem. Rev.* **2015**, *115*, 11718–11940.

[93] J. Li, J. Wang, H. Li, N. Song, D. Wang, B. Z. Tang, *Chem. Soc. Rev.* **2020**, *49*, 1144–1172.

[94] B. Li, H. Tian, X. Shen, D. Tang, S. Yin, *Polym. Chem.* **2019**, *10*, 796–818.

[95] T. Wu, J. Huang, Y. Yan, *Chem. – Asian J.* **2019**, *14*, 730–750.

[96] Y. Zhang, Y. Wang, J. Wang, X.-J. Liang, *Mater. Horiz.* **2018**, *5*, 799–812.

[97] R. Häner, S. M. Biner, S. M. Langenegger, T. Meng, V. L. Malinovskii, *Angew. Chem. Int. Ed.* **2010**, *49*, 1227–1230.

[98] S. M. Biner, D. Kummer, V. L. Malinovskii, R. Häner, *Org. Biomol. Chem.* **2011**, *9*, 2628–2633.

[99] I. Grabowska, D. G. Singleton, A. Stachyra, A. Góra-Sochacka, A. Sirko, W. Zagórski-Ostoja, H. Radecka, E. Stulz, J. Radecki, *Chem. Commun.* **2014**, *50*, 4196–4199.

[100] B. Kaur, K. Malecka, D. A. Cristaldi, C. S. Chay, I. Mames, H. Radecka, J. Radecki, E. Stulz, *Chem. Commun.* **2018**, *54*, 11108–11111.

[101] K. Malecka, B. Kaur, D. A. Cristaldi, C. S. Chay, I. Mames, H. Radecka, J. Radecki, E. Stulz, *Bioelectrochemistry* **2021**, *138*, 107723.

[102] E. Farjami, L. Clima, K. Gothelf, E. E. Ferapontova, *Anal. Chem.* **2011**, *83*, 1594–1602.

[103] J. Dronina, U. Samukaite-Bubniene, A. Ramanavicius, *J. Nanobiotechnology* **2022**, *20*, 41.

[104] N. C. Seeman, *J. Theor. Biol.* **1982**, *99*, 237–247.

[105] N. C. Seeman, N. R. Kallenbach, *Biophys. J.* **1983**, *44*, 201–209.

[106] N. R. Kallenbach, R.-I. Ma, N. C. Seeman, *Nature* **1983**, *305*, 829–831.

[107] N. C. Seeman, *Nature* **2003**, *421*, 427–431.

[108] M. R. Jones, N. C. Seeman, C. A. Mirkin, *Science* **2015**, *347*, 1260901.

[109] N. C. Seeman, H. F. Sleiman, *Nat. Rev. Mater.* **2017**, *3*, 17068.

[110] S. Nummelin, J. Kommeri, M. A. Kostiainen, V. Linko, *Adv. Mater.* **2018**, *30*, 1703721.

[111] Y.-J. Chen, B. Groves, R. A. Muscat, G. Seelig, *Nat. Nanotechnol.* **2015**, *10*, 748–760.

[112] Y. He, T. Ye, M. Su, C. Zhang, A. E. Ribbe, W. Jiang, C. Mao, *Nature* **2008**, *452*, 198–201.

[113] C. G. Evans, E. Winfree, *Chem. Soc. Rev.* **2017**, *46*, 3808–3829.

[114] C. Lin, Y. Liu, S. Rinker, H. Yan, *ChemPhysChem* **2006**, *7*, 1641–1647.

[115] S. Jiang, F. Hong, H. Hu, H. Yan, Y. Liu, *ACS Nano* **2017**, *11*, 9370–9381.

[116] W. Wang, T. Lin, S. Zhang, T. Bai, Y. Mi, B. Wei, *Nucleic Acids Res.* **2016**, *44*, 7989–7996.

[117] H. Yan, T. H. LaBean, L. Feng, J. H. Reif, *Proc. Natl. Acad. Sci. U. S. A.* **2003**, *100*, 8103–8108.

[118] D. K. Agrawal, R. Jiang, S. Reinhart, A. M. Mohammed, T. D. Jorgenson, R. Schulman, *ACS Nano* **2017**, *11*, 9770–9779.

[119] K. L. Lau, H. F. Sleiman, *ACS Nano* **2016**, *10*, 6542–6551.

[120] C. Tian, X. Li, Z. Liu, W. Jiang, G. Wang, C. Mao, *Angew. Chem. Int. Ed.* **2014**, *53*, 8041–8044.

[121] P. Wang, S. Wu, C. Tian, G. Yu, W. Jiang, G. Wang, C. Mao, *J. Am. Chem. Soc.* **2016**, *138*, 13579–13585.

[122] P. W. K. Rothemund, *Nature* **2006**, *440*, 297–302.

[123] U. Feldkamp, C. M. Niemeyer, *Angew. Chem. Int. Ed.* **2006**, *45*, 1856–1876.

[124] P. Wang, T. A. Meyer, V. Pan, P. K. Dutta, Y. Ke, *Chem* **2017**, *2*, 359–382.

[125] T. Tørring, N. V. Voigt, J. Nangreave, H. Yan, K. V. Gothelf, *Chem. Soc. Rev.* **2011**, *40*, 5636–5646.

[126] E. S. Andersen, M. Dong, M. M. Nielsen, K. Jahn, A. Lind-Thomsen, W. Mamdouh, K. V. Gothelf, F. Besenbacher, J. Kjems, *ACS Nano* **2008**, *2*, 1213–1218.

[127] S. M. Douglas, A. H. Marblestone, S. Teerapittayanon, A. Vazquez, G. M. Church, W. M. Shih, *Nucleic Acids Res.* **2009**, *37*, 5001–5006.

[128] E. Benson, A. Mohammed, J. Gardell, S. Masich, E. Czeizler, P. Orponen, B. Högberg, *Nature* **2015**, *523*, 441–444.

[129] H. Jun, T. R. Shepherd, K. Zhang, W. P. Bricker, S. Li, W. Chiu, M. Bathe, *ACS Nano* **2019**, *13*, 2083–2093.

[130] E. de Llano, H. Miao, Y. Ahmadi, A. J. Wilson, M. Beeby, I. Viola, I. Barisic, *Nucleic Acids Res.* **2020**, *48*, 8269–8275.

[131] H. Jun, X. Wang, M. F. Parsons, W. P. Bricker, T. John, S. Li, S. Jackson, W. Chiu, M. Bathe, *Nucleic Acids Res.* **2021**, *49*, 10265–10274.

[132] S. Dey, C. Fan, K. V. Gothelf, J. Li, C. Lin, L. Liu, N. Liu, M. A. D. Nijenhuis, B. Saccà, F. C. Simmel, et al., *Nat. Rev. Methods Prim.* **2021**, *1*, 13.

[133] X. C. Bai, T. G. Martin, S. H. W. Scheres, H. Dietz, *Proc. Natl. Acad. Sci. U. S. A.* **2012**, *109*, 20012–20017.

[134] K. F. Wagenbauer, C. Sigl, H. Dietz, *Nature* **2017**, *552*, 78–83.

[135] R. Veneziano, S. Ratanalert, K. Zhang, F. Zhang, H. Yan, W. Chiu, M. Bathe, *Science* **2016**, *352*, 1534.

[136] K. E. Bujold, A. Lacroix, H. F. Sleiman, *Chem* **2018**, *4*, 495–521.

[137] E. Stulz, *Chem. - Eur. J.* **2012**, *18*, 4456–4469.

[138] C. K. McLaughlin, G. D. Hamblin, H. F. Sleiman, *Chem. Soc. Rev.* **2011**, *40*, 5647–5656.

[139] E. Stulz, *Chimia* **2015**, *69*, 678–683.

[140] E. Stulz, *Acc. Chem. Res.* **2017**, *50*, 823–831.

[141] G. Fabrini, A. Minard, R. A. Brady, M. Di Antonio, L. Di Michele, *Nano Lett.* **2022**, *22*, 602–611.

[142] M. Walczak, R. A. Brady, L. Mancini, C. Contini, R. Rubio-Sánchez, W. T. Kaufhold, P. Cicuta, L. Di Michele, *Nat. Commun.* **2021**, *12*, 4743.

[143] R. A. Brady, N. J. Brooks, P. Cicuta, L. Di Michele, *Nano Lett.* **2017**, *17*, 3276–3281.

[144] S. I. S. Hendrikse, S. L. Gras, A. V. Ellis, *ACS Nano* **2019**, *13*, 8512–8516.

[145] J. R. Burns, E. Stulz, S. Howorka, *Nano Lett.* **2013**, *13*, 2351–2356.

[146] J. R. Burns, K. Göpfrich, J. W. Wood, V. V. Thacker, E. Stulz, U. F. Keyser, S. Howorka, *Angew. Chem. Int. Ed.* **2013**, *52*, 12069–12072.

[147] K. Göpfrich, C.-Y. Li, I. Mames, S. P. Bhamidimarri, M. Ricci, J. Yoo, A. Mames, A. Ohmann, M. Winterhalter, E. Stulz, et al., *Nano Lett.* **2016**, *16*, 4665–4669.

[148] L. Markova, M. Probst, R. Häner, *RSC Adv.* **2020**, *10*, 44841–44845.

[149] Y. Vyborna, S. Altunbas, M. Vybornyi, R. Häner, *Chem. Commun.* **2017**, *53*, 12128–12131.

[150] Y. Vyborna, M. Vybornyi, R. Häner, *Chem. Commun.* **2017**, *53*, 5179–5181.

[151] Y. Vyborna, M. Vybornyi, R. Häner, *Bioconjugate Chem.* **2016**, *27*, 2755–2761.

[152] Y. Vyborna, M. Vybornyi, R. Häner, *J. Am. Chem. Soc.* **2015**, *137*, 14051–14054.

[153] Y. Vyborna, M. Vybornyi, A. V. Rudnev, R. Häner, *Angew. Chem. Int. Ed.* **2015**, *54*, 7934–7938.

[154] A. Patwa, A. Gissot, I. Bestel, P. Barthélémy, *Chem. Soc. Rev.* **2011**, *40*, 5844–5854.

[155] S. P. W. Wijnands, E. W. Meijer, M. Merkx, *Bioconjugate Chem.* **2019**, *30*, 1905–1914.

[156] C.-J. Kim, J. Park, X. Hu, S. K. Albert, S.-J. Park, *ACS Nano* **2020**, *14*, 2276–2284.

[157] Y. Zhang, R. Peng, F. Xu, Y. Ke, *Bioconjugate Chem.* **2019**, *30*, 1845–1849.

[158] C. D. Bösch, J. Jevric, N. Bürki, M. Probst, S. M. Langenegger, R. Häner, *Bioconjugate Chem.* **2018**, *29*, 1505–1509.

[159] L. van Dam, N. Korolev, L. Nordenskiöld, *Nucleic Acids Res.* **2002**, *30*, 419–428.

[160] T. Thomas, T. J. Thomas, *Cell. Mol. Life Sci.* **2001**, *58*, 244–258.

[161] M. Mozdzan, J. Szemraj, J. Rysz, R. A. Stolarek, D. Nowak, *Int. J. Biochem. Cell Biol.* **2006**, *38*, 69–81.

[162] N. Seiler, F. Raul, *J. Cell. Mol. Med.* **2005**, *9*, 623–642.

[163] K. Igarashi, K. Kashiwagi, *Biochem. Biophys. Res. Commun.* **2000**, *271*, 559–564.

[164] H. C. Ha, N. S. Sirisoma, P. Kuppusamy, J. L. Zweier, P. M. Woster, R. A. Casero, *Proc. Natl. Acad. Sci. U. S. A.* **1998**, *95*, 11140–11145.

[165] E. Raspaud, I. Chaperon, A. Leforestier, F. Livolant, *Biophys. J.* **1999**, *77*, 1547–1555.

[166] B. G. Feuerstein, L. D. Williams, H. S. Basu, L. J. Marton, *J. Cell. Biochem.* **1991**, *46*, 37–47.

[167] U. Lächelt, E. Wagner, *Chem. Rev.* **2015**, *115*, 11043–11078.

[168] O. Boussif, F. Lezoualc'h, M. A. Zanta, M. D. Mergny, D. Scherman, B. Demeneix, J.-P. Behr, *Proc. Natl. Acad. Sci. U. S. A.* **1995**, *92*, 7297–7301.

[169] J.-L. Coll, P. Chollet, E. Brambilla, D. Desplanques, J.-P. Behr, M. Favrot, *Hum. Gene Ther.* **1999**, *10*, 1659–1666.

[170] Z. Chen, Z. Lv, Y. Sun, Z. Chi, G. Qing, *J. Mater. Chem. B* **2020**, *8*, 2951–2973.

[171] Y. Wang, C. Yu, *Angew. Chem. Int. Ed.* **2020**, *59*, 23374–23385.

[172] K. Ma, C.-L. Mi, X.-X. Cao, T.-Y. Wang, *Appl. Microbiol. Biotechnol.* **2021**, *105*, 525–538.

[173] M. L. Santana-Armas, C. Tros de Ilarduya, *Int. J. Pharm.* **2021**, *596*, 120291.

[174] D. van der Zwaag, E. W. Meijer, *Science* **2015**, *349*, 1056–1057.

[175] P. H. Lambrev, Z. Várkonyi, S. Krumova, L. Kovács, Y. Miloslavina, A. R. Holzwarth, G. Garab, *Biochim. Biophys. Acta* **2007**, *1767*, 847–853.

[176] G. S. Engel, T. R. Calhoun, E. L. Read, T. K. Ahn, T. Mančal, Y.-C. Cheng, R. E. Blankenship, G. R. Fleming, *Nature* **2007**, *446*, 782–786.

[177] S. Fery-Forgues, D. Lavabre, *J. Chem. Educ.* **1999**, *76*, 1260–1264.

[178] W. H. Melhuish, *J. Phys. Chem.* **1961**, *65*, 229–235.

[179] R. F. Goldstein, L. Stryer, *Biophys. J.* **1986**, *50*, 583–599.

[180] T. F. A. De Greef, M. M. J. Smulders, M. Wolffs, A. P. H. J. Schenning, R. P. Sijbesma, E. W. Meijer, *Chem. Rev.* **2009**, *109*, 5687–5754.

[181] D. Zhao, J. S. Moore, *Org. Biomol. Chem.* **2003**, *1*, 3471–3491.

[182] M. M. J. Smulders, M. M. L. Nieuwenhuizen, T. F. A. De Greef, P. Van Der Schoot, A. P. H. J. Schenning, E. W. Meijer, *Chem. - Eur. J.* **2010**, *16*, 362–367.

[183] P. Jonkheijm, P. van der Schoot, A. P. H. J. Schenning, E. W. Meijer, *Science* **2006**, *313*, 80–83.

[184] P. A. Korevaar, S. J. George, A. J. Markvoort, M. M. J. Smulders, P. A. J. Hilbers, A. P. H. J. Schenning, T. F. A. De Greef, E. W. Meijer, *Nature* **2012**, *481*, 492–496.

[185] T. Aida, E. W. Meijer, *Isr. J. Chem.* **2020**, *60*, 33–47.

[186] J. Dubochet, M. Adrian, J.-J. Chang, J.-C. Homo, J. Lepault, A. W. McDowall, P. Schultz, *Q. Rev. Biophys.* **1988**, *21*, 129–228.

[187] M. Adrian, B. ten Heggeler-Bordier, W. Wahli, A. Z. Stasiak, A. Stasiak, J. Dubochet, *EMBO J.* **1990**, *9*, 4551–4554.

[188] D. Demurtas, A. Amzallag, E. J. Rawdon, J. H. Maddocks, J. Dubochet, A. Stasiak, *Nucleic Acids Res.* **2009**, *37*, 2882–2893.

[189] M. J. Waring, *J. Mol. Biol.* **1965**, *13*, 269–282.

[190] C. G. Reinhardt, T. R. Krugh, *Biochemistry* **1978**, *17*, 4845–4854.

[191] F. J. Meyer-Almes, D. Porschke, *Biochemistry* **1993**, *32*, 4246–4253.

[192] J. Duhamel, J. Kanyo, G. Dinter-Gottlieb, P. Lu, *Biochemistry* **1996**, *35*, 16687–16697.

[193] S. Nafisi, A. A. Saboury, N. Keramat, J.-F. Neault, H.-A. Tajmir-Riahi, *J. Mol. Struct.* **2007**, *827*, 35–43.

[194] M. Hayashi, Y. Harada, *Nucleic Acids Res.* **2007**, *35*, e125.

[195] J. Cairns, *Cold Spring Harbor Symp. Quant. Biol.* **1962**, *27*, 311–318.

[196] J. B. Lepecq, C. Paoletti, *J. Mol. Biol.* **1967**, *27*, 87–106.

[197] J. Olmsted, D. R. Kearns, *Biochemistry* **1977**, *16*, 3647–3654.

[198] L. S. Lerman, *J. Mol. Biol.* **1961**, *3*, 18–30.

[199] M. A. Hink, N. V. Visser, J. W. Borst, A. van Hoek, A. J. W. G. Visser, *J. Fluoresc.* **2003**, *13*, 185–188.

[200] I. Z. Steinberg, *J. Chem. Phys.* **1968**, *48*, 2411–2413.

[201] I. Z. Steinberg, *Annu. Rev. Biochem.* **1971**, *40*, 83–114.

[202] D. P. Aden, A. Fogel, S. Plotkin, I. Damjanov, B. B. Knowles, *Nature* **1979**, *282*, 615–616.

[203] D. López-Terrada, S. W. Cheung, M. J. Finegold, B. B. Knowles, *Hum. Pathol.* **2009**, *40*, 1512–1515.

[204] B. Zhou, S. S. Ho, S. U. Greer, N. Spies, J. M. Bell, X. Zhang, X. Zhu, J. G. Arthur, S. Byeon, R. Pattni, et al., *Nucleic Acids Res.* **2019**, *47*, 3846–3861.

[205] S. I. Presolski, V. P. Hong, M. G. Finn, *Curr. Protoc. Chem. Biol.* **2011**, *3*, 153–162.

[206] Y. Wang, D. Wang, F. Jia, A. Miller, X. Tan, P. Chen, L. Zhang, H. Lu, Y. Fang, X. Kang, et al., *ACS Appl. Mater. Interfaces* **2020**, *12*, 45830–45837.

[207] X. Lu, K. Zhang, *Nano Res.* **2018**, *11*, 5519–5534.

[208] J. P. Bost, H. Barriga, M. N. Holme, A. Gallud, M. Maugeri, D. Gupta, T. Lehto, H. Valadi, E. K. Esbjörner, M. M. Stevens, et al., *ACS Nano* **2021**, *15*, 13993–14021.

[209] M. Nerantzaki, C. Loth, J.-F. Lutz, *Polym. Chem.* **2021**, *12*, 3498–3509.

[210] F. Jia, X. Lu, X. Tan, D. Wang, X. Cao, K. Zhang, *Angew. Chem. Int. Ed.* **2017**, *56*, 1239–1243.

[211] C. Bustamante, J. Vesenka, C. L. Tang, W. Rees, M. Guthold, R. Keller, *Biochemistry* **1992**, *31*, 22–26.

[212] J. Schindelin, I. Arganda-Carreras, E. Frise, V. Kaynig, M. Longair, T. Pietzsch, S. Preibisch, C. Rueden, S. Saalfeld, B. Schmid, et al., *Nat. Methods* **2012**, *9*, 676–682.

[213] J. C. Stachowiak, C. C. Hayden, D. Y. Sasaki, *Proc. Natl. Acad. Sci. U. S. A.* **2010**, *107*, 7781–7786.

[214] J. C. Stachowiak, E. M. Schmid, C. J. Ryan, H. Sook Ann, D. Y. Sasaki, M. B. Sherman, P. L. Geissler, D. A. Fletcher, C. C. Hayden, *Nat. Cell Biol.* **2012**, *14*, 944–949.

[215] D. J. Busch, J. R. Houser, C. C. Hayden, M. B. Sherman, E. M. Lafer, J. C. Stachowiak, *Nat. Commun.* **2015**, *6*, 7875.

[216] W. T. Snead, C. C. Hayden, A. K. Gadok, C. Zhao, E. M. Lafer, P. Rangamani, J. C. Stachowiak, *Proc. Natl. Acad. Sci. U. S. A.* **2017**, *114*, E3258–E3267.

[217] J. A. Kulkarni, D. Witzigmann, S. B. Thomson, S. Chen, B. R. Leavitt, P. R. Cullis, R. Van der Meel, *Nat. Nanotechnol.* **2021**, *16*, 630–643.

[218] S. Benizri, A. Gissot, A. Martin, B. Vialet, M. W. Grinstaff, P. Barthélémy, *Bioconjugate Chem.* **2019**, *30*, 366–383.

[219] A. D. Springer, S. F. Dowdy, *Nucleic Acid Ther.* **2018**, *28*, 109–118.

[220] Y. Huang, *Mol. Ther. - Nucleic Acids* **2017**, *6*, 116–132.

[221] A. J. Debacker, J. Voutila, M. Catley, D. Blakey, N. Habib, *Mol. Ther.* **2020**, *28*, 1759–1771.

[222] K. Schmidt, T. P. Prakash, A. J. Donner, G. A. Kinberger, H. J. Gaus, A. Low, M. E. Østergaard, M. Bell, E. E. Swayze, P. P. Seth, *Nucleic Acids Res.* **2017**, *45*, 2294–2306.

[223] P. C. N. Rensen, L. A. J. M. Sliedregt, M. Ferns, E. Kieviet, S. M. W. van Rossenberg, S. H. van Leeuwen, T. J. C. van Berkel, E. A. L. Biessen, *J. Biol. Chem.* **2001**, *276*, 37577–37584.

[224] P. H. Weigel, J. H. N. Yik, *Biochim. Biophys. Acta* **2002**, *1572*, 341–363.

[225] A. Cayley, *Phil. Mag.* **1859**, *17*, 123–128.

[226] M. Meier, M. D. Bider, V. N. Malashkevich, M. Spiess, P. Burkhard, *J. Mol. Biol.* **2000**, *300*, 857–865.

[227] W. E. Pricer, G. Ashwell, *J. Biol. Chem.* **1971**, *246*, 4825–4833.

[228] A. L. Schwartz, S. E. Fridovich, B. B. Knowles, H. F. Lodish, *J. Biol. Chem.* **1981**, *256*, 8878–8881.

[229] S. Wragg, K. Drickamer, *J. Biol. Chem.* **1999**, *274*, 35400–35406.

[230] T. P. Prakash, M. J. Graham, J. Yu, R. Carty, A. Low, A. Chappell, K. Schmidt, C. Zhao, M. Aghajan, H. F. Murray, et al., *Nucleic Acids Res.* **2014**, *42*, 8796–8807.

[231] J. Zhou, M. N. Creyer, A. Chen, W. Yim, R. P. M. Lafleur, T. He, Z. Lin, M. Xu, P. Abbasi, J. Wu, et al., *J. Am. Chem. Soc.* **2021**, *143*, 12138–12144.

[232] L. Lermusiaux, V. Many, P. Barois, V. Ponsinet, S. Ravaine, E. Duguet, M. Tréguer-Delapierre, A. Baron, *Nano Lett.* **2021**, *21*, 2046–2052.

[233] Y.-J. Kim, J.-H. Kim, I.-S. Jo, D. J. Pine, S. Sacanna, G.-R. Yi, *J. Am. Chem. Soc.* **2021**, *143*, 13175–13183.

[234] X. Liu, M.-A. Moradi, T. Bus, M. G. Debije, S. A. F. Bon, J. P. A. Heuts, A. P. H. J. Schenning, *Angew. Chem. Int. Ed.* **2021**, *60*, 27026–27030.

[235] W. Ma, A. Saccardo, D. Roccatano, D. Aboagye-Mensah, M. Alkaseem, M. Jewkes, F. Di Nezza, M. Baron, M. Soloviev, E. Ferrari, *Nat. Commun.* **2018**, *9*, 1489.

[236] V. Mangini, V. Maggi, A. Trianni, F. Melle, E. De Luca, A. Pennetta, R. Del Sole, G. Ventura, T. R. I. Cataldi, R. Fiammengo, *Bioconjugate Chem.* **2020**, *31*, 74–81.

[237] O. Vybornyi, S.-X. Liu, R. Häner, *Angew. Chem. Int. Ed.* **2021**, *60*, 25872–25877.

[238] S. Rothenbühler, C. D. Bösch, S. M. Langenegger, S.-X. Liu, R. Häner, *Org. Biomol. Chem.* **2018**, *16*, 6886–6889.

[239] E. I. Goksu, J. M. Vanegas, C. D. Blanchette, W.-C. Lin, M. L. Longo, *Biochim. Biophys. Acta* **2009**, *1788*, 254–266.

[240] J. Jevric, S. M. Langenegger, R. Häner, *Chem. Commun.* **2021**, *57*, 6648–6651.

[241] M. Kyropoulou, S. Yorulmaz Avsar, C.-A. Schoenenberger, C. G. Palivan, W. P. Meier, *Nanoscale* **2021**, *13*, 6944–6952.

[242] P. W. Münich, M. Pfäffli, M. Volland, S.-X. Liu, R. Häner, D. M. Guldi, *Nanoscale* **2020**, *12*, 956–966.

[243] Q. Sun, R. Zhang, J. Qiu, R. Liu, W. Xu, *Adv. Mater.* **2018**, *30*, 1705630.

[244] X. Zhou, G. Yu, *Adv. Mater.* **2020**, *32*, 1905957.

[245] M. Lackinger, *Chem. Commun.* **2017**, *53*, 7872–7885.

[246] L. Li, S. Mahapatra, D. Liu, Z. Lu, N. Jiang, *ACS Nano* **2021**, *15*, 3578–3585.

[247] A. M. Evans, M. J. Strauss, A. R. Corcos, Z. Hirani, W. Ji, L. S. Hamachi, X. Aguilar-Enriquez, A. D. Chavez, B. J. Smith, W. R. Dichtel, *Chem. Rev.* **2022**, *122*, 442–564.

[248] S. Kawai, M. Koch, E. Gnecco, A. Sadeghi, R. Pawlak, T. Glatzel, J. Schwarz, S. Goedecker, S. Hecht, A. Baratoff, et al., *Proc. Natl. Acad. Sci. U. S. A.* **2014**, *111*, 3968–3972.

[249] S. Kawai, A. Benassi, E. Gnecco, H. Söde, R. Pawlak, X. Feng, K. Müllen, D. Passerone, C. A. Pignedoli, P. Ruffieux, et al., *Science* **2016**, *351*, 957–961.

[250] R. Pawlak, J. G. Vilhena, P. D'Astolfo, X. Liu, G. Prampolini, T. Meier, T. Glatzel, J. A. Lemkul, R. Häner, S. Decurtins, et al., *Nano Lett.* **2020**, *20*, 652–657.

[251] R. Pawlak, X. Liu, S. Ninova, P. D'Astolfo, C. Drechsel, S. Sangtarash, R. Häner, S. Decurtins, H. Sadeghi, C. J. Lambert, et al., *J. Am. Chem. Soc.* **2020**, *142*, 12568–12573.

[252] R. Pawlak, X. Liu, S. Ninova, P. D'Astolfo, C. Drechsel, J.-C. Liu, R. Häner, S. Decurtins, U. Aschauer, S.-X. Liu, et al., *Angew. Chem. Int. Ed.* **2021**, *60*, 8370–8375.

[253] J. G. Vilhena, R. Pawlak, E. Gnecco, A. Hinaut, R. Pérez, T. Glatzel, T. Meier, E. Meyer, A. Baratoff, *Nat. Commun.* **2019**, *10*, 685.

[254] H. Dang, M. Levitus, M. A. Garcia-Garibay, *J. Am. Chem. Soc.* **2002**, *124*, 136–143.

[255] J. D. Wood, J. L. Jellison, A. D. Finke, L. Wang, K. N. Plunkett, *J. Am. Chem. Soc.* **2012**, *134*, 15783–15789.

[256] J. L. Jellison, C. H. Lee, X. Zhu, J. D. Wood, K. N. Plunkett, *Angew. Chem. Int. Ed.* **2012**, *51*, 12321–12324.

[257] C.-H. Lee, K. N. Plunkett, *Org. Lett.* **2013**, *15*, 1202–1205.

[258] X. Zhu, B. Yuan, K. N. Plunkett, *Tetrahedron Lett.* **2015**, *56*, 7105–7107.

[259] C. Schierl, W. Alex, L. M. Mateo, B. Ballesteros, D. Shimizu, A. Osuka, T. Torres, D. M. Guldi, G. Bottari, *Angew. Chem. Int. Ed.* **2019**, *58*, 14644–14652.

[260] X. Liu, Y. Du, A. Timmer, H. Mönig, X. Wan, X. Huang, Q. Ji, E. Kan, K. Ariga, J. P. Hill, et al., *J. Phys. Chem. C* **2019**, *123*, 16281–16287.

[261] A. Della Pia, M. Riello, J. Lawrence, D. Stassen, T. S. Jones, D. Bonifazi, A. De Vita, G. Costantini, *Chem. - Eur. J.* **2016**, *22*, 8105–8112.

[262] J. Hu, D. Zhang, F. W. Harris, *J. Org. Chem.* **2005**, *70*, 707–708.

[263] S. Kawano, M. Baumgarten, D. Chercka, V. Enkelmann, K. Müllen, *Chem. Commun.* **2013**, *49*, 5058–5060.

[264] G. Bianké, R. Häner, *ChemBioChem* **2004**, *5*, 1063–1068.

[265] H. Yang, H. F. Sleiman, *Angew. Chem. Int. Ed.* **2008**, *47*, 2443–2446.

[266] S. Ghosh, I. Pignot-Paintrand, P. Dumy, E. Defrancq, *Org. Biomol. Chem.* **2009**, *7*, 2729–2737.

[267] J. R. Burns, J. Zekonyte, G. Siligardi, R. Hussain, E. Stulz, *Molecules* **2011**, *16*, 4912–4922.

[268] M. A. Joaqui-Joaqui, Z. Maxwell, M. V. Ramakrishnam Raju, M. Jiang, K. Srivastava, F. Shao, E. A. Arriaga, V. C. Pierre, *ACS Nano* **2022**, *16*, 2928–2941.

[269] M. Linkert, C. T. Rueden, C. Allan, J.-M. Burel, W. Moore, A. Patterson, B. Loranger, J. Moore, C. Neves, D. MacDonald, et al., *J. Cell Biol.* **2010**, *189*, 777–782.

Declaration of Consent

Erklärung

gemäss Art. 18 PromR Phil.-nat. 2019

Name/Vorname: Rothenbühler Simon

Matrikelnummer: 13-103-783

Studiengang: Chemie und Molekulare Wissenschaften

Bachelor ☐ Master ☐ Dissertation ☑

Titel der Arbeit: DNA Architectonics: Self-Assembly of Amphiphilic Oligonucleotides into Supramolecular Nanostructures

LeiterIn der Arbeit: Prof. Dr. Robert Häner

Ich erkläre hiermit, dass ich diese Arbeit selbständig verfasst und keine anderen als die angegebenen Quel-len benutzt habe. Alle Stellen, die wörtlich oder sinn-gemäss aus Quellen entnommen wurden, habe ich als solche gekennzeichnet. Mir ist bekannt, dass andern-falls der Senat gemäss Artikel 36 Absatz 1 Buchstabe r des Gesetzes über die Universität vom 5. September 1996 und Artikel 69 des Universitätssta-tuts vom 7. Juni 2011 zum Entzug des Doktortitels be-rechtigt ist.
Für die Zwecke der Begutachtung und der Überprüfung der Einhaltung der Selbständigkeitserklärung bzw. der Reglemente betreffend Plagiate erteile ich der Univer-sität Bern das Recht, die dazu erforderlichen Perso-nendaten zu bearbeiten und Nutzungshandlungen vor-zunehmen, insbesondere die Doktorarbeit zu vervielfäl-tigen und dauerhaft in einer Datenbank zu speichern sowie diese zur Überprüfung von Arbeiten Dritter zu verwenden oder hierzu zur Verfügung zu stellen.

Ort/Datum

Unterschrift

Curriculum Vitae

Personal Information

Name: Simon Rothenbühler

Publications

S. Rothenbühler, I. Iacovache, S. M. Langenegger, B. Zuber, R. Häner. Complex DNA Architectonics – Self-Assembly of Amphiphilic Oligonucleotides into Ribbons, Vesicles, and Asterosomes. *Bioconjugate Chemistry* **2022**, DOI: 10.1021/acs.bioconjchem.2c00077.

S. Rothenbühler, A. Gonzalez, I. Iacovache, S. M. Langenegger, B. Zuber, R. Häner. Tetraphenylethylene-DNA Conjugates: Influence of Sticky Ends and DNA Sequence Length on the Supramolecular Assembly of AIE-Active Vesicles. *Organic & Biomolecular Chemistry* **2022**, DOI: 10.1039/d2ob00357k.

S. Rothenbühler, I. Iacovache, S. M. Langenegger, B. Zuber, R. Häner. Supramolecular Assembly of DNA-Constructed Vesicles. *Nanoscale* **2020**, *12*, 21118–21123.
Featured as *Hot Article* and among the most popular articles published in *Nanoscale* in 2020.

S. Rothenbühler, C. D. Bösch, S. M. Langenegger, S.-X. Liu, R. Häner. Self-Assembly of a Redox-Active Bolaamphiphile into Supramolecular Vesicles. *Organic & Biomolecular Chemistry* **2018**, *16*, 6886–6889.